Study of mechanical and electromechanical properties of SWCNTs materials by simulation and experimental methods in considering uncertainties

Xingling Tang

INSTITUT NATIONAL DES SCIENCES APPLIQUÉES DE ROUEN

ÉCOLE DOCTORALE SPMII

Sciences Physiques, Mathématiques et de l'Information pour l'Ingénieur

THÈSE

Pour obtenir le grade de

Docteur de Normandie Université délivré par l'Institut National des Sciences Appliquées de Rouen

Spécialité : Mécanique

Présentée et soutenue par

XingLing TANG

Soutenue le 24 mars 2015

Contribution à la simulation et à l'expérimentation des Nanotubes de carbones avec prise en compte d'incertitudes

Contribution to the properties of carbon nanotubes by simulation and experimental techniques considering uncertainties

Devant le jury composé de :

M. P.R. DAHOO	Rapporteur	Professeur à l'UVSQ
M. A. CHEROUAT	Rapporteur	Professeur à l'U.T de Troyes
M. X.L. GONG	Examinateur	Professeur à l'U.T de Troyes
M. P. POUGNET	Examinateur	PhD à VALEO, Paris
M. K. EL HAMI	Co-encadrant	Professeur à l'Université de Hassan1st, Maroc
M. M. EID	Co-encadrant	PhD Ingénieur-Chercheur, au CEA, Paris
M. A. EL HAMI	Directeur de thèse	Professeur à l'INSA de Rouen

Laboratoire d'Optimisation et de Fiabilité en Mécanique des Structures (LOFIMS)

Acknowledgements

First, I would like to express my deep gratitude to my supervisor, **Prof. Abdelkhalak EL HAMI,** for his invaluable guidance, support and patience throughout my PhD study. I am very grateful to **Dr. Mohamed EID** and **Prof. Khalil EL HAMI**, who gave me extraordinary support, read my thesis carefully and provided valuable suggestions.

I would like to acknowledge the China Scholarship Council (CSC) for the financial support during the period of my stay in France.

I would like to extend my appreciation to the **c**ommittee members: **Prof. Pierre Richard DAHOO, Prof. Abel CHEROUAT, Prof. Xiaolu GONG** and **Mr. Philippe POUGNET** for their encouragement and insightful comments on my thesis.

I would like to thank Prof. Hongqian XUE in Northwestern Polytechnical University (China) for his continuous encouragement and assistance since my master's study.

I would like to thank all the staff and all my colleagues who are working in LOFIMS in INSA de Rouen. Their support is gratefully acknowledged. I also would like to thank Mrs. Blanchard for her kind help in my work and life in France.

Special thanks to my friends: ZHANG Jie, TIAN Xilan, LI Renxian, DENG Hongju, YANG Biqi, GAO Xiaojuan, CHEN Yu, MI Hongmei and BAI Hao, my colleagues HUANG Changwu, CHU Lu, and Mickaël. I would like to give my thankfulness to the members of B606 and D110 in Northwestern Polytechnical University (China), and many other friends in France and in China for their valuable support and encouragement.

I am sincerely thankful and strongly indebted to my parents, my brother, my sisters and all my other family members for their continuous moral support and encouragement.

Finally, I offer my regards and blessings to all those who supported me in any respect during my PhD study.

Table of contents

List of figures

List of tables

Abstract

Carbon nanotubes (CNTs) are one of the most important nanomaterials today. It exhibits an exceptional combination of physical, electrical, mechanical, and chemical properties, which results in their great potential of industrial application in various fields. CNTs can be categorized as single-walled carbon nanotubes (SWCNTs) and multi-walled carbon nanotubes (MWCNTs). The structure of a SWCNT can be viewed as one-atom-thick layer of graphite rolled cylinder. Well understanding the property of SWCNTs is fundamental in both exploratory research and the potential applications for CNTs based products.

The present research is focused on evaluating the mechanical and electromechanical properties of SWCNTs materials under different morphologies. The elastic properties of the individual SWCNTs were studied using Finite element (FE) method. Effects of the diameter, chirality and length on the elastic moduli of SWCNTs were discussed based on numerical calculations. Furthermore, ultra-thin SWCNTs films (～200nm) were prepared by spin coating method. The elastic modulus of SWCNT thin film was estimated by nanoidentation test. Their elasto-plastic properties were then determined by FE simulation in considering the statistics constraints of the experimental results. The results showed that the mechanical performance of SWCNTs thin film during indentation can be approximately represented by a bilinear model. The mechanical properties of SWCNTs thin film obtained by experiment and numerical calculation are: the Young's modulus E=192.83± 13.922 Gpa, the tangent modulus $E_t \approx$ 42GPa, and the yield stress $\sigma_Y \approx$ 8.4GPa, respectively. The electrostrictive properties of SWCNT- based composite (SWCNT/P (VDF-TrFE)) were also investigated by FE method. Numerical results showed that the electrostriction of the SWCNT/P (VDP-TrFE) composite is greatly dependent on the volume fraction of SWCNT and the difference of dielectric constant between SWCNT and P (VDP-TrFE) copolymer.

In this work, we found that the properties of CNTs obtained either by theory or by experiments involve inevitable uncertainties, and some are relatively large. Therefore, uncertainty analysis for the predicted properties of CNTs becomes necessary in order to guarantee the performance requirements of products. The application of Reliability-Based Optimization (RBO) method in the elasto-plastic behavior estimation process for SWCNT thin film indicates that RBO method is an effective tool in ensuring the reliability of experimental and numerical results.

Keywords: Nanotechnology, Nanomaterials, Carbon nanotubes (CNTs), Single-walled carbon nanotubes (SWCNTs), Uncertainty, Reliability-Based Optimization (RBO)

Résumé

Possédants des propriétés physiques, électriques, mécaniques et chimiques exceptionnelles, les nanotubes de carbone (CNTs) sont considérés comme les nanomatériaux les plus importants aujourd'hui et donc sont proposées pour des applications industrielles potentielles en nanotechnologie. CNTs peuvent être classées en deux catégories : les nanotubes de carbone à paroi simple ou mono feuillet (SWCNTs) sous les initiales anglaises single walled carbon nanotubes et les nanotubes de carbone à parois multiples ou multi feuillet (MWCNTs) sous les initiales anglaises multi walled carbon nanotubes. La structure d'un SWCNT peut être considérée comme feuille de graphite d'épaisseur d'un atome roulé dans sous forme de tube cylindrique constitué d'anneaux de 6 carbones. Les tubes cylindriques peuvent avoir une ou deux extrémités enfermées par un hémisphère. Les propriétés des SWCNTs sont fondamentales pour la recherche scientifique et pour de nombreuses applications en médecine, en électronique, en environnement, pollution, …..

L'objectif de cette thèse est d'étudier les propriétés mécaniques et électromécaniques des matériaux SWCNTs avec différentes morphologies. Nous avons étudié les propriétés élastiques des SWCNTs individuels en utilisant la méthode des éléments finis (FE). Nous avons discuté et montré les effets du diamètre, de la chiralité et de la longueur sur les modules élastiques de SWCNTs. Nous avons montré que les modules élastiques augmentent significativement selon les plus petites valeurs du rayon. Lorsque le rayon devient plus grand, tous les modules élastiques convergent vers une valeur constante asymptotique. En outre, les modules des SWCNTs de types zigzag et chirale sont plus sensibles à la variation du rayon par rapport à celui du type fauteuil.

Nous avions pu déterminer expérimentalement, en utilisant le technique de la nanoindentation, le module élastique du film ultra-mince de SWCNT. En effet, les valeurs expérimentales du module d'Young E et celle de la dureté H du film ultra-mince de SWCNT sont respectivement E= 192.83± 13.922 GPa, H=12.57719 ± 0.759 GPa. Ensuite, nous avons élaboré un modèle par éléments finis qui représente le comportement des films ultra-minces de SWCNT dans le processus de la nanoindentation. Dans cette étude nous avons élaboré un modèle elasto-plastique pour décrire le comportement mécanique du matériau au cours de l'indentation. Une comparaison était présentée dans le but d'évaluer les propriétés élasto-plastiques du film ultra-mince de SWCNT en utilisant la simulation par éléments finis avec les données statistiques du test expérimental. Le modèle bilinéaire proposé donne une bonne approximation de la performance du film ultra-mince de SWCNT dans la nanoindentation.

Finalement, nous avons consacré une grande partie pour étudier, par la méthode des éléments finis, les propriétés électrostrictives du composite à base du copolymère de polyfluorure de vinylidene et trifluoroethylene P(VDF-TrFE) et des SWCNTs. Les résultats numériques trouvés montrent que l'électrostriction du composite (P(VDF-TrFE)/SWCNT) dépend considérablement de la fraction volumique de SWCNT et du rapport des constantes diélectriques du SWCNT et du P (VDF-TrFE).

Au cours de cette investigation, nous avons constaté que les propriétés des CNTs obtenues théoriquement ou expérimentalement impliquent des incertitudes inévitables. Par conséquent, la prise en compte de ces incertitudes dans la prediction des propriétés des CNTs s'avère nécessaire. Pour cela, nous avions recours à la méthode de l'optimisation basée sur la fiabilité (RBO). Cette méthode est un outil efficace pour assurer la fiabilité des résultats expérimentaux et numériques dans le processus d'estimation du comportement élasto-plastique pour SWCNT.

Mots-clés: nanotechnologies, les nanomatériaux, les nanotubes de carbone(CNT), les nanotubes de carbone à paroi simple(SWCNT), l'incertitude, l'optimisation de la fiabilité-Basé (RBO).

General Introduction

This thesis focuses on studying the excellent properties of nanomaterials, especially for the single wall based carbon nanotubes (SWCNTs). Carbon nanotube (CNT) materials exhibit a hierarchical structure with the diameter changing from ～1nm (single carbon nanotube) to ～1μm (carbon nanotube fiber). Properties of CNT material greatly depend on their structural states and dimensions. In this work, the properties of SWCNTs based materials were investigated with different SWCNTs formations, which includes: 1) study the mechanical properties of the individual SWCNTs using Finite Element (FE) method; 2) estimation of the elasto-plastic properties of SWCNT thin film by nanoindentation test and FE simulation; 3) exploring the electrostrictive properties of SWCNT based composite (the SWCNT /P (VDF-TrFE) composite).

Since the properties of CNTs are diverse and unstable (may sensitive to its structure, distribution, morphology, environment, etc.), this work estimated the uncertain factors of the elastic properties of SWCNT thin film in nanoindentation test. The Reliability-Based Optimization (RBO) method was adopted to estimate its elasto-plastic properties, which makes the numerical prediction efficient and reliable.

Motivation and objective

Motivation

To date, nanotechnology and nanomaterials are recognized to have a wide range of applications in a variety of fields. As one of the most important nanomaterials, CNTs have

CNTs can be categorized as single-walled carbon nanotubes (SWCNTs) and multi-walled carbon nanotubes (MWCNTs). The structure of a SWCNT can be viewed as one-atom-thick layer of graphite rolled cylinders with the diameter of 1～2 nm; while, MWCNTs are multi-layer graphite rolled either in concentric seamless cylinders or a helical layered cylinder. Since the superlative properties of CNTs are structural dependent (Li et al. 2007), well understanding the properties of SWCNTs is fundamental in exploring the new researches and the potential applications of CNTs based products. In recent years, much work has been done in describing the properties of CNTs. However, most of the predictions are based on an atomically-perfect or a structural-perfect ideal CNT model, which may be far from the practical situations. Due to the use of inappropriate model or the unexpected errors, some predictions may be even unacceptable. Therefore, uncertainty analysis for the prediction of CNTs properties becomes essential.

Reliability-based optimization (RBO) has been demonstrated as a powerful methodology for solving problems under uncertainty. In RBO, the uncertain factors are combined in the system performance model in terms of probability form under the target of a reliable solution. Successful applications of RBO in engineering enlighten us that RBO could be an effective tool in estimating the properties of CNT materials with great uncertainty.

Objective

Motivated by the research and the developments on CNTs as mentioned above, this thesis aims to study the mechanical and electromechanical properties of SWCNTs materials with different material morphologies. The elastic properties of the individual SWCNT were studied using FE method at first. The elastic modulus of SWCNT thin film was tested by nanoidentation technique, and its elasto-plastic properties were then evaluated in combination of FE simulation under the statistics constraints of the experimental test. The electrostrictive properties of SWCNT based composite (the SWCNT/P (VDF-TrFE) composite) were then investigated. The Organization of the thesis is described in the following.

Organization of the thesis

This thesis is organized as five chapters. In chapter 1, 2, 3, the mechanical properties of SWCNTs and SWCNT thin film were demonstrated. In chapter 4, the electrostrictive properties of SWCNTs based composite (SWCNT/P (VDF-TrFE)) was studied. As the estimated properties of SWCNT based material involve inevitable uncertainties, RBO method was proposed to solve these kinds of uncertain problems in chapter 5. This chapter also presented the application of RBO method in the estimation of elasto-plastic properties of SWCNT thin film. The contents of each part are as following:

In chapter 1, the basic concepts, fundamental properties, and main applications of nanotechnology and nanomaterials were briefly introduced. CNTs, as one of the most popular nanomaterials nowadays, their excellent properties in electronic, thermal, mechanic, and aspect ratio were summarized. Mainly methods for the preparation of CNTs were also presented briefly.

In chapter 2, the Young's and shear moduli of armchair, zigzag and chiral SWCNTs with different radii and lengths were numerically predicted. A 3D finite element model is presented. By establishing the approximate equivalent relationships between the molecular mechanics and the structural mechanics in SWCNTs, the interatomic interactions of C-C atoms were simulated by the appropriate straight spring and torsional spring elements. Through this approximation, a non-continuum finite element model was adopted to evaluate the influence of dimension, chirality and length on Young's and Shear moduli of SWCNTs.

In chapter 3, the SWCNT thin films (～200nm) were prepared by spin coating method. The hardness and elastic modulus of SWCNTs thin film were evaluated by nanoindentation test. Based on the principles and methods of uncertainty assessments in measurement, the uncertainties of the obtained elastic properties of SWCNT thin film in nanoindentation were calculated.

In chapter 4, the electrostrictive properties of the polyvinylidne fluoride and trifluoroethylene P (VDF-TrFE) copolymer and SWCNT based composites (SWCNT/P (VDF-TrFE)) were investigated. A 3D finite element model was proposed to predict the electrostrictive deformation of the SWCNT/P (VDF-TrFE) composite under electrostatic field. A bond electrical contact model was adopted in the numerical simulation process. The effects of volume fraction of SWCNT, the electric filed strength and the chirality of SWCNT to the electrostriction of SWCNT/P (VDF-TrFE) composite were discussed.

In chapter 5, as one of the efficient methods in dealing with engineering optimization problems under uncertainty, the reliability-based optimization (RBO) method was briefly presented. The elasto-plastic properties of the SWCNTs thin film were estimated by combining the FE technique and the nanoindentation results. RBO methodology was applied to ensure the reliability of estimation. In this study, the distribution of load-displacement curve in unloading process was considered in reliability analysis.

The conclusions and perspectives of this work are summarized at the end of this thesis.

Chapter 1. Introduction to Nanotechnology, Nanomaterials, and Carbon Nanotubes

In this chapter, we outline the fundamental properties and applications of nanomaterials and nanotechnology. Carbon nanotubes, as one of the most promising nanomaterials nowadays, their excellent properties in electronic, thermal, mechanic, and aspect ratio are summarized. Methods for the preparation of carbon nanotubes are also briefly introduced.

1.1. Introduction

Nanoscience is considered as the scientific study at nanometer scale including elaboration, observation, characterization, analysis, modeling of miniaturized materials with new properties.

Nanotechnology has many definitions in the literature but the trivial one, to our knowledge, can be defined as the application of nanoscience in industrial manner and daily lives. The prefix Nano can be referred to the application of extremely small things. Nanotechnology is almost involved in all engineering domains such as mechanic, electronic, computer, optic, energy, chemistry, biology, metrology, informatics, automotive industry, security (defense), aeronautic, medicine, intelligent textiles, cosmetic, etc. Nanotechnology is a scientific revolution in miniaturization. The surprising thing is that the market budget of the nanotechnology will reache 1000 billion dollars at the year 2015, and more than 70 countries have adopted the strategy of research and development in nanotechnology.

Richard Feynman, the brilliant physicist and Nobel Laureate in 1965, is generally recognized as the first person who introduced the concept of nanotechnology in his famous lecture in 1959 "There's Plenty of Room at the Bottom", in which he suggested that it would be possible to arrange the atoms in the way we want (American Elements 2014). Recently, development of nanotechnology has been spurred by incremental requirements in exploring the tailored properties of nanomaterials for industry, environmental, medicine, and science applications. Thanks to the invitations of Scanning Tunneling Microscope (STM), Transmission Electron Microscopy (TEM), Atomic Force Microscope (AFM), and other microscope devices, it is possible to precisely characterize and employ nanomaterials. The evolving synthesis and assembly strategies of nanomaterials enable to better control it in size, shape, structure, and arrangement. While, techniques in controlling the properties' stability of nanostructures or nanomaterials are still a challenge because of the nanoscale level.

Nanomaterials refer to materials in nanometer scale (10^{-9} meter). They are 1000 times smaller than a human hair, 10 times smaller than a bacterium, and some nanomaterials are just the size of a virus. Having unique properties derived from features present in them whose dimensions (at least one dimension) are less than 100 nanometers (Anon 2013a), nanomaterials can be metals, ceramics, polymeric materials, or composite materials. Since having outstanding electrical, optical, magnetic and mechanical properties, nanomaterials have attracted considerable interests over the past two decades. On the other hand, some kinds of nanomaterials have caused a lot of controversy on the toxicity phenomena. Up to now, the problem that nanomaterial effects on biological cell still persists and does not have good solution. We can just say that certain nanomaterials can cross biological barriers that the traditional materials cannot.

Carbon nanotube is one of the most extraordinary nanomaterials. Because of its

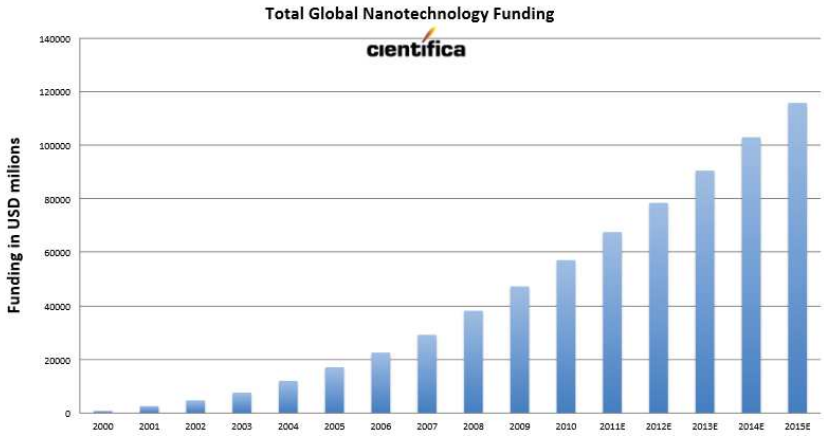

The applications of nanomaterials are dependent on their novel chemical, physical and mechanical properties. Rapidly developed nanotechnology enhances our understanding of the substance key properties of the materials and structures, and which offers us the possibility to further predict and control the materials properties at a sub-micron level in design and manufacturing processes. Nanostructures are manipulated through the tailor of architectures at atoms, molecular or super molecular levels. The improved physical, chemical, mechanical and biological properties give rise to the exploration of new materials and new technologies in applications. The most promising applications of nanotechnology are included as following:

Composites: one of the important applications of nanotechnology is composites. Materials designed in combining the properties of more than one component may exhibit optimized properties simultaneously in electrical, mechanical, chemical, and optical etc. For example, Multi- or Single-walled CNTs are used in polymer matrix to improve the mechanical strength and thermal resistance of structures (Wang et al. 2007).

Nanoelectronic devices: nanoparticles or fibers can be integrated into smart devices and has broad applications in variety of fields, such as computer chips, nano-sensor, electrical switching, emission amplification, and more efficient solar cells.

Biomedicine: Nanotechnology has great potential application in medical diagnosis and treatment. It has been reported that nanoparticles can be efficiently applied for drug delivery in cancer therapy; biological nanostructures can be synthesized for disease detection; and nanochemical structures can be applied in tissue engineering (Anon 2002).

Environment: applications of nanotechnology in environment have been developed over the past years, such as remediation of environmental pollution and renewable energy production (Mansoori, G. Ali, T. Rohani Bastami 2008).

1.2.1. Nanomaterials

There are different kinds of nanomaterials based on different ways of classifications. Based on the origin of the materials, nanomaterials can be classified as natural nanomaterials and man-made nanomaterials. Based on the dimensions of its structure, nanomaterials can be classified as zero-dimensional, one-dimensional, two-dimensional, and three-dimensional nanomaterials (Pokropivny et al. 2007). Based on the structure configuration, nanomaterials can be classified as carbon-based nanomaterials, metal-based nanomaterials, dendrimers nanomaterials, and nanocomposites (National Geographic 2014).

Nanomaterials classification according to the origin of the materials

- *Natural nanomaterials* are those that occur naturally in nature, such as nanoclays, the structure of foraminifera and viruses, horny materials of human body, etc. (Wikipedia 2014).
- *Man-made nanomaterials* are those that occur from objects or process synthetic by man like engineered nanomaterials.

Nanomaterials classification according to the dimensions

Zero−dimensional (0D) nanomaterials define materials wherein all the dimensions are measured within the nanoscale. The most common representation of 0D nanomaterials is nanoparticles, which possess the properties inherent to nanomaterials but not to single atoms, such as uniform particles arrays, heterogeneous particles arrays, hollow spheres, etc. The 0D nanomaterials have been extensively studied in the optimization of conventional components such as light emitting diodes (Stouwdam & Janssen 2008), solar cells (Beek et al. 2004), Optical filtres (Duyne et al. 2003), single-electron transistors (Bolotin et al. 2004), etc.

One−dimensional (1D) nanomaterials are nanomaterials with the one dimension quantum wires in diameter in nanoscopic but microscopic in length. 1D nanomaterials have stimulated an increasing interest in the last decade due to their wide range of potential applications. It has reported that 1D nanomaterials are a type of ideal materials for exploring the novel phenomena at nanoscale and their unique size-dependent properties. For example, with unique surface plasmon resonance (SPR) ranging from visible to near infrared (NIR) region, gold nanorods (GNRs) have been proved having great application potentials in biomedical imaging, drug delivery and photothermal (Ma et al. 2013), (Pissuwan et al. 2008). Carbon nanotubes are demonstrated exhibiting excellent electronic, optical, magnetic, thermal, and mechanical properties in recent, which is capable in the applications of nanoelectronics, nanodevices, energy resources, etc. (HARRIS & HARRIS 2009).

Two− dimensional (2D) nanomaterials are nanomaterials with two of the dimensions are not confined to the nanoscale, which exhibit plate-like shapes such as nanofilms, nanolayers, nanocoatings, and nanodisks. The 2D nanomaterials with unique layer structure characteristic exhibit novel capacity in application of nanodevices such as sensor, nanocreaters, nanocontainers, etc. ((Kam et al. 2013), (Kim et al. 2010)) .

Three−dimensional (3D) nanomaterials include powders, fibrous, multilayer and polycrystalline materials in which they possess a nanocrystalline structure or involve the features at the nanoscale, while their dimensions are not confined to the nanoscale. The properties of 3D nanomaterials strongly dependent on their

shape, dimensionality, and morphologies. Therefore control of the structure and morphology in synthesis is a hot topic in recent. Besides, owing to the large specific surface area and the quantum size resulted bulking property, 3D nanomaterials have attracted considerable interests in both academic and industry ((Kamarudin et al. 2009), (Nanomat Inc 2013)).

Fig. 1.2 illustrates the applications of nanomaterials with different dimensions. (i) 0D nanomaterial in therapeutic applications: some inorganic nanoparticles used for the imaging and treatment of tumours: superparamagnetic iron oxide nanoparticle (SPION), (A) inorganic core–shell nanoparticle such as QD (B), AuNP (C) and inorganic nanoclusters (D). (Nazir et al. 2014). (ii) 1D magnetite nanostructure: High aspect ratio Fe3O4 nanobelts with widths of 0.1–2 μm, thicknesses of about 10 nm and lengths of 20–30 μm (Shi1 et al. 2012). (iii) A phononic crystal device fabricated in silicon nitride (SiN) using electron-beam lithography. Green = SiN, blue and red lines = aluminium and copper heaters and thermometers, and black areas = holes (Zen et al. 2014). (iv) (SEM images and modeling of 3D structures made through a one photon process with mask 1 (d=570 nm, h=510 nm, p=710 nm, circular dot). (a) large area angled view, (b) top view, (c) cross sectional view and modeling (inset) (Jeon et al. 2006).

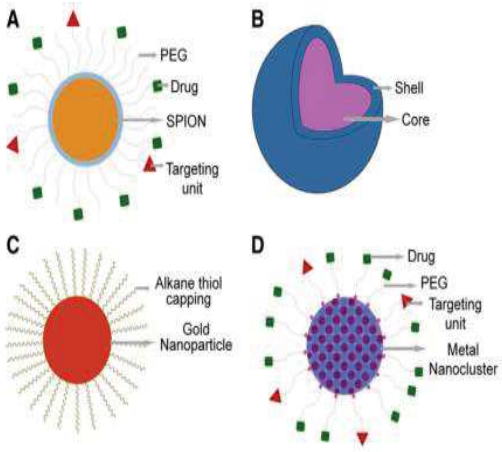

(i)

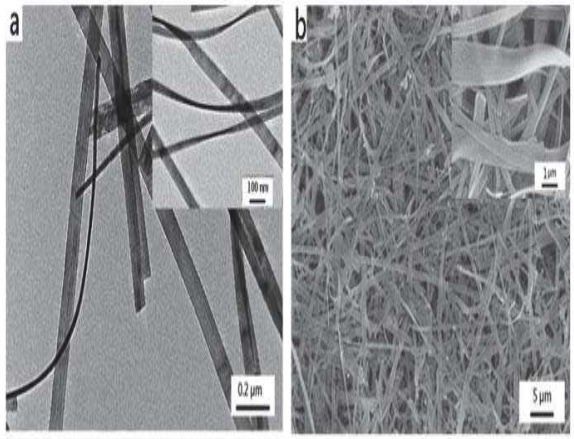

(ii)

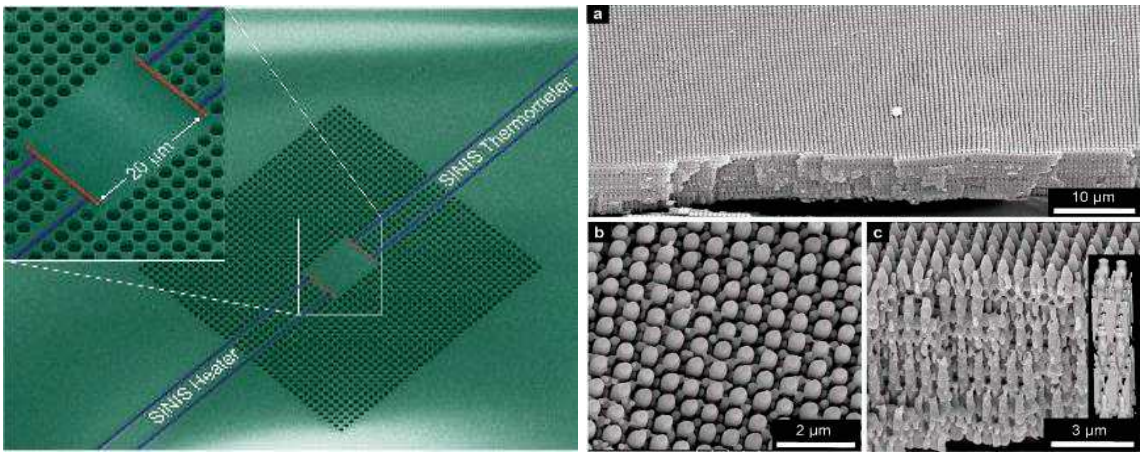

(iii) (iv)

Fig. 1.2 Nanomaterials in applications (Nazir et al. 2014), (Shi1 et al. 2012), (Zen et al. 2014),), (Jeon et al. 2006)

Nanomaterials classification according to the configurations

Carbon-based nanomaterials are intentionally produced fullerenes, which involve carbon nanotubes and buckyballs (National Geographic 2014). For carbon-based nanomaterial, their novel electronic, optical, mechanical and thermal properties are strongly structural and conformational dependent, such as the size, the length and the chirality. Various synthesis methods and techniques are developed for obtaining purity, optimized nanomaterial structure and physical orientation for specific application.

- *Metal-based nanomaterials* include gold nanoparticles and quantum dots. With distinctive properties of chemical stability, semiconductivity and its unique optical properties, gold nanoparticles and quantum dots have successfully applied in nionanotechnology (Hutter & Maysinger 2011), (Doria et al. 2012). For example, metal nanoparticles are being considered for potential use in catalytic converters since the catalytic reactivity would be significantly enhanced due to the increased surface area of the metal.
- *Dendrimers nanomaterials* are highly branched, star-shaped macromolecules with nanometer-scale dimensions as shown in Fig. 1.2 (i). Each dendrimer has three sections: a core, an inner shell, and an outer shell. The varied combination of these components yields products of different shapes and sizes with shielded interior cores that are ideal candidates for applications in biological, environmental and materials sciences (Hecht & Fre 2001), (Ren et al. 2013).
- *Nanocomposites* are composites in which at least one of the phases has one, two or three dimensions in the nanometer range. Nanocomposites are considered to be alternative materials that overcome the limits of monolithic materials. Nowadays, continuous refinements in synthesis technologies provide the possibilities in

controlling of elemental composition and stoichiometry in the nanocluster phase, which allow us to obtain a material with superior properties. For example, incorporation of nanotubes in polymer matrices can greatly improve material's properties in respects of physics, tribology, fracture toughness, and mechanics, even at very low fractions (Deshmukh & Ounaies 2009), (Zhang et al. 2008).

1.2.2. Preparation of nanomaterials

In nanotechnology, the development of synthesis technologies for preparing nanomaterials within a range of sizes, constructions, and chemical compositions is extremely important. The way of nanomaterials producing can be classified as: top-down approach and bottom-up approach. Both approaches can be done in either gas, liquid, supercritical fluids, solid states, or in vacuum. The schematic of these two approaches are presented in Fig. 1.3.

The top-down approach is to start with a bulk material and then break it into smaller pieces using mechanical, chemical or other form of energy. This approach often uses the traditional workshop or microfabrication methods where externally controlled tools are used to cut, mill, and shape materials into the desired shape and order, such as arc discharge, laser ablation, solar flux, anodizing, etc.

The bottom-up methods of nanomaterials synthesis start with atoms or molecules and build up to nanostructures through chemical reactions. Methods to produce nanomaterials through chemical transformations include sol-gel processing, chemical vapour deposition (CVD), plasma or flame spraying synthesis, laser pyrolysis, and atomic or molecular condensation.

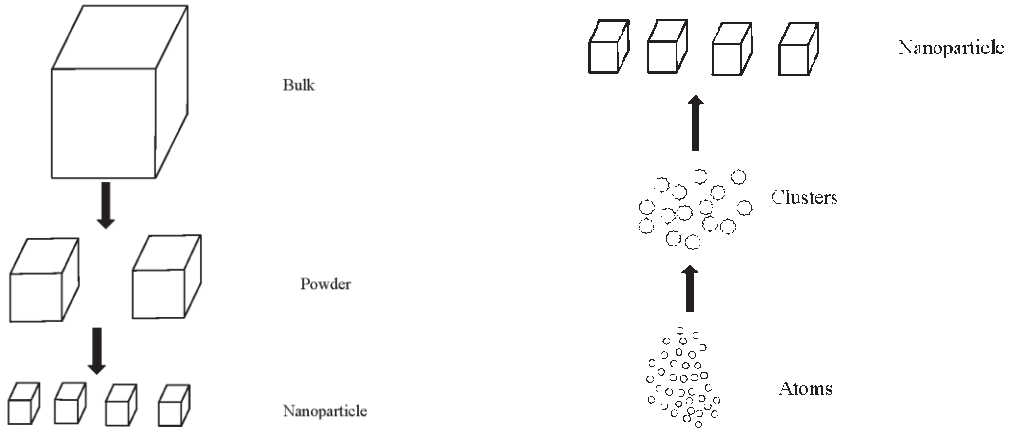

Fig. 1.3 Schematic representation of produce nanostructure by the top-down and bottom-up approaches (Sri D. Suneel n.d.)

1.3. Carbon nanotubes (CNTs)

Carbon nanotubes (CNTs) are allotropes of carbon with a cylindrical nanostructure, which have attracted great attention in both industry and academic since their discovery in 1991 (Iijima 1991). According to the number of rolled layer, CNTs are categorized as single-walled carbon nanotubes (SWCNTs) and multi-walled carbon nanotubes (MWCNTs). The structure of a SWCNT can be thought of as one-atom-thick layer of graphite rolled cylinders with the diameter of 1～2 nanometer; while, the MWCNTs are multi-layer graphite rolled either arranged in concentric seamless cylinders or arranged as a helical layer cylinder as shown in Fig. 1.4. The diameters of MWCNT are typically in the range of 4 ～50 nanometer (Mittal 2010), and its structure is less well understood because of the greater complexity and variety of different chiralities.

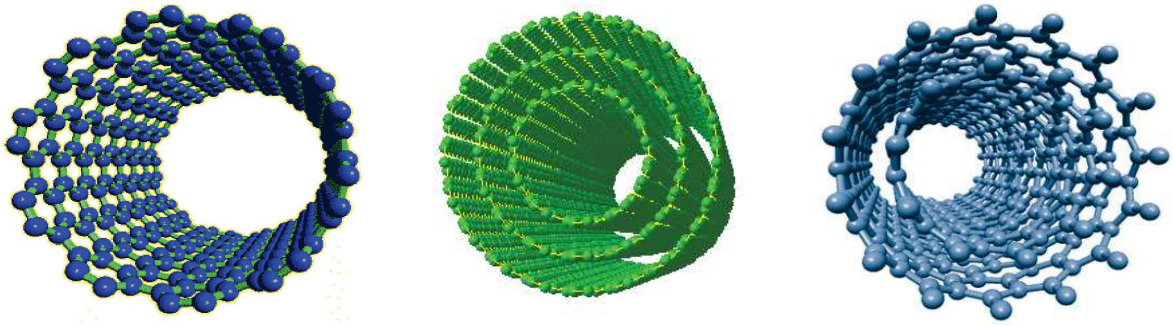

Fig. 1.4 Structures of SWCNTs and MWCNTs

1.3.1. Properties of CNTs

CNTs have become promising candidates in various nanometer scales of electronic and mechanical devices, and reinforcement in composite, due to the exceptional physical, electrical and mechanical properties. These novel properties and their applications are presented as following.

1.3.1.1. Electronic properties of CNTs

Electronic properties are one of the most important features of CNTs. For an individual SWCNTs, it exhibits either semiconducting or metallic performance depending on its diameter and chirality (Wilder et al. 1998). These different types of SWCNTs can be explored for the use of advanced microscopic devices. For example, semiconducting SWCNTs based field-effect transistors (FETs) were made due to the high mobility (up to ~10000cm^2/Vs at room temperature) and low resistance (~6 KΩ) (Tans et al. 1998), (Zhou et al. 2005); with

low resistance and high current-carrying capacities (up to ~10^9A/cm^2), metallic SWCNTs are adopted as conductors for advanced electrical interconnects (Yao et al. 1999).

Comparing with SWCNT, the MWCNTs, with larger number of atoms and inter-tube interactions make the theoretical studies of electronic properties more challenging. As the simplest MWCNTs, double-wall nanotubes (DWCNTs) are theoretically studied. The electronic properties of MWCNTs are then deduced analogically. For example, Kwon & Toma's study (Kwon & Toma 1998) indicates that the strong coupling between the libration mode and the electronic states at the Fermi level for DWCNTs may lead to the superconducting behavior, and this superconductive phenomenon can be extended to n-wall nanotubes (Takesue et al. 2006). Electrical measurement on individual MWCNTs was carried out by Langer et al (Langer et al. 1996) to measure the electrical resistance of an individual CNTs. Their test demonstrated that the electrical resistance is a function of temperature down to T=30mK, and was found to rise with falling temperature.

Theoretical and experimental researches also demonstrate that the external electric or magnetic field has a profound effect on the electronic properties of individual CNTs and nanotube bundles. Christian and his colleagues (Bachtold et al. 1999) reported their observation of Aharonov-Bohm oscillations in MWCNTs. In their experiment, the electrical resistance of MWCNTs with diameters around 16 nm were measured as a function of magnetic field B. Using Hartree-Fock and density functional quantum mechanics simulations, Guo &Tang predict a large axial electrostrictive deformation in SWCNTs under external electric field (Guo & Guo 2003), (Tang et al. 2006). Their simulation results also demonstrate that the electrostrictive deformation of nanotubes mainly caused by the elongation of the C-C bonds and the distortion of the carbon hexagonal rings under the changing electric field. A significant electrostriction strain was firstly observed in SWCNTs bundles in Khalil El-Hami's experiment by using the AFM technique (El-Hami & Matsushige 2005).

1.3.1.2. Thermal properties of CNTs

Both theoretical and experimental examinations demonstrate that the specific heat and thermal conductivity of CNTs are greatly dependent on their graphitic nature, the unique structure and size. Because of the quantum effects, the specific heat of CNTs is dominated by its phonon band structure at low temperature (as the ratio between the phonon and electron specific heat large $C_{ph}/C_{el}\approx100$), and exhibit a temperature dependent performance (Yi et al. 1999). Fig. 1.5 (a) illustrates the comparison of the measured specific heat of SWNTs and the predicted values of isolated (10, 10) tubes, SWCNT ropes, a graphene layer and graphite. Fig. 1.5 (b) illustrates the comparison of measured specific heat of MWCNTs with the calculated phonon specific heat of graphene, graphite, and isolated nanotubes (Hone 2001).

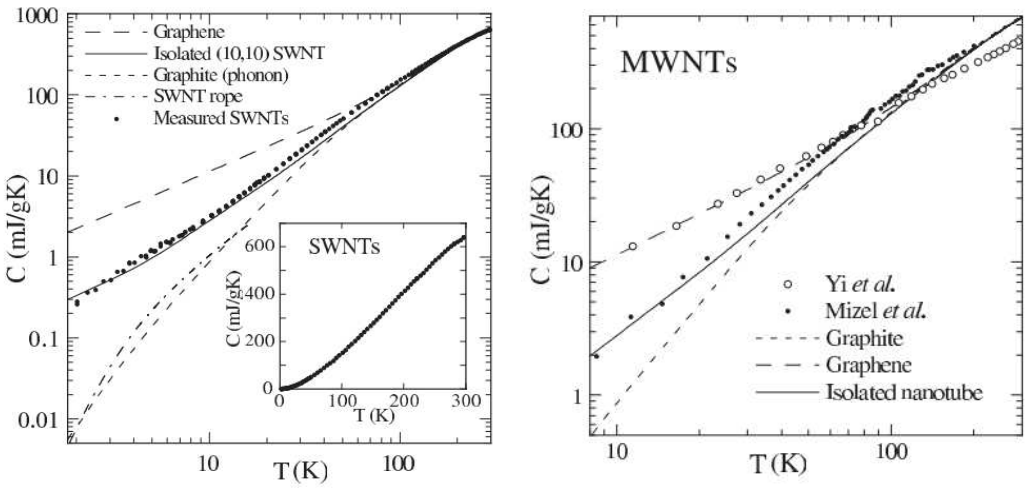

(a) (b)

Fig. 1.5 CNTs specific heat vs temperature (Hone 2001).

Crystalline carbons display the highest measured thermal conductivity of all known materials at moderate temperatures. For pure diamond, the thermal conductivity is at the range of 2000～2500 W/mK (Harris & Harris 2009). For CNTs, J. Hone *et al.* measured the temperature-dependent thermal conductivity of SWCNT ropes, and found the thermal conductivity vs temperature displays a linear relationship below 30 K (Hone et al. 1999). They proposed a model to explain the low temperature behavior, and found that the thermal conductivity for a single rope at room temperature could vary between 1800−6000 W/mK. Their suggestion of an unusually high value of thermal conductivity for SWCNT at room temperature was confirmed theoretically by Berber *et al.* (Berber et al. 2000), who suggested an unusually high value of thermal conductivity about 6600 W/mK for an isolated (10, 10) nanotube at room temperature. Berber *et al.* inferred that these high values of thermal conductivity would be due to the large phonon mean free paths in the systems. Both groups stated that these values for thermal conductivity are comparable to diamond or to a graphite layer. Measurement of thermal conductivity were also carried out for CNT films (Hone et al. 2000), (Aliev et al. 2010). Thermal conductivity of MWCNT films with thickness from10 to 50mm were measured around 15 W/m K at room temperature by Yang *et al.* (Yang et al. 2002), they indicated that the smaller thermal conductivity for bulk CNT samples compared with single tube may result from heat losses to internal gaps among the tubes, the intertube coupling and the high density defects of CNTs. The excellent thermal property makes CNTs potential candidate in the applications of heat conduction, thermal circuits, thermal management, etc.

1.3.1.3. Mechanical properties of CNTs

Mechanical properties study of CNTs is attracting as much interest as its electronic properties. To date, it is established that CNTs are the strongest and stiffest materials in nanoscale elements. The Young's modulus of the nanotube can be as high as ~1TPa and its tensile strength can be up to 63 GPa, which are much higher than the steel. Moreover, it has been demonstrated that the mechanical deformation of CNTs can cause considerable changes in its electronic, optical, magnetic, and chemical properties (Shima 2011), and display unique coupling between the electrical properties and mechanical deformation (Tombler et al. 2000). The high strength coupled with their low densities and other excellent electronic and thermal properties, CNTs are extensively introduced as the reinforcement in composites or applied in electromechanical coupling systems (EMS).

- **Theoretical predictions for mechanical properties of CNTs**

The primary reports for mechanical properties predictions of CNTs in theory are based on the method of bottom-up calculations. Robertson et al. (D.H.Robertson et al. 1992) predicted the elastic properties of CNTs with radii less than 0.9 nm by using Tersoff-Brenner potentials, and indicated that the elastic constants along the tube axis generally soften with a decrease in the tube radius. The similar results were later reported by other researchers by using tight-binding simulations , ab initial analysis, lattice dynamic analysis or structural mechanics calculations (Hernández et al. 1998), (Daniel et al. 1999), (Popov et al. 2000), (Li & Chou 2003a). Meanwhile, chirality dependent mechanical properties are also reported. Model the SWCNTs as equivalent beam frame structures, H. Li & Guo (Li & Guo 2008) demonstrated that the elastic properties of SWCNTs vary with the tube size and chirality, the smaller the tube diameter is, the stronger the dependences of the elastic properties on the tube size and chirality are. Meanwhile, molecular mechanics simulations also indicate that the fracture behaviors of CNTs are significantly dependent on the tube chirality (Belytschko et al. 2002), (Chang 2007), (Aghaei & Dayal 2012).

Opposite to bottom-up methods, top-down methods have been introduced soon after. They investigate the mechanical properties of CNTs by combining macroscopic methods. Typical top-down methods are continuum mechanical theories based classical shell model and finite element model. In shell model, the critical parameter of shell thickness h of CNTs is determined by fitting the tensile and bending stiffness obtained from molecular dynamics simulations with h from 0.066 to 0.089 nm (Yakobson et al. 1996), (Xin et al. 2000), (Kudin et al. 2001); or it is simply taken as the interlayer separation distance of graphene sheets in the bulk graphite as h≈0.34 nm (Lu 1997). Although the shell model method may substantially reduce the computational costs, the curvature and chirality effects on the mechanical behavior of CNTs cannot be taken into account. This is due to the ignorance of the discrete nature of the CNT geometry in an isotropic shell model. To incorporate the interatomic features of

CNTs into a continuum analysis, Liu et al developed an atomic-scale finite element method that uses atoms as FE nodes in the atomistic analysis (Liu et al. 2005). This method captures both the discreteness and multibody interactions of atoms and has the same formal structure in continuum FE model. Incorporating the effect of bending moment and curvature for a curved surface, Wu et al established an atomistic-based finite-deformation shell theory for SWCNTs from the interatomic potential (Wu et al. 2008). Chang developed a molecular based anisotropic shell model (MBASM) to predict the anisotropic elastic properties of SWCNTs (Chang 2010). Their method provides a combination of molecular and continuum mechanics solution which can predict the chirality induced anisotropic effects on some mechanical behaviors of SWCNTs. Combined molecular mechanics with FEM, Li et Chou developed a continuum beam modeling to predict the elastic modulus of SWCNTs and MWCNT (Li & Chou 2003a), (Li & Chou 2003b). Using similary method, Tserpes et Papanikos investigated the influence of tube wall thickness, diameter and chirality on the elastic moduli of SWCNTs (Tserpes & Papanikos 2005).

- **Experimental measurements for mechanical properties of CNTs**

Experimental characterization of mechanical properties of CNTs is great challenge in equipments and manipulations due to their nano-size. Generally, experimental tests are carried out by assimilating CNTs into standard structure members, such as beams, bars, and shells. The mechanical properties of these structure members are then obtained by observing their mechanical performance using transmission electron microscopy (TEM) and atomic force microscopy (AFM). Treacy et al were first reported to perform an experimental measurement for estimating Young's modulus of MWCNTs by analyzing the thermal vibration of an individual nanotubes by using TEM (Treacy et al. 1996). They used a cantilevered beam model and estimated a value of Young's modulus from 0.4 to 4.15 TPa, with an average of 1.8 TPa. Later, they estimated Young's modulus of SWCNTs and obtained an average value of 1.3-0.4/+0.6 TPa using the same experiment model (Krishnan, Dujardin, T. W. Ebbesen, et al. 1998). With the similar structure model as shown in Fig. 1.6, Poncharal et al measured the resonance frequency of MWCNTs by driving the resonance with a counter electrode and RF excitation and found that the elastic bending modulus as a function of diameter decrease sharply (from about 1 to 0.1 TPa) with increasing diameter (from 8 to 40 nanometers) (Poncharal et al. 1999). Salvetat et al measured the elastic and shear moduli of individual single-walled nanotube (SWNT) ropes to be the order of separately 1 TPa and 1 GPa by AFM with nanobeam model (the fundamentals of their experiment is demonstrated in Fig. 1.7 (Jean-Paul Salvetat et al. 1999).

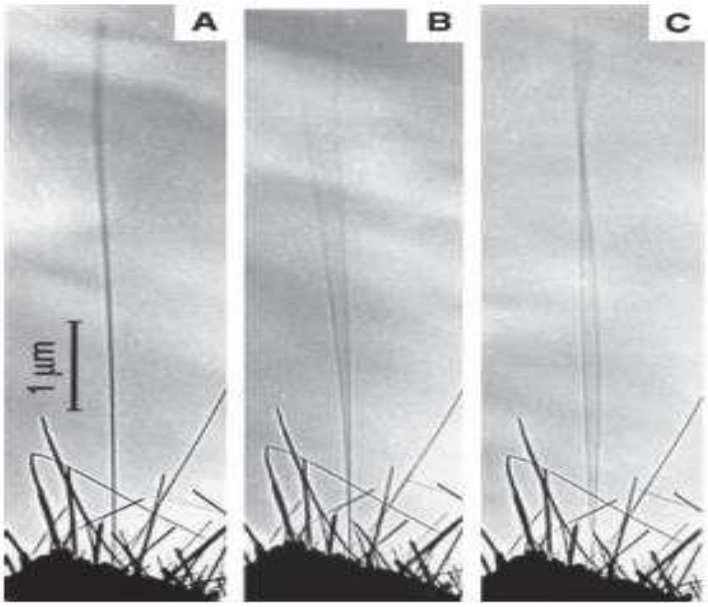

Fig. 1.6 Nanotube response to resonant alternating applied potentials. (A) In the absence of a potential, the nanotube tip (L=6.25µm, D=14.5 nm) vibrated slightly because of thermal effects. (B) Resonant excitation of the fundamental mode of vibration (v1=530 kHz); the shape corresponds closely to that expected for a cantilevered uniform beam. (C) Resonant excitation of the second harmonic (v2 = 3.01 MHz) (Poncharal et al. 1999)

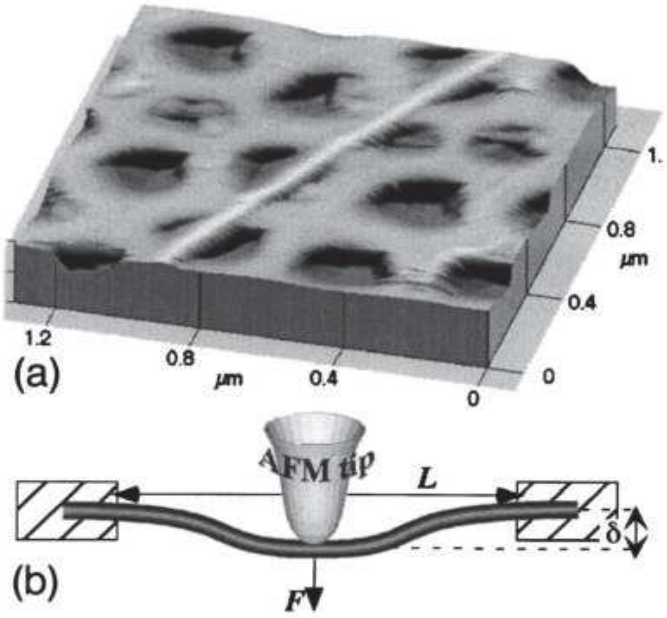

Fig. 1.7 Measurement of elastic and shear moduli of individual single-walled nanotube (SWNT) ropes: (a) AFM image of a SWNT rope adhered to the polished alumina ultrafiltration membrane, with a portion bridging a pore of the membrane. (b) Schematic of the measurement: the AFM is used to apply a load to the nanobeam and to determine directly the resulting deflection (Jean-Paul Salvetat et al. 1999).

Based on a bar model, Lourie et al. (O Lourie et al. 1998) estimated the elastic modulus of single and multiwall CNTs by using micro-Raman spectroscopy to monitor the cooling-induced compressive deformation of CNTs embedded in an epoxy matrix. They reported the

Young's modulus of 2.8–3.6 TPa for SWCNT and 1.7–2.4 TPa for MWCNT. The tensile strengths of individual single and multiwall CNTs were measured by Yu et al under tensile load (Yu, Files, et al. 2000), (Yu, Lourie, et al. 2000). They obtained the breaking strength of SWCNTs from 13 to 52 GPa, with an average of 30 GPa, and the Young's modulus from 320 to 1470 GPa, with an average of 1002 GPa; for MWCNTs the breaking strength from 11 to 63 GPa, and the Young's modulus from 270 to 950 GPa. Also they found that the MWCNTs broke in the outermost layer, and the load transfer into the inner layers was very weak, the measured shear strength was only 0.08 MPa and 0.3 MPa.

Buckling behavior is also a major topic in mechanical response of CNTs researches. Extensive efforts have been made to study the buckling behavior of CNTs under various loading conditions. (Despres et al. 1996), (Iijima et al. 1996), (Wong 1997). M. R. Falvo et al. observed that CNTs exhibit extra ordinarily flexible under large strains, and shown reversible and periodic buckling (Falvo et al. 1997). Based on the combination of experimental measurements and elastic stability theory, Lourie et al. found that the compressive strength of thin- and thick-walled nanotubes is more than 2 orders of magnitude higher than the compressive strength of any known fiber (O. Lourie et al. 1998). Moreover, it has been demonstrated that the buckling behavior may simultaneously trigger sudden changes in physical and mechanical properties of CNTs (Bozovic et al. 2001), (Paul & Klimeck 2011), (Tombler et al. 2000), which may significantly influence its performances in real applications.

1.3.1.4. Aspect ratio of CNTs

CNTs tend to undergo buckling when placed under compressive, torsional, or bending stress because of high aspect ratio (Jensen et al. 2007). Besides, recent studies have shown that the special high aspect ratio has a dramatic influence on the mechanical, rheological, and electrical properties of carbon nanocomposites (Jiang et al. 2007), (Wu et al. 2010), (Ayatollahi et al. 2011). Zhang et al. studied the effect of carbon nanotube dimensions and dispersion quality on fatigue crack growth suppression in epoxy nanocomposites (Zhang et al. 2008). They observed that the fatigue crack growth rates can be significantly reduced by reducing the nanotube diameter, increasing the nanotube length, and improving the nanotube dispersion. Dubnikova et al studied the effect of MWCNT dimensions and surface modification on the morphology, mechanical reinforcement and electrical properties of PP-based composites (Dubnikova et al. 2010). The study of both electrical and mechanical properties of nanocomposites showed maximal efficiency for the large diameter MWCNTs. Russ et al studied the effects of aspect ratio and CNT content on electrical and thermal characterization of carbon nanotube/epoxy nanocomposite (Russ et al. 2013). They observed a significant increase in the bulk electrical conductivity of the epoxy resin upon nanotube loading, and demonstrated that the electrical conductivity is strongly dependent on the aspect

ratio of the carbon nanotubes. These studies provide guidance for tailoring the nanotube aspect ratio to the intended applications in carbon nanocomposites.

Table 1.1 gives the summary of the novel properties of SWCNTs and MWCNTs obtained by theoretical and experimental analysis in literatures (Mittal 2010), (Thostenson et al. 2005), (Cao & Rogers 2009), (Vajtai 2013).

Table 1.1 Summary of theoretical and experimental properties of SWCNTs and MWCNTs (Mittal 2010), (Thostenson et al. 2005), (Cao & Rogers 2009), (Vajtai 2013)

properties	SWCNTs	MWCNTs
Specific gravity	0.8g/cm^3	1.8g/cm^3
density	1.33 ~ 1.40 g/cm^3	1.74 ± 0.16 g/cm^3
electrical resistivity	10^{-6}Ωcm	3×10^{-5} Ωcm
Current-carrying capacities	~1×10^9 A/cm^2	~1.8×10^{10} A/cm^2
Thermal conductivity	1800−6000 W/mK	15 W/m K
Elastic modulus	1 ~ 2 Tpa	0.3 ~ 1 Tpa
Tensile strength	13 ~ 53 GPa	11 ~ 150 GPa
Specific surface ratio	~ 50m^2/g	~1315 m^2/g

1.3.2. Methods of CNTs synthesis

Diverse applications of CNTs in variety of fields have stimulated the development of methods for the synthesis of CNTs with expected structure and morphology. Among these methods, arc discharge, laser ablation, and chemical vapor deposition (CVD) are the three main synthesis methods. Arc discharge and laser ablation are high temperature based preparation techniques (>1700°C) which were first used to produce CNTs products; CVD is a later developed method with the principle of decomposition of various hydrocarbons under the help of transition metal catalyst. To date, the continuous refined traditional synthesis methods together with the novel techniques have been developed, the orientation, alignment, nanotube length, diameter, purity and density of CNTs can be precisely controlled. Fig. 1.8 illustrates the current methods for CNTs synthesis.

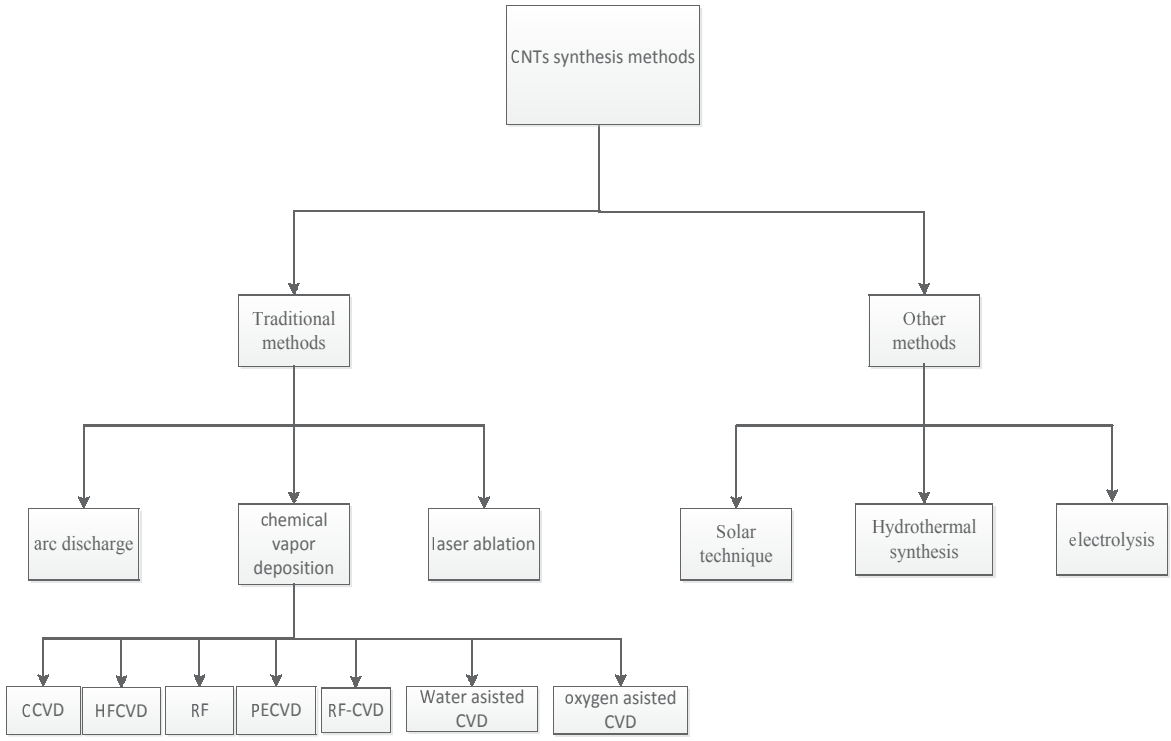

Fig. 1.8 Methods for CNTs synthesis in the current

- **Arc discharge method**

The electric arc discharge is one of the oldest methods for the carbon nanotube production. The principle of arc discharge technique is generally described by using two high-purity graphite electrodes. The anode is either pure graphite or contains metals which are mixed with the graphite powder and introduced in a hole made in the anode center. The synthesis is carried out at low pressure in controlled atmosphere which is composed of inert and/or reactant gas. When reaction happens, the temperature in the inter-electrode zone becomes so high in momentary that carbon sublimes from the positive electrode and converts into carbon vapor, after the carbon vapor undergoes a phase change and a crystallization process, the liquid carbon steadily deposits on the cathode. During the reaction, various kinds of products are formed. Therefore, control of the product purity is critical in arc discharge synthesis process. As reported, the main factors that affect the yield, the quality and the structures of CNT products are the catalyst composition, the carbon sources and the reaction environment (which composes of pressure of gases, arc discharge method, and temperature) (Prasek et al. 2011), (Harris & Harris 2009). With the continuous improvement in technology, arc discharge is still an important method in the production of high quality MWCNTs, SWCNTs, DWCNTs, and super bundle in nowadays (Prasek et al. 2011).

- **Laser ablation method**

The principle of laser ablation method is similar to the arc discharge method. What the difference is that the energy in laser ablation is provided by laser hitting the mixed graphite and metallic catalysts materials. Laser ablation method was first presented by Guo *et al.* to produce SWCNTs (Guo et al. 1995), and later their group developed this technique to the 'mass production' of SWNTs (Hafner et al. 1998). Compared with arc discharge method, laser ablation produce higher purity (up to about 90% pure) and better graphitized structure of CNTs but small carbon deposit (Szabó et al. 2010). Recently, this technique has been successfully applied to the commercial CNT composite thin films coating process (Bonaccorso et al. 2007), (Stramel et al. 2010).

- **Chemical vapor deposition (CVD) method**

Chemical vapor deposition (CVD) is considered as the standard method for producing large scale and quite pure CNTs products now. Compared with arc discharge and laser ablation methods, CVD is a simple and economic technique for synthesizing CNTs. Although the growth mechanism of CNTs is still under discussion, there are two general accepted growth models proposed by Baker and his colleagues as "tip-growth model" and "base-growth model" (Baker et al. 1972). For the former, as depicted in Fig. 1.9 (a) when the catalyst–substrate interaction is weak, the hydrocarbon decomposes on the top surface of the metal; the carbon diffuses down through the metal and pushing the whole metal particle off the substrate. Then the CNTs continues to deposit on the trailing face until the metal is fully covered with excess carbon, that its catalytic activity ceases and the CNT growth is stopped. For the other case, the initial hydrocarbon decomposition and carbon diffusion take place similar to that of the tip-growth case, while as the catalyst–substrate interaction is strong, the CNT precipitation fails to push the metal particle up; so the precipitation is compelled to emerge out from the metal's apex and CNT grows up on the base of the catalyst particle, as depicted in Fig. 1.9 (b).

It is stated that the CNTs growth patterns are mainly dependent on the catalyst–substrate interaction and the structure of CNTs is governed by the size of the catalyst particle (Kumar & Ando 2010). Therefore, the choice of catalyst is one of the most important factors that influence the CNTs growth. Other factors such as hydrocarbon, temperature, pressure, gas-flow rate, deposition time, reactor geometry are also discussed in literatures (HARRIS & HARRIS 2009), (Prasek et al. 2011).

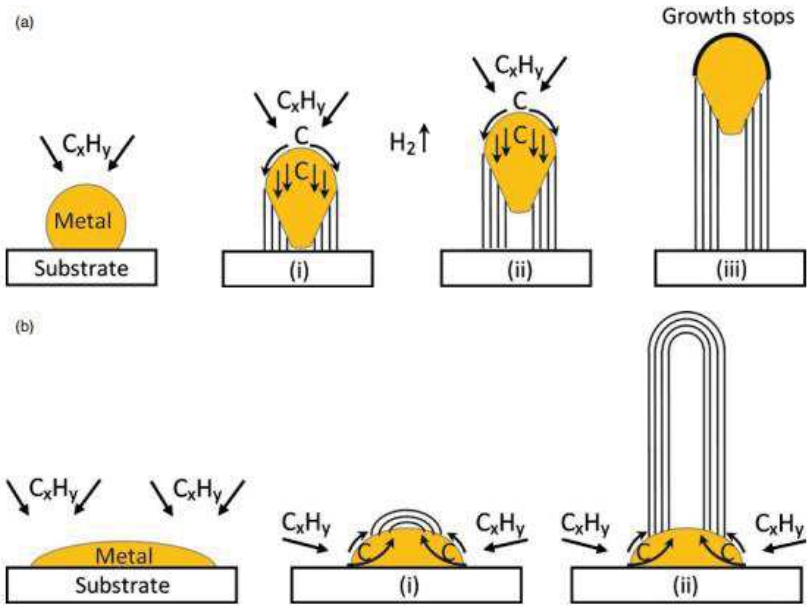

Fig. 1.9 Widely-accepted growth mechanisms for CNTs: (a) tip-growth model, (b) base-growth model (Kumar & Ando 2010).

- **Other methods**

Besides the traditionally used synthesis methods, some other synthesis methods are proposed as well in considering the various types (MWCNTs, SWCNTs, and DWCNTs), the morphology, the extended scale and the different collective arrangements of CNTs. For example, the hydrothermal technique with low temperature process has many advantages in obtaining different carbonaceous such as easily obtained starting materials, no needs for hydrocarbon or carrier gas in operation. An important feature of hydrothermal nanotubes is its small wall thickness, which is about 10% of the large inner diameter of 20–800 nm (Gogotsi et al. 2000). Methods have been explored by using electrolysis or solar energy were also demonstrated have unique advantages for the production of CNTs for different applications (Novoselova et al. 2008), (Laplaze et al. 1998).

1.4. Conclusion

In this chapter, we briefly introduced the fundamental concepts of nanomaterials and nanotechnology. CNTs, as one of the most interesting topic in both academic and industry in the world, their novel electronic, thermal, mechanical, and aspect ratio properties were summarized. Since the properties and applications of CNTs are mainly dependent on their preparation methods, synthesis technologies for CNTs are also concisely introduced.

It is demonstrated that CNTs exhibit excellent physical, chemical, and mechanical properties, and these properties are greatly structural and conditional dependent. Therefore, it is interesting to explore the variety and the potential properties of CNTs.

Chapter 2. Mechanical properties of SWCNT by FE method

In this chapter, we present the numerical prediction for Young's and shear moduli of armchair, zigzag and chiral SWCNTs with different radii and lengths. Under the approximated relationship between the molecular mechanics and classical structural mechanics in SWCNTs proposed in the literature, a three-dimensional FE model for armchair, zigzag and chiral SWCNTs is constructed. A non-continuum FE model is adopted to evaluate the influence of dimension, chirality and length on Young's and Shear moduli

2.1. Introduction

So far, comprehensive experimental and theoretical studies have been carried out to investigate the elastic properties of both multi- and single-walled carbon nanotubes (Yu 2004), (Ruoff et al. 2003), (Wong 1997), (Krishnan, Dujardin, T. Ebbesen, et al. 1998), (Brenner et al. 2002). However, experimental studies for the mechanical response of CNTs are very difficult and expensive due to the nanoscale dimension. The development of appropriate theoretical models to predict the mechanical performances of CNTs is essential. Based on molecular mechanics, a lot of work has been done to predict the mechanic properties of CNTs (Rajasekaran & Chitra 2009), (Tsang et al. 1996), (Miller & Tadmor 2009), (Wan & Delale 2009). Using the tersoff-brenner potential to account for the inter- and intra-tube interactions, Shuchi Gupta et K. Dharamvir calculated the elastic properties of SWCNTs and their ropes (Gupta et al. 2005). by establishing a linkage between classical structural mechanics and molecular mechanics, Li et Chou (Li & Chou 2003a) presented a structure mechanics approach to model the deformation of carbon nanotubes. The fundamental notion of Li's approach is that a CNT is a geometrical frame-like structure, where the primary bonds between the nearest two neighboring atoms act like a load-bearing beam element. This modeling approach did not consider the indirect bond angle bending of C-C-C. According to their approach, K.I.Tserpes and P. Papanikos (Tserpes & Papanikos 2005) proposed a three-dimensional FE model for armchair, zigzag and chiral SWCNTs to investigate the influence of tube wall thickness, diameter and chirality on the elastic moduli. Their study indicated that the elastic moduli of SWCNTs are dependent on the value of wall thickness, diameter and chirality. By using the force field method, Lutz Nasdala and Gerald Ernst (Nasdala & Ernst 2005) introduced a 4-nodes FE model to represent the different force forms. G.I and P.A. (Giannopoulos et al. 2008) developed a non-continuum FE method to compute the mechanical response of armchair and zigzag SWCNTs. In this approach, the force constants that

corresponding to the intermolecular force are included in the model straightforwardly, while the extracted relationship between the cross-sectional properties of beam element and the molecular force field constants was not considered. Among these methods, the FE method has been proved to be an effective and convenient method to characterize the mechanical responses of SWCNTs.

In this chapter, we present the numerical prediction for Young's and shear moduli of armchair, zigzag and chiral SWCNTs with different radii and lengths. Based on the concept of Li et Chou (Li & Chou 2003a) and G.I et P.A. (Giannopoulos et al. 2008), a 3D FE model for armchair, zigzag and chiral SWCNTs is proposed. A non-continuum FE model is adopted to evaluate the influence of dimension, chirality and length on the Young's and Shear moduli of SWCNTs. From the molecular theory point of view, the atomic bonds always remain straight and cannot be bended. The interatomic interactions of C-C bond are modeled using straight spring and torsional spring elements, while the indirect bond angle bending of C-C-C is represented by linear elastic spring elements. In this way, different interatomic interaction forms are simulated separately for purpose of accuracy.

In this chapter, The atomic structure of SWCNTs and the interatomic interactions modeling are described briefly in section 2.2.1 and 2.2.2, respectively; the demonstration of finite element model of SWCNTs is explained in section 2.3.1; Section 2.3.2 presents the calculations of Young's modulus and shear modulus of SWCNTs.

2.2. Atomic structure of SWCNTs

2.2.1. Geometric depict for SWCNTs

A SWCNT can be viewed as a hollow cylinder produced by rolling up a sheet of graphite. The simplest way of specifying the structure of an individual nanotube is in terms of a chiral vector $\mathbf{C}_h$, which can be defined as:

$$\boldsymbol{C_h}=n\boldsymbol{a_1}+m\boldsymbol{a_2} \tag{2–1}$$

where $\mathbf{a}_1$ and $\mathbf{a}_2$ are the unit cell base vectors of the graphite sheet, (n, m) are a pair of integers, and n≥ m. As shown in Fig. 2.1, m = 0 for all zigzag tubes, n = m for all armchair tubes, and all other tubes are chiral tubes.

$$\boldsymbol{T} = \left(\frac{2m+n}{W}\right)\boldsymbol{a_1} + \left(-\frac{2n+m}{W}\right)\boldsymbol{a_2} \tag{2–2}$$

where W is the highest common divisor of 2m+n and 2n+m. Chiral vector $\mathbf{C}_h$ and the translational vector **T** define the ideal rectangular cutting area of graphite sheet.

In order to simply generate the atomic structure from a 2D graphite sheet to a 3D nanotube, the original coordinate system of the graphite sheet (x_0, y_0) is converted to a new system (x, y, z) of nanotube according to:

$$(x, y, z) = [R\cos(\frac{x_0}{R}), R\sin\left(\frac{x_0}{R}\right), y_0] \tag{2–3}$$

y_0 - axis is along the direction of T (Ghaderi & Hajiesmaili 2012), and R is the radius of nanotube given by the following equation:

$$R = \frac{a_{c-c}\sqrt{3(n^2+mn+m^2)}}{2\pi} \tag{2–4}$$

$a_{c\text{-}c}$ is the distance between two neighboring carbon atoms which approximately equal to 0.142nm. The chiral angle Ψ ($0 \leq \Psi \leq 30°$) is defined as:

$$tan\,\Psi = \frac{\sqrt{3}m}{(2n+m)} \tag{2–5}$$

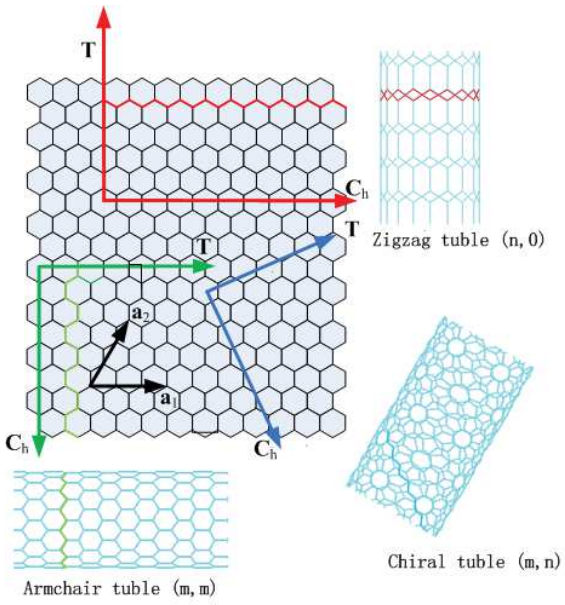

Fig. 2.1 Diagram of armchair, zigzag, and chiral SWCNTs structure

2.2.2. Interatomic interactions modeling

The construction of an individual nanotube can be regarded as a regular collection of point masses connected by elastic springs. Omitting the electrostatic interactions, the interatomic forces can be expressed in terms of potential energy function of various structural features as bond length, bond angle, bond torsion and non-bonded interactions which are

shown in Fig. 2.2. The force field is a combination of these potential energy terms and can be expressed by (Ghaderi & Hajiesmaili 2012):

$$U = \sum U_r + \sum U_\theta + \sum U_\phi + \sum U_\omega + \sum U_{vdw} + \sum U_{el} \tag{2–6}$$

where U_r, U_θ, U_Φ, U_ϕ, U_ω,U_{vdw} and U_{el} are respectively the energy referable to the bond strength interaction, the bond angle bending, the dihedral angle torsion, the out-of-plane torsion, the van der Walls interaction, and the electrostatic interactions.

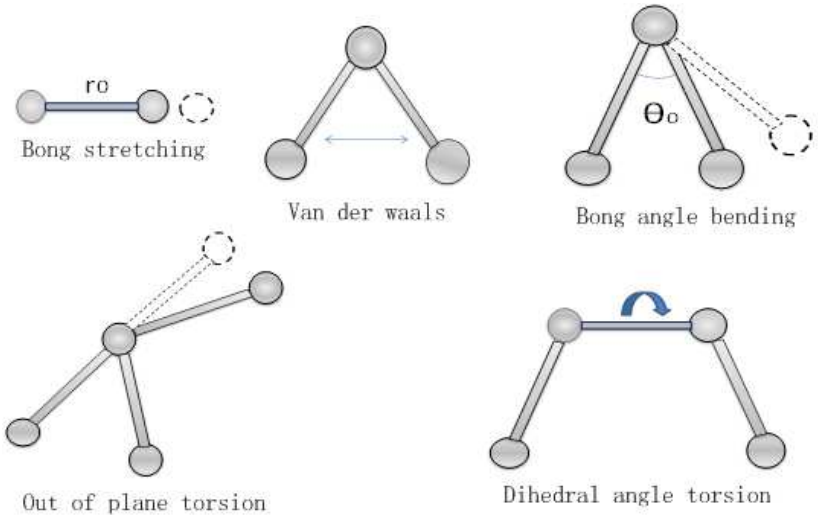

Fig. 2.2 Interatomic interactions in molecular mechanics

Generally, for the covalent systems, the main contributions to the total steric energy come from the first four terms of (2–6). Under the assumption of small deformation, the harmonic approximation is adequate for describing the energy (Li & Chou 2003a). Adopting the simplest harmonic forms and merging the dihedral angle torsion U_ϕ and the out-of-plane torsion U_ω in to a single equivalent term U_τ, we get each of the energy as:

$$U_r = \frac{1}{2}k_r(r - r_0)^2 = \frac{1}{2}k_r(\Delta r)^2 \tag{2–7}$$

$$U_\theta = \frac{1}{2}k_\theta(\theta - \theta_0)^2 = \frac{1}{2}k_\theta(\Delta\theta)^2 \tag{2–8}$$

$$U_\tau = U_\phi + U_\omega = \frac{1}{2}k_\tau(\Delta\phi)^2 \tag{2–9}$$

where k_r, k_θ and k_τ are the bond stretching force constant, bond bending force constant and torsional resistance, respectively. Δr, $\Delta\theta$ and $\Delta\emptyset$ are separately the bond stretch, the bond angle and the twisting angle bond variations.

Since the structure of a nanotube is regarded as the connection of elastic springs, by adopting Hookes law, it is reasonable to conclude that the potential energy term of bond strength interaction is equivalent to the potential energy of a compression/extension of a

spring with stiffness of k_r, which is longitudinally deformed by Δr. While the potential energy terms of bond angle bending and torsions are equivalent to the potential energy of a torsion spring with stiffness of k_θ and $k_\tau$rotated by $\Delta\theta$ and $\Delta\emptyset$, respectively. Through this conversion, the molecular mechanics parameters k_r , k_θ and k_τ are correspondingly equivalent to the bond stretching, bond angle and torsional resistance force constant, respectively. Then, the resistance force constants in eqs. (2–7)~ (2–9) can be introduced into the model as spring stiffness coefficients straight forwardly. Here the resistance force constants are taken to be k_r=6.52×10^{-7} N nm^{-1}, k_θ=8.76×10^{-10} N nm rad^{-2} and k_τ=2.87×10^{-10} N nm rad^{-2} (Ghaderi & Hajiesmaili 2012).

2.3. Finite element model

As the molecular theory states that a C-C bond always remains straight and cannot be bended, in this work, a straight spring and a torsional spring are introduced to model the C-C interaction of bond strength and bond torsion, separately. In addition, for the purpose of accuracy, the C-C-C bend angle resistance is replaced by a linear straight spring member, as illustrated in Fig. 2.3.

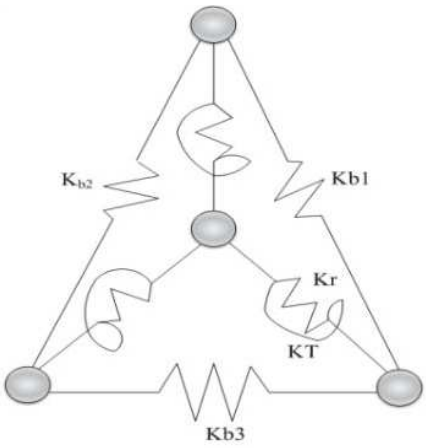

Fig. 2.3 Interatomic interactions spring model of CNT

For a small deformation, the equivalent transformation between the variation of C-C-C bend angle and the corresponding compression/elongation of straight spring (Fig. 2.4) can be formulated as:

$$\Delta l = a_{c-c}\Delta\theta \tag{2–10}$$

$$\cos\varphi \approx \cos(90° - \gamma) = \frac{\Delta x}{\Delta l} \tag{2–11}$$

The potential energy of bond angle rotation in Fig. 2.4 (a) is:

$$U_\theta = \frac{1}{2}k_\theta(2\Delta\theta)^2 \tag{2–12}$$

And the elastic deformation energy in Fig. 2.4 (b) is:

$$U_b = \frac{1}{2} k_b (2\Delta x)^2 \tag{2–13}$$

Considering Eq. (2–10) and (2–11) and setting $U_\theta = U_b$, we obtain the stiffness of the equivalent straight spring k_b:

$$k_b = \left(\frac{1}{a_{c-c}\, cos(90°-\gamma)}\right)^2 k_\theta \tag{2–14}$$

where γ = 30° in the hexagonal lattice of the graphite. However, this angle may vary in a CNT due to the cylindrical shape, and here γ = 30° in approximation.

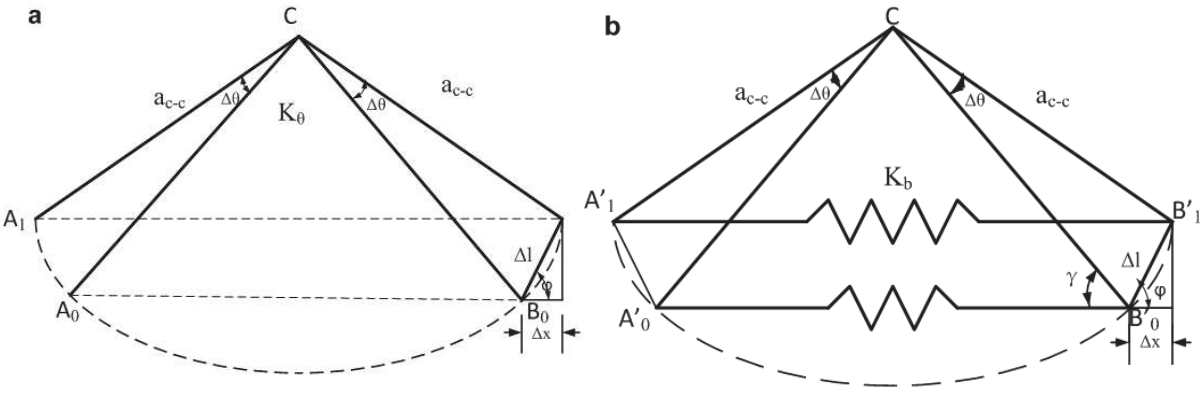

Fig. 2.4 Variation of C-C-C bend angle: (a) a torsion deformation, (b) the stretching of elastic spring.

2.3.1. Results and discussion

The 3D FE model for armchair, zigzag and chiral SWCNTs has been developed based on the code ANSYS. Being a spring-based structure, the carbon atoms are modeled as the joint nodes of the spring members. The bond stretching is modeled by the link8 element, this element is a two-node element, and for each node there are three degrees of freedom (x, y, z translations). By using link8 element, the cross section effect is taken into consideration. The bond twist of C-C bond interaction is modeled by the spring element combin14, in which the performance of torsion is considered, and with each node there are three rotational degrees of freedom. The bond bending of C-C-C angle bending interaction is modeled by the spring element combin14, which just carries the axial force, and with each node there are three translational degrees of freedom (x, y, z translations). Because of the same angle γ, two of the three bending spring stiffness (k_{b2}=k_{b3}) are equal for armchair and zigzag nanotubes. However, for chiral nanotubes, the three bending spring stiffness are different as showed in Fig. 2.5. Table 2.1 presents the geometric and stiffness properties of the joint elements used in analysis.

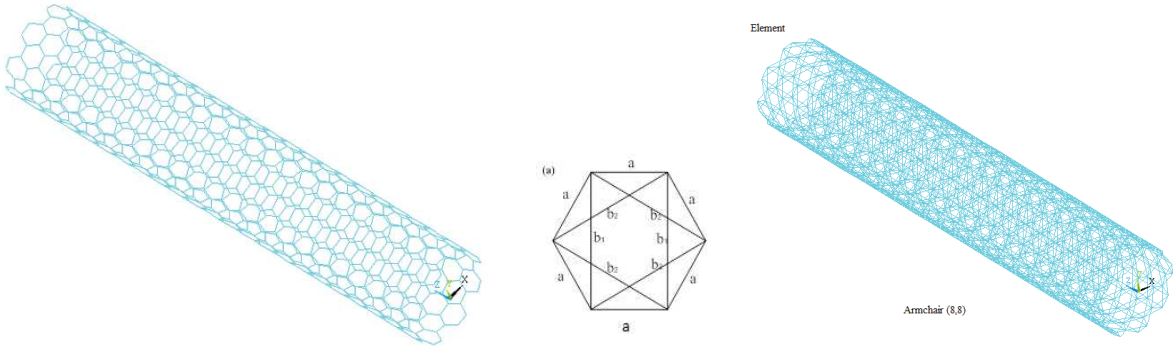

(a) Armchair (8, 8)

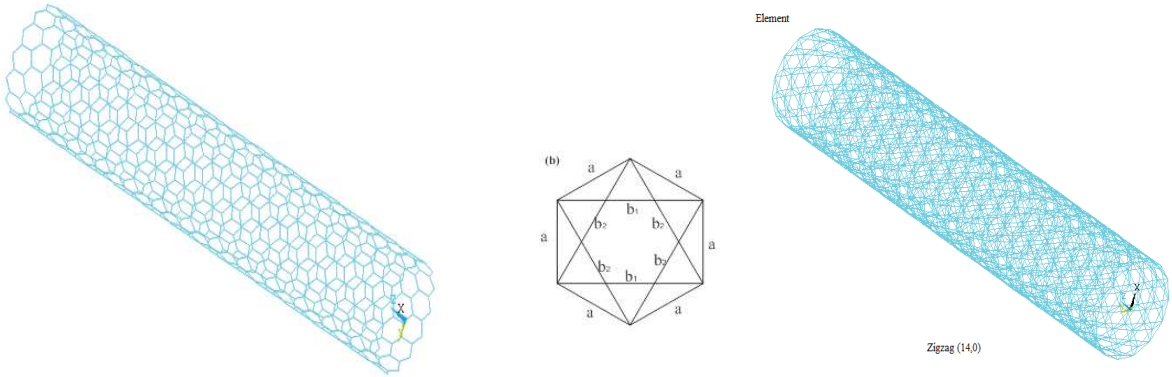

(b) Zigzag (14, 0)

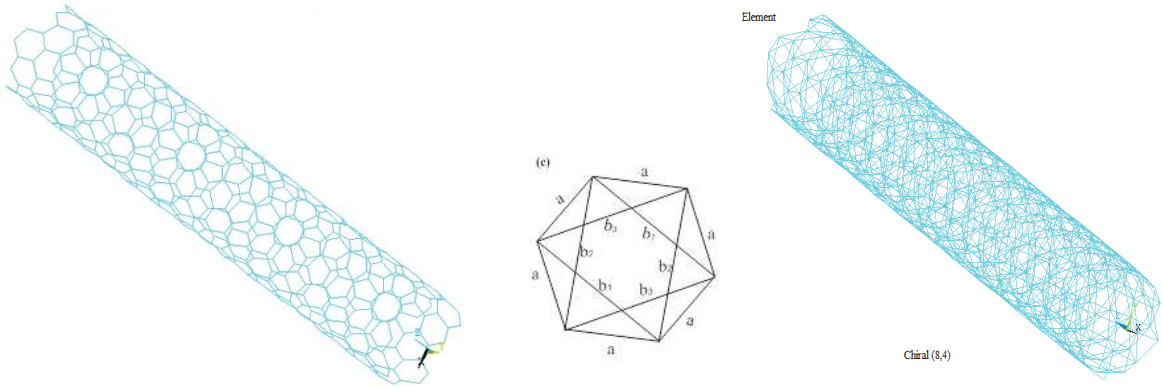

(c) Chiral (8, 4)

Fig. 2.5 The geometry and elements of armchair (8, 8), zigzag (14, 0), chiral (8, 4).

Table 2.1 Geometric characteristics and stiffness properties of the models used in analysis

Nanotube type		r (nm)	h (nm)	t (nm)	k_r (10^7N nm^{-1})	k_r (10^{10}N nm rad^{-2})	k_{b1} (10^7N nm^{-1})	k_{b2} (10^7N nm^{-1})	k_{b3} (10^7N nm^{-1})
	(3,3)	0.2035	2.2167				1.7486	1.6044	1.6044
	(4,4)	0 .2714	2.9556				1.7428	1.6583	1.6583
Armchair	(5,5)	0.3392	3.5686	0.34	6.52	2.78	1.7401	1.685	1.685
	(8,8)	0.5428	5.6609				1.7322	1.7152	1.7152
	(12,12)	0.8142	8.2445				1.7361	1.7263	1.7263
	(5,0)	0.1959	1.9884				1.3256	1.6941	1.6941
	(7,0)	0.2742	2.842				1.4952	1.7139	1.7139
Zigzag	(9,0)	0.3525	3.6946	0.34	6.52	2.78	1.5806	1.7222	1.7222
	(14,0)	0.5484	5.6129				1.6667	1.7299	1.7299
	(21,0)	0.8226	8.3839				1.7044	1.732	1.732
	(3,1)	0.1412	1.4772				1.2148	1.6911	1.8093
	(6,3)	0.3109	2.2558				1.6009	1.7048	1.7175
Chiral	(8,4)	0.4146	4.5116	0.34	6.52	2.78	1.6564	1.7175	1.7416
	(9,6)	0.5122	5.678				1.6903	1.716	1.7385
	(12,6)	0.6218	6.3135				1.7057	1.7336	1.7394

2.3.1.1. Young's modulus of SWCNTs

In order to calculate the Young's modulus of SWCNTs, proper boundary conditions and tension forces are applied. All degree of freedom of the nodes at $z = 0$ are constrained. While at the plane of $z = h$, axial forces f_z are uniformly imposed, where h is the total length of SWCNT. In order to reduce the edge effect, h is selected according to the length to radius ratio ($h/r \geq 10$). Then the Young's modulus E is calculated by the average stress over the average strain at the plane of $z = h$.

$$E = \frac{\sigma_z}{\varepsilon_z} = \frac{nf_z/2\pi rt}{\Delta h/h} \tag{2–15}$$

where n is the number of nodes at the plane of $z = h$, t is the wall thickness of tubes, and Δh is the axial deformation of nodes at the plane of $z = h$.

Fig. 2.6 shows the variations of Young's moduli of armchair, zigzag and chiral SWCNTs with radius. It demonstrates that the radius has a significant effect on the Young's moduli of SWCNTs. For armchair, zigzag and chiral SWCNTs with small radius, the Young's moduli increase with the radius. Here, the armchair and zigzag SWCNTs with the radius changes from 0.2035 to 0.8142 nm and from 0.1959 to 0.8226 nm, respectively, the Young's moduli correspondingly vary from 0.7501 TPa to 0.8022 TPa and from 0.6866 TPa to 0.7967 TPa. When the radius increases to a certain higher value, the Young's moduli tend to steady. The steady value of Young's moduli at larger nanotube radius is mainly due to the effect of curvature. As the diameter of nanotube increases, the distortion of C-C bond becomes less significant.

It is also indicate that with a similar radius, the armchair SWCNTs have slightly higher Young's moduli than armchair SWCNTs; and the armchair SWCNTs have slightly higher Young's moduli than chiral SWCNTs. This is in agreement with the literature trends (Giannopoulos et al. 2008), (Mahmoudinezhad et al. 2012), (Lu & Hu 2012), (Kalamkarov et al. 2006), (Xiao et al. 2005).

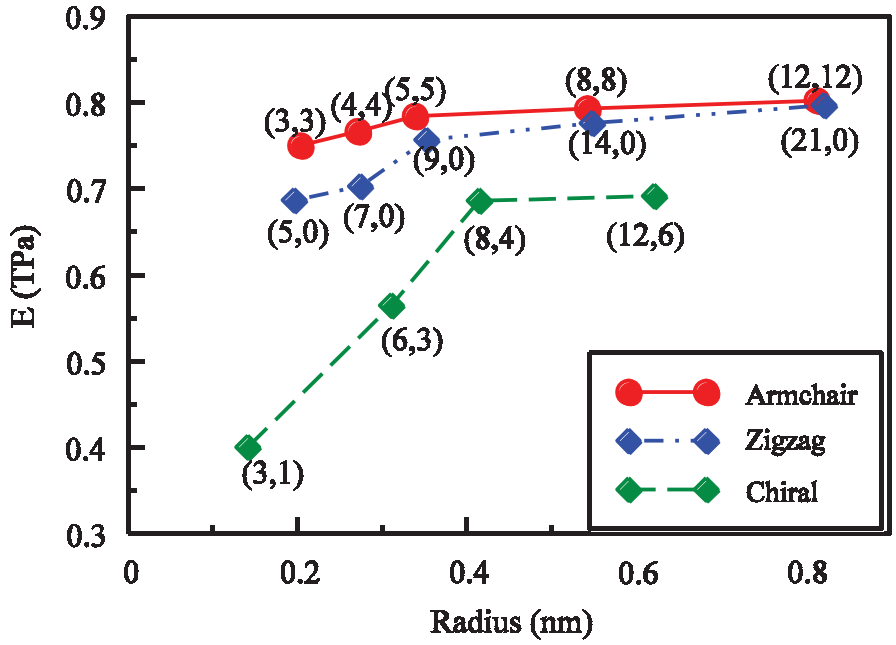

Fig. 2.6 Variation of Young's moduli of armchair, zigzag and chiral SWCNTs with radius.

Fig. 2.7 shows the comparison of Young's moduli of presented calculations with the literatures' results. The calculated Young's moduli in present is smaller than the conclusion of G.I. Giannopoulos and P.A.K.N (Giannopoulos et al. 2008) and Shuchi Gupta et K.D.A.V'sstudy (Brenner et al. 2002). The measurement of Young's moduli at the work of (J.-P. Salvetat et al. 1999), (Krishnan, Dujardin, T. Ebbesen, et al. 1998) are 0.81±0.41 TPa and 1.25-0.35/+0.45 TPa. This is mainly due to the effects of element model we adopted, which considers the effects of the element cross-section.

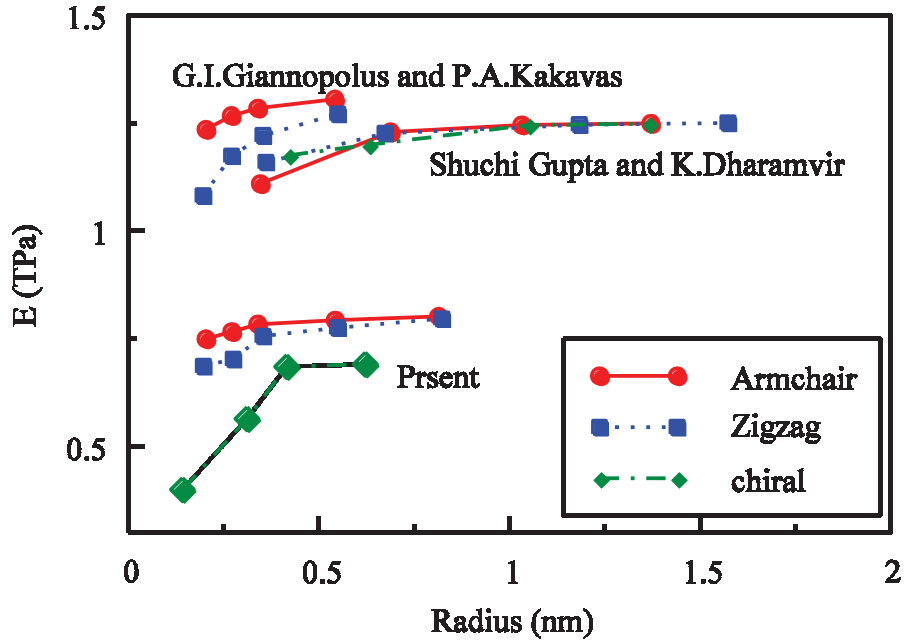

Fig. 2.7 Comparison of computed values of Young's moduli with corresponding results in literatures.

Fig. 2.8 illustrates the variations of Young's moduli with the length of SWCNTs. The computational results demonstrate that with the length of the armchair (8, 8), the zigzag (14, 0) and the chiral (9, 6) SWCNTs change from 3.57 nm to 8.24 nm, 3.27 nm to 8.38 nm and 3.56 nm to 9.28 nm, respectively. The corresponding maximum difference of Young's modulus is 2%, 5%, 14%, respectively. This may be due to the effect of aspect ratio of SWCNTs (Jiang et al. 2007).

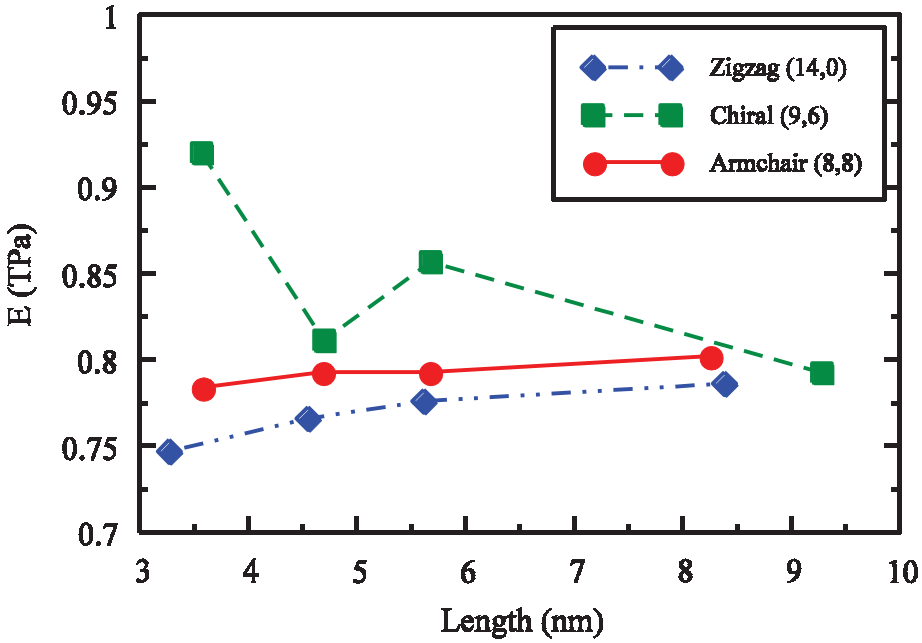

Fig. 2.8 Variation of Young's moduli of armchair, zigzag and chiral SWCNTs with length.

2.3.1.2. Shear modulus of SWCNTs

Similarly, by calculating the shear modulus G of SWCNTs, all degrees of freedom of the nodes at $z = 0$ are constrained. A tangential force f_r is applied uniformly at each node of the plane $z = h$. The shear modulus is proportional to the specific value of the torque M_z over the corresponding torsional angle θ_z, and is calculated according to:

$$G = \frac{M_z h}{\theta_z J} = \frac{n f_r r h}{tan^{-1}(\frac{\Delta s}{r})\frac{\pi}{2}((r+\frac{t}{2})^4-(r-\frac{t}{2})^4)} \tag{2–16}$$

It can be seen in Fig. 2.9, when the radius is small, the shear moduli of armchair, zigzag and chiral SWCNTs increase manifestly with the radius. When the radius becomes higher, the shear moduli tend to be stable. The results also indicate that the shear moduli of zigzag SWCNT are higher than the shear moduli of armchair and chiral SWCNTs. This is mainly due to the different constructions of the atomic structure in SWCNT. In armchair SWCNT, one-third of the C-C bonds are aligned with the radial loading direction, while, all C-C bonds are at angle with the radial loading direction in zigzag and chiral SWCNT.

In addition, for chiral SWCNTs, the shear modulus is more sensitive to the variations of chirality. As illustrated in Fig. 2.9, for the chiral SWCNTs (3, 1), (6, 3), (8, 4), the variations of shear moduli are significant compared with the armchair and zigzag SWCNTs. The comparison of shear modulus of present calculation with other computational results show that the predicted shear modulus is in good agreement with other literature work (Brenner et al. 2002), (Ghaderi & Hajiesmaili 2012), (Xiao et al. 2005), (Lau et al. 2003), as illustrated in Fig. 2.10.

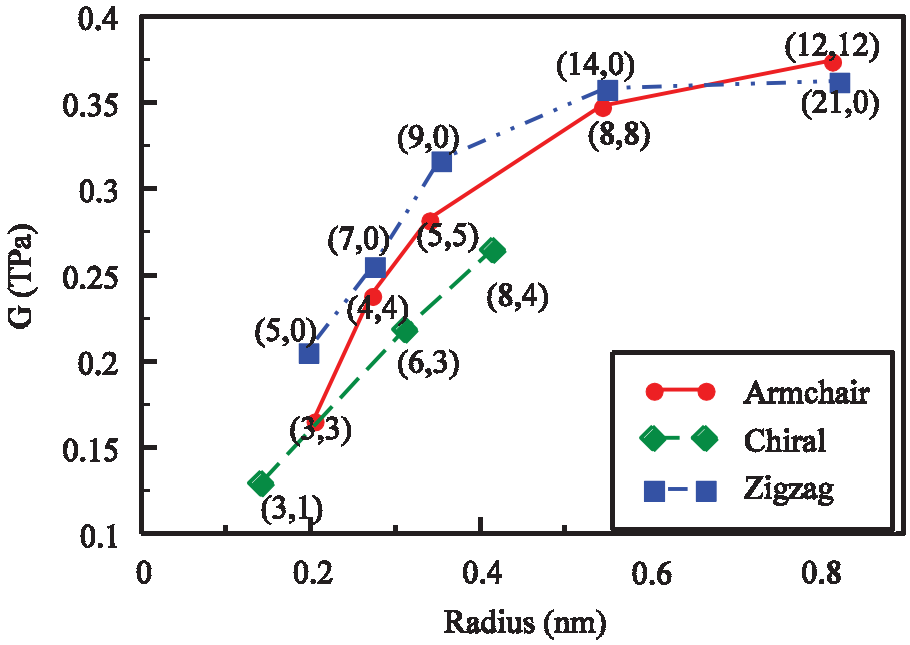

Fig. 2.9 Variation of shear moduli of armchair, zigzag and chiral SWCNTs with radius.

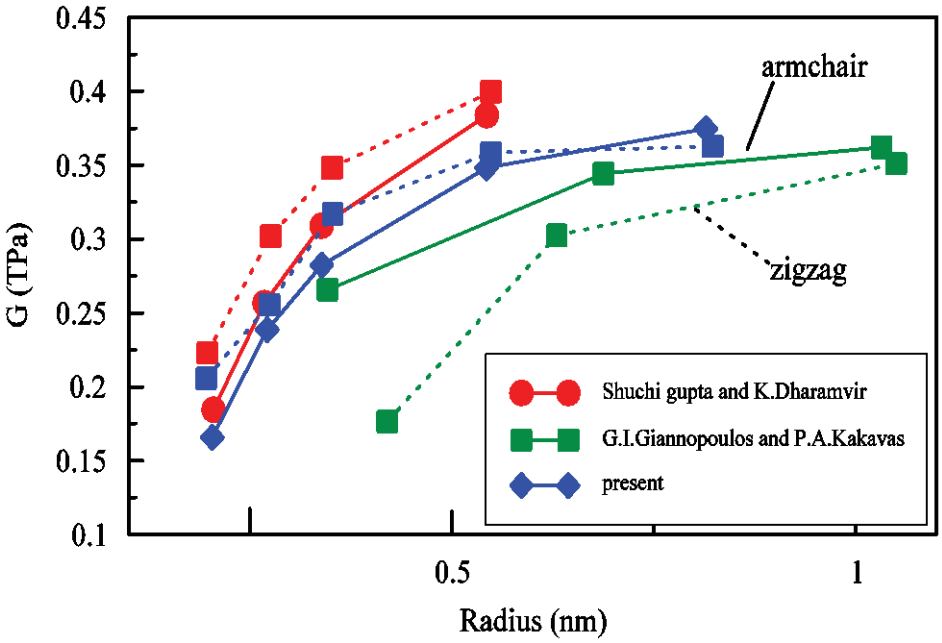

Fig. 2.10 Comparison of computed values of shear moduli with corresponding results in literatures.

2.4. Conclusion

In this chapter, a 3D finite element model is presented for armchair, zigzag and chiral single-walled carbon nanotubes (SWCNTs). The interatomic bonds of the carbon atoms are approximately expressed in terms of potential energy function of various structural features. By establishing the approximate equivalent relationships between molecular mechanics and structural mechanics, the interatomic interactions of C-C atoms are simulated by the appropriate straight spring and torsional spring elements. Besides the carbon atoms are modeled as the connecting nodes. The advantage of this method is that the interatomic interactions of bond length, bond angle, bond torsion and non-bonded interactions are separately modeled by using relevant structure features.

The computational results show that the elastic moduli (Young's modulus and shear modulus) of SWCNTs are strongly dependent on the radius and chirality of nanotubes. For small values of radius, the elastic moduli increase with the radius. When the radius becomes larger, all the elastic moduli converge to an asymptotic steady value. Furthermore, the moduli of zigzag and chiral SWCNTs are more sensitive with the radius change as compared to armchair SWCNTs. The obtained moduli agree well with the corresponding theoretical and experiment conclusion in literature.

Chapter 3. Elastic properties of SWCNTs thin film by using nanoindentation test

Exploring the potential of carbon nanotube (CNT) films has become a popular research issue since the fabrication and purification of thin films of CNTs became a relatively mature techniques. The discovery of exceptional transparency, conductivity, and flexibility properties suggests CNT films to be a kind of potential materials in the applications of different fields of electronic, optoelectronic, and sensor systems (Xie et al. 2005), (Timmermans et al. 2012), (Wu et al. 2004), (Zhang et al. 2006), (Cao et al. 2008), (Cai et al. 2013).

In this chapter, we investigated the elastic properties of SWCNTs thin film by nanoindentation test. SWCNTs thin films were prepared by using spin-coating method. Nanoindentation test with a Berkovich indenter is carried out to study the hardness and the elastic modulus of SWCNTs films. The tested hardness and elastic modulus of SWCNTs films are derived from information of load and displacement of indenter under certain assumptions. Then the uncertainty analysis for guarantee the accuracy of the estimated material properties becomes a crucial task in indentation test process. The uncertainty of elastic properties of SWCNTs film in nanoindentation is then estimated.

3.1. Introduction

Recently, a lot of work has been done in the fabrication of thin CNT films with optimized collective electrical, optical, and mechanical properties by controlling the tube density, the overall spatial layouts, the lengths, and their orientations. K.B K.Teo and his colleagues used plasma-enhanced chemical-vapor deposition (PECVD) technique produced perfectly aligned, untangled CNTs (Teo et al. 2001). Wet methods such as drop drying or electrophoretic deposition have been proposed to prepare thin films of CNTs with controlled morphology and desired function (Banerjee et al. 2005), (Moriyama 2011). Compared the efforts which focused on the techniques of producing well defined CNT films, little attention has been paid to the mechanical properties of these thin films, even though the elastic properties should be an important issue in their ultimate application. In fact, the mechanical properties of the CNT films are strongly dependent on the chemical components or material preparation process. Lee J and his colleagues found that the poisson's ratio of SWCNTs and MWNTs sheets can change from 0.06 to -0.20 as the wt% of MWNTs changes from 0 to 100% (Hall et al. 2008). Yin and his colleagues discovered that the Poisson's ratio of CNT films can change from

negative to positive during a uniaxial tensile loading (Ma et al. 2010). These interesting findings indicate that the estimation of the mechanical properties of CNT films is essential for their application.

Characterization of the mechanical properties of thin-film materials is a great challenge due to their vastly increased ratio of surface area to volume. With the great development in the relevant techniques, numerous methods are developed to evaluate the mechanical properties of such materials. For example, the tensile test (Ginga & Sitaraman 2011), cantilever beam bending test (Romano-rodr et al. 1999), membrane deflection testing (Huh et al. 2009), and frequency resonant test (K. Kim et al. 2008). Among these methods some are expensive or difficult, some are just specific to a certain material. It has been proved that load and depth sensing indentation method could be very useful in extracting the mechanical properties of thin films (Zhi-Qiang Feng, Qi-Chang He & Joli 2010), (Schuh 2006), (Maier et al. 2002). With high-resolution of load and displacement data, nanoindentation technique has been widely used to determine the mechanical properties of materials in nano/micro-scale. For example, using nanoindentation technique, researchers measured the bending stiffness, wall modulus and axial modulus of the constituent nanotubes and demonstrates the deformation characteristics of single-walled and multiwalled CNTs and CNT clusters (Qi et al. 2003), (Liu et al. 2008). Furthermore, technique improvements in nanoindentation test provide broad range of applications for other properties extraction in physical sciences. For example, the continuous stiffness measurement (CSM) technique which was developed in conjunction with nano-scratch, friction and wear tests can satisfactorily be used for characterizing the magnetic storage of materials and the micro-electromechanical systems (MEMS) devices (Li & Bhushan 2002). It also presents considerable potential in understanding the discrete atomic rearrangements under stress, ranging from phase transformations in small volumes of material to the motion and formation of individual defects (Maier et al. 2002). Those experimental and theoretical studies indicate that nanoindentation technique is an effective tool in determining the mechanical properties of CNTs.

In this chapter, we described the preparation process of the ultrathin SWCNT films (～ 200nm) by using spin coating method. The hardness and the elastic modulus of SWCNTs film were evaluated using nanoindentation test. Due to the inevitable uncertain factors in experimental process, uncertainty analysis was carried out in order to assess the reliability of the tested values of elastic properties for SWCNTs thin film.

3.2. Material preparation

3.2.1. Spin coating technique

Spin coating is a frequently used technique in the fabrication of thin (>200 nm thick) or ultrathin (<200 nm thick) films on a planar substrate (Hall et al. 1998). Compared with other thin film preparation techniques, spin coating is more cost-effective and compatible with various substrates which is suitable for large areas production. As illustrated in Fig. 3.1, in spin coating process, a drop of liquid is deposited in the center of the substrate. The rotation of the spin coater spreads the coating material by centrifugal force. The resultant film continues to thin slowly until it turns to solid-like due to solvent evaporation. The films thinning process is divided into two distinct stages: liquid radial outflow and solvent evaporation (Hall et al. 1998). The homogeneous quality of the films dependents on several important factors (Anon 2013b):

- The viscosity of solution,
- The concentration of solute,
- The evaporation rate of the solvent,
- The rotational speed and acceleration,
- The spinning time.

The final thickness and other properties of the film depend on the natures of the solution and the spinning process parameters mentioned above.

Fig. 3.1 Spin coating process

3.2.2. Preparation of SWCNT thin films by spin coating method

In this study, thin SWCNT films were prepared at the mechanical engineering center, university of Coimbra (Portugal) using spin-coating technique.

A dilute suspension of SWCNTs in ethanol was ultrasonicated for 20 min to spread out the nanotubes. The diffused suspension deposited on the well-polished silicon substrates of 10 mm × 10 mm using spin-coating method. There are two common dispense methods: static dispense and dynamic dispense, and we used the static dispense method here. The process is chronologically described as: 1) fixing the silicon chips on the spin coater; 2) dropping the SWCNT solution on the silicon chips; 3) starting up the spin coater. As the viscosity of the SWCNT solution is low and the size of the substrate to be coated is small, at the beginning of the spin-coating process, a relative low spin speed of 200 rpm during ～20 seconds is carried out to spread the solution over the substrate. The spin coater is then accelerated to a relatively high rotational speed of 1000 rpm to thin the samples to the final desired thickness within the appropriate rotation time. To obtain ultra-thin films, various factors need to be controlled (substrate roughness, solvent quantity, rotation speed, rotation time…). After spin-coating, the ethanol solvent was evaporated at room temperature. The samples were then subjected to heat treatment for 2 h under the temperature of 300ºC and slowly cooled to room temperature. After heat treatment, nanotubes stuck and randomly oriented on the silicon substrate by Van der Waals force. Fig. 3.3 shows the optical microscope images of nanotube clusters distribution on the silicon substrates under 5 times magnification (a) and 50 times magnification (b).

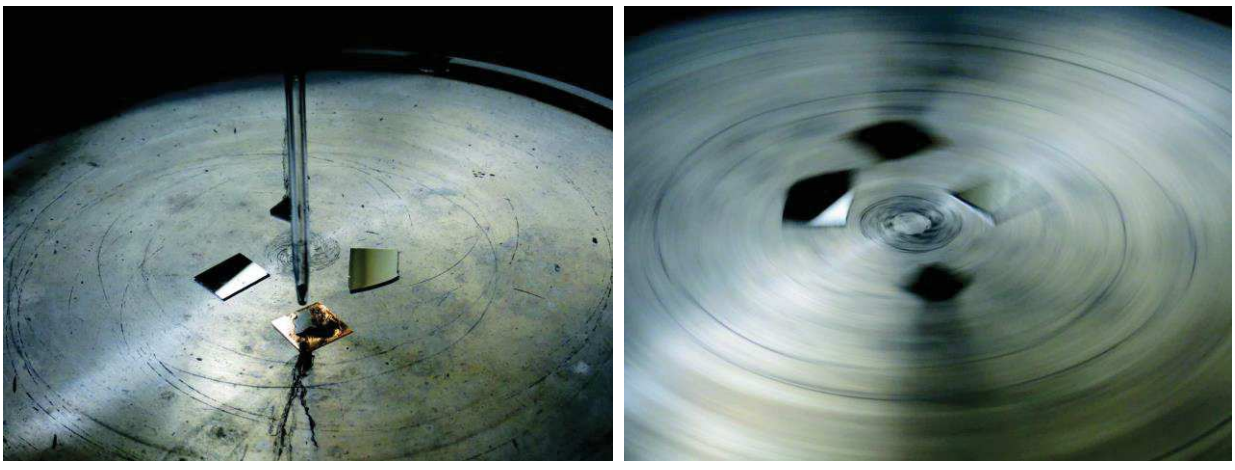

(a) (b)

Fig. 3.2 SWCNT Spin coating process, (a) static dispense process, (b) spin-coating process.

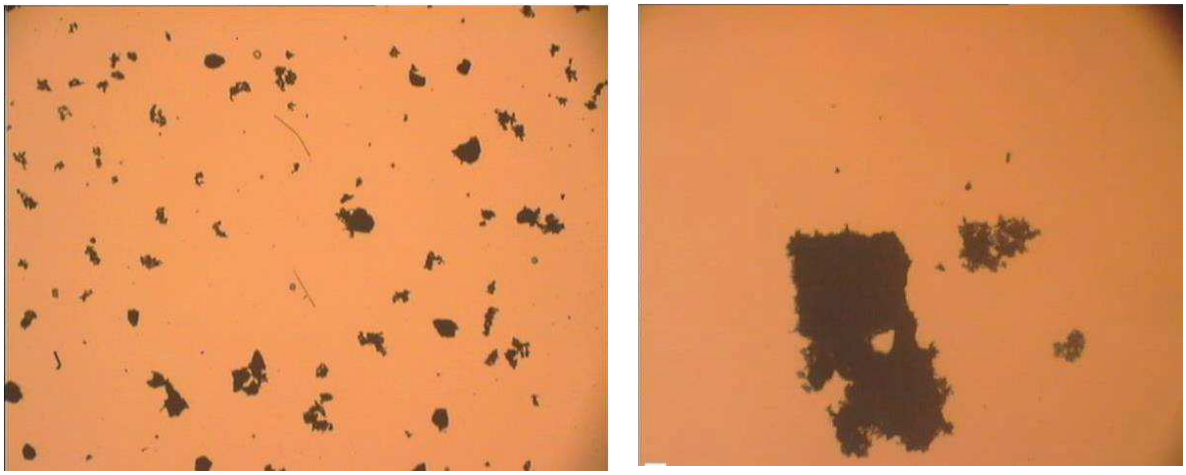

(a) (b)

Fig. 3.3 The optical microscope images of nanotube clusters distributed on silicon substrates: (a) image of 5 times magnification, (b) image of 50 times magnification.

3.3. Nanoindentation test for SWCNT thin film

3.3.1. Brief description of nanoindentation setup

Fig. 3.4 shows the schematic description of the nanoindentation setup. At the heart of the nanoindentation system is a pendulum that rotates on a friction-less pivot. A coil is mounted at the top of the pendulum. When the coil current is present, the coil is attracted towards a permanent magnet, producing motion of the diamond towards the sample and into the sample surface. The displacement of the diamond is measured by means of a parallel plate capacitor, one plate of which is attached to the diamond holder. When the diamond moves, the capacitance changes, and this is measured by means of a capacitance bridge. The capacitance bridge unit is located close to the measuring capacitor in order to minimize stray capacitance effects.

Sample manipulation is achieved by means of three DC motors driving micrometer stages in an XYZ configuration. The electronics motor control consists of a mother board containing three power modules, an IEEE interface module and a backlash control board. These plug into expansion slots in the computer. The motor power supply is derived from the computer, with motor positioning is by means of magnetic encoders. The motor control board communicates with the system computer via the IEEE bus.

The limit stop defines the maximum outward movement of the diamond, and also the operating orientation of the pendulum, when a load is applied. Its position is manually

adjusted with a micrometer. The equilibrium position of the pendulum, with zero load current, is adjusted with balance weights which are movable along both the horizontal and vertical axes.

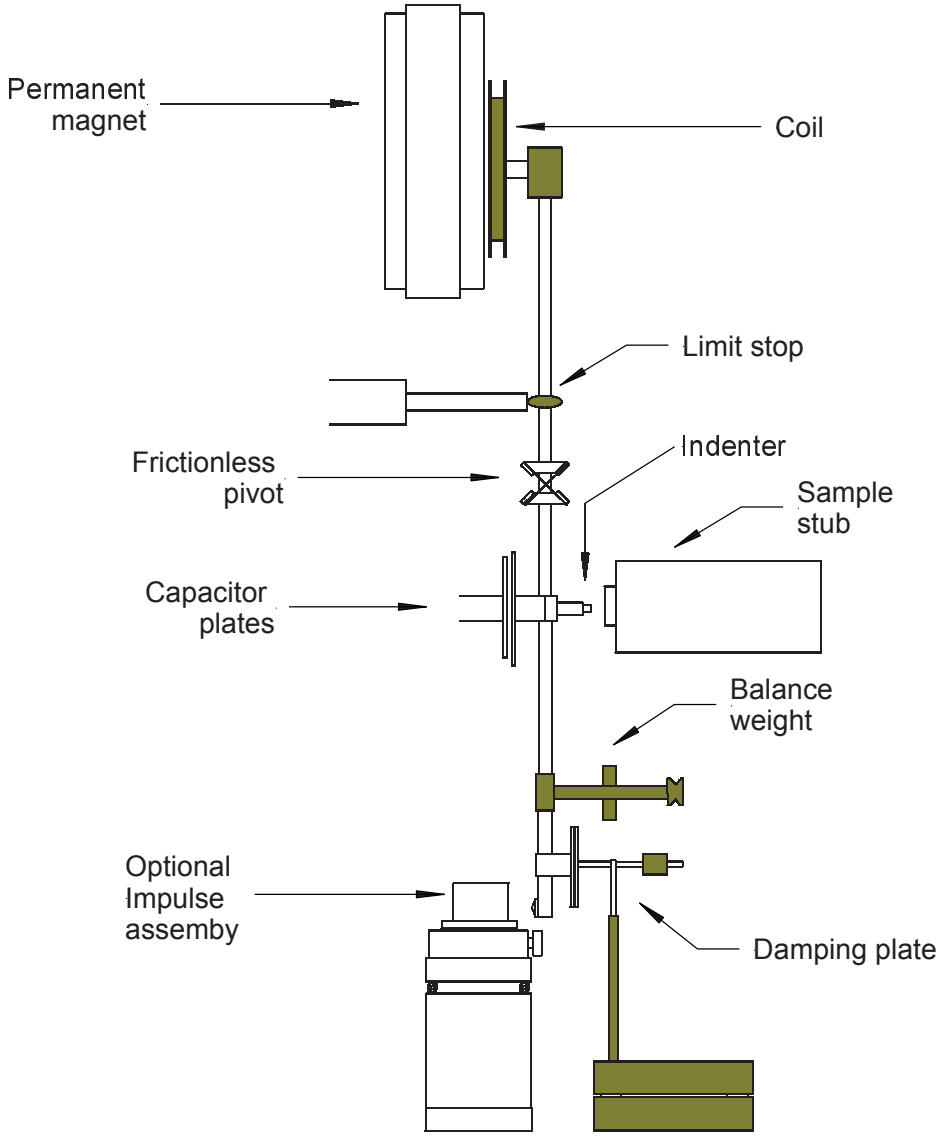

Fig. 3.4 Schematic of the NanoTest setup

3.3.2. Principal of nanoindentation technique

Nanoindentation test measures the movement of a diamond probe in contact with the material surface. For indentation measurements, the indenter is impressed into the material surface under an increasing load. After it reaching a pre-determined maximum load or displacement, the load is reduced and the penetration depth decreases due to elastic recovery of the deformed material. Fig. 3.5 shows the schematic of a cross section of indentation.

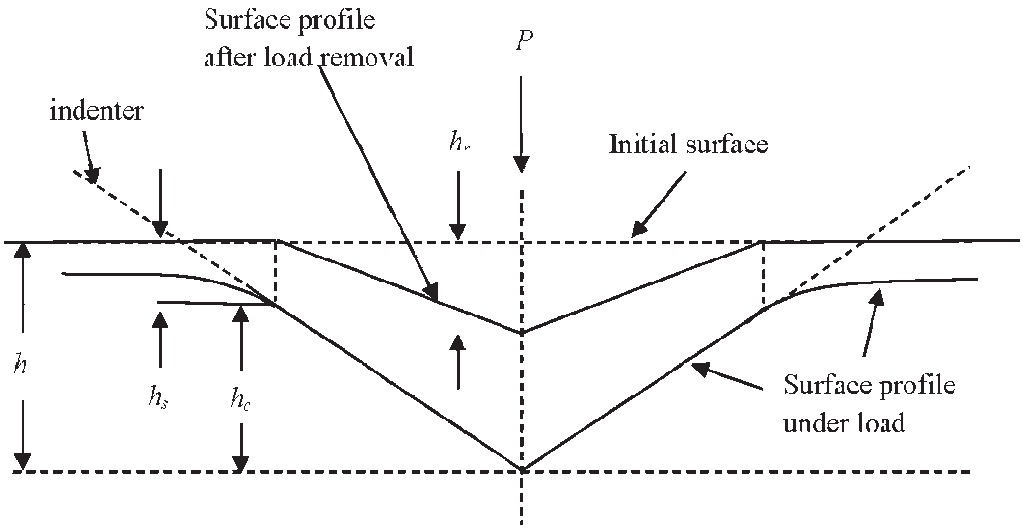

Fig. 3.5 Schematic representation of a section through an indentation

During the indentation process, the load and depth of the indenter are monitored continuously which allows both hardness and Young's modulus of the material to be derived. In nanoindentation technique, it is common to define the hardness of the material as the mean pressure:

$$H = \frac{P_{max}}{A} \tag{3–1}$$

where P_{max} is the maximum load and A is the projected contact area at maximum load calculated from the contact depth h_c (Oliver, Warren Carl 1992)

$$A = A(h_c)$$

$$= 24.5h_c^2 + C_1h_c^1 + C_2h_c^{1/2} + C_3h_c^{1/4} + \cdots + C_8h_c^{1/128} \tag{3–2}$$

The Young's modulus is obtained by contact mechanics.

$$\frac{1}{E_r} = \frac{(1-v^2)}{E} + \frac{(1-v_i^2)}{E_i} \tag{3–3}$$

where E and v are Young's modulus and Poisson's ratio of the tested material; E_i and v_i are the same parameters for the indenter; E_r is reduced modulus, which can be deduced from the initial slope of the unloading data (Fig. 3.6) as:

$$E_r = \frac{1}{2}\frac{dp}{dh}\frac{\sqrt{\pi}}{\sqrt{A}} \tag{3–4}$$

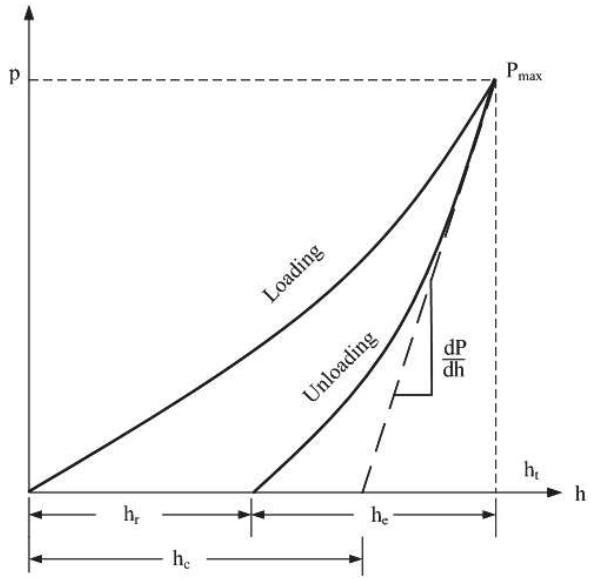

Fig. 3.6 Typical load-displacement curve in nanoindentation

3.3.3. Nanoindentation test for SWCNT thin film

Experimental tests for SWCNTs films were performed at the nanoindentation platform system. The system has the load and displacement resolution of 1 nN and 0.0002 nm, respectively. The measurement range of film thickness is more than 200nm. Berkovich indenter, a three-sided pyramid with a half angle of 65.3˚ was used in the experiment. The test surrounding temperature is controlled within 25º±1ºC. The test system was placed on a vibration free isolated chamber as shown in Fig. 3.7. The surface of the specimen is first scanned, and then a relatively large and uniform area of the film on the substrate was chosen for the test subject, as shown in Fig. 3.3 (b). The indenter was first loaded and unloaded three times successively at a constant rate to examine the reversibility of the deformation. Indentations were made at eighteen different nodes on the chosen area. Table 3.1 is the parameters setting in indentation procedure.

Table 3.1 Parameters setting in indentation procedure

Maximum Load	3.0000mN
Limit stop load	0.1500 mN
Initial load	0.0500 mN
Loading rate	0.1000 mN/s
Unloading rate	0.1000 mN/s
indentations	18
Dwell period at maximum load	5s

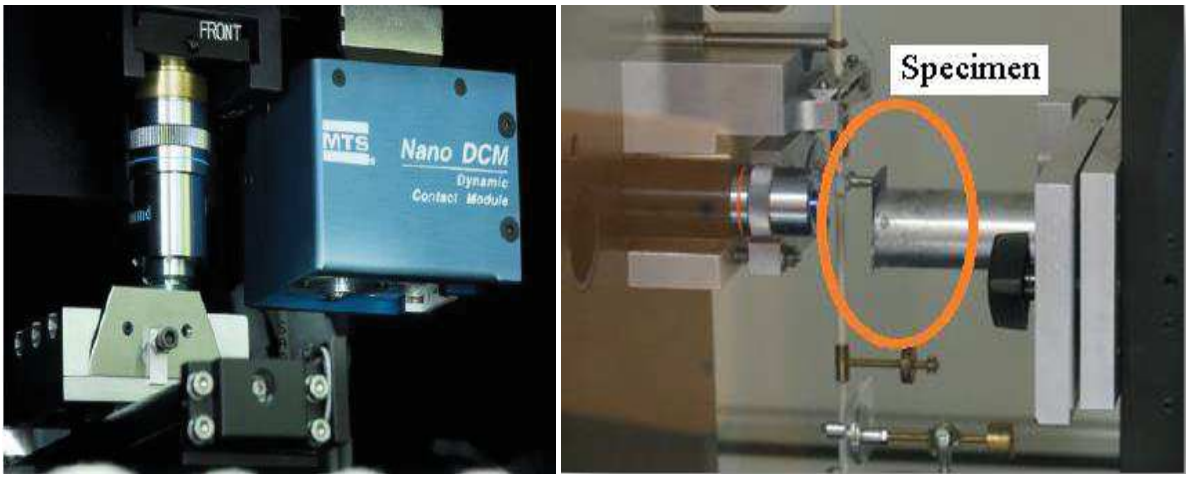

Fig. 3.7 Nanoindentation test system

3.3.4. Experimental results

The experimental results were corrected for the thermal drift of the equipment, and for the uncertainty in the zero position. The hardness and elastic modulus were the average of 18 indentations on different position of the tested surface. The hardness is defined by eq. (3–1). Doerner and Nix observed that for some materials, the initial portions of unloading curves are linear (Doerner & Nix 1986), the unloading stiffness is then related the modulus and contact area through the relationship equivalent to equation

$$S = \frac{dP}{dh} = \frac{2}{\sqrt{\pi}} E_r \sqrt{A} \tag{3–5}$$

S = dP/dh is the initial unloading stiffness obtained by the initial portion of the unloading data, A is the projected area of the elastic contact, it is assumed that the contact area between the indenter and the material remains constant and moves elastically during unloading, and the plastic area is always equal to the contact area, and it was calculated using a polynomial function of order 2 in the experiment. In this study, the hardness and elastic modulus was determined by using method of power law fitting between 100% and 20% of unloading data.

$$p = \alpha(h - h_f)^m \tag{3–6}$$

The overview of the experimental results for the 18 groups of load-displacement curves is demonstrated in Fig. 3.8. The experimental loading-unloading curves show that there are two groups of curves which are not consistent with the bulk of the data. This inconsistent may be

caused by the defects of the SWCNTs film sample, dislocation, etc., and will be further discussed in the following part.

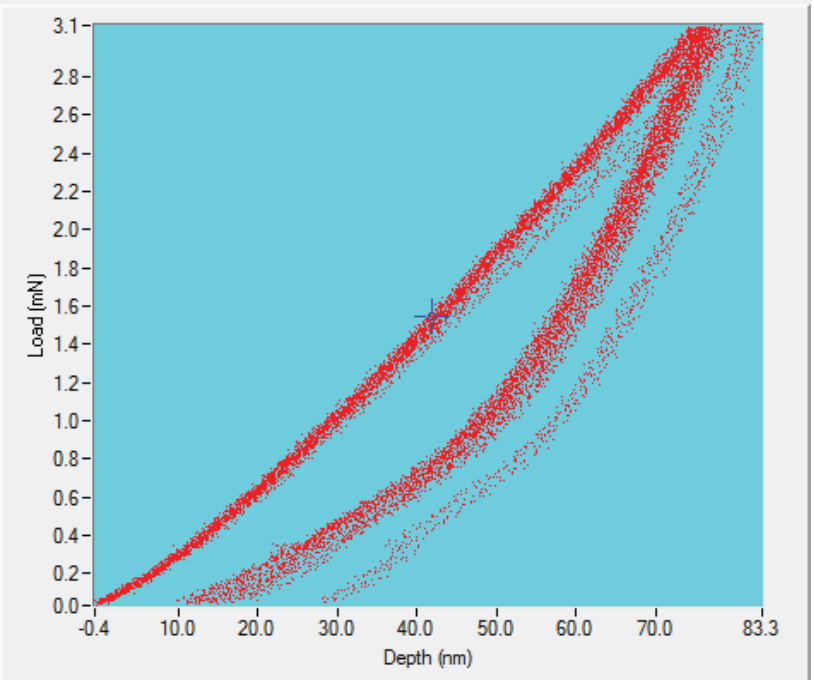

Fig. 3.8 The overview of the experimental results

Table 3.2 representing the averages results of 18 indentations obtained automatically by the test system. Yong's modulus of the SWCNT film is calculated according to (3–3).

Table 3.2 Nanoindentation results

Maximum Load (mN)	3.054 ± 20.007
Maximum Depth (nm)	77.68 ± 2.06
Plastic depth (nm)	54.2± 3.31
Hardness (GPa)	12.57719 ± 0.759
Reduced modulus (GPa)	169.81778± 4.911

3.4. Uncertainty analysis for the estimated elastic properties of SWCNTs thin film

3.4.1. Source of uncertainty in nanoindentation

In practice, various errors are associated with nanoindentation process. Some errors arise from environmental changes during the test (like temperature variation); some are due to equipment defects (like non-ideal shape of the indenter, frame vibrations), or some are affected by material issues. Jaroslav Menčík (Menčík 2012) suggests that the errors and uncertainties of nanoindentation measurement mainly caused by the following parameters:

1) The properties of the tested material

2) The models used for data evaluation

3) The properties of the indenter

4) The device properties

5) The specimen properties

6) The initial depth of penetration

7) The temperature changes, drift

8) The contact profile, pile-up

9) The indentation size effect

10) The surface forces and adhesion

11) The scatter of measured values

For the component of SWCNTs thin film coated on the silicon substrate in this study, the value of the indentation modulus may be greatly affected by material behavior, which is not accounted for in the analysis of load-displacement data and other factors (the theoretical model used in indentation, approximate assumption, etc.)

3.4.2. Uncertainty evaluation

3.4.2.1. Models used for data evaluation

The determined mechanical properties of SWCNTs film are the hardness H and the elastic modulus E_r, which are separately defined in equations (3–1) and (3–4). In Eqns. (3–1) and (3–4), the contact area A is calculated from the contact depth h_c, which is related to the total displacement h_{max} of indenter as:

$$h_c = h_{max} - \varepsilon\left(\frac{P_{max}}{S}\right) \tag{3–7}$$

where S is the contact stiffness equals to the tangent at the maximum load.

$$\mathrm{S} = \frac{dP_{max}}{dh_{max}} = m\alpha\left(h_{max} - h_f\right)^{m-1} \tag{3–8}$$

The value of ε depends on the indenter geometry. For a Berkovich indenter ε is 0.75.

3.4.2.2. Load calibration

The Load calibration establishes the forces that can be applied at the diamond tip during a measurement. Calibration consists of hanging a series of masses from a set point (the balance point) at the bottom of the pendulum while the coil applies a countering force equal to a known voltage for each mass (Beake et al. 2002). Typical results for the calibration for different load range are:

NT1 − 45mN maximum load (high load range) and 10mN maximum load (low load range)

NT2 −500mN maximum load (high load range) and 70mN maximum load (low load range)

MT − 20N maximum load (high load range) and 2N maximum load (low load range)

Using the uncertainty propagation law, the standard force uncertainty u (F) of nanoindentation system can be expressed as:

$$[u(F)]^2 = [g \times u(I_m)]^2 + [I_m \times u(g)]^2 + [u(F_r)]^2 + [u(\Delta_F)]^2 \tag{3–9}$$

where u (I_m) is the standard uncertainty of electronic balance, u (g) is the standard uncertainty of acceleration of gravity, u (F_r) is the standard uncertainty resulting from the resolution of force transducer, $u(\Delta_F)$ is the standard uncertainty of indication error.

3.4.2.3. Displacement calibration

The Depth calibration is fairly sensitive to operating conditions. The Depth calibration relates the changes in capacitance to a known distances moved by a sample in contact with the pendulum. The sample movement is determined directly from the stage movement (encoder displacement). The sensitivity and hence the depth range can be altered in the schedule by changing the value of Amplifier Gain, with maximum sensitivity at 100% and minimum at 15%. Typical results for the calibration are:

NT − Depth Calibration Factor = 0.05-0.06 nm/bit (+/- 5 x 10^{-4})

MT − Depth Calibration Factor = 0.2-0.23 nm/bit (+/- 5 x 10^{-3})

The standard displacement uncertainty $u(h)$ of nanoindentation system can be expressed as:

$$[u(h)]^2 = [u(I_h)]^2 + [u(\Delta I_h)]^2 + [u(h_r)]^2 + [u(h_t)]^2 + [u(h_z)]^2 + [u(h_c)]^2 \qquad (3\text{–}10)$$

where $u(I_h)$is the standard uncertainty from the optical interferometer, $u(\Delta I_h)$is the standard uncertainty from the gauge, $u(h_r)$ is the standard uncertainty from the displacement repeatability, $u(h_t)$ is the standard uncertainty from the thermal drift, $u(h_z)$is the standard uncertain resulting from the zero point, $u(h_c)$is the standard uncertainty resulting from the uncertainty of machine compliance of nanoindentation system .

3.4.2.4. Errors identification in the experiment

As aforementioned, estimation of experimental errors is a basic task in the system uncertainty assessment. In our study, the interested quantities of SWCNT film hardness H and elastic modulus E_r are derived from the direct measurand of indentation loads and displacements. Parameters in the power law model (3–6) are obtained by making a power function regression analysis for the test data between 100% and 30% of the unloading process. Fig. 3.9 is the data fitting and uncertainty analysis for unloading process of the 18 set of indentation nodes. Table 3.3 is the estimated parameters of model (3–6) for each set of indentation nodes.

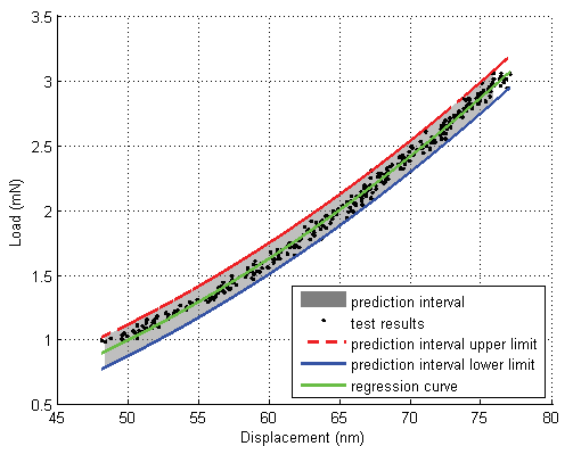
Load (mN)
Displacement (nm)
prediction interval
test results
prediction interval upper limit
prediction interval lower limit
regression curve

(1)

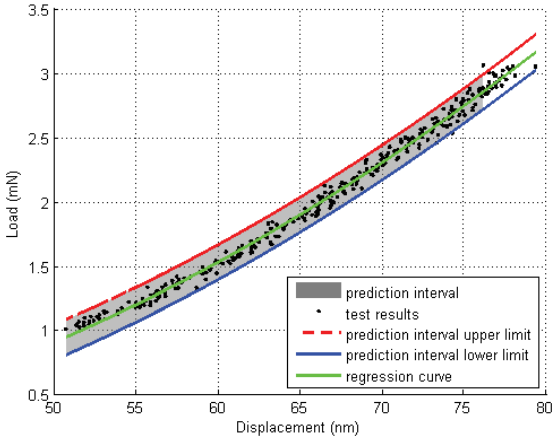
Load (mN)
Displacement (nm)
prediction interval
test results
prediction interval upper limit
prediction interval lower limit
regression curve

(2)

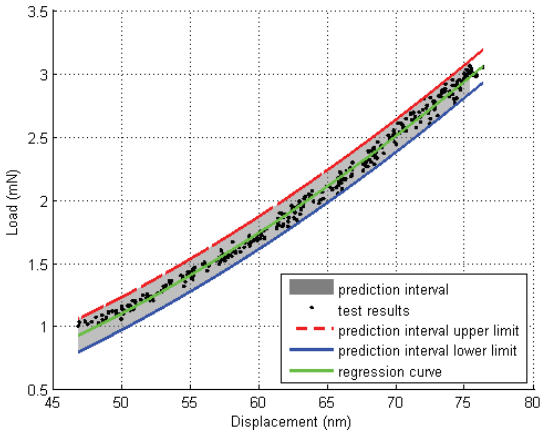
Load (mN)
Displacement (nm)
prediction interval
test results
prediction interval upper limit
prediction interval lower limit
regression curve

(3)

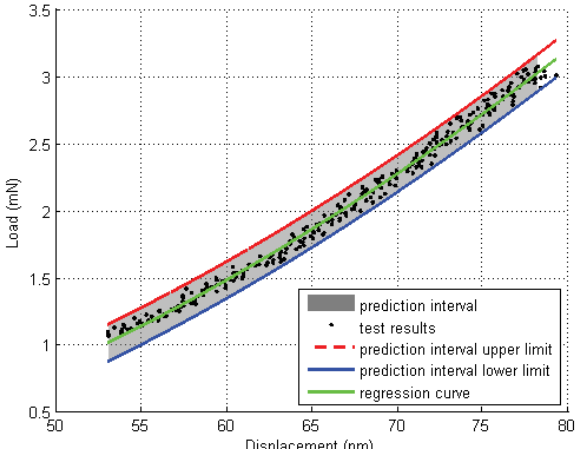
Load (mN)
prediction interval
test results
prediction interval upper limit
prediction interval lower limit
regression curve

(4)

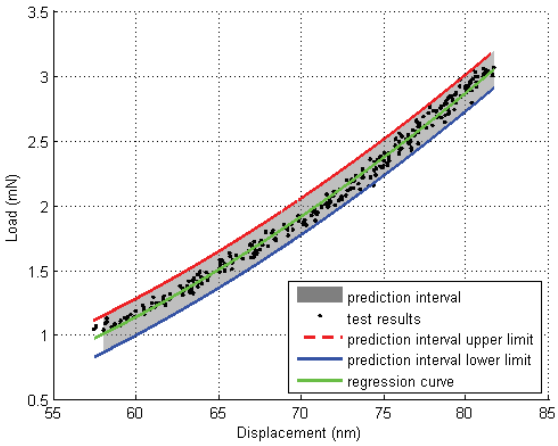
Load (mN)
Displacement (nm)
prediction interval
test results
prediction interval upper limit
prediction interval lower limit
regression curve

(5)

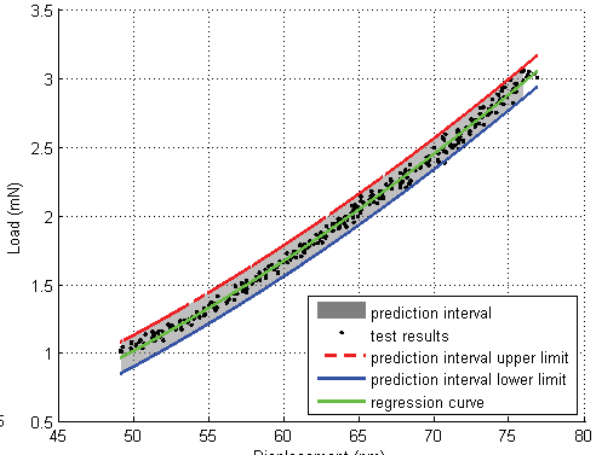
Load (mN)
prediction interval
test results
prediction interval upper limit
prediction interval lower limit
regression curve

(6)

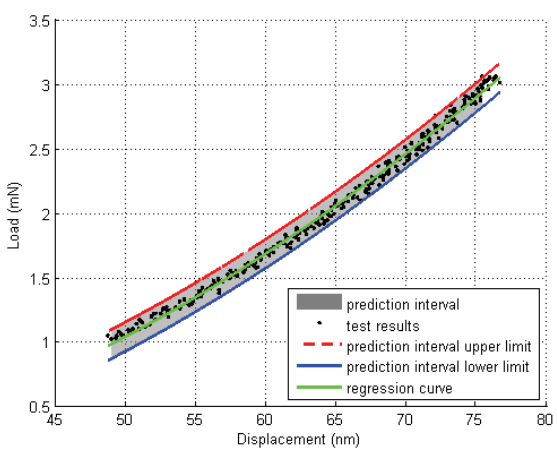
Load (mN)
Displacement (nm)
prediction interval
test results
prediction interval upper limit
prediction interval lower limit
regression curve

(7)

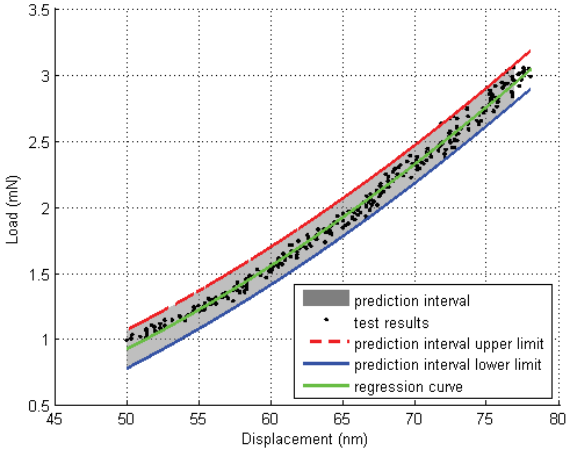
Load (mN)
Displacement (nm)
prediction interval
test results
prediction interval upper limit
prediction interval lower limit
regression curve

(8)

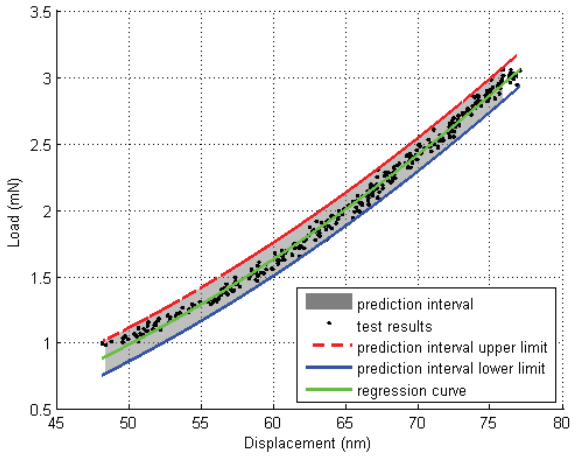
Load (mN)
Displacement (nm)
prediction interval
test results
prediction interval upper limit
prediction interval lower limit
regression curve

(9)

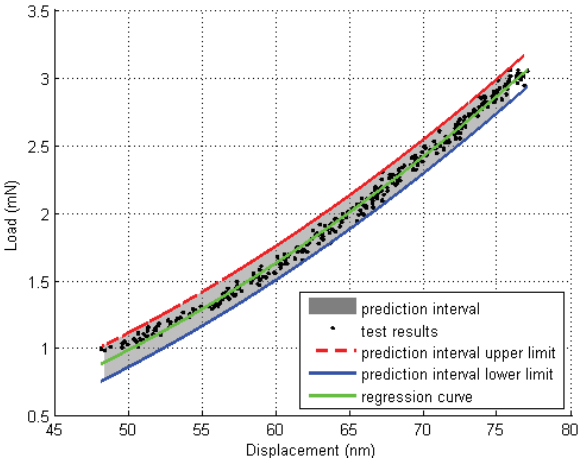
Load (mN)
Displacement (nm)
prediction interval
test results
prediction interval upper limit
prediction interval lower limit
regression curve

(10)

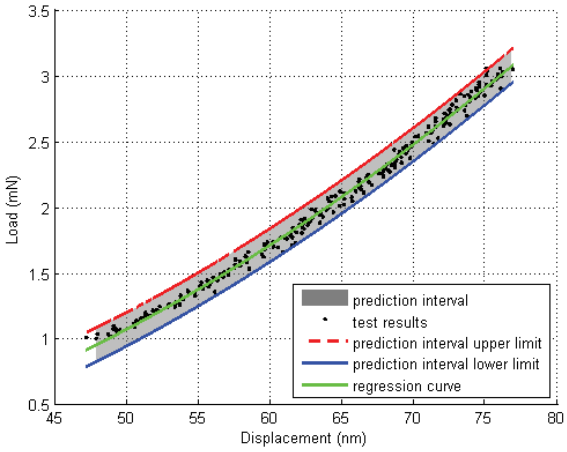
Load (mN)
Displacement (nm)
prediction interval
test results
prediction interval upper limit
prediction interval lower limit
regression curve

(11)

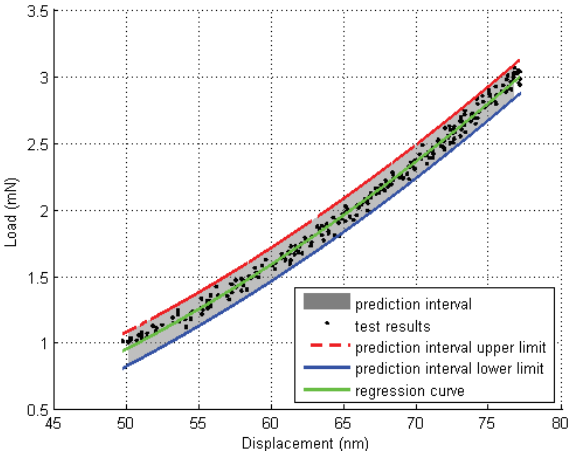
Load (mN)
Displacement (nm)
prediction interval
test results
prediction interval upper limit
prediction interval lower limit
regression curve

(12)

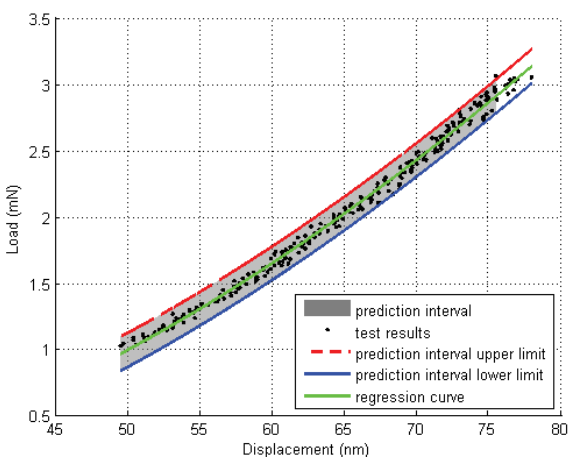

(13)

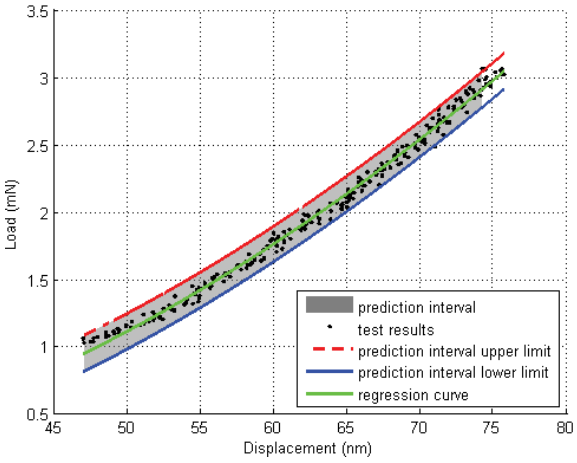

(14)

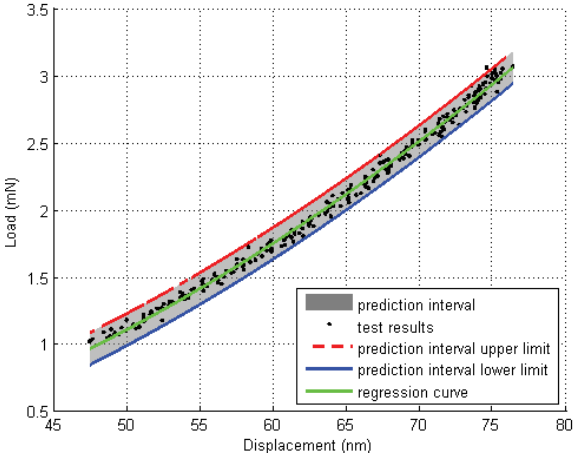

(15)

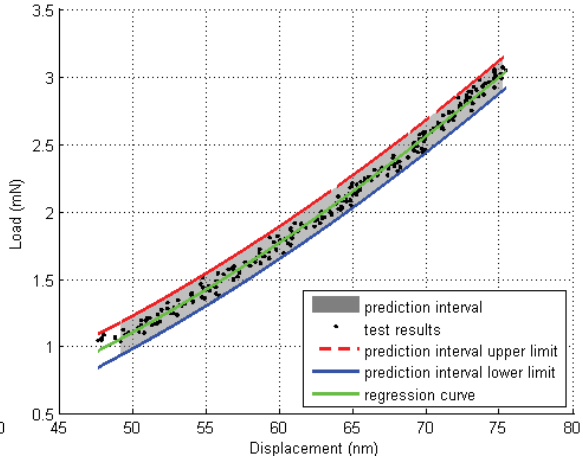

(16)

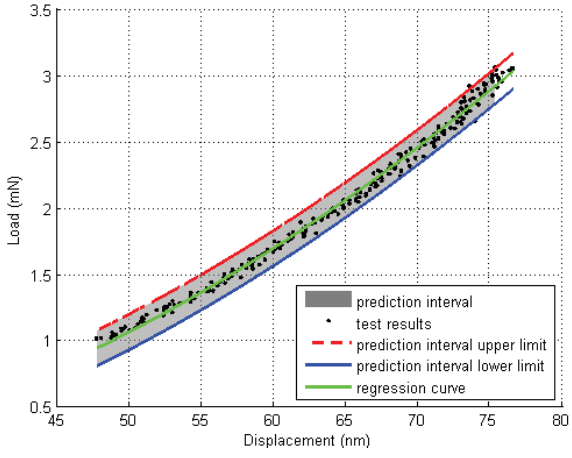

(17)

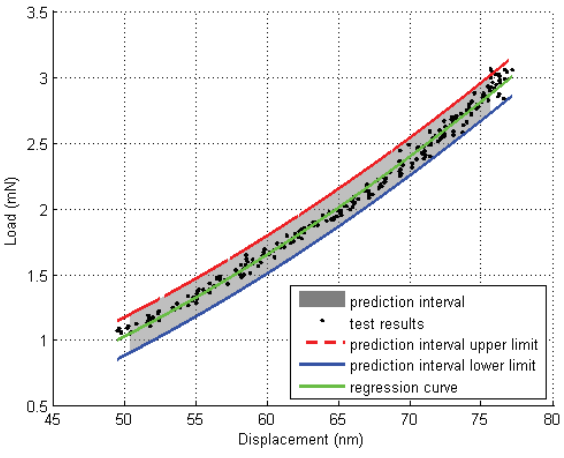

(18)

Fig. 3.9 Uncertainty prediction of unloading process for 18 set of indentation nodes

Table 3.3 Estimated parameters by Power-law fitting

	α	h_f (nm)	m	F_{max} (mN)	h_{max} (nm)	σ^2
1	0.00133	16.97903	1.890	3.050	76.90	0.002
2	0.0013	18.58379	1.892	3.046	79.29	0.0023
3	0.00144	14.20107	1.856	3.055	76.20	0.0022
4	0.00230	22.86779	1.790	3.069	79.23	0.0025
5	0.00152	27.89517	1.908	3.058	81.61	0.0026
6	0.00213	18.23268	1.786	3.055	76.75	0.0016
7	0.00193	17.27196	1.803	3.053	76.58	0.0016
8	0.00189	19.64588	1.816	3.047	77.91	0.0026
9	0.00140	16.22530	1.870	3.047	77.79	0.0018
10	0.00148	28.73417	1.909	3.045	83.34	0.0031
11	0.00184	16.06429	1.807	3.059	76.83	0.002
12	0.00188	19.11446	1.817	3.060	77.16	0.0021
13	0.00208	18.56658	1.793	3.046	77.87	0.002
14	0.00149	14.38536	1.851	3.054	75.66	0.0022
15	0.00123	12.92586	1.884	3.062	76.28	0.0016
16	0.00146	14.64508	1.861	3.063	75.29	0.002
17	0.00129	14.38413	1.879	3.051	76.51	0.0021
18	0.00169	16.12715	1.821	3.048	77.04	0.0025
mean	0.00165	18.15832	1.846	3.0538	77.68	0.0022
median	0.00151	17.1255	1.854	3.0535	76.97	
range	0.00107	15.8083	0.1229	0.024	8.05	
skewness	0.51469916	1.293	0.004	0.51	1.5	
Standard deviation	0.00032	4.4099	0.042	0.0069	2.058	

- **Parameter distribution in model**

After analyzing the skewness of parameter α, h_f, and m in Table 3.3, we can see that α and h_f obey the right skewed distribution and m obeys a symmetric distributions. Fig.3.10 displays the distribution of parameter α, h_f, m, f_{max}, and h_{max} in Table 3.3. According to a visual analysis of the probability distribution for α, h_f, and m and the statement in (Anon 2014), we preliminarily hypothesize thatα and h_f may obey the lognormal distribution and m may obey the normal distribution. That is:

$$\ln\alpha \sim N(\mu_\alpha, \sigma_\alpha^2) \tag{3–11}$$

$$\ln h_f \sim N(\mu_{h_f}, \sigma_{h_f}^2) \tag{3–12}$$

$$m \sim N(\mu_m, \sigma_m^2) \tag{3–13}$$

By fitting the experimental distributions of the values of α, h_f, and m in Table 3.3 to the hypothetical distribution, we obtain μ_α and σ_α equal to -6.42 and 0.19, respectively; and μ_{h_f} and σ_{h_f} equal to 2.87 and 0.22 , respectively. Applying the bootstrap method, a theoretical $1-\alpha$ level confidence interval for α, h_f, and m are estimated. Table 3.4 lists the 0.95 level of confidence interval for α, h_f, and m.

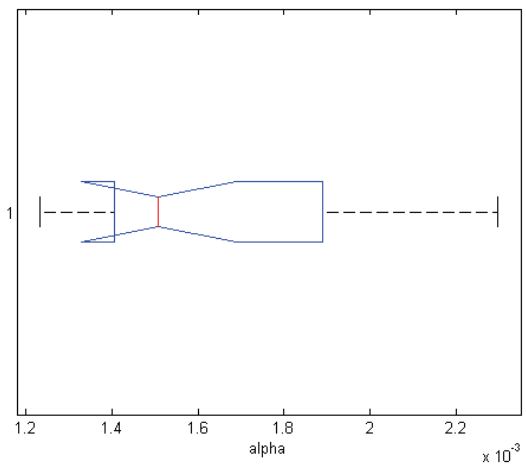

(a1)

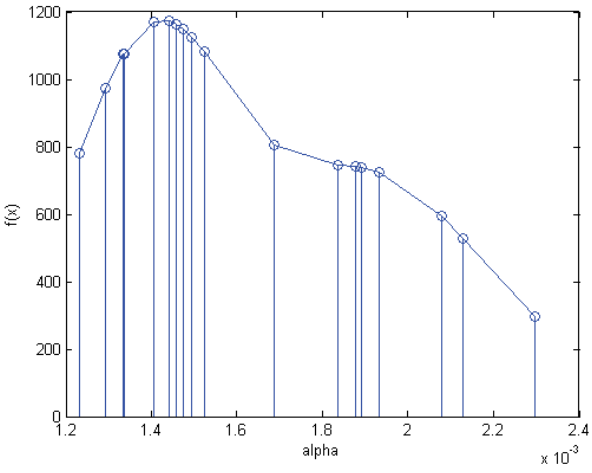

(a2)

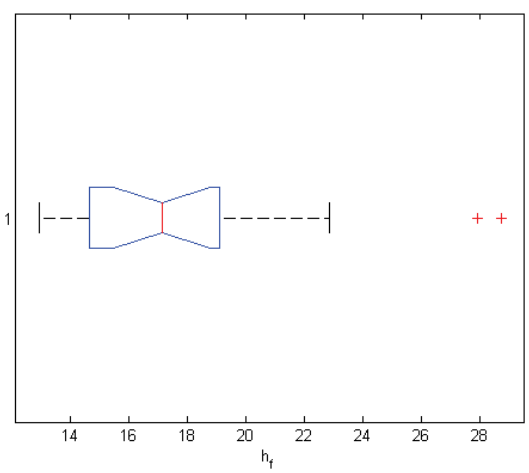

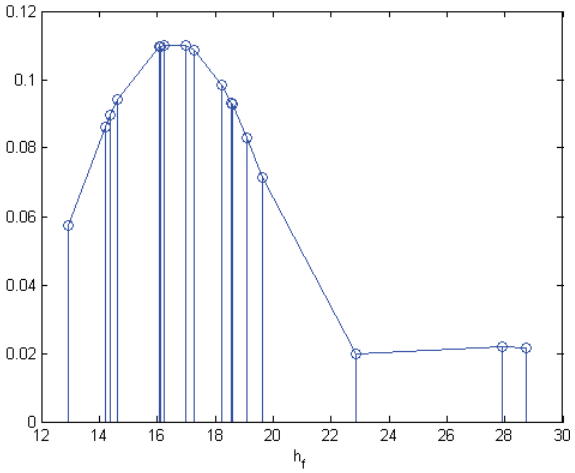

(b1) (b2)

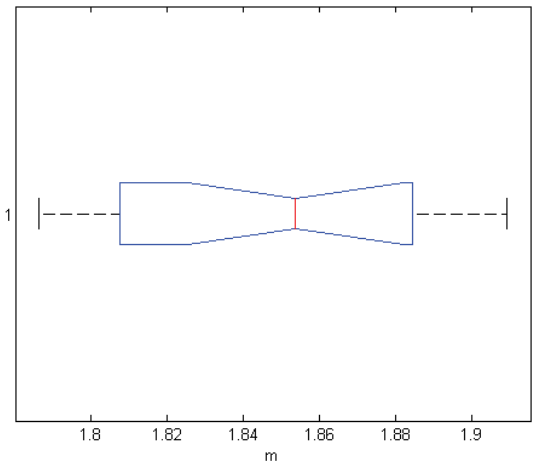

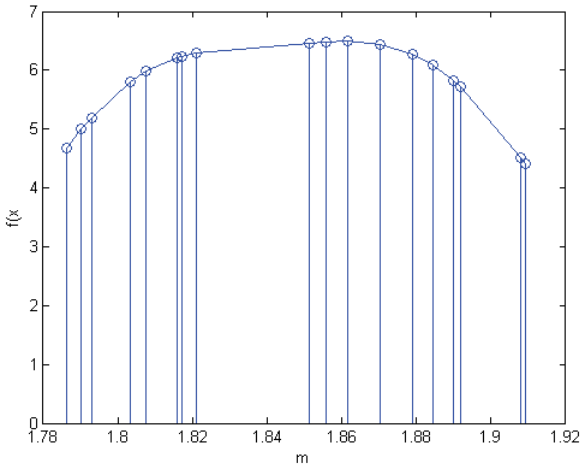

(c1) (c2)

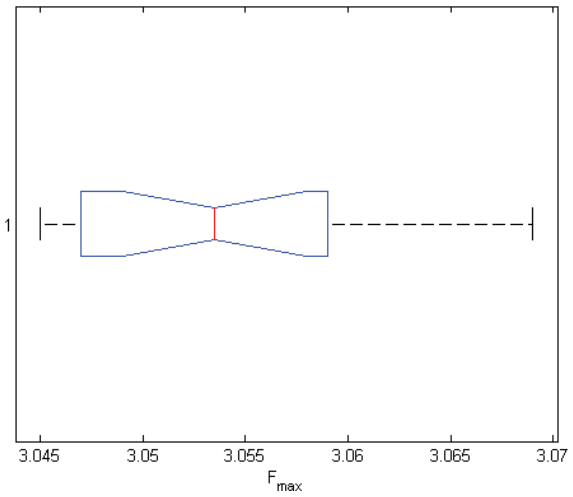

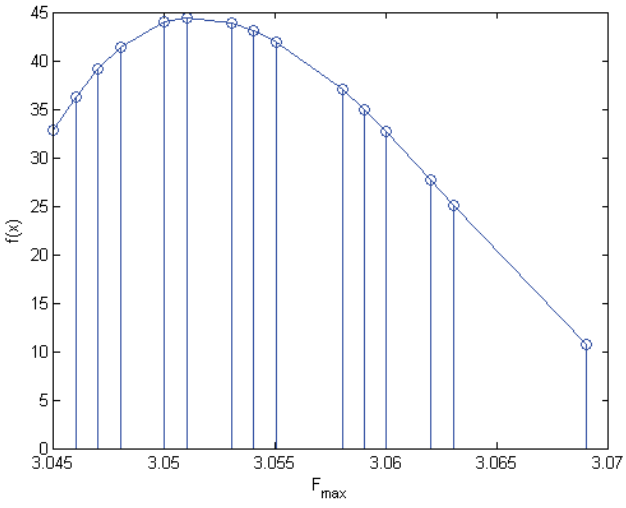

(d1) (d2)

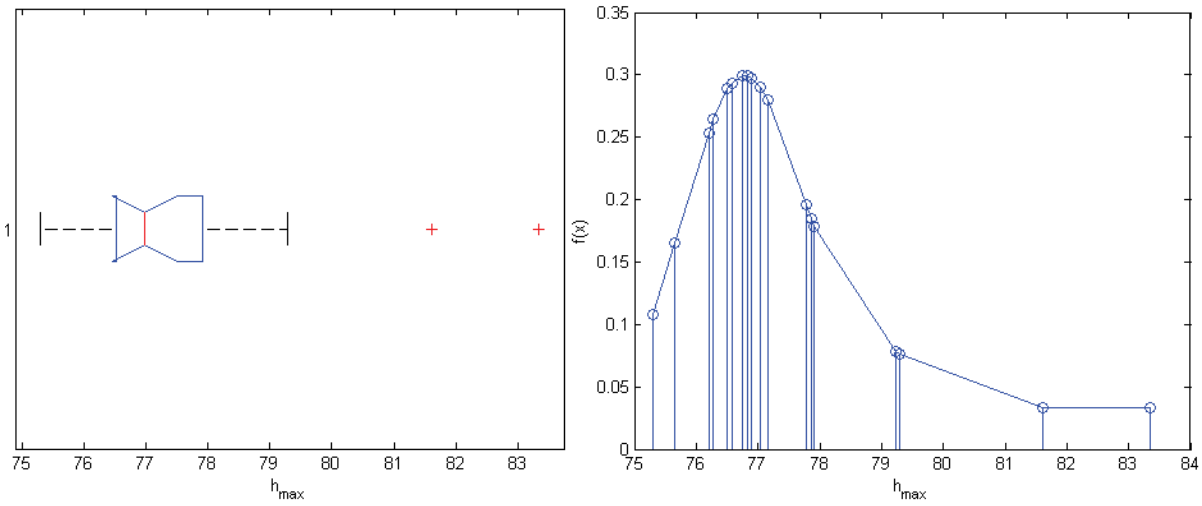

(e1) (e2)

Fig.3.10 (a1), (b1), (c1), (d1), (e1): boxplot of α, h_f, m, f_{max}, and h_{max} in Table 3.3; (a2), (b2), (c2), (d2), (e2): Pdf of α, h_f, m, f_{max}, and h_{max}

Table 3.4 95% confidence interval by parametric bootstrap method

parameter	alpha	h_f	m
mean	0.00165	18.15689	1.846
confidence interval	[0.00112, 0.00214]	[10.71969,25.28685]	[1.762,1.930]

For testing whether the parameter α, h_f, and m in Table 3.3 follow the expected probability distribution, we take a goodness of fit test. As the sample size is small (n=18), we use the Kolmogorov - Smirnov goodness of fit test method here, and the hypotheses H are taking as the following:

H_0**:** The data are consistent with the specified distribution

H_1: The data are *not* consistent with the specified distribution

From the table of the Kolmogorov-Smirnov Test, with α=0.05, n=18, the critical value is 0.3094. The observed value of the test statistic D is stated in Table 3.5, which indicates that for the hypothesized distribution of parameter α, h_f, and m, the test statistic D is smaller than the critical value. So, we cannot reject the claim that the data were sampled from the expected distribution at the level α=0.05. Fig.3.11 is the comparison of empirical and theoretical fitted distribution for the parameter distribution, it shows that the experimental distribution for α, h_f, and m can satisfactorily fit with the hypothetical distribution.

Table 3.5 Results of goodness of fit test for parameter distribution

	alpha	h_f	*m*
H	0	0	0
p	0.4562	0.7384	0.626
D	0.1932	0.1529	0.1686

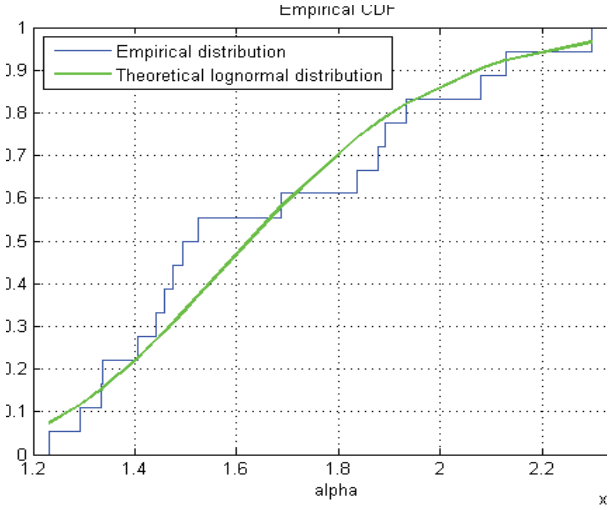
Empirical distribution
Theoretical lognormal distribution
alpha
x

(a1)

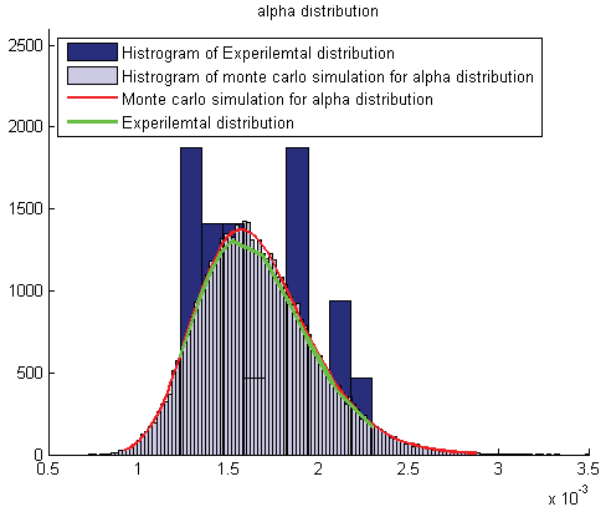
alpha distribution
Histrogram of Experilemtal distribution
Histrogram of monte carlo simulation for alpha distribution
Monte carlo simulation for alpha distribution
Experilemtal distribution
x 10^-3

(a2)

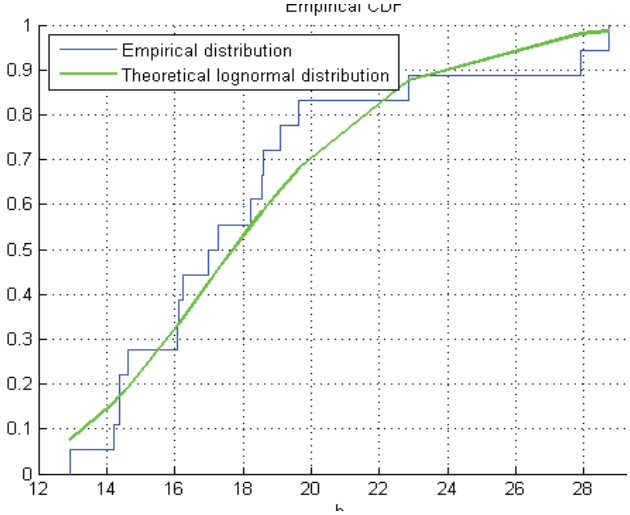
Empirical distribution
Theoretical lognormal distribution

(b1)

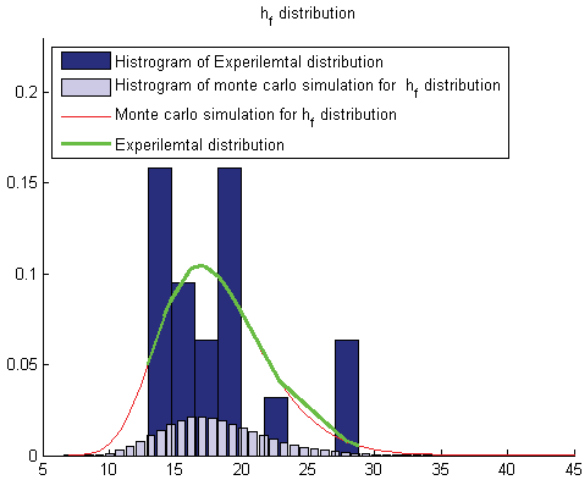

(b2)

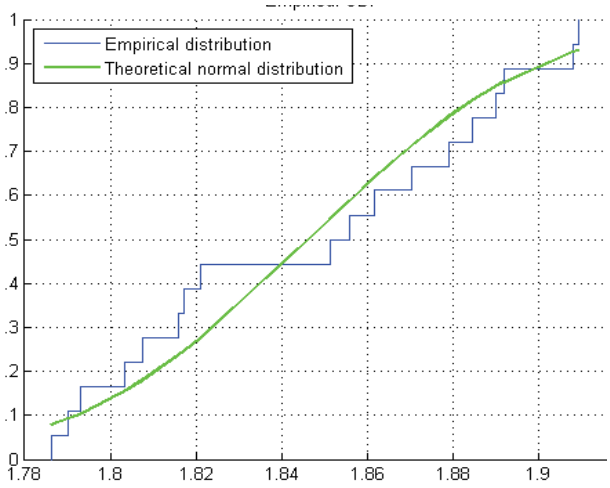

(c1)

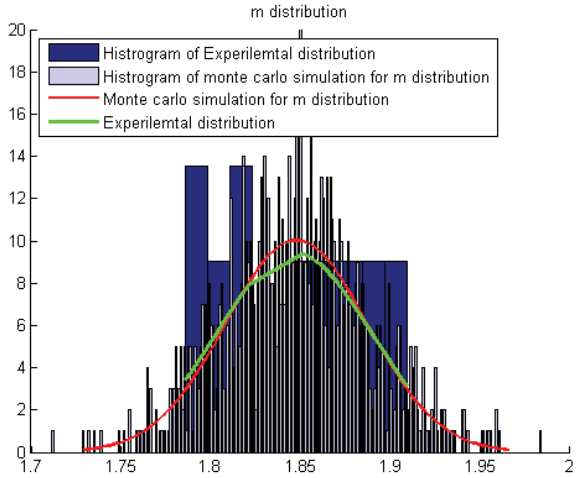

(c2)

Fig.3.11 Parameter distribution. (a1), (b1), (c1): The empirical CDF distribution and theoretical CDF distribution of the hypothesized function; (a2), (b2), (c2): Comparison of empirical and theoretical fitted distribution

- **Uncertainty analysis for unloading process curve**

Based on the statistic estimation of the parameters α, h_f, and m distribution, we characterize the load-displacement curve for the 70% upper part of unloading process using Monte Carlo simulation method. Fig.3.12 illustrates the comparison between the experimental and the simulation with a sample size of 1000 load-displacement curves for the upper part of unloading process. Fig.3.12 Indicates that the experimental curves are rigorously inside the 60% confidence interval of the numerical simulation results (the black line). The red line presents the load distribution at the displacement of h= 55nm in the simulation through a probability distribution fitting.

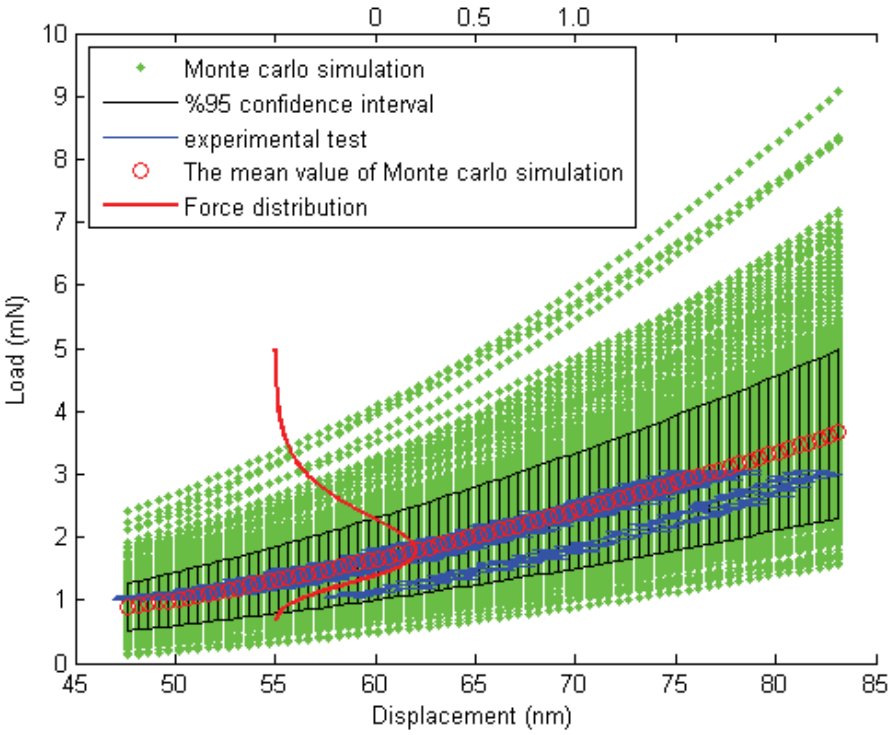

Fig.3.12 Comparison of the simulation and experimental load-displacement curve for unloading process

3.4.2.5. Area calibration and uncertainty evaluation

The area calibration relates the actual, non-ideal diamond contact area to the depth of penetration. The target of the area calibration is to find the function which can be used for a wide indentation range to obtain accurate hardness and modulus values. In our study, the diamond area (A) is approximately calculated using a polynomial function of order 2:

$$\mathrm{A} = c_2 {h_c}^2 + c_1 h_c + c_0 \tag{3–14}$$

For an ideal Berkovitch indenter c_2= 24.5, c_1 =c_0= 0. For a real Berkovitch indenter, the typical values are c_2 = 20~24, c_1 = 1500~3000 (Beake et al. 2002) (Although each diamond is slightly different, these values are only a guideline). Here the coefficients are: c_2= 21.93, c_1 =2330.6, c_0=52726.9.

According to the uncertainty propagation law, the standard area uncertainty *u(A)* can be expressed as:

$$[u(A)]^2 = (2c_2 h_c + c_1) \times [u(h_c)]^2 + u_\Delta^2 \tag{3–15}$$

$u_\Delta^2$is the residuals of fitting curve,$u(h_c)$is the uncertainty of contact depth which can be derived from (3–7)

$$[u(h_c)]^2 = [u(h_{max})]^2 + \left[\frac{\varepsilon}{S} u(F_{max})\right]^2 + \left[\frac{\varepsilon}{S^2} F_{max} u(S)\right]^2 \tag{3–16}$$

where $u(h_{max})$ is the uncertainty of maximum contact depth, $u(F_{max})$ is the uncertainty of maximum applied load, and $u(S)$ is the uncertainty of contact stiffness that can be obtained from (3–8)

$$\begin{aligned}[u(S)]^2 = {} & m\alpha(m-1)\left(h_{max} - h_f\right)^{m-2}\left[u(h_{max})^2 + u(h_f)^2\right] \\ & + m\left(h_{max} - h_f\right)^{m-1}[u(\alpha)]^2 + \alpha ln(m-1)\left(h_{max} - h_f\right)[u(m)]^2\end{aligned} \tag{3–17}$$

In this work, the standard maximum load uncertainty $u(F_{max})$ and the standard maximum contact depth uncertainty $u(h_{max})$ are calculated by the standard deviation of 18 node indentation test. According to the parameter distribution analysis in 3.4.2.4 that α and h_f follow a lognormal distribution, the uncertainty are calculated as the root of the variance $u(\alpha) = 0.00032$, $u(h_f) = 4.024$, $u(m) = 0.042$, the uncertainty of F_{max} and h_{max} are $u(F_{max}) = 0.0069mN, u(h_{max}) = 0.4851\ nm$. So:

$$u(S) = 4.75 \text{ nm}$$

The relative standard uncertainty of contact stiffness $u(S)/\mathrm{S}$ is:

$$u(S)/S = 4.75\ /96.4 = 4.94\% \quad (3–18)$$

Then: $$u(h_c) = 1.4385\ nm \quad (3–19)$$

The relative standard uncertainty of contact depth $u(h_c)/h_c$ is:

$$u(h_c)/h_c = 1.4385/53.96 = 2.67\% \quad (3–20)$$

$$u(A)=1029\ nm^2$$

The relative standard uncertainty of contact depth $u(A)/A$is:

$$u(A)/A = 1029/259240 = 3.97\% \quad (3–21)$$

3.4.2.6. Evaluation of hardness uncertainty

The uncertainty of indentation hardness *u(H)* can be obtained from (3–1):

$$[u(H)]^2 = \left[\frac{1}{A}u(F_{max})\right]^2 + \left[\frac{F_{max}}{A^2}u(A)\right]^2 \quad (3–22)$$

Then the relative standard uncertainty of indentation hardness is:

$$\left[\frac{u(H)}{H}\right]^2 = \left[\frac{u(F_{max})}{F_{max}}\right]^2 + \left[\frac{u(A)}{A}\right]^2 \quad (3–23)$$

The relative expanded standard uncertainty of hardness corresponding to a level of confidence of 95% $U(H)$ is:

$$U(H) = 2 \times \frac{u(H)}{H} = 12.07\% \quad (3–24)$$

3.4.2.7. Evaluation of reduced modulus uncertainty

The uncertainty of reduced modulus *u(E_r)* can be obtained from (3–4):

$$[u(E_r)]^2 = \left[\frac{\sqrt{\pi}}{2}\frac{1}{\sqrt{A}}u(S)\right]^2 + \left[\frac{\sqrt{\pi}}{4}\frac{S}{A^{3/2}}u(A)\right]^2 \quad (3–25)$$

The relative standard uncertainty of reduced modulus can be calculated by

$$[\frac{u(E_r)}{E_r}]^2 = \left[\frac{u(S)}{S}\right]^2 + \left[\frac{1}{2}\frac{u(A)}{A}\right]^2 \quad (3\text{–}26)$$

The relative expanded standard uncertainty of reduced modulus corresponding to a level of confidence of 95% $U(E_r)$ is:

$$U(E_r) = 2 \times \frac{u(E_r)}{E_r} = 10.64\% \quad (3\text{–}27)$$

3.4.2.8. Evaluation of Young's modulus uncertainty

As stated in chapter3, the reduced modulus E_r is obtained from (3–3), which is influenced by the Young's modulus of SWCNTs thin film and the indenter. The Young's modulus of SWCNTs thin film can be derived as:

$$E = (1 - v^2)/(\frac{1}{E_r} - \frac{1 - v_i^2}{E_i}) \quad (3\text{–}28)$$

This value depends not only on the reduced modulus E_r, but also on the modulus of indenter and the Poisson's ratio of sample. According to the literature, Young's modulus of the Polycrystalline diamond changes from 1106 *GPa* to 1164 *GPa* depending on the orientation of the crystallites. For the randomly orientated aggregates of diamond crystallites, the Polycrystalline diamond has mean modulus and Poisson's ratio of $\bar{E}$*=1143 GPa*, $\bar{v}$*=0.0691* (Klein & Cardinale 1993). While, the Poisson's ratio of SWCNTs sheets are dependent on the inter-tube torsional angle and the tubes orientation to sheet plan (Hall et al. 2008). The uncertainty of the Young's modulus of SWCNNTs thin film *u(E)* can be obtained from (3–25).

$$\begin{aligned}[u(E)]^2 = &\left[2v/(\frac{1}{E_r} - \frac{1 - v_i^2}{E_i}) \cdot u(v)\right]^2 \\ &+ \left[(1 - v^2)/(\frac{1}{E_r} - \frac{1 - v_i^2}{E_i})^2 \frac{1}{{E_r}^2} \cdot u(E_r)\right]^2 \\ &+ \left[(1 - v^2)(1 - v_i^2)/(\frac{1}{E_r} - \frac{1 - v_i^2}{E_i})^2 \frac{1}{{E_i}^2} \cdot u(E_i)\right]^2\end{aligned} \quad (3\text{–}29)$$

The relative standard uncertainty of the Young's modulus can be calculated by

$$[\frac{u(E)}{E}]^2 = \left[\frac{2v}{(1-v^2)}\cdot u(v)\right]^2 + \left[1/(\frac{1}{E_r}-\frac{1-v_i^2}{E_i})\frac{1}{{E_r}^2}\cdot u(E_r)\right]^2 + \left[(1-v_i^2)/(\frac{1}{E_r}-\frac{1-v_i^2}{E_i})\frac{1}{{E_i}^2}\cdot u(E_i)\right]^2 \quad (3\text{–}30)$$

Here, for a standard diamond indenter probe, $\overline{E_i}$=1143GPa, $\overline{v_i}$=0.07. Some researchers also take $\overline{E_i}$=1100 GPa in the literatures. We suppose that the uncertainty of indenter's Young's modulus is about 0.038 percent at most, and the uncertainty is assumed to be uniformly distributed in the absence of better information, then the standard uncertainty of Young's modulus $u(E_i) = \frac{43}{\sqrt{3}} = 24.83$ GPa. According to Lee J's (Hall et al. 2008), we adopted $v = 0.18$, and the uncertainty is assumed to be uniformly distributed, the standard uncertainty of Poisson's ratio $u(v) = 0.069$. Then, the relative expanded standard uncertainty of reduced modulus corresponding to a level of confidence of 95% $U(E)$ is:

$$U(E) = 2 \times \frac{u(E)}{E} = 13.54\% \quad (3\text{–}31)$$

3.5. Conclusion

In this chapter, the SWCNT thin film (～200nm) is prepared by spin coating method. The hardness and the elastic modulus of SWCNTs thin film are estimated by nanoindentation test. The tested results show that the average elastic modulus and hardness of SWCNT thin film are E=192.83± 13.054 Gpa and H=12.57719 ± 0.759 Gpa in separate.

Since the obtained material properties are derived from the information of load and displacement of the indenter and some approximate assumptions. Uncertainty analysis is crucial in assuring the effectiveness of the estimated material properties in nanoindentation test. Uncertainty analysis indicates that the Young's modulus of SWCNTs film obtained by nanoindentation technique is not only affected by the usual encountered sources of uncertainty in measurement, but also affected by the properties of the material itself, which need further study. The results reveal that the relative expanded standard uncertainty of hardness corresponding to a level of confidence of 95% is 12.07%.The relative expanded standard uncertainty of reduced modulus corresponding to a level of confidence of 95% is 10.64%. Finally, the relative expanded standard uncertainty of Young's modulus corresponding to a level of confidence of 95% is 13.54%.

Chapter 4. Electrostrictive properties of SWCNTs based composite by FE method

This chapter investigated the electrostrictive properties of the P (VDF-TrFE) copolymer and single-walled carbon nanotube (SWCNT) based composites (SWCNT/P (VDF-TrFE)). Effects of the volume fraction of SWCNT, the electric filed strength and the chirality of SWCNT on the electrostrictive deformation of SWCNT/P (VDF-TrFE) composite were discussed.

4.1. Introduction

Since the discovery of the piezoelectricity by the Curie brothers in 1880-1881 (Manbachi & Cobbold 2011), piezoelectric materials have been extensively adopted as sensors, actuators, and transducers in a variety of smart structure applications. Polyvinylidne fluoride and trifluoroethylene P (VDF-TrFE) copolymer, which has the properties of ferroelectricity, piezoelectricity, and pyroelectric to convert the electrical excitation to mechanical motion directly, shows promising prospects in practical applications. It is demonstrated that the P(VDF-TrFE) copolymer under a proper irradiation treatment can produce an electrostrictive strain of 5% (Cheng et al. 2001). The significant electrostrictive property makes P (VDF-TrFE) copolymer to be a preferred piezoelectric material.

Piezoelectricity is triggered from small changes of the internal polarization of a dielectric material under applied mechanical stress. Li and Rao (Li & Rao 2002), (Li & Rao 2004) presented a microstructure analysis for the electrostriction of the P(VDF-TrFE) polymer based composite and elaborated the mechanism of the electrostriction enhancement in the composite. Their reports demonstrated that using the concept of composite, the effective electrostriction of the material can be indeed enhanced by incorporating a second phase with much larger dielectric constant than that of the ferroelectric polymer, even if the electrostriction of the second phase is zero. The phenomenon of enhanced dielectric constant for Polymer matrix composite materials also have been reported in both analytical and experimental works (Bai et al. 2000), (Dinulović & Rašuo 2009), (Crippa et al. 2013), (Li & Landis 2012), (affe B, Cook Jr W 1971).

Recent developments in nano-technology show that the carbon nanotube (CNT) rolled single (SWCNT) or multiple (MWCNT) sheets of graphite with diameter in nanometer size have unique electronical, mechanical, and chemical properties (Harris & Harris 2009), which

make them preferred candidates in the applications of nanocomposite and nano-devices. Guo demonstrated an exceptionally large axial electrostrictive deformation in SWCNTs using the density functional theory (Guo & Guo 2003), (Tang et al. 2006). Khalil El-Hami and Kazumi Matsushige used the AFM technique combined with lock-in amplifier to apply a voltage across an aligned bundle of SWCNTs; the electrostriction strain ～ 2.6% was detected under an applied electric field of 160 V/μm (El-Hami & Matsushige 2005). Deshmukh and Ounais investigated the coupled electromechanical response in a non-polar polymer composite (Deshmukh & Ounaies 2009). They discovered that the neat polyimide does not show any response under electric fields, while SWCNT-PI composites exhibit an electrostrictive behavior above the percolation threshold, and the strain is strongly dependent on SWCNTs' content. Those results indicate that carbon nanotube could be a prior reinforcement for electrostrictive composite.

This chapter intends to investigate the electrostrictive effect of the P (VDF-TrFE) copolymer and single-walled carbon nanotube (SWCNT) based composites. Here we propose a 3D finite element method to predict the electrostrictive deformation of SWCNT based polyvinylidne fluoride and trifluoroethylene P (VDF-TrFE) copolymer (SWCNT/P (VDF-TrFE)) composite under electrostatic field. Using finite element method, a bond electrical contact model is developed. Based on this model, the intrinsic electrostrictive properties of dielectric composite are intuitively demonstrated, which provides a numerical guideline for the design and optimization of the electrostriction for dielectric composites. The finite element model developed for SWCNT/P (VDF–TrFE) composite is presented in section 4.2.2. The interfacial properties of SWCNT and P (VDP-TrFE) are described in section 4.2.3. In section 4.2.4, factors that affect electrostriction of SWCNT/P (VDF–TrFE) composite are analyzed and commented.

4.2. Electrostriction study for single-walled carbon nanotubes based composite by FE method

4.2.1. Constitutive relationship of SWCNT/ P (VDF-TrFE) composite

The present numerical investigation is based on the experimental model of Khalil El Hami (Khalil El-Hami & Kazumi Matsushige 2005), (Khalil El-Hami & Kazumi Matsushige 2003). In El Hami's work, the SWCNT/ P (VDF-TrFE) composite was prepared with good physical properties. The morphology images of the P (VDF-TrFE) copolymer and the SWCNT/ P (VDF-TrFE) nanocomposite under AFM are shown in Fig. 4.1. As demonstrated in Fig. 4.1 (b), The SWCNTs were assembled in bundles that incorporated and embedded in

the crystalline lamellae. Fig. 4.2 illustrates schematically how the SWCNTs are incorporated in the P (VDF-TrFE) copolymer in bundles state in El Hami's work.

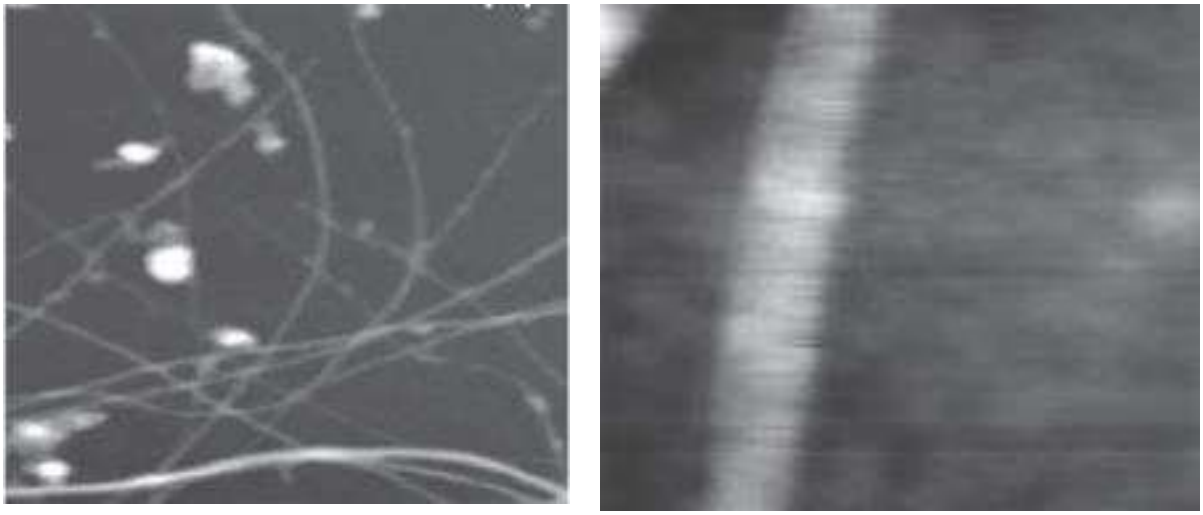

(a) (b)

Fig. 4.1 Atomic Force Microscopy images: (a) SWCNT bundles 1000nm x 1000nm, (b) P(VDF/TrFE)/SWCNT 500nm x 500nm (Khalil El-Hami & Kazumi Matsushige 2003)

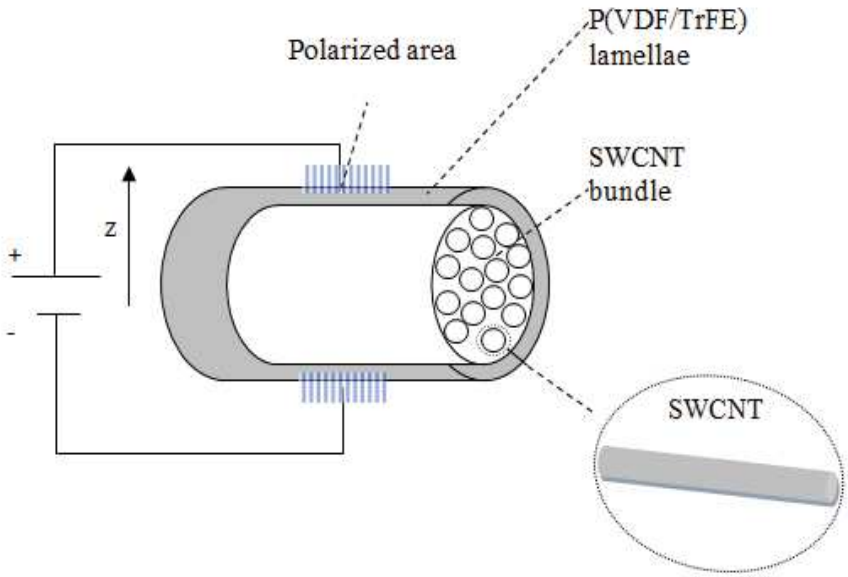

Fig. 4.2 Schematic illustration of SWCNT bundle covered by P (VDF-TrFE) lamellae with visible polarization domains.

In order to study the effect of different structures of SWCNTs on the electrostriction of the composite, we assumed that the SWCNT is individually aligned in the P (VDF-TrFE) copolymer matrix, as illustrated in Fig. 4.3. Generally, the stiffness and the distribution of the electric filed in composites are dependent on the contact media. In order to evaluate the whole deformation of the composites under electric field, the behavior of the contact region should be studied.

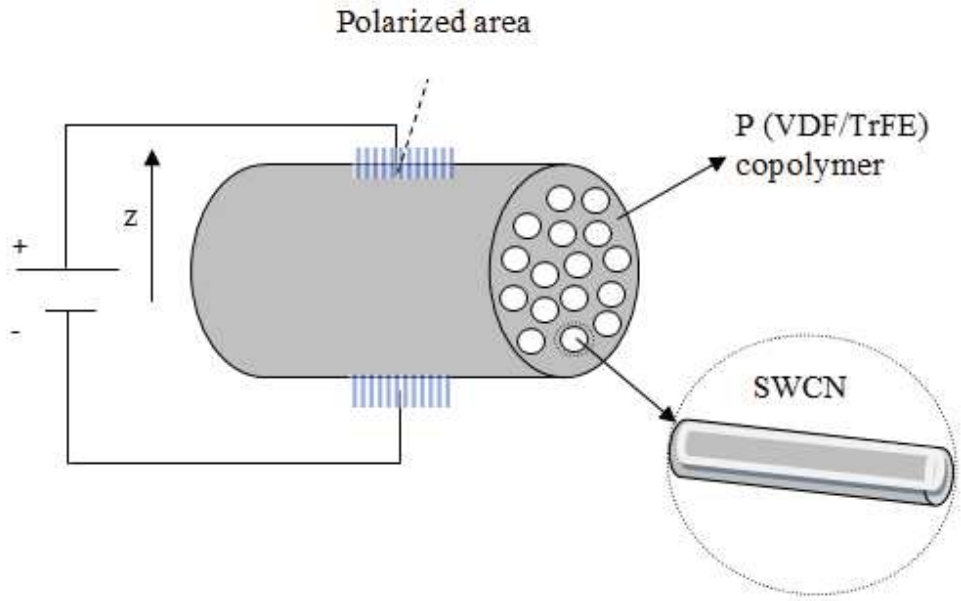

Fig. 4.3 Schematic illustration of individual SWCNT aligned in the P (VDF-TrFE) copolymer matrix.

4.2.2. Finite element model of SWCNT/ P (VDF–TrFE) composite

Micromechanics technique is generally used by many researchers to study the properties of composites at the macroscopic level. The aim of micromechanics method is to transform a body of heterogeneous material into a constitutively equivalent body of homogeneous material. Using micromechanics method, M. C. Ray and R. C. Batra determined the effective piezoelectric coefficient of armchair SWCNTs and piezoelectric fibers based composite (Ray & Batra 2009). However, under the external electric field excitation, the interfacial particle of SWCNT dielectric fiber and its surrounded piezoelectric polymer matrix are not free to deform because of the elastic clamping imposed by the second phase of material. Besides, the electrical and mechanical properties in composite media are different in matrix and reinforcement, which will causes inhomogeneous electrostrictive strain. The traditional technique of micromechanics modeling could not take those factors into consideration. Therefore, it is crucial to define a rational interfacial relationship between SWCNT and copolymer matrix to predict the overall electrostrictive behavior of the composite.

For the sake of simplicity, only one of the individual SWCNT and its surrounded copolymer matrix is taken from the composite as the analysis target. Fig. 4.4 presents the configuration of the model employed in this work. The P (VDF-TrFE) copolymer matrix is regarded as isotropic continuum medium that wrap outside the carbon nanotube. The inner radius of the cylindrical medium is equal to the radius of nanotube. The nanotube is viewed as a transversely isotropic column. As the piezoelectric effect of CNT is very small (Ray &

Batra 2009), a comparable small value of piezoelectricity constant for SWCNTS is set in the model. The piezoelectric constitutive equations for the P (VDF-TrFE) and SWCNT are

$$\begin{aligned} T^P &= C^P S^P - e^P E \\ D^P &= e^P S^P + \varepsilon^P E \\ T^N &= C^N S^N - e^N E \\ D^N &= e^N S^N + \varepsilon^N E \end{aligned} \tag{4–1}$$

where T^p, C^p, S^p, D^p, ε^p, e^P, and T^N, C^N, S^N, D^N, ε^N, e^N are the stress vector, elasticity matrix, strain vector, electric displacement, dielectric permittivity, and the piezoelectric stress matrix of the P(VDF-TrFE) copolymer and SWCNT respectively, and E is the electric field intensity vector, respectively.

According to Laplace's equation for the electric potential (Ø), the governing equation for Ø in each media is (Takuma & Techaumnat 2010):

$$\nabla^2 \emptyset = \frac{\partial^2 \emptyset}{\partial^2 x} + \frac{\partial^2 \emptyset}{\partial^2 y} + \frac{\partial^2 \emptyset}{\partial^2 z} = 0 \tag{4–2}$$

The boundary conditions at the interface of SWCNT and P (VDP-TrFE) are as follows.

1) The continuous tangential field strength is defined as

$$\emptyset_N = \emptyset_P \tag{4–3}$$

or

$$E_{tN} = E_{tP} \tag{4–4}$$

2) The continuity of normal electric flux density D_n is expressed as

$$D_{nN} = D_{nP} \tag{4–5}$$

which can also be written as

$$\varepsilon^N E_{nN} = \varepsilon^P E_{nP} \tag{4–6}$$

In Eqs (4–3) – (4–6), $Ø_N$, D_{nN} and $Ø_p$, D_{nP} are the electric potential and normal electric flux density at the interface of SWCNT and P (VDP-TrFE).

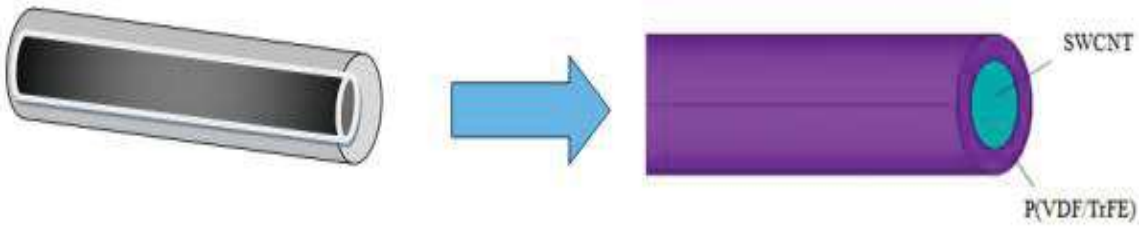

Fig. 4.4 . The configuration of the SWCNT/P (VDP-TrFE) composite

The finite element model developed in this study is based on the ANSYS code (ANSYS 2005). A three-dimensional twenty-node element and a three-dimensional ten-node element in ANSYS are adopted to model the P (VDF-TrFE) copolymer and SWCNT material, respectively. The electrostatic analysis is performed. The structure is symmetric about the Z-axis. The finite element model and the boundary conditions of the composite are shown in Fig. 4.5.

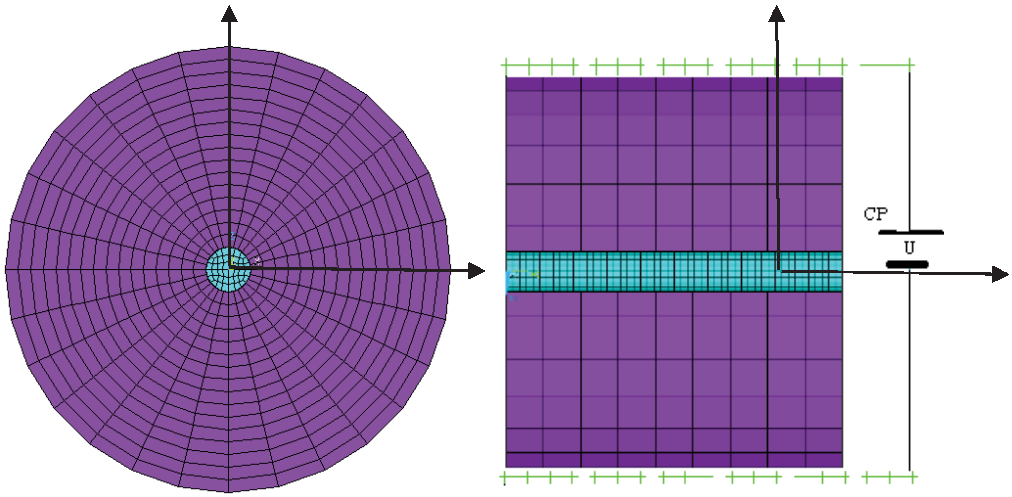

Fig. 4.5 . The finite element model of the SWCNT/P (VDP-TrFE) composite

4.2.3. SWCNT/P (VDP-TrFE) interfacial properties

At the interface of SWCNT and its surrounded P (VDF-TrFE) copolymer, the increased dielectric constant will enhance the electrostriction of the composite. However, the effect of dielectric constant is usually restricted by the high stiffness of the SWCNT, which may cause a lower strain compared to the theoretical value. Besides, as the dielectric composite media composes multiple dielectrics, the electric field near the contact region may significantly increase, which will induce a higher electric force. However, the resultant high electric force may result in a local debonding near the interface, which will further weaken the electric field of the material. These contradictions make the electrostrictive prediction complicate.

In order to correctly characterize the interaction between SWCNT and P(VDF-TrFE) copolymer, the electrical/mechanical behavior of SWCNT/P (VDF-TrFE) interface is

modelled through the contact/target (conta174/ targe170) element pairs in ANSYS (Kohnke 2001). The surface-to-surface contact model is applied in this work, as illustrated in Fig. 4.6. In this work, the bond strength of the interface was not taken into consideration. The interfacial bond strength between SWCNT and the surrounding matrix is assumed to be average along the length of composite, the bond stiffness is supposed to be strong enough that there is no decohesion under the electric excitation. At the interface, since the stiffness of SWCNT is much larger than that of the matrix, the SWCNT is selected as the target, which is overlaid by the contact element of P (VDF-TrFE) copolymer. The initial stiffness of the interface depends on the normal and tangential stiffness, which is determined by the relative stiffness of the two materials and the initial contact surface condition setting in ANSYS. The contact stiffness is updated automatically after each iteration based on the initial condition of interface. The interaction between the SWCNT and the P (VDFTrFE) copolymer matrix is determined by the properties assigned to the contact element/target element pairs.

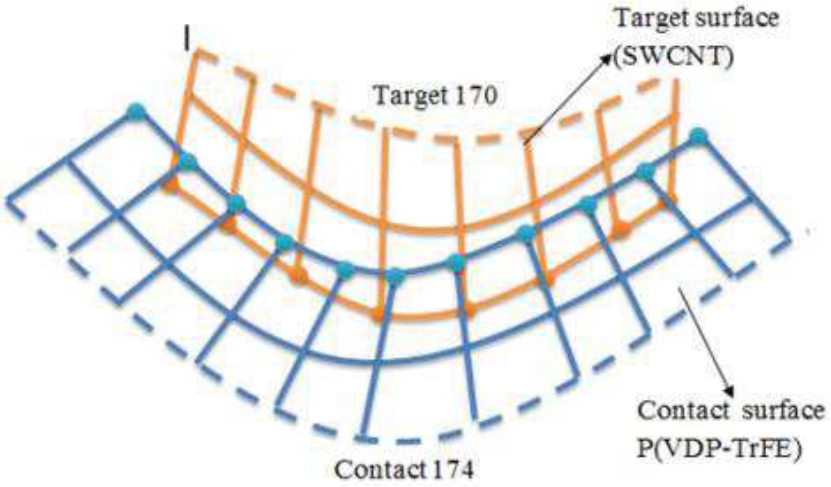

(a)

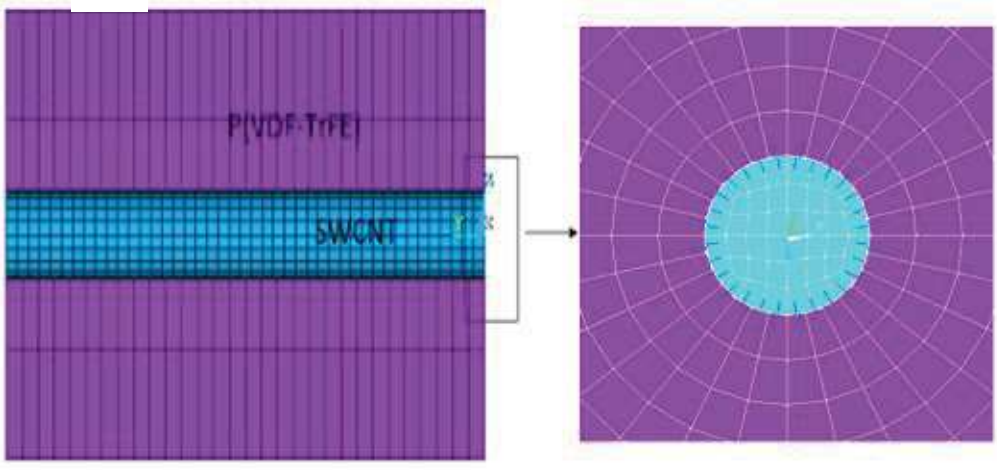

(b)

Fig. 4.6 (a) The configuration of the SWCNT/P (VDP-TrFE) interface (b) the finite element model of SWCNT/P (VDP-TrFE) interface.

4.2.4. Results and discussion

SWCNTs can be metallic or semiconductor, which depends on the diameter and helicity of the carbon atoms. Band structure calculations predicted that armchair SWCNTs with (n, n) indices exhibit metallic conduction with finite density of states at the Fermi level, while, Zigzag SWCNTs with indices (m,0) and chiral SWCNTs with indices (m,n) are predicted to be metallic when m-n = 3×integer and semi metallic when m-n ≠ 3×integer (Wilder et al. 1998). Paul L. McEuen and his colleagues found that metallic tubes have conductivity and current density meet or exceed the best metals; and semiconducting tubes have mobility and transconductance meet or exceed the best semiconductors (McEuen et al. 2002). The electrical resistivity of individual SWCNTs has been measured under ballistic conduction of around $10^{-6}\Omega$cm (Guo et al. 2004). In this work the conductivity of SWCNTs is adopted as the commercial carbon value of 285 Scm^{-1} (Li et al. 2007). The elastic moduli and the dielectric constants of SWCNTs estimated from ((Lu 1997), (Baowan & M. Hill 2007), (Kozinsky & Marzari 2008)). The elastic constant and electrical properties of P(VDF-TrFE) copolymer are obtained from (Rao & Li 2004) and (Lonjon et al. 2010). The capacitance of SWCNT/ P (VDF-TrFE) interface is obtained from K.J.LohetJ.Kim (Loh et al. 2008).

4.2.4.1. The effect of volume fraction of SWCNTs

In this part, the effect of volume fraction of SWCNTs for the electrostriction of composite is studied. In order to avert the impact of radius, we studied the variance of electrostriction to the corresponding volume fraction of armchair (5, 5), Zigzag (10, 0), and chiral (6, 4) SWCNTs based composite. The SWCNT/P (VDF-TrFE) composites have the approximate diameters at the same SWCNT fraction.

A constant DC electric field of 0.1MV/m is applied to the series of SWCNT/P (VDF-TrFE) composites. In order to reduce the edge effect and save the computational time, the length of the composite is selected according to the length to radius ratio (h/r≥10), the electrostrictive strain in thickness is calculated by measuring the deformation of diameter ΔD in Z direction.

$$s_{33} = \frac{\Delta D}{D} \tag{4–7}$$

where S_{33} is the thickness strain, and D is the diameter of composite in Z direction.

The thickness strains S_{33} for composite with the volume fraction of SWCNT from 0.5 vol% to 10 vol% are plotted in Fig. 4.7. The results show that the strains increase nonlinearly with the volume fraction of SWCNT. This result is in agreement with J. Kim et al's study (J. Kim et al. 2008). J. Kim et al indicated that SWCNT/P (VDP-TrFE) composites exhibit higher

dielectric constants and ferroelectricity than P (VDP-TrFE) copolymer, and the increments are dependent on the weight fraction of CNT.

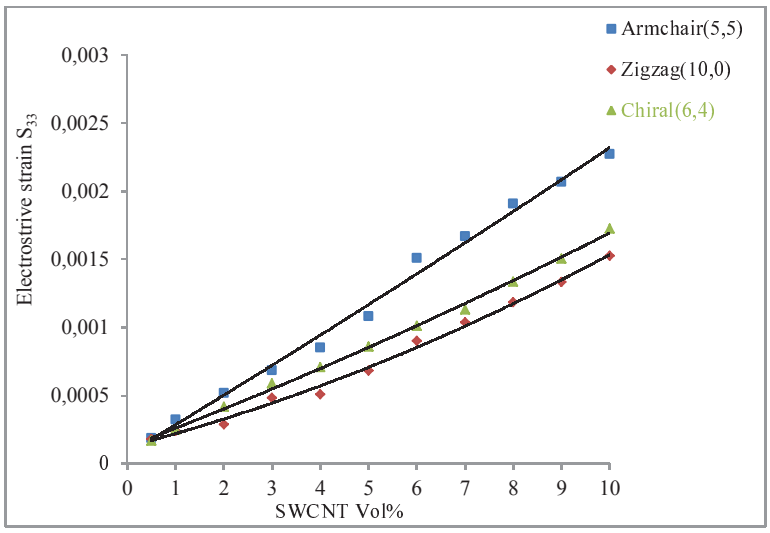

Fig. 4.7 The electrostrictive deformation of the SWCNT/P (VDP-TrFE) composite with SWCNT fraction. Solid lines are quadratic fit of the simulation results.

4.2.4.2. The effect of electric field

The variation of electrostrictions for armchair (5, 5), Zigzag (10, 0), and chiral (6, 4) SWCNTs based composite with respecte to the electric field are then studied. As we assumed that there is no decohesion between SWCNT and P (VDP-TrFE) copolymer under electric force, a series of relatively small electric fields to the composite was applied. Fig. 4.8 shows the electrostrictive strains of SWCNT/ P (VDF-TrFE) composite with 1vol% of the SWCNT under different electric field, which demonstrates that the strains increase approximate linearly with the electric field.

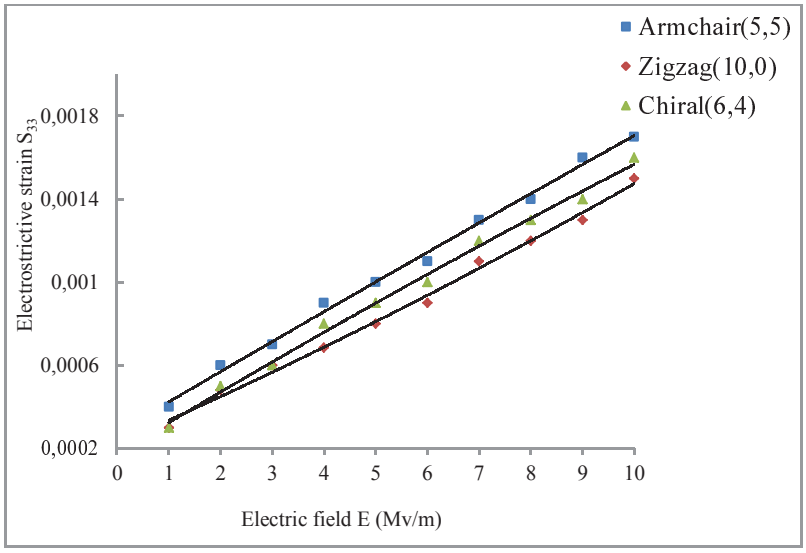

Fig. 4.8 The electrostrictive deformation of the SWCNT/P (VDP-TrFE) composite with electric field. Solid lines are linear fit of the simulation results.

From Fig. 4.7 and Fig. 4.8, we find that the volume fraction of SWCNT has more influence on the electrostriction of the SWCNT/P (VDP-TrFE) composite than the electric field. This could be due to: (a) the variation of dielectric constant of the composite caused by different structures of SWCNT, (b) the increased electric field intension in composite because of the second phase reinforcement.

Fig. 4.9 illustrates the electric field distribution in 0.5vol% armchair (5, 5) SWCNT/P (VDP-TrFE) composite. Fig. 4.9 (a) and (b) show that the electric fields strength at the interface is more than hundredfold of the edge.

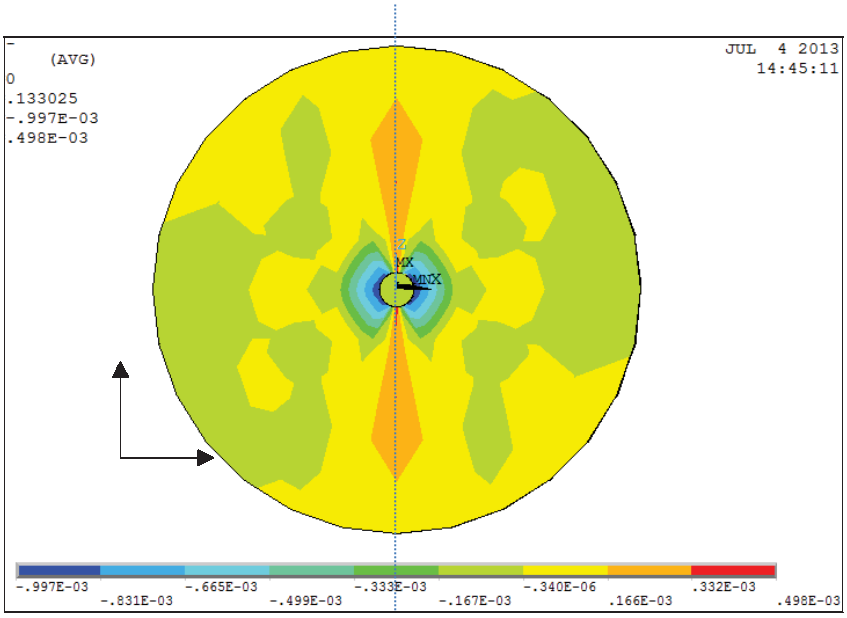

(a)

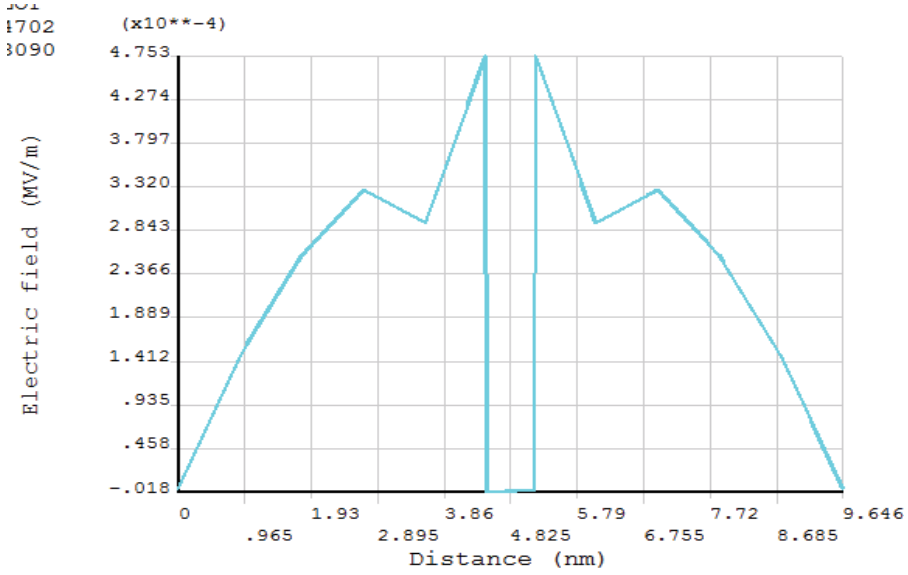

(b)

Fig. 4.9 The electric field distribution of 0.5vol% armchair (5, 5) SWCNT based composite. (a) The z-component of electric field distribution, (b) Electric field distribution along the symmetry axis.

The results obtained in Fig. 4.9 can be explained by the work of Takuma and T., Kouno's study (Takuma & Techaumnat 2010). The contact of a cross-section straight dielectric interface is represented in Fig. 4.10 (a). At some points on the boundary of two dielectrics, the electric field strength E may change as a function of k·lm, where l is the distance from the contact point, and K is a constant depending on the overall physical configuration and the ratio of the two dielectric constants ε1/ε2. The exponent m could be negative or positive according to whether the ratio of the two dielectric constants is greater or less than unity. This means the electric field distribution of composite is strongly dependent on the ratio of two dielectric constants. Fig. 4.10 (b) illustrates the electric field strength on the A and B sides along the interface with different ratio of two dielectric constants. Fig. 4.10 (b) also indicates that the more the dielectrics near the interface, the larger the field strength will be, the further the dielectrics away from the interface, the more the field strength tends to the initial field of E0 (E0=U/D). Our numerical results (Fig. 4.9 (a), (b)) agree well with this expectation.

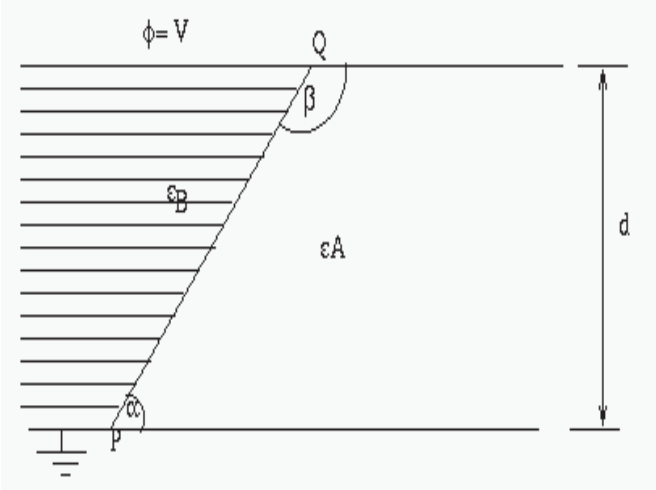

(a)

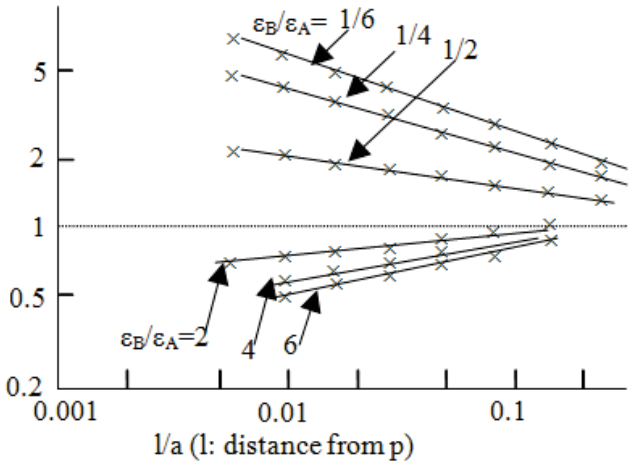

(b)

Fig. 4.10 (a) The interface of two dielectrics, (b) Electric field strength on the A and B sides along the interface (Takuma & Techaumnat 2010).

4.2.4.3. The effect of chirality

From Fig. 4.7 and Fig. 4.8 we can also conclude that with the approximate diameters but different chiralities of SWCNT based SWCNT/P(VDP-TrFE) composite, the armchair (5, 5) /P(VDP-TrFE) composite has the largest electrostrictive deformation, while, Zigzag (10,10) /P(VDP-TrFE) composite has the smallest electrostrictive deformation at the same external electric field and volume fraction of SWCNT. G.Y.Guoet K.C.Wang's study (Guo et al. 2004) showed that armchair (5, 5) SWCNT has a larger static dielectric constant than Zigzag (10, 0) SWCNT, and Zigzag (10, 0) SWCNT has a larger static dielectric constant than chiral (6, 4). While, the tendency of the electrostrictive deformations for those three kinds of SWCNT/P (VDP-TrFE) composites in Fig. 4.7 and Fig. 4.8 does not consistent with this rule.

The effect of SWCNT chirality to the electrostriction of composite in Fig. 4.7 and Fig. 4.8 may be mainly due to the difference of dielectric constants between SWCNT and P (VDP-TrFE). The static dielectric constant for SWCNT and the ratio of two dielectric constants are listed in Table 4.1. Results demonstrated in Fig. 4.7 and Fig. 4.8 are well consistent with the ratio of dielectric constants for SWCNT to P (VDP-TrFE). This result agree well with the theoretical analysis for dielectric composite properties in Takuma & Techaumnat's study (Takuma & Techaumnat 2010).

Table 4.1 Static dielectric constant for SWCNT from (Guo et al. 2004) and dielectric constant for P(VDP-TrFE) from (Baowan & M. Hill 2007)

	ε_{xx} (ε_{zz})	ε_{yy}	$\varepsilon_{zz,CNT}/\varepsilon_p$
Armchair (5, 5)	16	34.1	16/11
Zigzag (10, 0)	8.2	26.8	8.2/11
Chiral (6, 4).	7.3	22.1	7.3/11
P(VDP-TrFE)	11	11	–

4.3. Conclusions

This chapter proposes a 3D finite element method to study the electrostrictive property of SWCNT/ P (VDP-TrFE) composite. The electrostriction of armchair (5, 5), Zigzag (10, 0), and chiral (6, 4) SWCNT based composite are studied. The mechanism of the enhanced electrostriction in SWCNT/ P (VDP-TrFE) composite is intuitively demonstrated in the model proposed. Numerical results show that the electrostriction of SWCNT/P (VDP-TrFE) composite is greatly dependent on the volume fraction of SWCNT and the differences of dielectric constant between SWCNT and P (VDP-TrFE) copolymer. While, the dielectric constant of SWCNT is dependent on the chirality of SWCNT, which means the electrostriction of SWCNT/P (VDP-TrFE) composite is also greatly dependent on the chirality of the SWCNT. The results of this study provide a numerical guideline for the design and optimization for SWCNTs based nano-composites and other electrostrictive composite.

Chapter 5. A bilinear model for SWCNTs films characterization using Reliability-based optimization (RBO) method

This chapter focuses on obtaining the elasto-plastic properties of the SWCNTs thin film from a single indentation load-displacement curve. FE technique combined with the nanoindentation results is used to estimate the mechanical properties of the SWCNTs thin film. As mentioned in chapter 3, various uncertainties are associated with nanoindentation process. Reliability-based optimization (RBO) method is an efficient method in dealing with optimization problems under uncertain. In this work, the RBO methodology is applied to ensure the reliability of estimation. The distribution of load-displacement curves in unloading process is considered in reliability analysis.

5.1. Introduction

Methods of extracting material properties systematically from a single indentation load-displacement curve have been investigated in a number of studies (Cheng & Cheng 1998), (Cheng et al. 1998), (Chollacoop et al. 2003), (Kucharski & Mróz 2007), (Zhang et al. 2011), (Khan et al. 2010) . For example, Hill et al. developed a self-similar solution for the plastic indentation of a power law plastic material under spherical indentation (Hill et al. 1989). Giannakopoulos and his colleagues did significant studies on the instrumented sharp indentation problems, and proposed a comprehensive analytical framework to extract material elasto-plastic properties from a complete load-unload cycle data (Giannakopoulost & Vestergaard 1994), (Giannakopoulos, A.E. Larsson 1997), (A. E. Giannakopoulos and S. Suresh 1999). In order to comprehensively elucidate the deformation mechanisms in instrumented indentation, Jennett et Meneve investigated the sensitivity of modulus measured by Depth Sensing Indentation (DSI) as a function of the indentation parameters: maximum load; loading rate; hold time at maximum load; single vs. repeated loading; instrument compliance, indenter area function and in-plane anisotropy (Jennett & Meneve 1998) .

Recently, methodologies based on the idea of dimensional analysis for predicting an indentation response from a given set of elasto-plastic properties, or extracting elasto-plastic properties from depth-sensing indentation response by developing algorithms derived from computational simulations are recommended. For example, considering problems of uniqueness and accuracy in depth-sensing indentation, N.Chollacoop and his coworkers

established a forward and reverse analysis algorithms to extent the elasto-plastic properties of materials. Using dimensional analysis, they constructed a set of dimensionless functions to relate indentation response to elasto-plastic properties for different indenter tip geometries. (Chollacoop et al. 2003), (Dao et al. 2001). However, the process of dimensionless function constructing in dimensional analysis is very complicated. Besides, the load-displacement curves in loading process is greatly dependent on the properties of substrate, indenter, and the contact conditions, that makes the loading process based dimensional model unreliable.

The objective of this chapter is to evaluating the elasto-plastic properties of the SWCNTs thin film systematically from a single indentational load-displacement curve. FE technique combined with the nanoindentation results is used to estimate the mechanical properties of the SWCNTs thin film. The RBO methodology is applied to ensure the reliability of estimation. At the beginning of this chapter, an overview of main approaches for dealing optimization problems under uncertainty is presented. The basic reliability problem and mainly methods for reliability-based optimization are then stated. Finally, applications of RBO method in the estimation of the elasto-plastic properties of the SWCNTs thin film are demonstrated.

5.2. Optimization in engineering

Optimization is a powerful methodology for dealing with problems that demand either minimizing the expended cost or maximizing the desired benefit under given circumstances. Optimization has a broad range of applications in diverse set of fields from economics to engineering. For example, an engineer always wishes to design the products with the best performance while under the lowest-cost, and this is usually a contradictory objective which needs some kind of compromise.

Design optimization is a basic problem for engineers to design and manufacture high quality products at a minimum costs. It is still a hot topic in industry applications with the rapid development in new materials, technologies, and people's requirements. Mathematically speaking, optimization is the minimization or maximization of an objective function subjected to a set of constraints. Formally, the optimization problem can be written as:

$$\min_{x \in R^n} f(x)$$

$$subject\ to \begin{cases} h_i(x) = 0, i \in \varepsilon \\ g_j(x) \leq 0, j \in I \\ x^L \leq x \leq x^U \end{cases} \tag{5–1}$$

Where x is the vector of design variables; f is the objective function which depends on the certain characteristics of the system; h_i and g_j are constraint functions and expressed as

equalities and inequalities functions that the unknown vector x must satisfy, i and j are sets of indices for equality and inequality constraints, and x^L, x^U are separately the lower and upper bounds of x. The general optimization process is illustrated in Fig. 5.1. The first step in optimization is the appropriate identification of the objective, variables, and constraints for the given problems (as shown the dashed box in Fig. 5.1); once the model has been formulated, an appropriate optimization algorithm can be chosen to find its solutions. The choice of algorithm is very important in optimization process, which may determine the computational efficiency and even decide whether the solution can be found at all.

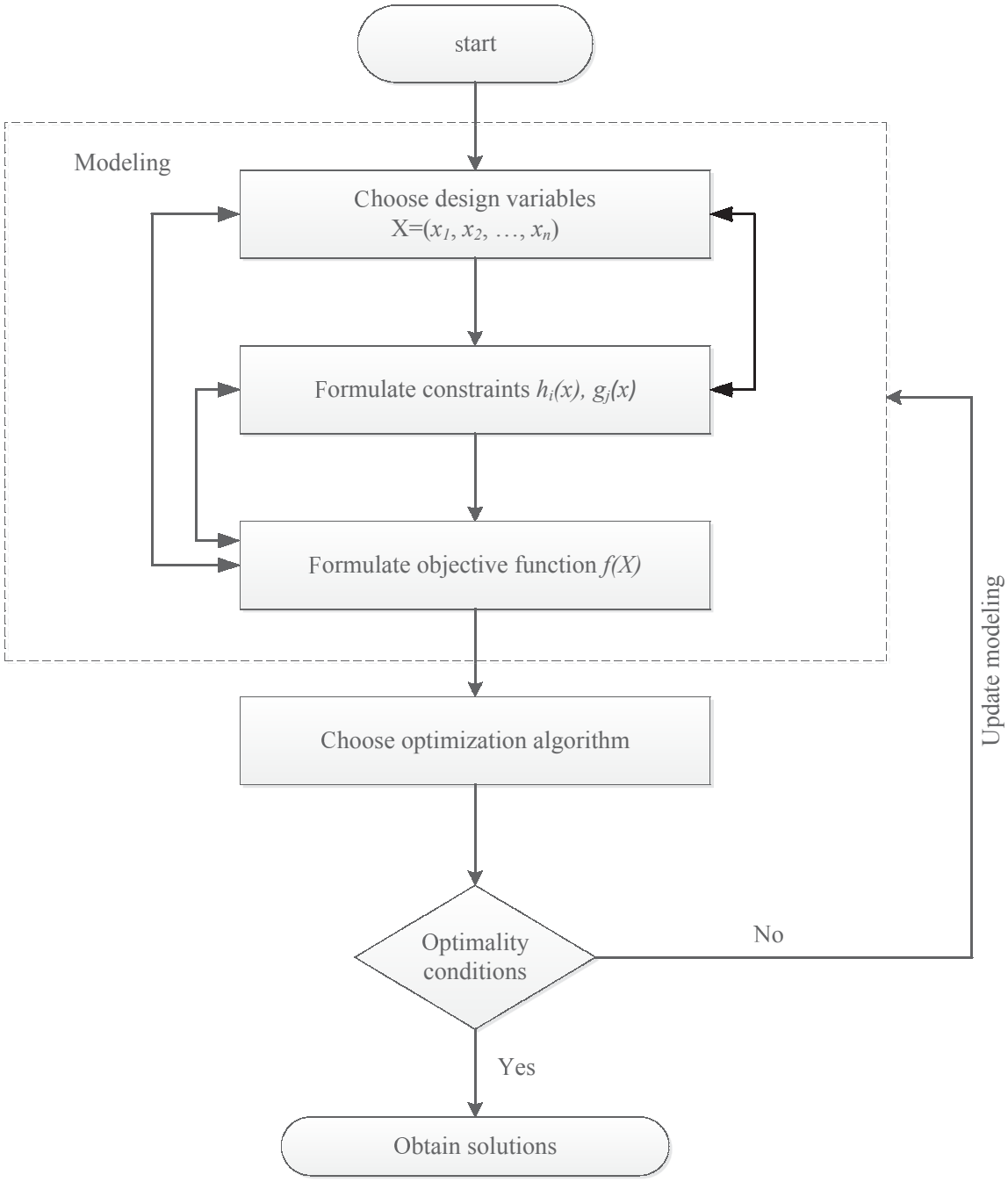

Fig. 5.1 Flowchart of the optimization design procedure

5.2.1. General problems in optimization

5.2.1.1. Constrained and unconstrained optimization

Optimization problem in equation (5−1) can be classified as constrained and unconstrained problems according to whether there are constraints on the variables or not. For unconstrained problems, the objective of optimization is just minimizing the cost function *f(x)*. If *f(x)* is continuous, conditions of a point x^* to be the minimum point are derived by analyzing the derivatives of *f(x)* (Nocedal et al. 1999). Constrained problems are usually more difficult than unconstrained problems. One strategy for solving constrained problems is to reformulate constrained problems as unconstrained optimization problems by replacing the constraints with penalization terms in the objective function. The optimized conditions for constrained problems can be expressed by several ways, and the most commonly used in literatures are the Karush-Kuhn-Tucker (KKT) conditions.

The classical Karush-Kuhn-Tucker conditions method says if x^* is a local minimum of nonlinear problem (5−1), the objective function *f* and the constraint functions g_j, h_i: $R^n \rightarrow R$ are continuously differentiable at x^*. And also the gradients of the constraints at x^* are linearly independent. Then there exist unique constants μ_j $(j = 1, \cdots, I)$ and λ_i $(i = 1, \cdots, \varepsilon)$ such that

$$\nabla f(x^*) + \sum_{i=1}^{\varepsilon} \lambda_i \nabla h_i(x^*) + \sum_{j=1}^{I} \mu_j \nabla g_j(x^*) = 0 \tag{5–2}$$

$$h_i(x^*) = 0, 1 \leq i \leq \varepsilon \tag{5–3}$$

$$g_j(x^*) \leq 0, 1 \leq j \leq I \tag{5–4}$$

$$\mu_j \geq 0, 1 \leq j \leq I \tag{5–5}$$

$$\mu_j g_j(x^*) = 0, 1 \leq j \leq I \tag{5–6}$$

The KKT conditions are necessary for nonlinear optimization program. A solution would exist if there is a unique point that satisfies the Karush-Kuhn-Tucker conditions. In particular, if there are no inequality constraints, the KKT conditions turn into the Lagrange conditions.

5.2.1.2. Local and global optimization

If the cost function *f(x)* has a smallest value at point x^* within its immediate neighborhood S, then x^* is called the local minimum point of *f(x)*.

$$f(x^*) \leq f(x), |x - x^*| < \delta, x \in S \tag{5–7}$$

If equation (5–7) holds for all *x* in the feasible space S, then x^* is called the global minimum point and $f(x^*)$ is the global minimum in S.

Usually the optimum solution of a problem is not a global minimum, which may cause the designed object unacceptable. While, finding the global optimization is usually difficult, which is often computationally extensive, especially for large-scale problems. One special case is the convex programming, in which all local solutions are also global solutions (Arora 2007). For the other un-convex problems, some methods have been specifically developed. One example for engineering design is the *worst-case analysis*, which in principle is finding the *worst-case* value of parameters, if the *worst-case* value is acceptable, we can certify the system as safe (or reliable).

5.2.1.3. Convex problems

The term 'convex programming' is used to describe a special case of the general constrained optimization problem which:

- The objective function is convex,
- The equality constraint functions $h_i(\cdot)$, $i \in \varepsilon$, are linear, and the inequality constraint functions $g_j(\cdot)$, $j \in I$, are concave. Which means the program satisfies the properties:

$$f_i(\alpha x + \beta y) \leq \alpha f_i(x) + \beta f_i(y) \tag{5–8}$$

For all $x, y \in R^n$ and all $\alpha, \beta \in R$ with $\alpha+\beta= 1$, $\alpha \geq 0$, $\beta \geq 0$.

Convex optimization is fundamental in optimization. In practice, convex optimization plays an important role not only in problems which possess the properties of inequality (5–8), but also in problems that are not convex formulated (Boyd & Vandenberghe 2009). The representative convex optimizations in practical applications are the least-squares and the linear optimization problems.

5.2.1.4. Deterministic and stochastic optimization

Deterministic and stochastic optimizations are two classical branches of algorithms for global optimization. Deterministic optimization algorithms provide general way in obtaining a global or an approximately global optimized solution of the problem. It is based on the rigorous mathematical formulation not considering the uncertain factors and its effects on the reliability of the solutions. Although the convergence of deterministic optimization algorithms is usually much faster compared with the stochastic optimization, deriving a globally optimal solution for complexity problem by deterministic optimization algorithms may not be easy. For example, solving nonconvex or large-scale optimization problems, deterministic algorithms may be time consuming or even fail due to the high complexity of the problem. In contrast, stochastic optimization algorithms make use of the quantifications of uncertainty factors to obtain the optimized performance of the model more effective. One of the specific applications of stochastic optimization algorithms is when some of the variables or the performance of the design model are uncertain. In this section, the main methods of optimization under uncertainty are briefly demonstrated.

5.2.2. Optimization under uncertainty

In the context of optimization, uncertainties arise both from the nature and from the technologies of the engineering system to be optimized. For example, in actual engineering design optimization process, uncertainties may arise due to the variability of material properties, external conditions, modeling and numerical errors, etc. Optimization under uncertainty has experienced rapid development and has been considered as one of the most important problems in modern optimization. In more and more cases, the effects of uncertainties in a problem need to be described properly to support a decision-making. The elements of uncertainty in a problem can be modeled as random variables when their probability distributions are known or by uncertainty ranges when little probability information is known. To date, some methods have been developed to perform optimization under uncertainties, which proved effective and have significantly decreased the likehood of products failure.

5.2.2.1. Stochastic programing

In problems concerning uncertainties, stochastic programming has a long history. It takes the advantages of the statistic information about the distribution of expected values appeared in the objective and constraint functions. This technology was firstly applied on solving some linear problems with uncertainty conditions, and then extended to integer and non-linear programming. One typical example of stochastic programming is the *stochastic programs*

with recourse (Salvendy 2001), in which the decision-maker assigns a cost (due to all the violation in the constraints) to recourse in order to ensure the feasibility of the problem. The fundamental in stochastic programs with recourse is the two-stage problems with finite numbers of realizations which provides a foundation for multistage methods (Fábián & Szőke 2007). Another example of stochastic programming is the *Probabilistic programming*, which focuses on the reliability of the system. This reliability is expressed as a minimum requirement on the probability of satisfying constraints. In probabilistic programming, some of the constraints or the objectives are expressed in terms of probabilistic statements about first-stage decisions. The description of second-stage or recourse actions is thus avoided. This is particularly useful when the cost and benefits of second-stage decisions are difficult to assess (Birge & Louveaux 2011).

5.2.2.2. Robust optimization

The idea of "robust design" was first proposed by Dr. Genichi Taguchi in 1950's, who later developed and defined his own concept in the 1980's as: "a product whose performance is minimally sensitive to factors causing variability (at the lowest possible cost)". Taguchi method is an off-line quality control method, which guaranty the product quality by controlling the entire process of a product at both developing and manufacturing stages under uncertainty. Based on Taguchi methods, the concept of "robust design" has been greatly developed and applied in variety of fields, such as engineering (Phadke 1995), biotechnology (Rao et al. 2008), marketing and advertising (Bell n.d.).

In the context of optimization, the performances of the system sometimes exhibit great dependency on the perturbation of parameters in design, which may cause the solutions of problem infeasible (Ben-Tal & Nemirovski 2000). In fact, the problem of un-robust in real optimization is very common (Mulvey et al. 1995), (Bertsimas et al. 2011), which attract plenty of researchers and engineers in different domains. Robust optimization methods are based on traditional optimization theory, especially focus on the robustness of system settings with the goal of computational tractable and application flexible simultaneously.

5.2.2.3. Reliability-based optimization

In reliability-based optimization (RBO), uncertain factors of a system are considered in the requirement of its performance during a period of life time. These effects are combined in the system performance model in terms of probability form with the target of a reliable solution. RBO methods incorporate uncertainty constraints in the members of system or the system itself with a concurrent subspace optimization that allows the optimized solutions satisfy all disciplines simultaneously. Although RBO has been demonstrated as one of the most powerful methodology for solving problems in engineering (Choi et al. 2007), its

application in reality could still be challenging. To perform a RBO, one has to couple the reliability evaluation and optimization, which makes the computational cost expensive. Therefore, one of the critical issues in RBO is finding technologies with trade-off between computational cost and solution reliability.

5.3. Reliability based optimization

5.3.1. Fundamental definition of reliability analysis

In general, a repeated measurement of the same physical phenomena may generate multiple outcomes. Among these multiple outcomes, some are more frequent than others. This means that the outcome is obtained with some intrinsic uncertainty. So in view of uncertainty, satisfactory performance cannot be absolutely assured. Instead, assurance can only be made in terms of the probability of success in satisfying some performance criterions. The assurance of successful performance can be described by the reliability or by the probability of failure.

A vector of basic random variables $X=(x_1,\ldots, x_n)$ represents the uncertain quantities of an engineering system. The output of the system is represented by the performance function $Z=g(X)$, in which the functional relationships among all random variables are explicitly or implicitly characterized. The limit state can be defined as $g(X)=0$. This is the boundary between the safe and unsafe regions. For example, in a structure reliability analysis, the basic random variables are the relevant load S and resistance R that is X=(*R, S*). The failure surface is $g(R, S)=0$. When $g(R, S)>0$, the structure is considered to be safe; when $g(R, S)<0$, the structure is considered cannot fulfill the required performances. So, failure occurs when $g(X)<0$, as shown in Fig. 5.2. The probability of failure P_f is:

$$P_f = P[g(X) \leq 0] = \int_{g(X)\leq 0} f_X(x_1, \cdots, x_n) dx_1 \cdots dx_n \tag{5–9}$$

where $f_X(x_1, \cdots, x_n)$ is the joint probability density function of basic variables $x_1, \cdots, x_n$.

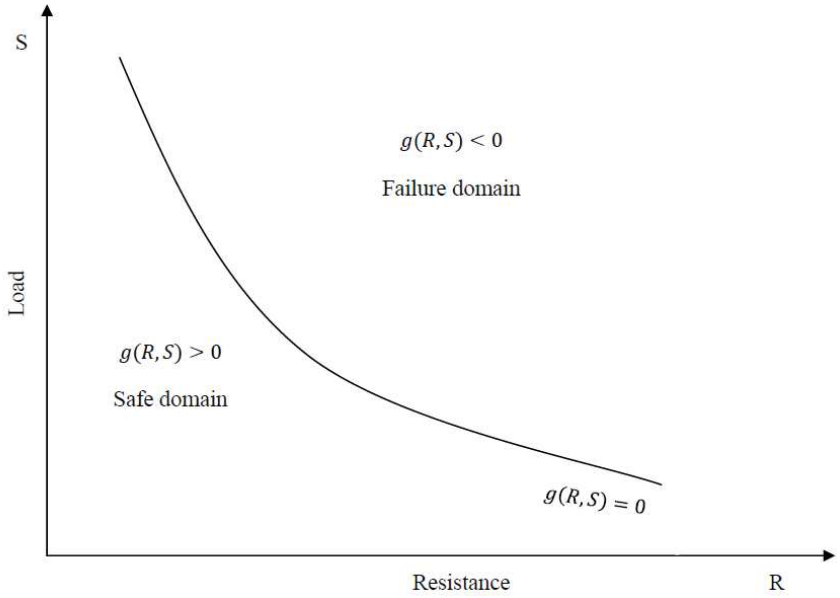

Fig. 5.2 General principal of reliability analysis

Assume μ_g and σ_g are the mean and standard deviation of limit state function *g(·)*, the reliability index β is defined as

$$\beta = \frac{\mu_g}{\sigma_g} \tag{5–10}$$

The safety index indicates the distance from the mean value μ_g to the limit state surface *g(·)* =0, that is $\mu_g = \beta\sigma_g$. In special case, if the limit state function *g(·)* follows the standard normal distribution, the probability of failure P_f is

$$\begin{aligned} P_f = P[g(\cdot) \le 0] &= \int_{-\infty}^{0} f_g(g)dg \\ &= \int_{-\infty}^{0} \frac{1}{\sqrt{2\pi}\sigma_g} \exp\left(-\frac{1}{2}\left(\frac{0-\mu_g}{\sigma_g}\right)^2\right) dg \\ &= \int_{-\infty}^{0} \frac{1}{\sqrt{2\pi}\sigma_g} \exp\left(-\frac{1}{2}(\beta)^2\right) dg \\ &= 1 - \Phi(\beta) \\ &= \Phi(-\beta) \end{aligned} \tag{5–11}$$

where $\Phi(\cdot)$ is the standard normal cumulative distribution function.

5.3.2. Methods of reliability analysis

In engineering reliability analysis, two different methods: the reliability index approach (RIA) and the performance measure approach (PMA) are usually used to estimate the probabilistic constraint of system.

5.3.2.1. Most probable point (MPP)

In general, the design variables may not normally distribute, it is necessary to transform the design space (X-space) to the standard normal space (U-space). Hasofer and Lind originally proposed a linear mapping of the normally distributed variables X *($X=x_1, \ldots, x_n$)* into a set of independent and standardized normal vector U *($U=u_1,\ldots,u_n$)* through the standardization process

$$U = \frac{X - \mu_X}{\sigma_X} \tag{5–12}$$

where μ_X and σ_X are separately the mean value and standard deviation of random variables X. The limit state surface *g(X)* =0 in original design space is then transformed into the standard normalized U-space, as shown in Fig. 5.3. The reliability index β is the shortest distance from the origin of the U-space to the failure surface *g(U)* =0, and the corresponding point P(U*) on *g(U)* =0 is defined as *Most probable point (MPP)*.

Hasofer-Lind method assumes that the random variables are normally distributed. Rackwitz and Fiessler extended the transformation of (5–12) for dependent non-Gaussian variables cases. The idea of the extended approximate transformation is to transform the non-Gaussian variables into equivalent normal variables with the equivalent normal distribution. In other words, transformation needs to match the cumulative distribution function and probability density function of the original non-Gaussian variables with the equivalent normal variables distribution, that is

$$\begin{aligned} F_{x_i}(x_i) &= F_{u_i}(u_i) \\ &= \Phi[T(x_i)] \end{aligned} \tag{5–13}$$

and

$$\begin{aligned} f_{x_i}(x_i) &= f_{u_i}(u_i) \\ &= \emptyset[T(x_i)] \end{aligned} \tag{5–14}$$

where *F(·)* and *f(·)* are separately the cumulative distribution function and probability density function of variables in original X-space, T is the transformation, $\emptyset(\cdot)$is the standard normal density distribution function.

When the variables are not mutually independent, the transformation becomes more complicated and which is not discussed here. Information for this situation are referred to (Rosenblatt 1952), (Brockwell 2007).

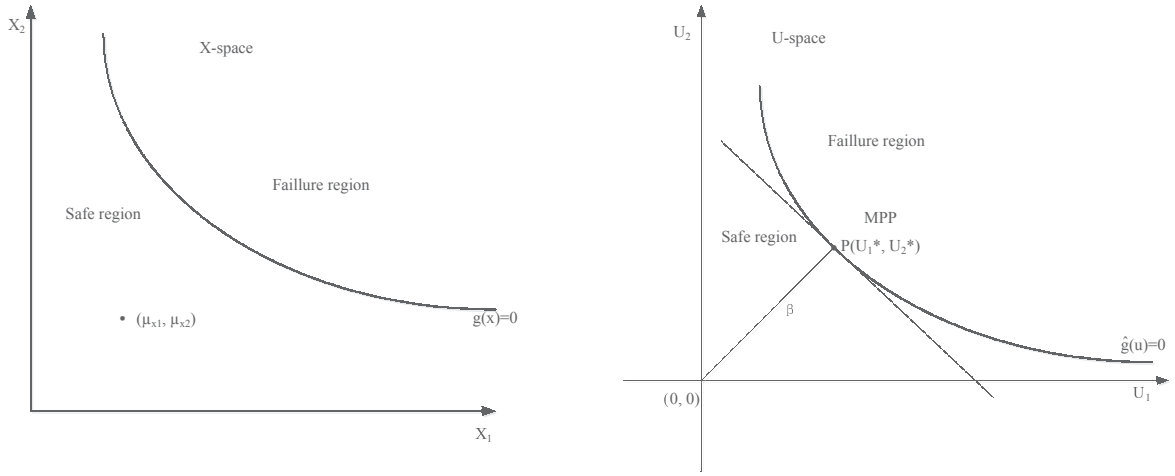

(X-space) (U-space)

Fig. 5.3 Mapping of limit state surface from X-space to U-space

5.3.2.2. Reliability index approach (RIA)

The reliability index approach (RIA) refers to formulation of the probabilistic constraints in terms of the reliability index. It uses the first-order reliability approximation to evaluate the probabilistic constrains. The formulation of RIA can be expressed as

$$\begin{aligned} &\min_{X} \ f(X) \\ &s.t. \begin{cases} \beta_i(X,Y) \geq \beta_i^T, & i = 1, \dots, m \\ h_j(X) \leq 0, & j = 1, \dots, n \end{cases} \end{aligned} \tag{5–15}$$

Where X and Y are the vectors of design and random variables, β_i and β_i^T are separately the design and the target reliability index for the ith probabilistic constraint. By transforming the random variables X into the corresponding normal standard variables U, the reliability analysis problem transforms into a deterministic optimization process:

$$\begin{aligned} &\min_{U}: \|U\| \\ &s.t.\ g_i(U) \le 0 \end{aligned} \tag{5–16}$$

The optimized point U* is the most probable failure point (MPP), and the reliability index is given by β=||U*||. The RIA is actually a mathematical optimization problem with the aim of finding the *MPP* on the failure surface *g(U)* =0 (Fig. 5.4).

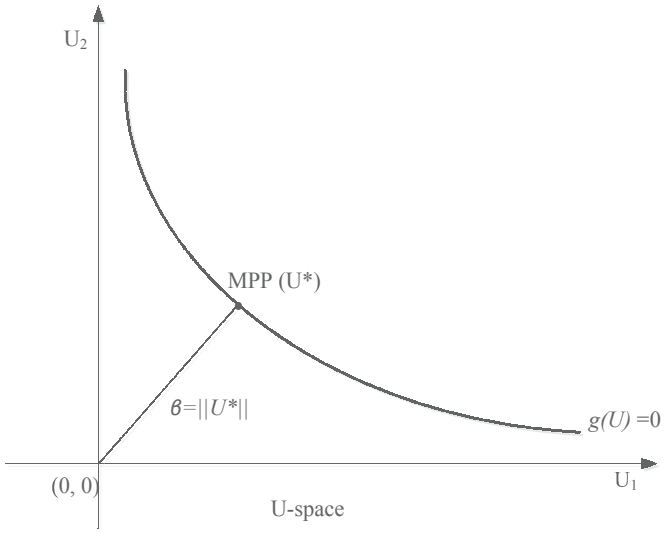

Fig. 5.4 Formulation of RIA

5.3.2.3. Performance measure approach (PMA)

The performance measure approach (PMA) aims to find a target value (MPP) in U-space corresponding to the target reliability level β^T. It is the inverse formulation of reliability analysis in RIA.

$$\begin{aligned} &\min_{X}\ f(X) \\ &s.t.\begin{cases} g_i(X,Y) \ge 0, & i = 1,\dots,m \\ h_j(X) \le 0, & j = 1,\dots,n \end{cases} \end{aligned} \tag{5–17}$$

where g(X,Y) is the probabilistic performance measure. It is obtained from a nonlinear optimization problem in U-space as:

$$\begin{aligned} &\min_{U}: g(U) \\ &s.t.\ \|U_i\| = \beta_i^T \end{aligned} \tag{5–18}$$

with $U=T(X,Y)$ and $g(U) = g(T(X,Y))$. In PMA, the search direction in iterative optimization process is determined by exploring the spherical equality constraint in (5–18), as shown in Fig. 5.5.

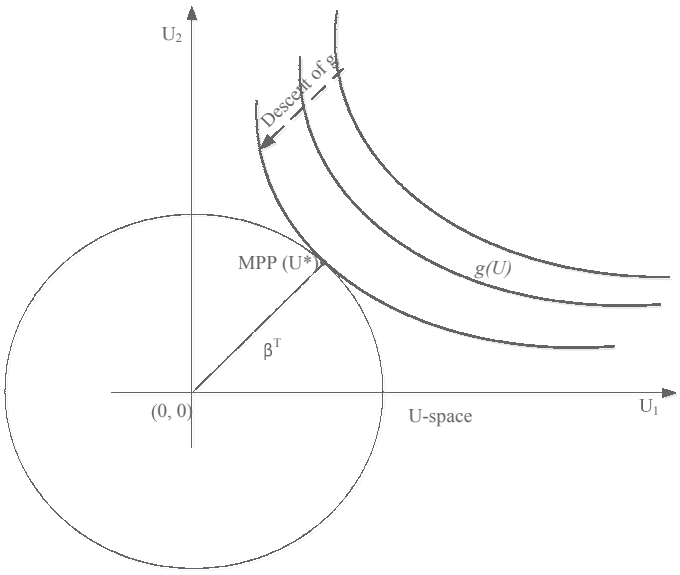

Fig. 5.5 Formulation of PMA

5.3.3. RBO formulations

A typical formulation of RBO consists in minimizing an objective function under constraints including probabilistic terms. Suppose X is the vector of design variables, Y is the vector of uncertain parameters. The RBO problem can be typically expressed as:

$$\min_{x} f(X) \tag{5–19}$$

$$s.t. \begin{cases} P_Y[g_i(X,Y) \le 0] \le P_i^T, i = 1, \cdots, m \\ h_j(X) \le 0, \qquad\qquad j = 1, \cdots, n \end{cases} \tag{5–20}$$

where f is the objective function, g_i is the ith performance function, P_Y is the probability operator, h_j are deterministic constraints, P_i^T is the ith acceptable probability. The solution of RBO problem involves two levels of assessment, the optimization and the reliability in expectation. To access these two requirements, three kinds of formulations are proposed: double loop approach, single loop approach, and serial loop approach (Valdebenito & Schuëller 2010).

5.3.3.1. Double loop approach

Double loop approach is a most direct RBO approach. It includes two nested optimization processes: the inner loop for reliability assessment on the probabilistic constraints and the outer loop for regular optimization. The reliability analysis (inner loop) is nested in the optimization process (outer loop) (Fig. 5.6). Due to these two nested optimization, double loop approach is computational expensive. Two important cases that double loop approach is usually applied are MPP-based reliability analysis and dimension reduced method (DRM).

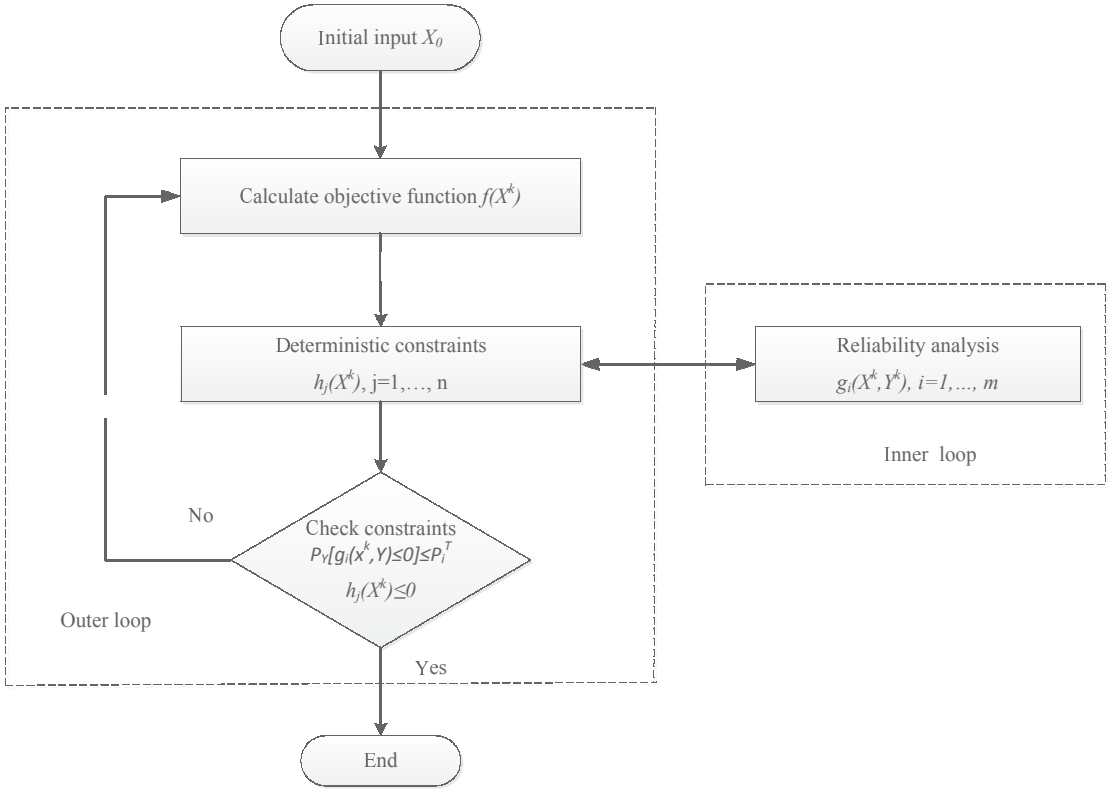

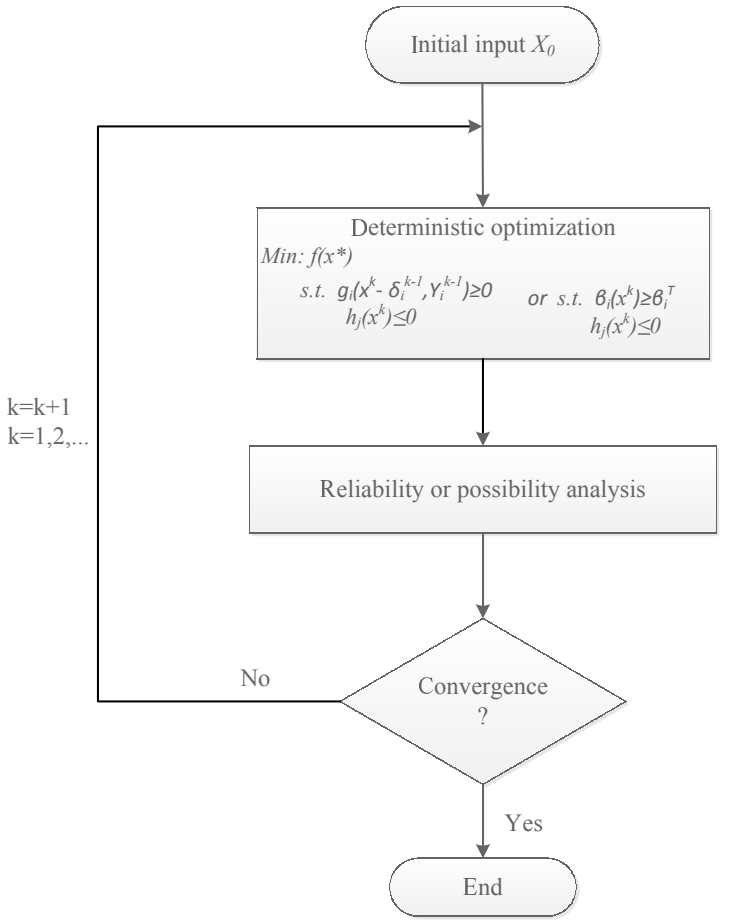

Fig. 5.7 Schematic represent of decoupling loop approach

5.3.3.3. Single loop approach

Single loop approach was initially proposed by Chen et al (CHEN et al. 1997). In their study, the design variables correspond to the mean value of all uncertainty parameters, the probabilistic constraint is transformed to an approximate deterministic constraint through the following transformations:

$$\min_X \ f\left(X^{(k)}\right) \tag{5–21}$$

$$s.t. \begin{cases} g_i\left(X^{(k)}, Y^{(k)}\right) \geq 0, & i = 1, \dots, m \\ h_j\left(X^{(k)}\right) \leq 0, & j = 1, \dots, n \end{cases} \tag{5–22}$$

Where:

$$Y_i^{(k)} = \mu_{Y_i}^{(k)} - \beta_i^T \sigma_{Y_i} \alpha_i^{(k)} \tag{5–23}$$

$$\alpha_i^{(k)} = \frac{\nabla_{Y_i} g_i\left(X^{(k)}, Y_i^{(k-1)}\right)}{\left\|\nabla_{Y_i} g_i\left(X^{(k)}, Y_i^{(k-1)}\right)\right\|} \tag{5–24}$$

where $X^{(k)}$ and $Y^{(k)}$ are the vectors of design variables and uncertain parameters in *k*th iteration, $\mu_{Y_i}^{(k)}$ is the mean value of *i*th uncertainty variable in kth iteration, σ_Y is the vector of standard deviation, β_i^T and $\alpha_i^{(k)}$ are separately the required reliability index and normalized sensitivity factor in the *i*th performance function.

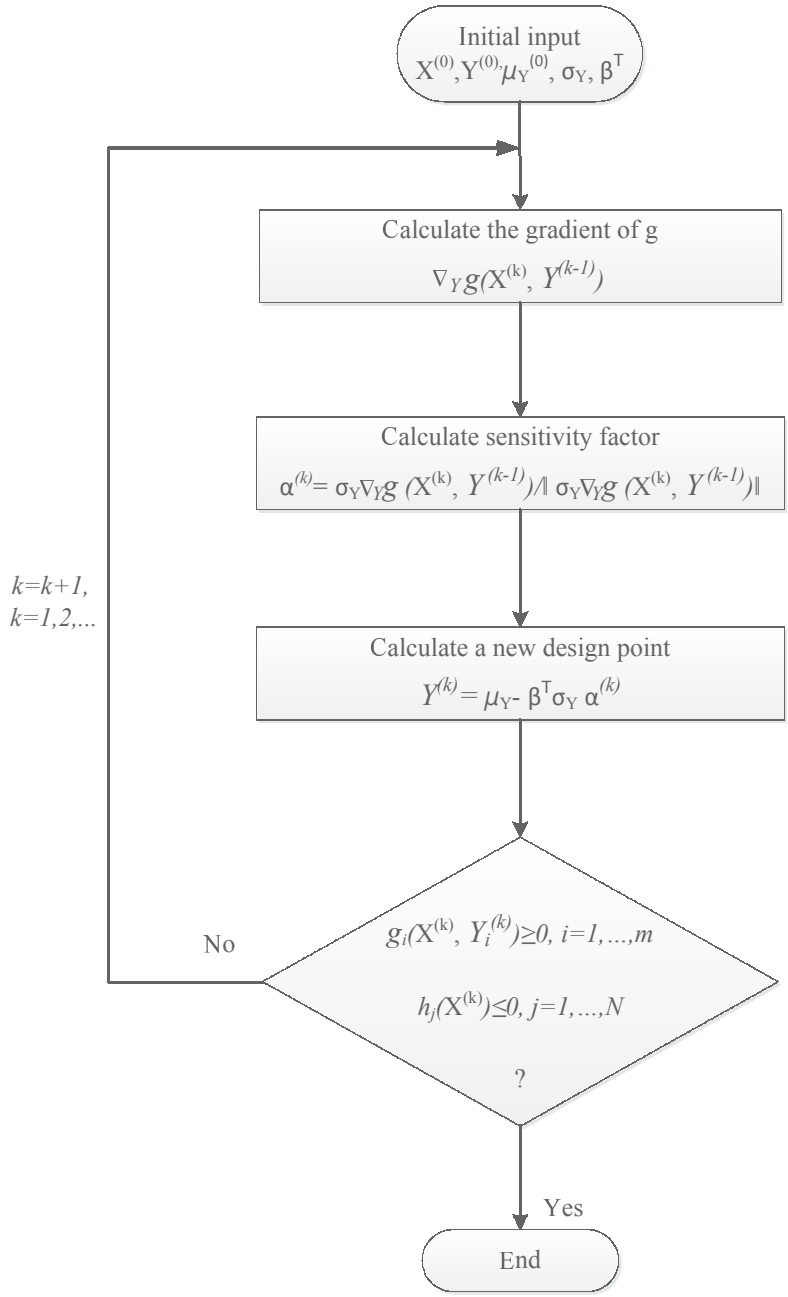

Fig. 5.8 Schematic represent of single loop approach

5.3.4. Computational methods for RBO

Due to the complexity of the multiple integral in failure probability calculation, many methods are used to simplify the integration process of (5–9). Taylor series expansion is often used to analytically approximate the limit state function. The Taylor expansion approach is further classified into *first-order reliability method* (FORM) and *second-order reliability method* (SORM) according to the limit state of interest that has been approximately represented by the first-order or the second-order expansion.

5.3.4.1. First-order reliability method (FORM)

In the FORM, the limit state function is approximately represented as a tangent plane at the MPP. The FORM is an optimization problem to find the MPP on the limit state surface. Reliability index β is the shortest distance from the origin to the limit state surface in U-space (Fig. 5.9). The limit state surface can be approximated by:

$$g(U) = -\alpha^T U + \beta \tag{5–25}$$

where α is the normal direction to the approximated limit surface

$$\alpha = -\frac{\nabla g(U)}{\|\nabla g(U)\|}\Big|_{U=U^*} \tag{5–26}$$

The probability of failure is express as

$$P_f = \Phi(-\beta) \tag{5–27}$$

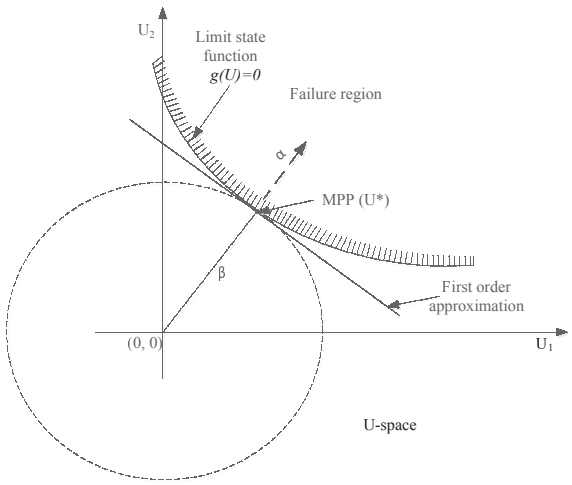

Fig. 5.9 The FORM

The Hasofer Lind (HL) and Hasofer Lind-Rackwitz Fiessler (HL-FR) algorithm is commonly used to find U* in the U-space in solving the deterministic optimization problem:

$$\begin{aligned} &\min_{U}: \ \beta(\mathrm{U}) = (U^T \mathrm{U})^{\frac{1}{2}} \\ &s.t. \ g(U) = 0 \end{aligned} \tag{5–28}$$

The iteration algorithm is

$$U^{(k+1)} = \frac{\left[\nabla g^T\left(U^{(k)}\right)U^{(k)} - g\left(U^{(k)}\right)\right]}{\nabla g^T(U^{(k)})\nabla g(U^{(k)})}\nabla g\left(U^{(k)}\right), \qquad k = 0,1,\cdots \tag{5–29}$$

where $\nabla g\left(U^{(k)}\right)$ is the gradient vector of $g(U)$ at $U^{(k)}$, k is the *k*th iteration in U-space. The convergence criterion is:

$$\frac{\left|U^{(k+1)} - U^{(k)}\right|}{U^{(k)}} \leq \varepsilon \tag{5–30}$$

In the FORM, the limit state function is approximated by the first-order Taylor expansion at the design point $U^{(k)}$. The accuracy of the results depend on how well the linearized limit-state function $\tilde{g}(U) = 0$ approximates a nonlinear function *g(U)* in terms of the failure probability P_f. When the failure surface is highly nonlinear, the failure probability estimated by FORM may give unreasonable and inaccurate results. In this situation, the Second-order Taylor series expansion is considered.

5.3.4.2. Second-order reliability method (SORM)

In the SORM, the limit state function is represented by a second-order approximation. The probability of failure is given by:

$$P_f = \Phi(-\beta)\prod_{i=1}^{n-1}(1 + \beta k_i)^{-1/2} \tag{5–31}$$

where k_i is the principal curvature of the limit state surface at MPP. To compute the principal curvature k_i, it is necessary to rotate the U-space to a new standard normal Y- space, that is:

$$\mathrm{Y=HU} \tag{5–32}$$

where H is the orthogonal matrix. The second-order approximation of the limit state function in the U-space is

$$\tilde{g}(U) \approx \alpha^T(U - U^*) + \frac{1}{2}(U - U^*)^T B(U - U^*) \tag{5–33}$$

Where

$$\alpha = \frac{\nabla g(U^*)}{|\nabla g(U^*)|} \tag{5–34}$$

and

$$\beta = \frac{\nabla^2 g(U^*)}{|\nabla^2 g(U^*)|} \tag{5–35}$$

Substituting (5–32) into (5–33) ~ (5–35), we have

$$\tilde{g}(Y) \approx -y_n + \beta + \frac{1}{2}(Y - Y^*)^T HBH^T(Y - Y^*) \tag{5–36}$$

By a series of orthogonal transformation of $\bar{Y}' = H_1, H_2, \cdots, H_m \bar{Y}$, the first (n-1)×(n-1) vector of matrix of HBH^T becomes a diagonal matrix

$$\overline{H}\overline{B}\overline{H}^T = \begin{pmatrix} k_1 & \cdots & 0 \\ \vdots & \ddots & \vdots \\ 0 & \cdots & k_{n-1} \end{pmatrix} \tag{5–37}$$

And (5–36) becomes

$$y_n = \beta + \frac{1}{2}\sum_{i=1}^{n-1} k_i \, y_i'^2 \tag{5–38}$$

The main curvature of the limit state surface k_{ij} is

$$k_{ij} = (\overline{HBH}^T)_{ij}, \quad (i, j = 1,2,\cdots,n-1) \tag{5–39}$$

Once the main curvatures k_i are obtained, the formula (5–31) can be used to compute the second-order approximation of the limit state surface.

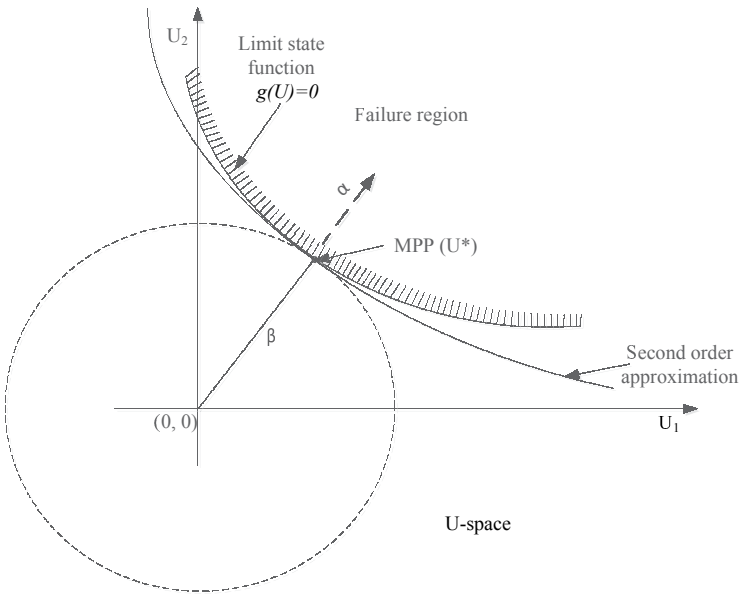

Fig. 5.10 SORM

In this part, the general problems under uncertainty were presented. The reliability-based optimization method, as one of an efficient method in dealing with optimization problem under uncertain was briefly stated. Application of RBO in evaluating the elasto-plastic properties of the SWCNT thin film to ensure the reliability of estimation was demonstrated as following.

5.4. Bilinear model for SWCNTs films

5.4.1. Problem formulation

The overview comparison between the experimental results in Fig. 3.8 and the typical load-depth curves of indentation into elastic-plastic materials in Fig. 5.11 (Menčík 2012) give a general information to the characteristics of SWCNTs thin film. The comparison indicates that the SWCNTs thin film could be a hard elasto-plastic material; meanwhile, it experiences the phase transformation during the unloading process according to Fig. 5.11(e). The nanoindentation induced phase transformation can be explained by the mechanisms of radial deformation of SWCNTs (or SWCNT bundles) under hydrostatic pressure under the scope of nano-deformation. Lots of studies demonstrated that nanotube can experience modifications in their radial geometry under radial squashing ((Zhao et al. 2013), (Chan et al. 2003)). Sun et al. (Sun et al. 2004) represented a hydrostatic pressure-induced hard-to-soft transition of an isolated single wall carbon nanotube by classical and ab initio constant-pressure MD simulations and the continuum elastic theory analysis. Their study found that with the cross

section of a SWCNT shows a circular-to-elliptical phase transition. At some critical pressure the material exhibits the hard-to-soft transition, and the ratio of modulus in the hard and soft phase scales with the square of the tube radius. Similar investigations that the radially deformed SWCNT bundles under hydrostatic pressure show a continuum phase transition from circular-to-elliptical-to-peanut under increased pressure (as shown in Fig. 5.12) were also reported ((Woods 2008), (Hasegawa & Nishidate 2006), (Lu et al. 2011)). These studies indicate that the tendency of radial collapse dependent on the SWCNT diameter and the critical diameter from a hardly collapsed condition to a relative easy plastic deformed, and the collapsed condition are respectively 2.5nm in ((Hasegawa & Nishidate 2006), (Nishidate & Hasegawa 2010)) and 2.1nm in (Lu et al. 2011), which in good consistency. In our study, the diameters of the SWCNTs are around 1.2nm, which means without the consideration of the sample's preparation defect, the SWCNT thin film in this study should be highly elastic and experiences plastic deformation with continuum phase transformation if the pressure exceeds a critical value, and this hypothesis also in consistent with R. Rao et al's observation in nanoindentation-induced phase transformation on silicon (Rao et al. 2007).

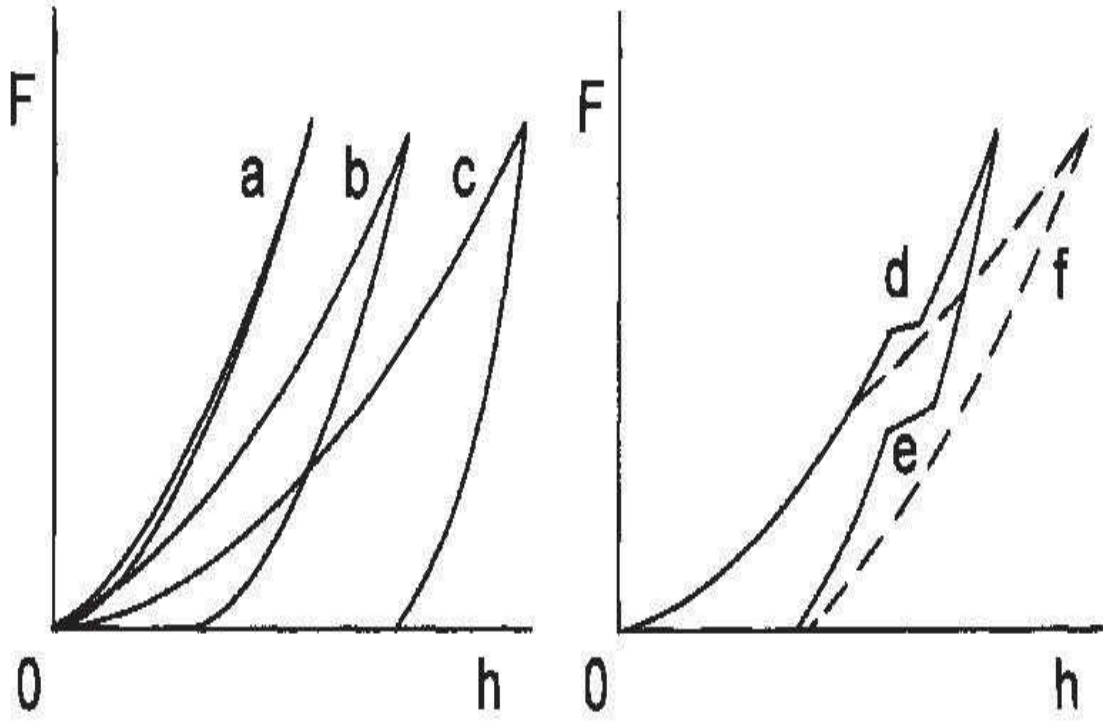

Fig. 5.11 Typical load-depth curves of indentation into elastic-plastic materials – a schematic. a – highly elastic material, b – hard elasto-plastic material, c – soft elasto-plastic material, d – formation of cracks during loading, e – phase transformation during unloading, f – delamination of the indented coating from substrate (Menčík 2012).

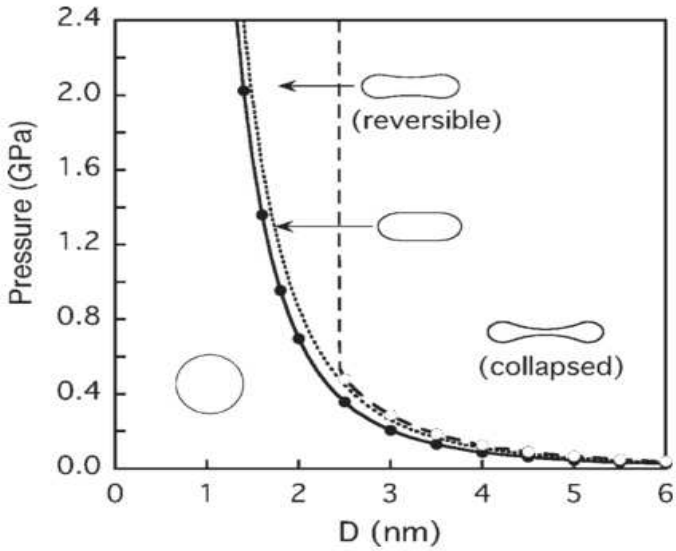

Fig. 5.12 Circular-to-oval transition pressure (P1, closed circles), oval-to-peanut transition pressure (P2, broken line), and collapse pressure (Pcollapse, open circles) as functions of tube diameter. The solid and broken lines are smooth interpolations of the calculated results (Hasegawa & Nishidate 2006).

Among the numerous methods which aims to extract the elasto-plastic properties from the indentation data, Kick's Law is typically used to describe the load–displacement response during the loading process (Cheng & Cheng 1998). In Kick's Law, the p-h curve is normally described by the relation: $P = Ch^2$, where C is the indentation curvature, and represents the "resistance" of the material to indentation. However, the tested results in Fig. 5.13 shows that the loads of SWCNT thin film obviously not have a square relation with its displacements. In fact, it well fits the power law relation $P = C(h)^m$ with $m \approx 1.18$ after a Least-squares regression analysis. It means that during the indentation process the load-displacement relationship more tends to be linear.

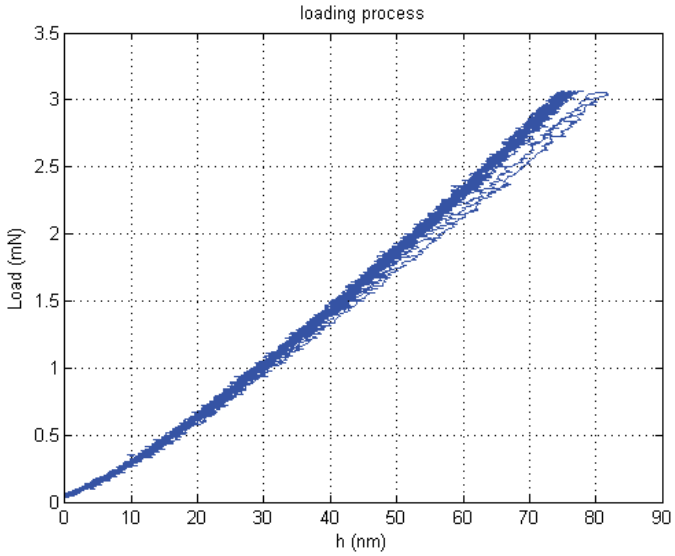

Fig. 5.13 Loading process of SWCNT thin film in nanoindentation

Based on the analysis for P-h response of SWCNT thin film in nanoindentation process as demonstrated above, we primarily inferred that: during the indentation process SWCNT thin film has a phase change, and the phase change process is accompanied with plastic deformation. That is the total work done by p in indentation process is combination work of elastic, plastic and phase transformation.

$$W_t = W_e + W_p + W_t \tag{5–40}$$

where W_t is the total work done in indentation process, W_e is the released elastic work, W_p is the stored plastic work, W_t is the stored phase transformation work. The complicated combination work of plastic deformation and phase transformation cannot be derived just from a single load-displacement curve. Therefore, dimensional or dimensionless methodology proposed in literatures (Tunvisut et al. 2002), (Cheng & Cheng 1998), (Dao et al. 2001) not are fit for this situation. In this chapter, we seek to extract the elasto-plastic properties of SWCNT thin films by fitting the load-displacement data of the unloading process in nanoindentation through realiability-based FE computation.

5.4.2. SWCNTs thin film properties confirmation

According to the analysis of the complete load-unload cycles of SWCNT film indentation, we approximated the elasto-plastic behavior of the SWCNT thin film by a linear expression, and its true stress-strain behavior is assumed to follow the bilinear model:

$$\sigma = \begin{cases} E\varepsilon, & for\ \sigma \le \sigma_Y \\ \sigma_Y + E_t(\varepsilon - \varepsilon_Y), & for\ \sigma \ge \sigma_Y \end{cases} \tag{5–41}$$

where σ_Y and ε_Y are the yield stress and strain respectively, with $\varepsilon_Y = \sigma_Y/E$; E is the Young's modulus, and E_t is the tangent modulus. According to the performance analysis for SWCNTs thin film during nanoindentation, material exhibits a pressure-dependent phase transitional behavior. Therefore, in unloading process, features of stress-strain should not be a straight line but as a fold line, as demonstrated in Fig. 5.14.

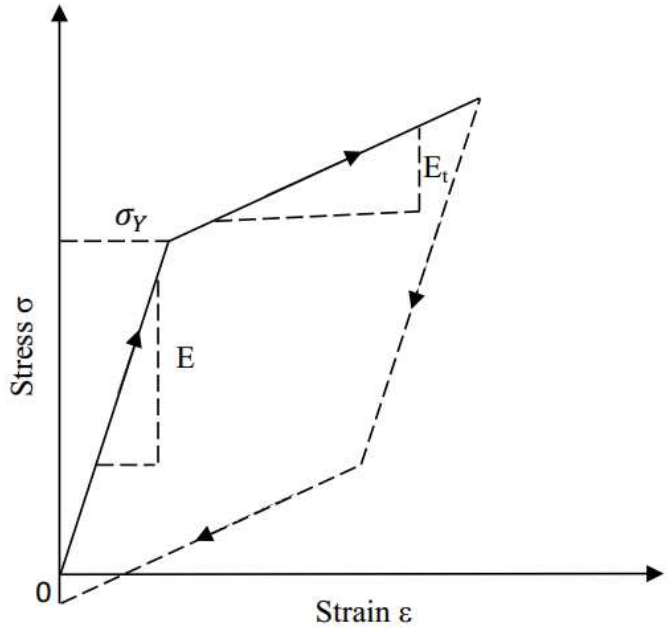

Fig. 5.14 Schematically of the bilinear elasto-plastic stress-strain behavior used in the current study

The indentation load makes a projected contact area A at the maximum depth h_{max} in nanoindentation process. Based on the assumed bilinear-hardening plastic model in Fig. 5.14 and pressure-dependent phase transition hypothesis, the reduced modulus E_r in unloading process should be changed in consistence with the change of the gradient of the load-depth curve in unloading process, as illustrated in Fig. 5.15. The reduced modulus of transformed phase 2 can be expressed analogically as:

$$E_r^* = \frac{1}{2}\frac{\sqrt{\pi}}{\sqrt{A}}\frac{dP}{dh}|_{\text{phase2}} \tag{5–42}$$

where E_r^* is the reduced modulus of transformed phase 2, $\frac{dP}{dh}|_{\text{phase2}}$ is the slop of later part in unloading curve as shown in Fig. 5.15. According to contact mechanics, the tangent modulus E_t can be obtained by:

$$\frac{1}{E_r^*} = \frac{(1-v^2)}{E_t} + \frac{(1-v_i^2)}{E_i} \tag{5–43}$$

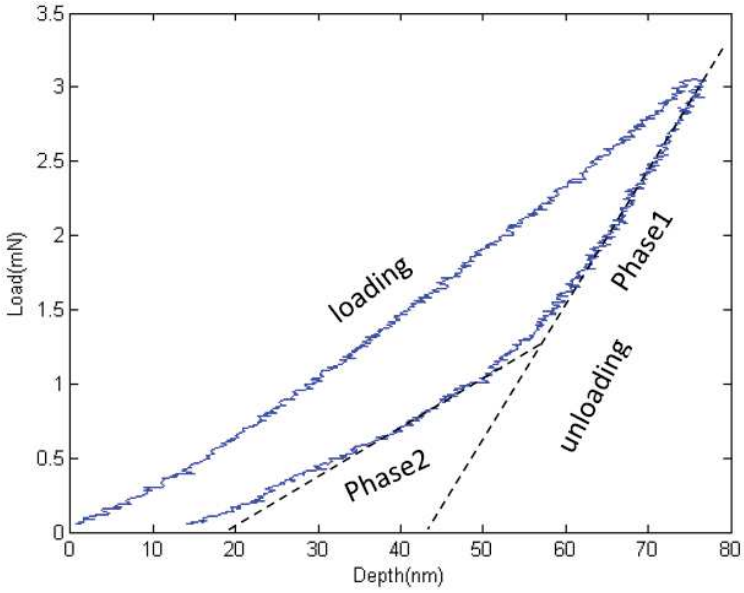

Fig. 5.15 Schematic illustration of a load-displacement response of the SWCNT thin film indentation

Because of the complexity due to material phase change in its morphology, we describe the load-displacement (p-h) relationship of SWCNT film in indentation implicitly as:

$$p = P(h, E_r, \sigma_y, E_t, \theta) \tag{5–44}$$

where θ is the apex angle of indenter.

The program for material properties evaluation is performed by realiability-based FE computation. That is, based on the estimated mechanical parameters of SWCNT thin film $(E, \sigma_y, E_t, \theta)$, the unloading load-displacement curve obtained by FE simulation must in consistence with the tested result which demonstrated in chapter 3 as:

$$\text{min:} \quad \left\| p^i - \overline{p}_t \right\| \tag{5–45}$$

Subject to:

$$\left| \frac{\overline{h}_{max} - h^i_{max}}{\overline{h}_{max}} \right| \leq \Delta_1 \tag{5–46}$$

$$\left| \frac{\bar{s} - S^i}{\bar{S}} \right| \leq \Delta_2 \tag{5–47}$$

where p^i is the vector of load in ith iteration, $\overline{p}_t$ is the vector of mean value in indentation teste, and the distribution of p_t is demonstrated in chapter 3. $\overline{h}_{max}$ and $\bar{s}$ are mean values of maximum displacement and contact stiffness, separately. Δ_1, Δ_2 are the variation constrain of h_{max} and S, which are dependent on the distribution of load-distribution of experimental test demonstrated in chapter 3. The evaluation procedure is illustrated in Fig. 5.16.

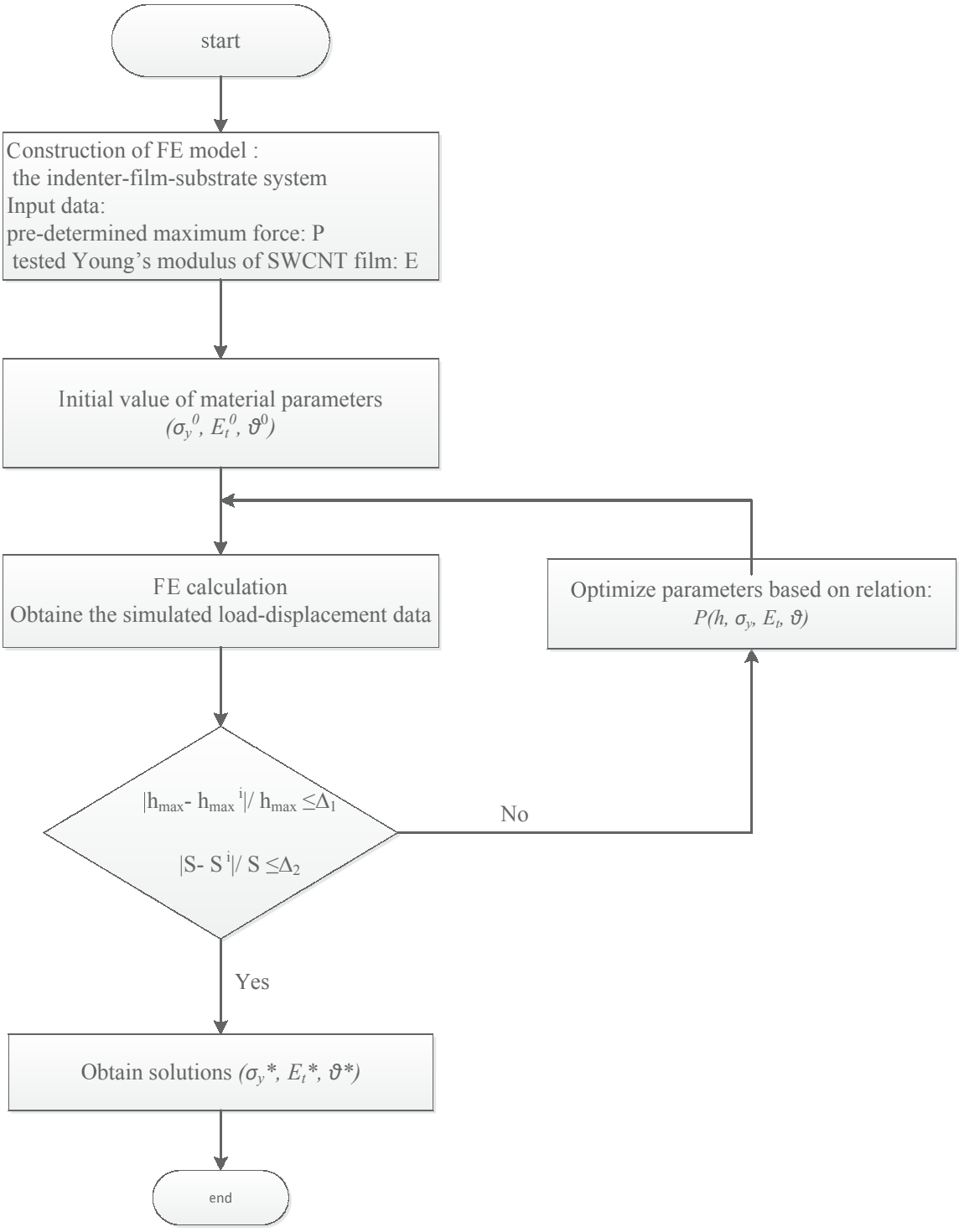

Fig. 5.16 Flowchart for the proposed analysis procedure to determine the mechanical properties SWCNT thin film from indentation and FE simulation data

5.4.3. Computational model of SWCNT thin film

5.4.3.1. The initial material properties setting

The Yong's modulus and Poisson's ratio of the indenter and the silicon substrate are respectively taken as 1143 GPa and 0.07 (Klein & Cardinale 1993), 180 GPa and 0.278 (Hopcroft et al. 2010). Young's modulus of SWCNT thin film is originated from nanoindentation test results as 192.83±13.922 GPa; the initial value of yield stress Y_0 is derived from the empirical equation of relation between Vickers hardness of material and yield stress (Tabor 1956),(Larsson 2001), (Busby et al. 2005).

$$H_v \cong KY \tag{5–48}$$

where H_v is the hardness of the plastic material, and Y is it's yield stress, K=1.5 ~ 3 is a constant that depends on the geometry of the indenter and material properties. Here the mean hardness of SWCNT film is 12.57719 ± 0.759 from experimental results, K_0=3, so the initial value of yield stress is taken as Y_0=4.2 GPa. The tangent modulus E_t is initially calculated according to equations (5–42) and (3–3) from the lower part of unloading information that E_t is about 42 GPa. As the Poisson's ration of indented material has little impact on the overview of the load-depth curve, here we assume that the Poisson's ration of SWCNTs film doesn't change during the indentation process and adopt it from literature as $v = 0.18$ (Hall et al. 2008).

5.4.3.2. FEM model construction

In this work, computations were performed using the finite element package ANSYS (Canonsburg 2009). As discussed above, the "Von Mises with Bilinear isotropic Hardening" material criterion is used in program code to approximately extract the plastic properties of the SWCNT thin film. The linear hardening process follows Von Mises isotropic criterion and can be written in the following form

$$f(\sigma_{ij}) = \sigma_e(\sigma_{ij}) - \sigma_Y = \sqrt{\frac{3}{2} S_{ij} S_{ij}} - \sigma_Y = 0 \tag{5–49}$$

When the stress is beyond the yield stress, it begins to deform plastically. With the plastic flow developed, the diameter of the Von Mises cylinder increased.

$$f\left(\sigma_{ij}, k(\epsilon_{ij}^{p})\right) = \sigma_e(\sigma_{ij}) - \sigma_f(\epsilon_{ij}^{p}) = \sqrt{\frac{3}{2}S_{ij}S_{ij}} - \sigma_f(\epsilon_{ij}^{p}) = 0 \qquad (5\text{–}50)$$

Fig. 5.17 illustrates the deformations of (5–49) and (5–50), the yield strength and elastic modulus parameters can be defined by bilinear elasto-plastic, as presented in Fig. 5.14.

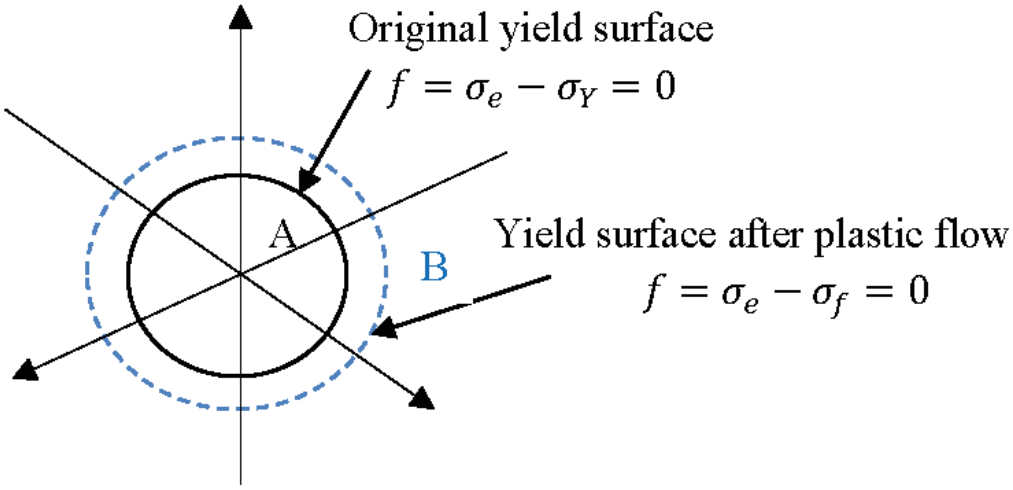

Fig. 5.17 Von Mises with isotropic Hardening

The ideal three-sided pyramid Berkovich indenter with a half angle of 65.3˚C was used in the initial computation. Fig. 5.18 is the geometric schematic of Berkovich indenter tip, and the geometry of the indenter is defined from (5–51) ~ (5–53). The SWCNT film is modeled as a thin block with a dimension of 1000nm×1000nm×200nm. Fig. 5.19 shows the FE-model of the indenter-film-substrate system in nanoindentation.

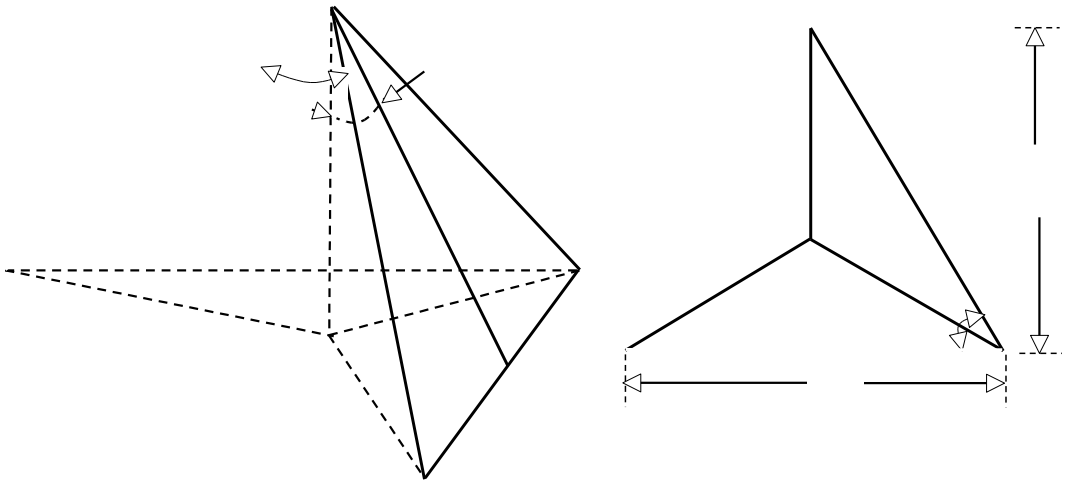

Fig. 5.18 Berkovich indenter tip

$$a = 2\sqrt{3}h\ tan65.3° \tag{5–51}$$

$$l = \frac{\sqrt{3}}{2}a \tag{5–52}$$

$$A_{proj} = 3\sqrt{3}h^2\ tan^2 65.3° = 24.56h^2 \tag{5–53}$$

The indenter, thin films and the substrate are meshed by a 3-D 20-node solid element solid 186. This element supports plasticity, stress stiffening, large deflection, and large strain deformation. The interaction of the indenter and the specimen is modeled as surface-to-surface contact pair without friction. Contact element TARGET 170 is applied to the tip of indenter as 'master' surfaces, and CONTACT 174 is applied to the top surface of specimen as 'slave' surfaces, and the contact direction was always taken as being normal to the master surface. The interface between film and the substrate was assumed to be perfect bonded. The meshes near the indenter were refined to describe the deformation and stress gradient accurately, as shown in Fig. 5.19 (b). An average force is continuously applied on the top surface of the indenter in z-direction; all degrees of freedom for the bottom nodes of substrate are fixed. The pre-determined maximum value of the force is set according to the experimental setting of 3mN. Large deformation of FEM calculations were performed under the continuous load and unloading process.

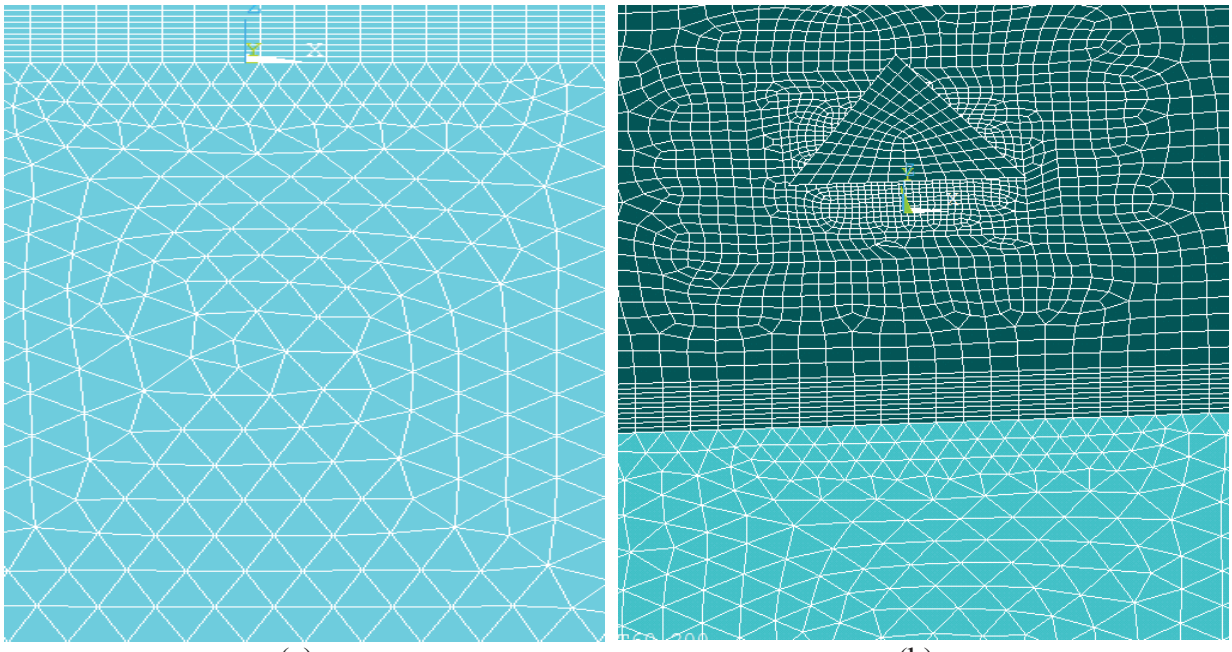

(a) (b)

Fig. 5.19 FE-model of the indenter-film-substrate system

5.4.3.3. Numerical results

Fig. 5.20 is the comparison of typical test results with simulation results. The comparison shows that with the same pre-determined maximum indentation force the simulation result has a much larger deformation (about 40% larger).

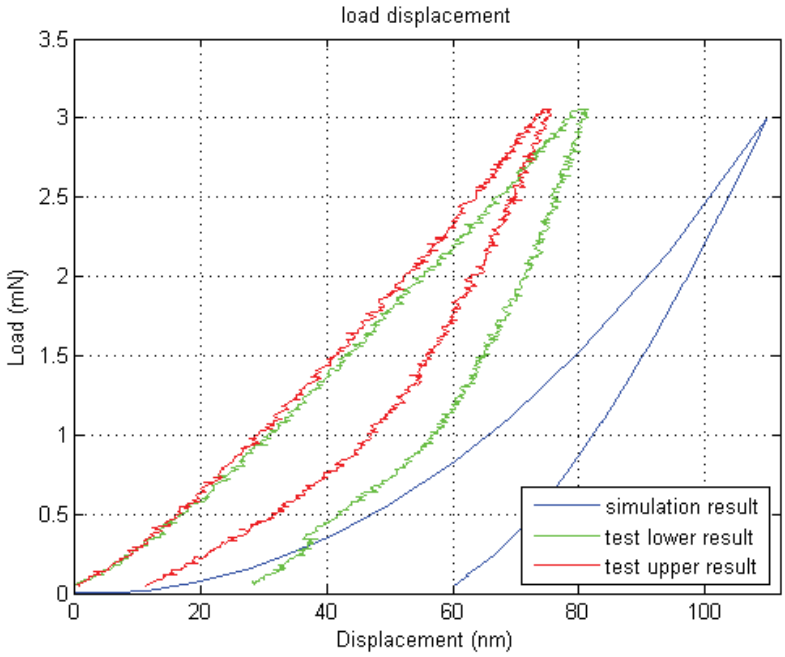

Fig. 5.20 Comparison of typical test results with simulation results

As demonstrated in the former part, the errors and uncertainties of nanoindentation may be caused by both the properties of the tested material and the indenter. One of the important factors is the shape of the indenter. The shape of a real indenter can never be ideal sharp, but blunt to some extent. This deviation is important especially for very small depths of penetration (Chen & Chang 2007). Even more, the actual angle can slightly differ from the norminal value, and even vary with the depth (Menčík 2012). Therefore, as elaborated above, an area calibration needs to be made to estimate the projected contact area as a function of contact depth A=A(h_c). Another important factor is the effect of substrate, which may cause problems of the so called pile-up or sink-in (Saha & Nix 2002). Fig. 5.21~Fig. 5.23 are the distributions of deformations and stress for the SWCNT film-substrate system. Fig. 5.22 and Fig. 5.23 indicate that the displacement of indenter is the combination of deformations in SWCNT film and silicon substrate.

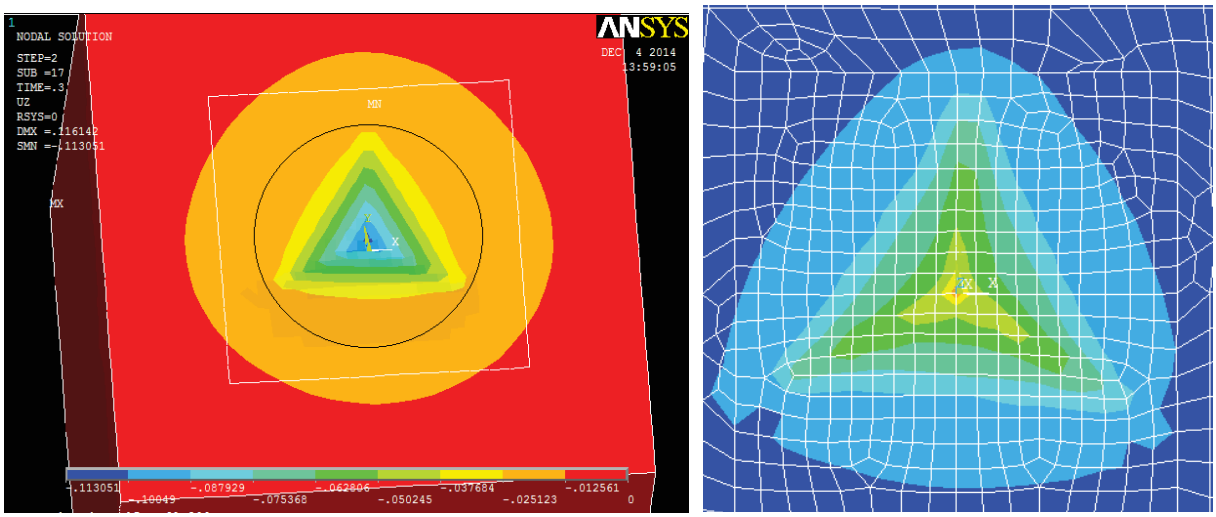

Fig. 5.21 Deformation of the SWCNT film-substrate system

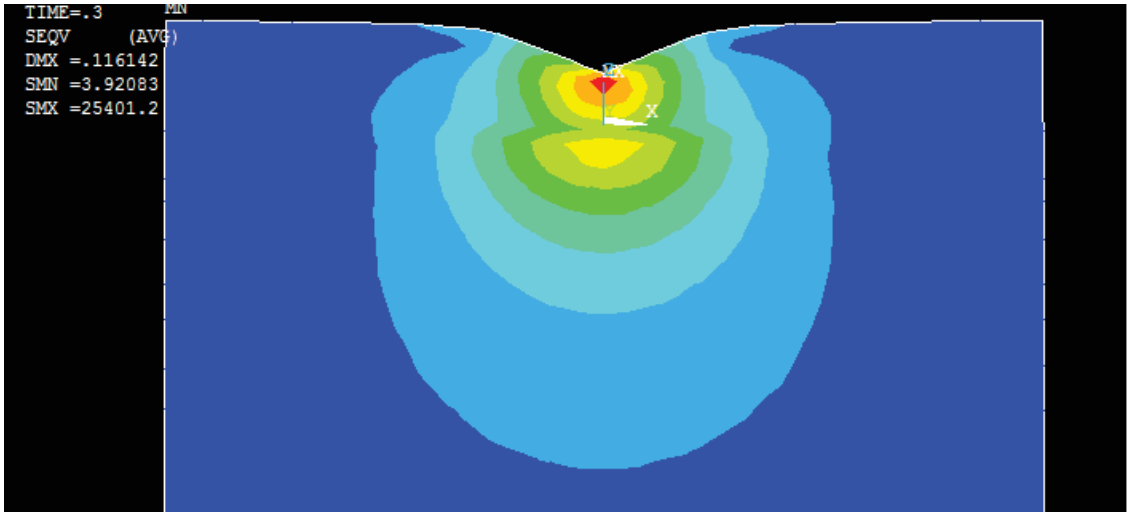

Fig. 5.22 Stress distribution of the SWCNT film-substrate system

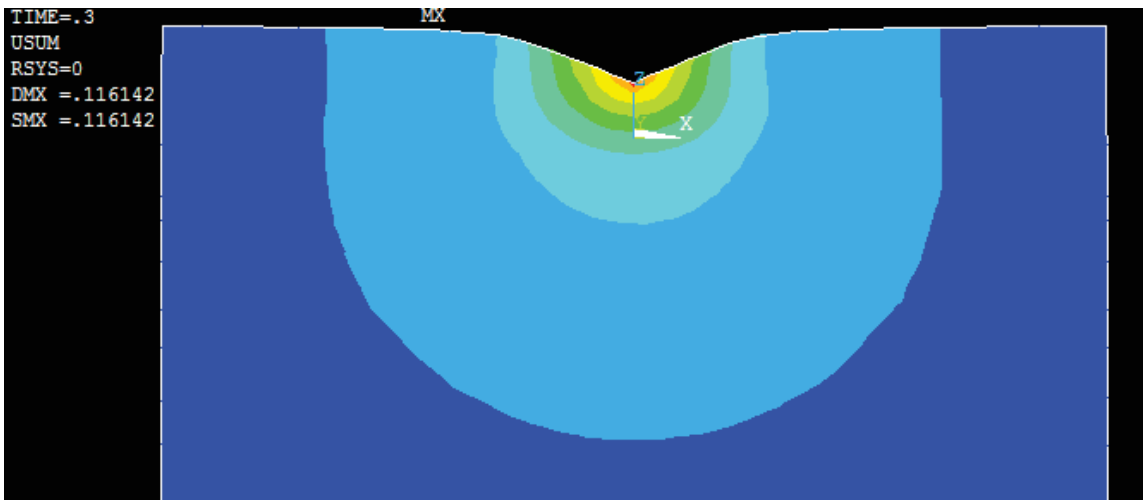

Fig. 5.23 Strain distribution of the SWCNT film-substrate system

To comprehensively understand the uncertain factors of SWCNT thin film properties in nanoindentation, and alleviate the burden in parameters updating, the orthogonal simulations are carried out. Effects of indenter shape, SWCNT thin film thickness, and the Young's modulus of silicon substrate are analyzed. Fig. 5.24 illustrates the comparisons of SWCNT thin film performance under different parameters setting with the same maximum load. The comparison in Fig. 5.24 indicates that the shape of indenter has much larger effect on material load-displacement performance (about 21.3%) than the effect of film thickness and substrate Young's modulus variations, which are about 4.7% and 7%.

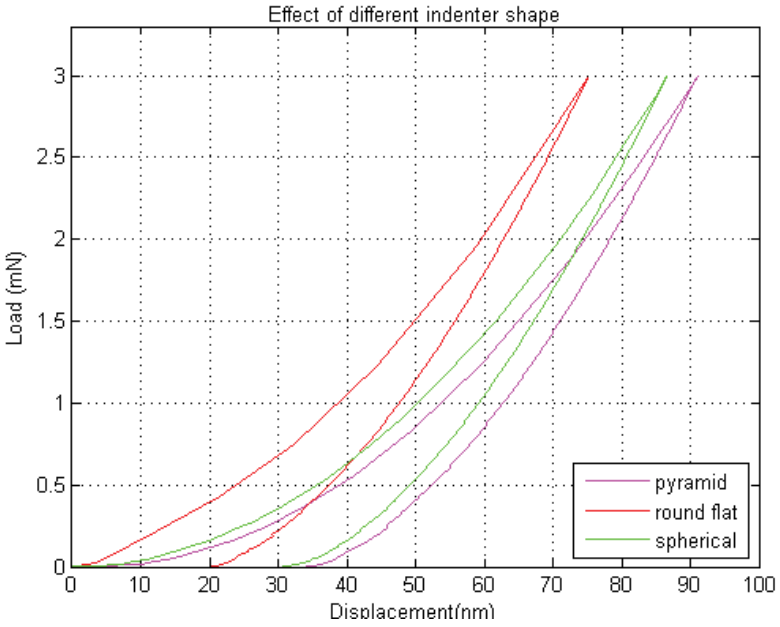

(a)

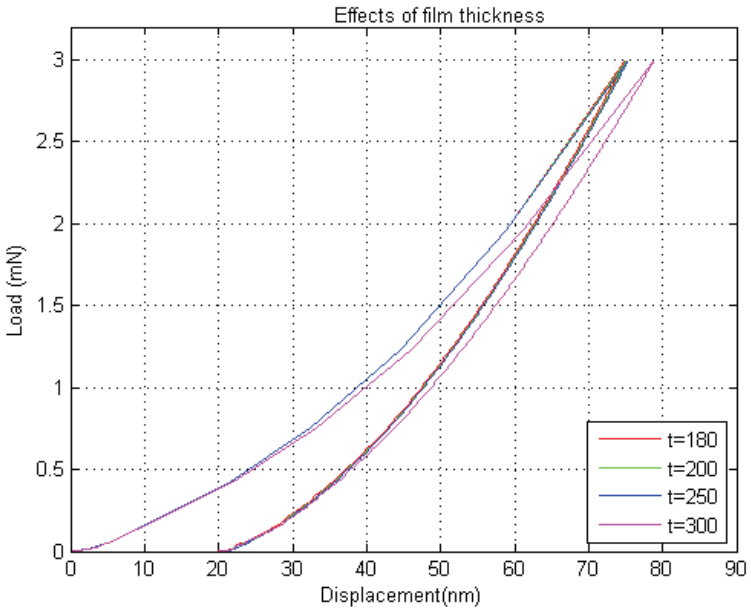

(b)

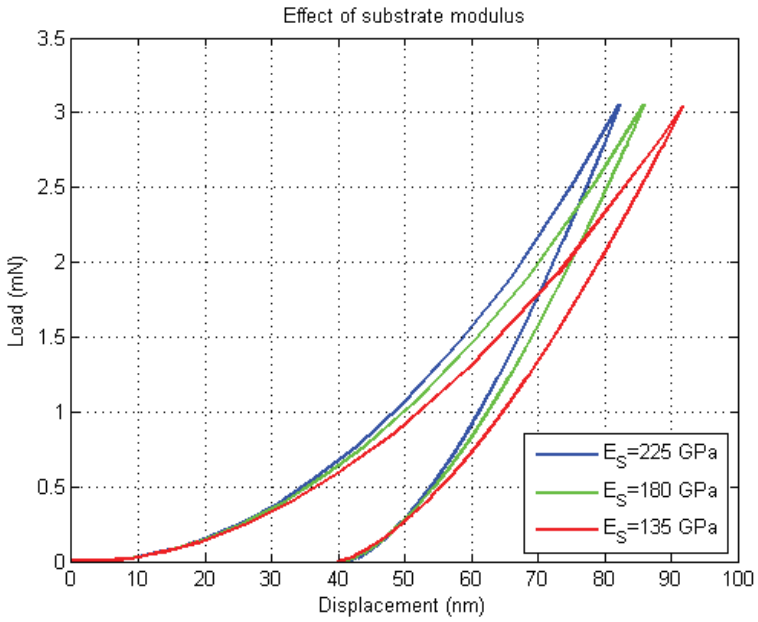

(c)

Fig. 5.24 Comparisons of SWCNT thin film performance under different parameters setting: (a) Effects of different indenter shape; (b) Effects of SWCNT thin film thickness; (c) Effects of Young's modulus of silicon substrate.

Since the importance of indenter errors in indentation, calibration needs to be made to compensate the projected contact area A and Young's modulus E. As the indenter defect directly affects the projected contact area in indentation, we compensate the errors of indenter in FE simulation by update the apex angle of indenter through equations of (3–14) and (5–53):

$$A_{proj} = c_2 {h_c}^2 + c_1 h_c + c_0 = 3\sqrt{3} {h_c}^2 tan^2\theta \tag{5–54}$$

According to the estimated projected contact area 'A' in chapter 3, θ is around 70°. Table 5.1 is the iteration results of FE simulations. It shows that after five iterations the simulation data fit the experiments results very well. Comparisons of load-displacement performances for experiment tests and FE simulations in iteration are illustrated in Fig. 5.25.

Fig. 5.26 illustrates the unloading data distribution for experiment, Monte Carlo simulation and FE simulations. Fig. 5.26 demonstrates that the numerical results well fits the indentation results.

Table 5.1 Iteration results of FE simulations

Parameters / Items		θ ˚C	σ_y (Gpa)	E_t (Gpa)	h_{max}		$\frac{dp}{dh}$	
					h_{max} nm	Δ_1	$\frac{dp}{dh}$ mN/nm	Δ_2
Mean value of experiment test		–	–	–	77.68	–	0.0963	–
FE simulation	Iteration 1	65.3	4.2	42	108.881	40.17%	0.0867	9.97%
	Iteration 2	70	4.2	42	87.59	12.76%	0.10845	12.62%
	Iteration 3	70	2.1	42	90.4407	16.43%	0.114	18.38%
	Iteration 4	70	8.385	21	85.903	10.6%	0.10256	6.5%
	Iteration 5	70	8.385	31.5	84.6446	8.97%	0.10098	4.86%
	Iteration 6	70	8.385	42	82.8116	6.61%	0.09858	2.37%

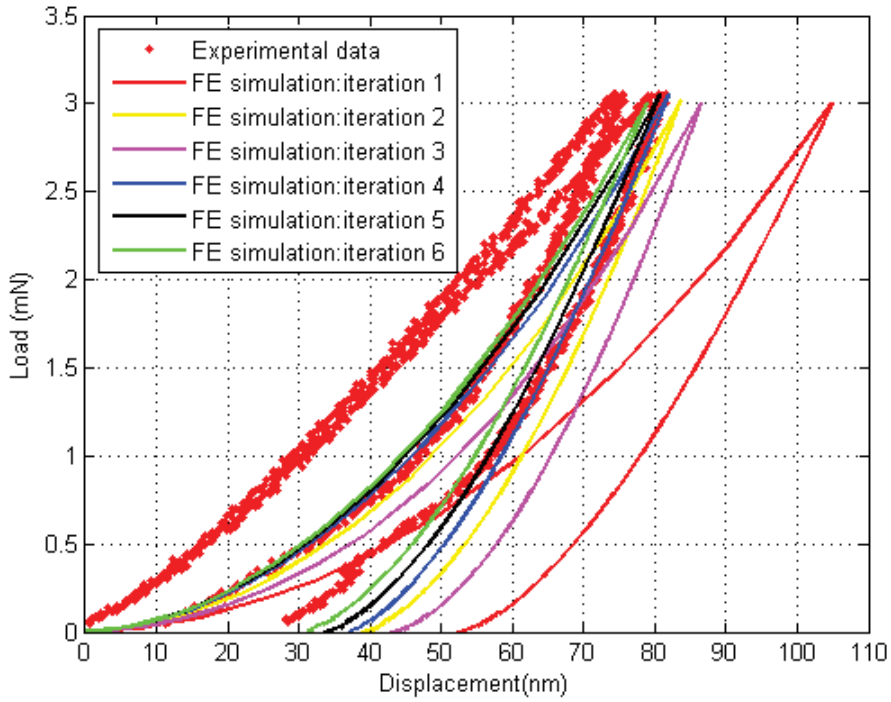

Fig. 5.25 Comparisons of load-displacement curves for experiment and FE simulations

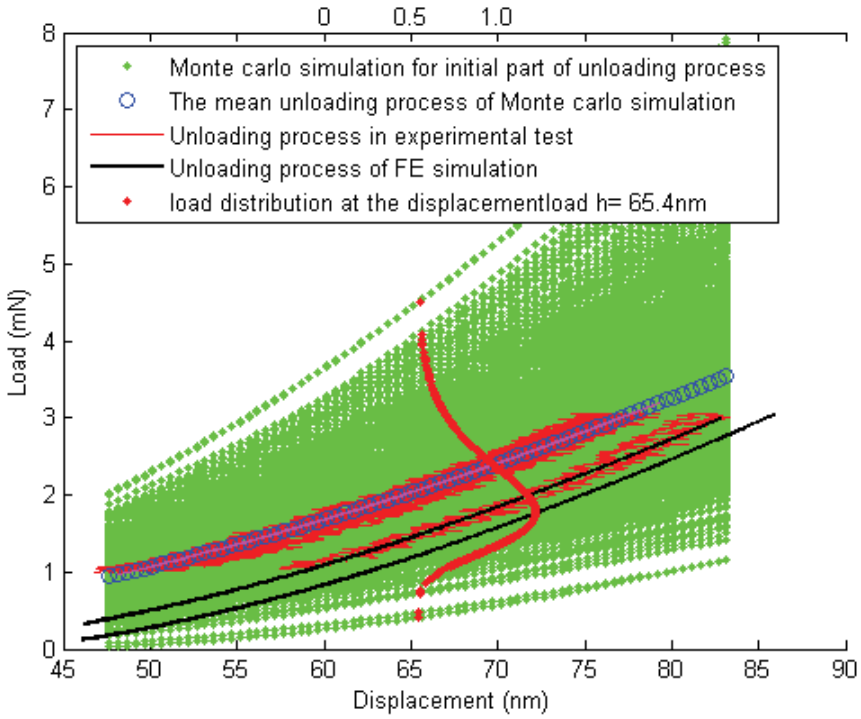

Fig. 5.26 Unloading curves distribution for experiment, Monte Carlo simulation and FE simulations

5.5. Conclusion

In this chapter, the general problems under uncertainty were briefly elucidated. The basic reliability problem and main methods for reliability-based optimization were then presented. The mechanical properties of the SWCNTs thin film were evaluated by combining FE technique with the nanoindentation tested. RBO methodology is applied to ensure the reliability of estimation. The distribution of load-displacement curve in unloading process is considered in reliability analysis. Numerical simulation results indicate that the performance of SWCNTs thin film can be approximately represented by a bilinear model, with the tangent modulus E_t about 42GPa, and yield stress σ_Y about 8.4GPa.

Conclusions and perspectives

Conclusions

The mechanical and electromechanical properties of SWCNTs are two of the most important issues in engineering applications (Nano-Electro-Mechanical System (NEMS), electronic chips, reactor, etc.). The contribution of this work is to model, simulate and assess the mechanical and electromechanical properties of SWCNTs materials with different morphologies following the hierarchical order (individual SWCNT→SWCNT combined film →SWCNT based composite).

The properties of individual SWCNTs are fundamental for CNTs research and applications. By establishing the approximate relationships between the molecular mechanics and the structural mechanics in SWCNTs, the elastic properties of SWCNTs are estimated. Numerical simulations indicate that the elastic properties of SWCNTs are dependent on their diameter, chirality and length. For small value of radius, the elastic moduli increase with the radius. When the radius becomes larger, all the elastic moduli converge to an asymptotic steady value. Besides, the moduli of zigzag and chiral SWCNTs are more sensitive to the radius in compared with armchair SWCNTs. With a similar radius, armchair SWCNT has a slight higher value of Young's modulus than zigzag and chiral SWCNTs. While zigzag SWCNT has a slight higher value of shear modulus than armchair and chiral SWCNTs.

The novel properties of CNTs make them as ideal filler for reinforcing polymer matrix to obtain advanced composites with high mechanical, electrical, and thermal properties. Motivated by the experimental observations and theoretical predictions as mentioned in chapter 4, this work investigates the effect of SWCNTs in application of electromechanical coupled composite. A 3D finite element model is proposed to predict the electrostrictive deformation of the SWCNT/P (VDF-TrFE) composite under electrostatic field. The mechanism of the enhanced electrostriction in SWCNT/ P (VDP-TrFE) composite is intuitively demonstrated by a bond electrical contact model in the numerical simulation process. Numerical results show that the electrostriction of SWCNT/P (VDP- TrFE) composite is greatly dependent on the volume fraction of SWCNT and the difference of dielectric constant between SWCNT and P (VDP-TrFE) copolymer. While, the dielectric constant of SWCNT is dependent on the chirality of SWCNT, which means the electrostriction of SWCNT/P (VDP-TrFE) composite is in fact also greatly dependent on the chirality of the SWCNT.

SWCNT thin films could be randomly oriented or aligned combination of SWCNTs based on its synthesis method and application demands. In this work, the randomly oriented SWCNT thin film is obtained by spin coating method. The hardness and elastic modulus are estimated by nanoindentation test. Combined with FE simulation, material's performance in indentation process is predicted. The elasto-plastic behavior of the SWCNT thin film is approximately represented by a bilinear model.

The numerical and experimental estimation indicates that properties of CNTs obtained either by theory or by experiments involve inevitable uncertainties, and some are relatively large. These uncertain factors mainly caused by:

- The adopted theoretical and experimental models
- The device properties
- The specimen properties
- The test error
- The models used for data evaluation
- The scatter of the measured values
- The material preference hypothesis
- The algorithmic uncertainty
- The parametric variability

For the sake of an effective and robust estimation, strategies need to be adopted in order to assess uncertainties. Application of RBO method in the process of elasto-plastic behavior estimation for SWCNT thin film indicate that RBO method is an effective tool to ensure the tested results reliability.

Perspectives

During the thesis process, some issues have been identified. Recommendations for the future studies may be:

1. The properties of an individual CNT are independent and interacting. For example, the mechanical deformation of CNTs can causes considerable change in its electronic, optical, magnetic, and chemical properties (Shima 2011), and display unique coupling between the electrical properties and mechanical deformation (Tombler et al. 2000). These properties interdependency may result in material performance unstable. In real application, especially for some high precision demands, the risk of instable properties should be taken into account.

2. The CNTs in composite are usually not perfectly aligned in the copolymer matrix. It could be randomly oriented or dispersed in the matrix as bundles. As the properties of CNTs are orientation and morphology dependent, the dispersion of CNTs in matrix could be a critical issue in real large-scale applications. Besides, the electrostrictive deformation of the SWCNT/P(VDF-TrFE) composite is an electro-mechanical coupled process. The distribution of electric field in the material is greatly dependent on the contact conditions. Threshold of the applied voltage should be predicted according to the mechanical properties of CNTs and matrix and their contact strength.

3. As demonstrated in chapter 5, SWCNT thin film exhibits a phase transformation behavior in nanoindentation process. This means, the microstructures of SWCNT thin film may significantly change under hydrostatic pressure. The criterion of hydrostatic stress could be essential in real applications (Like strain sensor).

These problems mentioned above commonly exist for CNTs applications. Due to the diversity and variability of material properties, good controlling of material performance is challenging.

RBO method is an effective tool in incorporating uncertainties regarding SWCNT thin film characterization by nanoindentation test.

Chapter 6. Résumé de la thèse en français

Possédants des propriétés physiques, électriques, mécaniques et chimiques exceptionnelles, les nanotubes de carbone (CNTs) sont considérés comme les nanomatériaux les plus importants aujourd'hui et donc sont proposées pour des applications industrielles potentielles en nanotechnologie. CNTs peuvent être classées en deux catégories : les nanotubes de carbone à paroi simple ou mono feuillet (SWCNTs) sous les initiales anglaises single walled carbon nanotubes et les nanotubes de carbone à parois multiples ou multi feuillet (MWCNTs) sous les initiales anglaises multi walled carbon nanotubes. La structure d'un SWCNT peut être considérée comme feuille de graphite d'épaisseur d'un atome roulé dans sous forme de tube cylindrique constitué d'anneaux de 6 carbones. Les tubes cylindriques peuvent avoir une ou deux extrémités enfermées par un hémisphère. Les propriétés des SWCNTs sont fondamentales pour la recherche scientifique et pour de nombreuses applications en médecine, en électronique, en environnement, pollution, …..

L'objectif de cette thèse est d'étudier les propriétés mécaniques et électromécaniques des matériaux SWCNTs avec différentes morphologies. Nous avons étudié les propriétés élastiques des SWCNTs individuels en utilisant la méthode des éléments finis (FE). Nous avons discuté et montré les effets du diamètre, de la chiralité et de la longueur sur les modules élastiques de SWCNTs. Nous avons montré que les modules élastiques augmentent significativement selon les plus petites valeurs du rayon. Lorsque le rayon devient plus grand, tous les modules élastiques convergent vers une valeur constante asymptotique. En outre, les modules des SWCNTs de types zigzag et chirale sont plus sensibles à la variation du rayon par rapport à celui du type fauteuil.

Nous avions pu déterminer expérimentalement, en utilisant la nanoindentation technique, le module élastique du film ultra-mince de SWCNT. En effet, les valeurs expérimentales du module d'Young E et celle de la dureté H du film ultra-mince de SWCNT sont respectivement E= 192.83± 13.922 GPa, H=12.57719 ± 0.759 GPa. Ensuite, nous avons élaboré un modèle par éléments finis qui représente le comportement des films ultra-minces de SWCNT dans le processus de nanoindentation. Dans cette étude nous avons élaboré un modèle elasto-plastique pour décrire le comportement mécanique du matériau au cours de l'indentation. Une comparaison était présentée dans le but d'évaluer les propriétés élasto-plastiques du film ultra-mince de SWCNT en utilisant la simulation par éléments finis avec les données statistiques du test expérimental. Le modèle bilinéaire proposé donne une bonne approximation de la performance du film ultra-mince de SWCNT dans la nanoindentation.

Finalement, nous avons consacré une grande partie pour étudier, par la méthode des éléments finis, les propriétés électrostrictives du composite à base du copolymère de polyfluorure de vinylidene et trifluoroethylene P (VDF-TrFE) et des SWCNTs. Les résultats numériques trouvés montrent que l'électrostriction du composite (P (SWCNT/VDF-TrFE)) dépend considérablement de la fraction volumique de SWCNT et du rapport des constantes diélectriques du SWCNT et du P (VDF-TrFE).

Au cours de cette investigation, nous avons constaté que les propriétés des CNTs obtenues théoriquement ou expérimentalement impliquent des incertitudes inévitables. Par conséquent, la prise en compte de ces incertitudes dans la prediction des propriétés des CNTs s'avère nécessaire. Pour cela, nous avions recours à la méthode de l'optimisation basée sur la fiabilité (RBO). Cette méthode est un outil efficace pour assurer la fiabilité des résultats expérimentaux et numériques dans le processus d'estimation du comportement élasto-plastique pour SWCNT.

6.1. Motivation et objectif

Introduction

Le but de la thèse est la contribution à l'élaboration des excellentes propriétés des nanomatériaux, en particulier pour les nanotubes de carbone (CNTs). Les CNTs matériau présente une structure hiérarchique avec le diamètre passant de ~ 1 nm (un nanotube individuel) à ~ 1 μm (fibre de nanotubes de carbone). Les propriétés du matériau CNTs dépendent de leurs états et des dimensions de leurs structures. Nous étudions les différentes propriétés de SWCNTs qui sont :

1) étude des propriétés mécaniques des SWCNTs individuels en utilisant la méthode des éléments finis.

2) estimation des propriétés élasto-plastique de SWCNT film mince par le test de nanoindentation et la simulation par la méthode éléments finis;

3) explorer les propriétés électrostrictives de composite à base de SWCNT (le P (VDF-TrFE)/SWCNT composites).

Pour assurer la fiabilité de l'estimation des propriétés élasto-plastique de SWCNT film mince, nous avons proposé la méthode d'optimisation basée sur la fiabilité (RBO).

Les résultats numériques indiquent que la méthode RBO est un outil efficace pour estimer les propriétés des matériaux CNT qui présentent une grande incertitude en raison de la diversité des structures et de la morphologie à l'échelle nano.

Motivation

Actuellement, la nanotechnologie et les nanomatériaux ont un grand nombre d'applications dans des domaines variés, et d'attirer une grande attention à la fois académique industriel dans monde. Comme l'un des nanomatériaux les plus importants, les CNTs ont suscité un intérêt considérable depuis sa découverte en 1991 (Iijima 1991). En raison des propriétés physiques, électriques, mécaniques et chimiques exceptionnelles, les CNTs sont considérés comme les candidats les plus prometteurs dans la technologie de la micro-électronique ou dans des dispositifs mécaniques, des puces électroniques, et dans le renforcement en matériau composite.

Ces dernières années, la plupart des pays développés ont fait un grand nombre d'investissements dans les programmes de recherche sur les CNT et de grands développements concernant les structures de la CNT, de la synthèse, et les paramètres importants ont été apportés. Les investissements dans la recherche CNT augmentent chaque année.

CNTs sont classés comme les nanotubes de carbone à paroi simple (SWCNT) et des nanotubes de carbones multi-parois (MWCNT). La structure d'un SWCNT peut être considérée comme un atome d'épaisseur de couche de graphite laminé à cylindres avec le diamètre de 1-2 nm; tandis que, les MWCNT sont multi-couche de graphite laminé soit disposé dans des cylindres concentriques ou sans soudure agencé comme un cylindre de couche hélicoïdale. Au cours des dernières années, un nombre important de travaux ont été fait sur les propriétés de CNT. Cependant, la plupart des prévisions sont basées sur une structure atomiquement parfaite avec un modèle idéal CNT qui peut loin de la production réelle. En raison des modèles ou inattendues erreurs inappropriées, certaines prédictions peuvent même inacceptable. Par conséquent, l'analyse de l'incertitude pour les propriétés de CNTs devient nécessaire avec les diverses exigences croissantes des performances du produit.

La méthode de l'optimisation basée sur la fiabilité (RBO) a été utilisée pour résoudre les problèmes des incertitudes.

Objectif

Motivé par ces chercheurs et les développements mentionnés ci-dessus, Cette thèse vise à étudier les propriétés mécaniques et électromécaniques de matériaux de SWCNT avec différentes morphologies de la matière. Les propriétés élastiques des SWCNTs individuels sont étudiées en utilisant la méthode des éléments finis d'abord. Le module d'élasticité de SWCNT film mince est estimé par notre test de nanoidentation, ses propriétés élasto-plastique sont ensuite déterminées par la combinaison de la simulation par éléments finis et la base des

données statistique des résultats expérimentaux. En fin nous étudions les propriétés électrostrictives de composite à base de SWCNT (le P (VDF-TrFE) - SWCNT composite).

6.2. Organisation du mémoire

La thèse est organisée en cinq chapitres. Les chapitres 1, 2, 3 et 4 élaborent les propriétés mécaniques de SWCNTs et SWCNT film mince et les propriétés électromécaniques de composite SWCNTs de base (SWCNT / P (VDF-TrFE)). Le chapitre 5 est consacré à l'étude des incertitudes des propriétés de SWCNT film mince. La méthode RBO a été proposée pour résoudre ce genre de problèmes, en particulier l'estimation des propriétés élasto-plastique de SWCNT film mince.

6.2.1. Le premier chapitre: Introduction à la Nanotechnologie, Nanomatériaux et Nanotubes de carbone

Dans ce chapitre, nous avons présenté brièvement les propriétés fondamentales des nanomatériaux et des nanotechnologies. CNTs, comme l'une des questions les plus intéressantes à la fois académique et industrielle dans le monde actuellement. Ces propriétés électroniques, thermiques, mécaniques sont présentées.

Les propriétés et les applications des nanotubes de carbone sont principalement dépendantes des technologies de fabrication, donc nous présentons à la fin de ce chapitre les méthodes de synthèse de CNTs.

Il est démontré que les CNTs présentent d'excellentes propriétés physiques, chimiques et mécaniques. Ces propriétés dépendent de environnement de la structure (température, champs électrique, les efforts, …). Par conséquent nous présentons une synthèse des différentes propriétés potentielles de CNTs et l'état de l'art actuel.

6.2.2. Le deuxième chapitre: Les propriétés mécaniques des SWCNT par la méthode des éléments finis

Le chapitre 2, est consacré à la prédiction numérique du module de Young et de celui du cisaillement des SWCNTs fauteuil, zigzag et chiraux avec des rayons et des longueurs différentes. Nous présentons un modèle éléments finis 3D pour les SWCNT du fauteuil, zigzag et chiraux. En établissant les relations approximatives d'équivalence entre la

mécanique moléculaire, les mécanismes structuraux dans SWCNT. Pour les interactions entre les atomes C-C, nous avons élaboré un modèle de simulation par les éléments de type ressort linéaire et ressort de torsion.

En mécanique des structures, la construction d'un nanotube individuel peut être considérée comme un assemblage régulier des masses ponctuelles reliées par des ressorts élastiques. En omettant les interactions électrostatiques, les forces interatomiques peuvent être exprimées en termes de fonction d'énergie potentielle de diverses caractéristiques structurelles. Le champ de force est la combinaison des termes d'énergie potentielles et peut être exprimé par (Ghaderi & Hajiesmaili 2012):

$$U = \sum U_r + \sum U_\theta + \sum U_\phi + \sum U_\omega + \sum U_{vdw} + \sum U_{el} \qquad (6\text{–}1)$$

Où

U_r: L'énergie rapportée à l'interaction de la force de liaison,

U_θ : L'énergie rapportée à l'interaction de l'angle de liaison de flexion

U_Φ : L'énergie rapportée à l'interaction de torsion dièdre d'angle

U_ω : L'énergie rapportée à l'interaction de la torsion out-of-plan

U_{vdw} : L'énergie rapportée à l'interaction du Van der Walls

U_{el} : L'énergie rapportée à l'interaction électrostatique

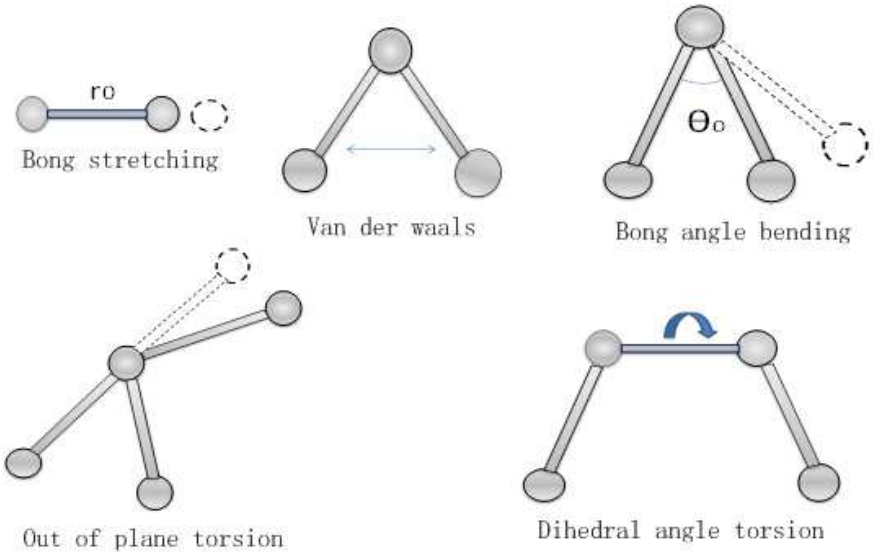

Fig. 6.1 Interactions interatomiques dans la mécanique moléculaire

Généralement, pour les systèmes covalents, les contributions plus significatives à l'énergie stérique totale proviennent des quatre premiers termes de l'équation (6–1). Sous l'hypothèse de petite déformation, l'approximation harmonique est adéquate pour la description de l'énergie (Li & Chou 2003a). Adopter la forme harmonique simple, nous obtenons les énergies suivantes :

$$U_r = \frac{1}{2}k_r(r - r_0)^2 = \frac{1}{2}k_r(\Delta r)^2 \tag{6–2}$$

$$U_\theta = \frac{1}{2}k_\theta(\theta - \theta_0)^2 = \frac{1}{2}k_\theta(\Delta\theta)^2 \tag{6–3}$$

$$U_\tau = U_\phi + U_\omega = \frac{1}{2}k_\tau(\Delta\phi)^2 \tag{6–4}$$

Où

k_r : la raideur de la liaison force constante étirement, Δr : la traction de liaison

k_θ : la raideur de la liaison de flexion constante, $\Delta\theta$: l'angle de liaison

k_τ : la raideur de torsion, $\Delta\emptyset$: les variations de la liaison d'angle et de torsion

Puisque la structure d'un nanotube est considérée comme la connexion de ressorts élastiques et en appliquant la loi de Hooke on obtient l'expression du potentiel énergétique de l'interaction de la force de liaison qui est équivalente à l'énergie potentielle d'une compression / extension d'un ressort de la rigidité k_r. Les termes d'énergie potentielles de l'angle de liaison de flexion et de torsion sont équivalentes à l'énergie potentielle d'un ressort en torsion avec une raideur de k_θ et k_τ respectivement. Grâce à cette conversion, les paramètres de la mécanique moléculaire k_r, k_θ et $k_\tau$sont par conséquent équivalente à la liaison d'étirement , l'angle de la liaison et la constante de la résistance à la torsion respectivement. Les constantes de force de résistance sont considérées comme k_r=6.52×10^{-7} N nm^{-1}, k_θ=8.76×10^{-10} N nm rad^{-2} et k_τ=2.87×10^{-10} N nm rad^{-2} (Ghaderi & Hajiesmaili 2012). Fig. 6.2 illustre le modèle de ressorts des interactions interatomiques du CNT modèle éléments finis.

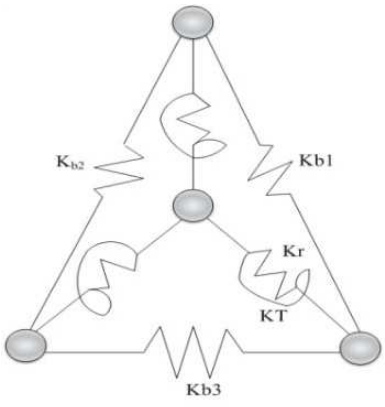

Fig. 6.2 Interatomique modèle de CNT

6.2.2.1. Le module d'Young de SWCNTs

La Fig. 6.3 montre les variations du module d'Young des SWCNTs de Fauteuil, zigzag et chiraux avec le rayon. Il peut être vu que le rayon a un effet significatif sur les modules d'Young de SWCNT. Pour SWCNTs de Fauteuil, zigzag et chiraux avec petit rayon, les modules de Young augmente avec au rayon. Lorsque le rayon augmente jusqu'à une certaine valeur plus élevée, les modules d'Young restent stables. La valeur stable des modules de Young sur plus grand rayon de nanotubes est principalement due à l'effet de courbure. Lorsque le diamètre des nanotubes augmente, la déformation de la liaison C - C devient moins importante.

Nous avons constaté également qu'avec le même rayon, les SWCNTs fauteuil ont un module d'Young légèrement supérieurs que celui des SWCNTs zigzag; et ceux des SWCNTs zigzag sont légèrement supérieurs aux modules d'Young des SWCNTs chiraux. Ce qui est conforme aux résultats de la littérature (Giannopoulos et al. 2008), (Mahmoudinezhad et al. 2012), (Lu & Hu 2012), (Kalamkarov et al. 2006), (Xiao et al. 2005).

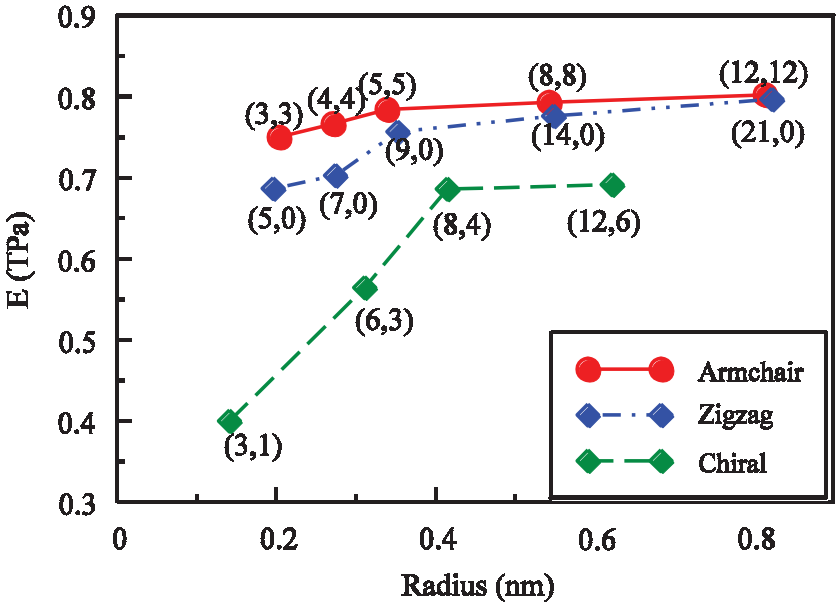

Fig. 6.3 Variation de modules d'Young des SWCNTs de Fauteuil, zigzag et chiraux avec le rayon

La Fig. 6.4 illustre les variations du module d'Young avec la longueur de SWCNT. Les résultats numériques montrent que la longueur du fauteuil (8, 8), zigzag (14, 0) et chirale (9, 6) SWCNT changent de 3.57 nm à 8.24 nm, de 3.27 nm à 8.38 nm et de 3.56 nm à 9.28 nm, La différence maximale correspondant du module d'Young est de 2%, 5%, 14%, respectivement.

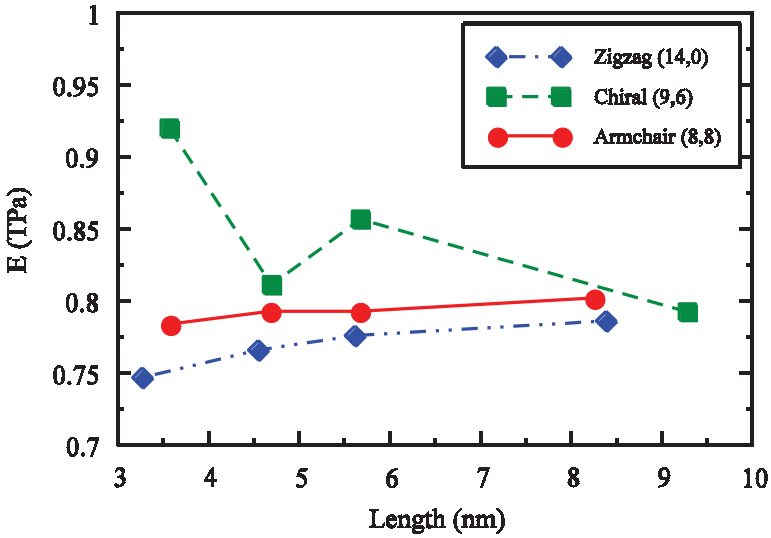

Fig. 6.4 Variation de modules d'Young des SWCNTs de Fauteuil, zigzag et chiraux avec la longueur

6.2.2.2. Le module de cisaillement de SWCNTs

La Fig. 6.5 illustre la variation du module de cisaillement de SWCNT Fauteuil, zigzag et chiraux avec le rayon. Elle montre que lorsque le rayon est petit, les modules de cisaillement de SWCNT Fauteuil, zigzag augmente avec la variation du rayon. Lorsque le rayon devient plus élevé, les modules de cisaillement ont tendance à se stabiliser. Les résultats montrent également que les modules de cisaillement de SWCNT zigzag sont plus élevés que les modules de cisaillement de SWCNT fauteuil et chiraux. Cela est principalement dû à la différence de la construction de la structure atomique de SWCNT. Dans SWCNT fauteuil, un tiers des liaisons C-C sont alignés avec la direction du chargement radiale, alors que toutes les liaisons C-C sont à angle avec la direction de chargement radiale dans SWCNT zigzag et chiral. En outre, pour SWCNT chiraux, le module de cisaillement est plus sensible aux variations de chiralité, comme illustré sur la Fig. 6.5.

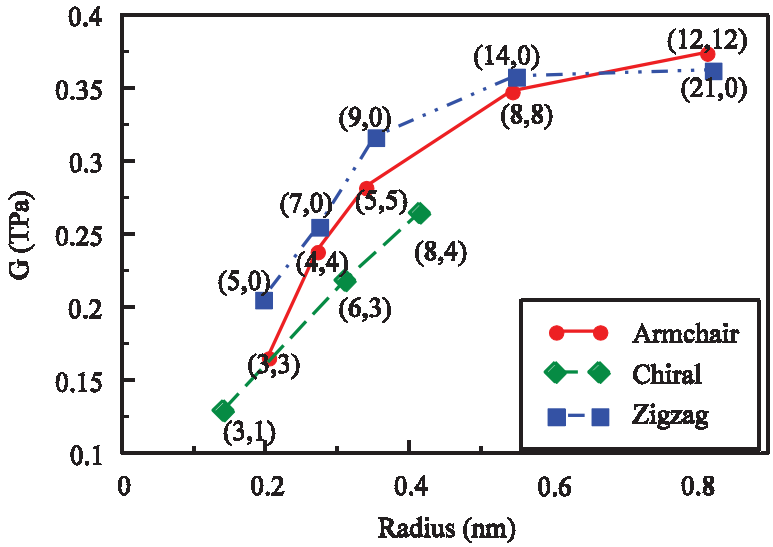

Fig. 6.5 Variation des modules de cisaillement de SWCNTs fauteuil, zigzag et chiraux avec le rayon

6.2.2.3. Conclusions

Les résultats numériques démontrent que les modules d'élasticité (module de cisaillement et le module d'élasticité de Young de SWCNT) sont fortement dépendants du rayon et de la chiralité des nanotubes. Pour la petite valeur du rayon, le module d'élasticité augmente avec le rayon d'incrémentation. Lorsque le rayon devient plus grand, tous les modules élastiques convergent vers une valeur constante. En outre, les modules de SWCNT zigzag et chirales sont plus sensibles à la variation du rayon par rapport au SWCNT Fauteuil. Les modules que nous avons obtenus correspondent bien à ceux de la littérature.

6.2.3. Le troisième chapitre: Propriétés élastiques de SWCNTs film mince en utilisant la nanoindentation

Dans le chapitre 3, le film mince de SWCNT (~ 200 nm) est préparé par la méthode l'induction centrifuge. La dureté et le module d'élasticité de SWCNTs film mince est estimé par le test de nanoindentation. Puisque la dureté testée et le module d'élasticité de SWCNT films sont tirés de la courbe de la charge-déplacement du pénétrateur sous certaines hypothèses. Nous avons pris en compte l'impact des incertitudes sur les propriétés élastiques de SWCNTs le film testé par nanoindentation.

6.2.3.1. Préparation du matériel

Dans cette étude, des films minces de SWCNT ont été préparés à l'ingénierie de l'université centre mécanique de Coimbra en utilisant la méthode l'induction centrifuge.

Une suspension diluée de SWCNT dans l'éthanol a été exposé aux ultrasons pendant 20 min pour étaler les nanotubes. Nous avons élaboré les cheminements suivants :

- Fixer les puces de silicium sur la tournette
- Déposer la solution de SWCNT sur les puces de silicium
- Démarrage de la tournette pour étaler le fluide sur toute la surface par centrifugation jusqu'à ce que la couche ait l'épaisseur voulue, comme indiqué sur la Fig. 6.6.

Après centrifugation, le solvant éthanol a été évaporé à la température ordinaire. Les échantillons sont ensuite au traitement thermique pendant 2 h sous la température de 300 ° C et refroidis lentement à température ambiante. Après le traitement thermique, les nanotubes orientés arbitraire sur le substrat de silicium et interagissent par l'intermédiaire de Van der Waals. La Fig. 6.7 représente des échantillons de film de SWCNT et des images au microscope des grappes de nanotubes distribués sur des substrats de silicium.

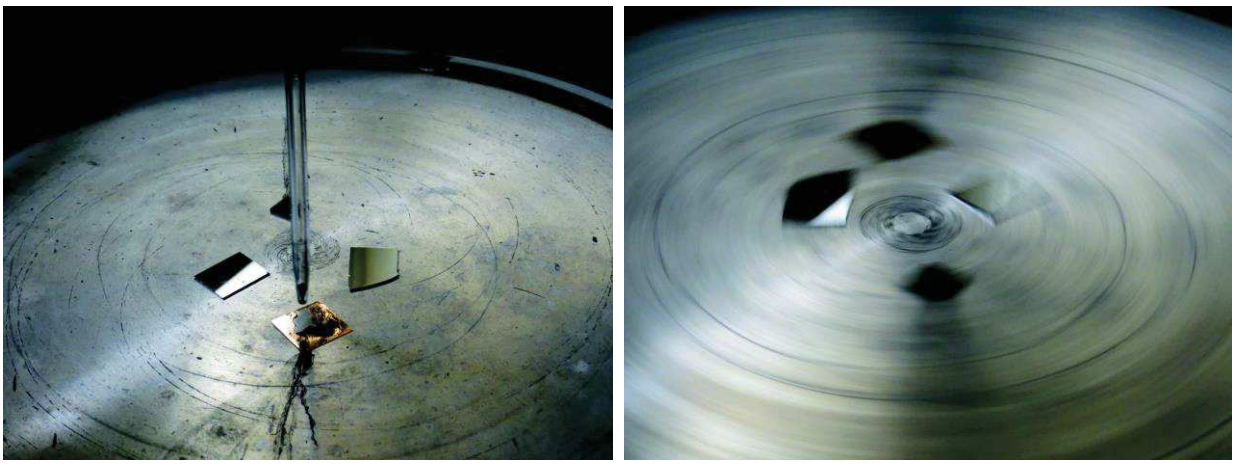

(a) (b)

Fig. 6.6 Procédé de l'induction centrifuge pour films minces de SWCNT (a) processus de distribution statique, (b) étapes de l'induction centrifuge.

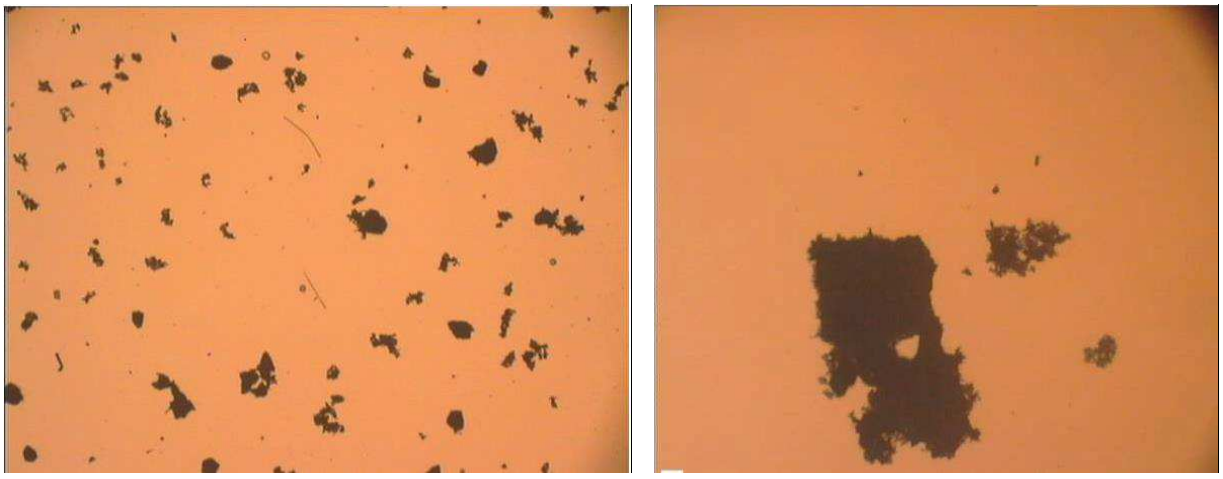

(a) (b)

Fig. 6.7 Les images au microscope de nanotubes distribués sur des substrats de silicium

6.2.3.2. Nanoindentation

Des essais expérimentaux de SWCNT films ont été réalisés sur la plate-forme de système de nanoindentation. Le système offre une résolution de charge 1 nN et le déplacement 0.0002 nm séparément, les plages de mesure de l'épaisseur des films est plus de 200 nm. La pointe utilisée sur notre appareillage est une pointe Berkovich (géométrie pyramidale à base triangulaire). La température ambiante du test est contrôlée à 25º ± 1º. Le système d'essai a été placé sur une chambre isolée en vibration libre comme représenté sur la Fig.8. La surface de l'échantillon est d'abord numérisée, puis une zone relativement grande et uniforme du film sur le substrat a été choisie pour les d'essai. Les indentations ont été faites à dix-huit nœuds

différents sur la zone choisie. Table1 présente les paramètres de réglage dans la procédure de retrait.

Table1. Les paramètres de réglage dans la procédure d'indentation

La charge maximum	3.0000mN
La charge d'arrêt de limite	0.1500 mN
Le chargement initial	0.0500 mN
Taux de chargement	0.1000 mN/s
Taux de déchargement	0.1000 mN/s
Indentations	18
Période de maintien à la charge maximale	5s

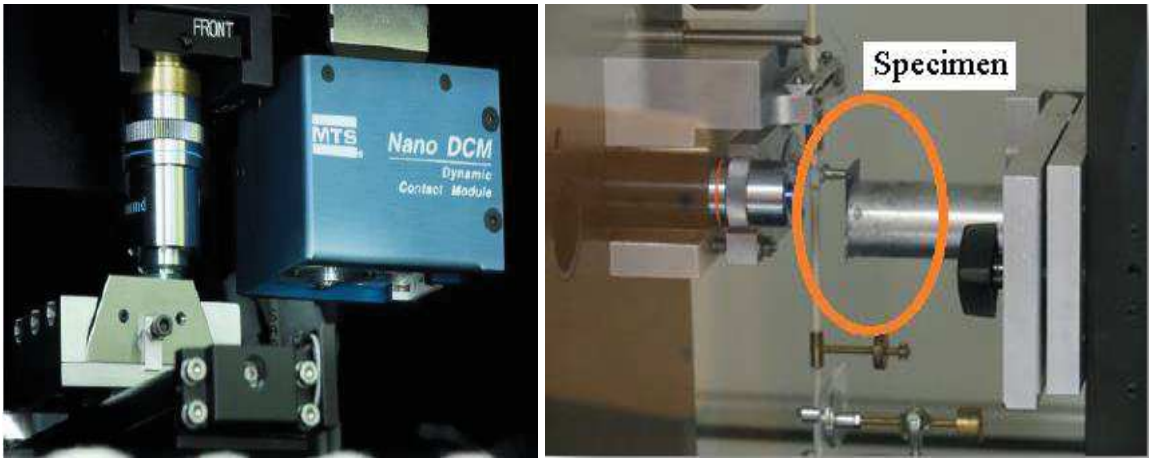

Fig. 6.8 Système de Nanoindentation

6.2.3.3. Les résultats expérimentaux

La dureté et le module élastique sont la moyenne des 18 indentations sur les différentes positions de la surface testée. Doerner et Nix ont observé que pour certains matériaux, les premières portions de courbes de déchargement sont linéaires (Doerner & Nix 1986), la rigidité de déchargement est ensuite liée à la zone de contact par le module et la relation équivalente à l'équation suivante.

$$S = \frac{dP}{dh} \tag{6–5}$$

$$= \frac{2}{\sqrt{\pi}} E_r \sqrt{A}$$

où S = dP/dh est la rigidité de déchargement initial obtenu par la partie initiale des données de déchargement, 'A' est la surface projetée du contact élastique, et il a été calculée en utilisant une fonction polynomiale d'ordre 2 dans l'expérience. Dans cette étude, la dureté et le module élastique ont été déterminé en utilisant la méthode de la loi de puissance raccord entre 100% et 20% de déchargement données.

$$p = \alpha(h - h_f)^m \tag{6–6}$$

L'aperçu général des résultats expérimentaux pour les 18 groupes de courbes de charge-déplacement sont présentés dans Fig. 6.9.

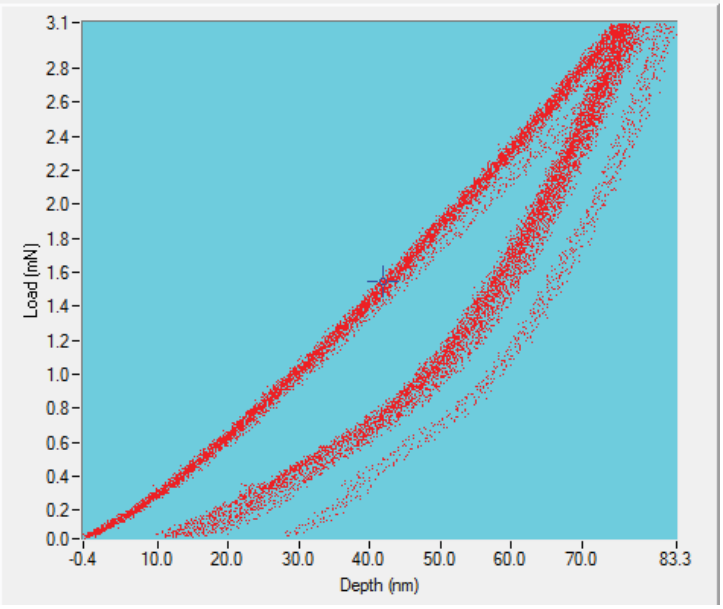

Fig. 6.9 La aperçu général des résultats expérimentaux

Table 2 Résultat de la Nanoindentation

Charge maximum (mN)	3.054 ± 20.007
Profondeur maximale (nm)	77.68 ± 2.06
la dureté (GPa)	12.57719 ± 0.759
Module réduit (GPa)	169.81778± 4.911
Le module d'Young (GPa)	192.83± 13.922

Dans ce chapitre, les incertitudes sur de propriétés élastiques de SWNT film mince dans le test de nanoindentation sont calculées. Les courbes de charge-déplacement pour la partie supérieure de 70% du processus de déchargement ont été caractérisées en utilisant la méthode de simulation de Monte Carlo. Fig.10 présente la comparaison de les courbes charge-déplacement de la partie supérieure du processus de déchargement entre le expérimental et la simulation avec une taille d'échantillon de 1,000. Fig.10 indique que les courbes expérimentales sont rigoureusement à l'intérieur de l'intervalle de confiance de 95% des résultats de la simulation numérique.

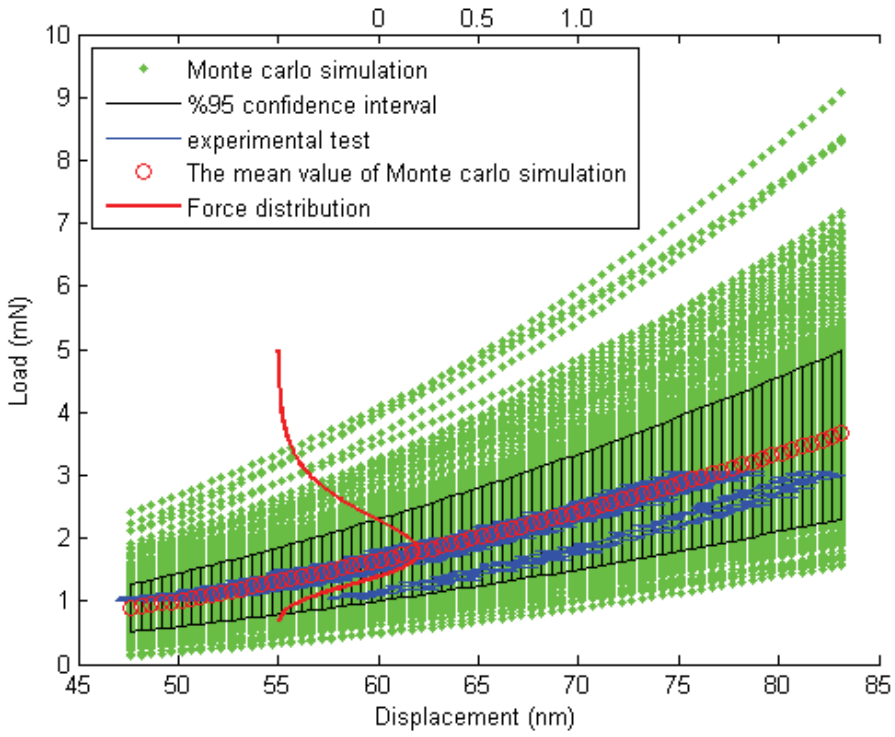

Fig. 6.10 la comparaison de courbe charge-déplacement déchargement pour la simulation et expérimental

L'incertitude de la dureté et le module de Young du film SWCNTs par le test de nanoindentation sont également déterminés dans ce chapitre. Les résultats montre que l'incertitude normalisée sur la dureté correspond à un niveau de confiance de 95% est 12.07%. L'incertitude sur le module réduit correspondant à un niveau de confiance de 95% est de 10.64%.

6.2.4. Le quatrième chapitre: Électrostrictifs propriétés de composite à base de SWCNT

Dans le chapitre 4, nous avons étudié les propriétés électrostrictif des composites à base de fluorure de polyvinylidne et de trifluoroéthylène P (VDF-TrFE) et SWCNT (SWCNT / P (VDF-TrFE)). Un modèle d'éléments finis 3D est proposé de prévoir la déformation de la électrostrictif SWCNT / P (VDF-TrFE) composite sous champ électrostatique.

6.2.4.1. Modèle numérique

Cette analyse numérique est basée sur l'expérimentation de Monsieur El Hami (El-Hami & Matsushige 2005), (El-Hami & Matsushige 2003). Ses les travaux montre que le composite SWCNT / P (VDF-co-TrFE) a été préparé avec une bonne propriété physique. La représentation de la SWCNT composite dans la Fig. 6.11 (a) indique comment les SWCNT sont incorporés dans le P (VDF-co-TrFE) dans l'état des liasses.

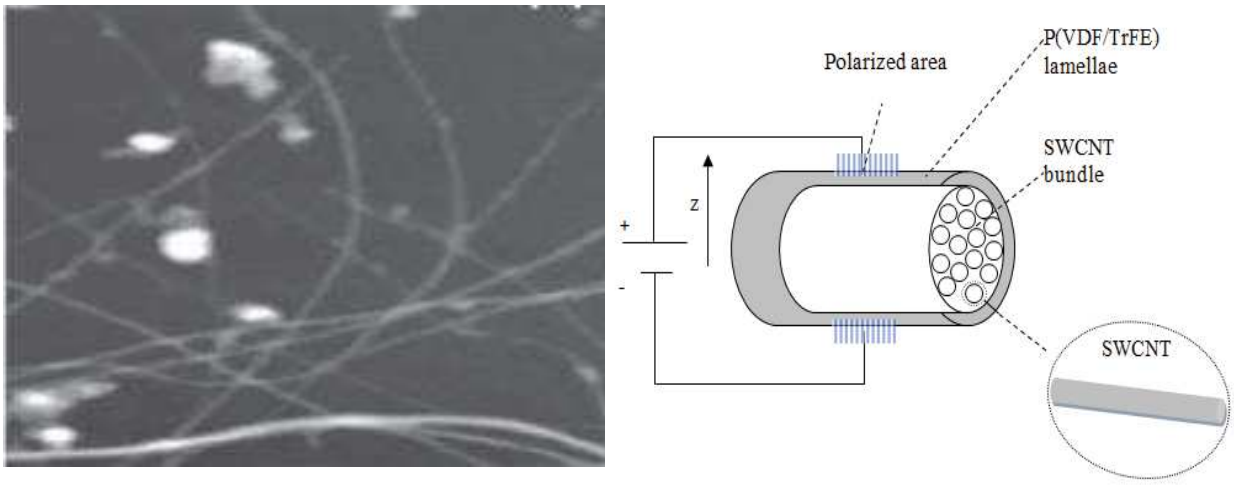

(a) (b)

Fig. 6.11 (a) l'image de topographie de SWCNT Bundles, la zone de numérisation: 1000×1000 nm^2 (El-Hami & Matsushige 2003), (b) Illustration schématique des SWCNT liasse couverte par P (VDF-TrFE) lamelles avec des domaines de polarisation visibles.

Dans ce travail, nous supposons que le SWCNT individuel est aligné dans la matrice de copolymère P (VDF-TrFE), comme illustré sur la Fig. 6.11. Et l'un des SWCNT individul et sa matrice de copolymère entouré proviennent du composite en tant que cible d'analyse. Généralement, la rigidité et la distribution électrique déposé des composites dépendent des phénomènes de contact. Pour évaluer les déformations sous champ électrique de ces composites on doit étudié le comportement de la zone de contact.

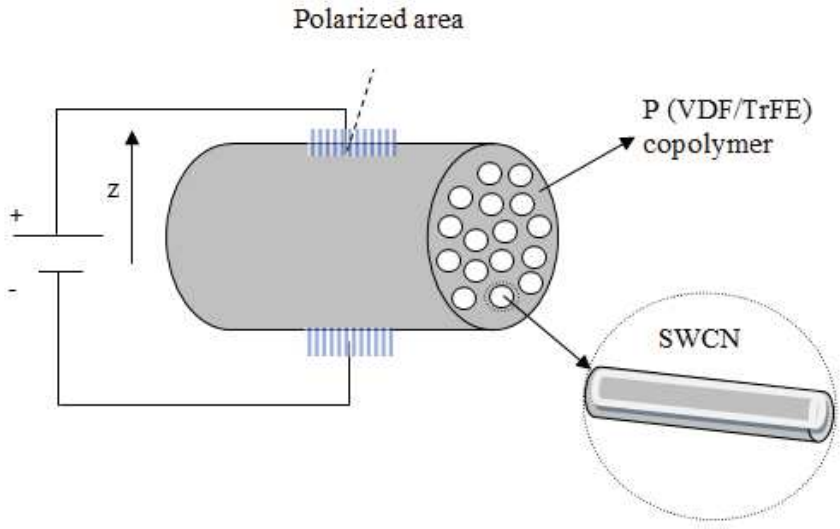

Fig. 6.12 Illustration schématique de SWCNT individuel aligné dans la P (VDF-TrFE) matrice de copolymère

Le modèle d'éléments finis développé dans cette étude est basé sur le code ANSYS (ANSYS 2005). L'analyse électrostatique est effectuée. La structure est symétrique autour de l'axe-Z. Le modèle d'éléments finis et les conditions aux limites du composite sont présentés dans la Fig. 6.12.

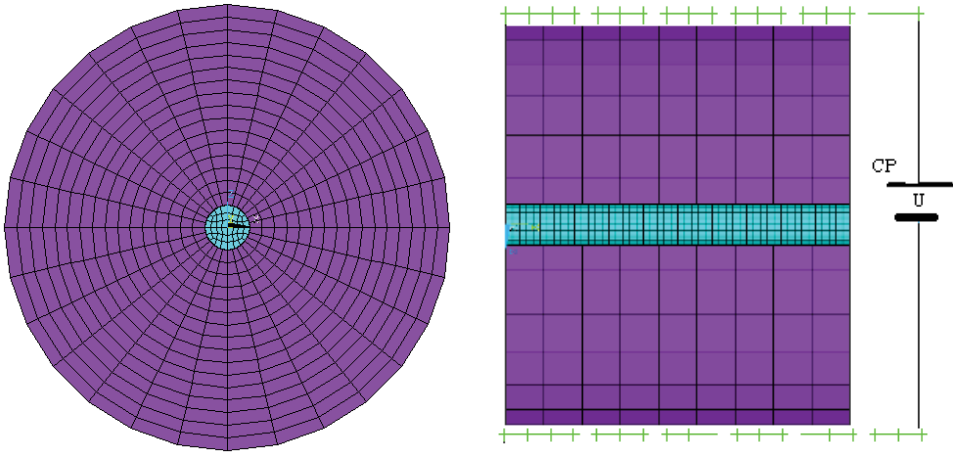

Fig. 6.13 Le modèle éléments finis de la SWCNT / P (VDP-TrFE) composite

Le modèle de contact - surface - contre surface est appliqué dans ce travail, ce qui est illustré sur la Fig. 6.13. La force d'adhérence interfaciale entre les SWCNT et la matrice est supposé être en moyenne sur la longueur du composite. La raideur de la liaison est supposée être assez forte qu'il n'y a aucune décohésion sous l'excitation électrique. La raideur de contact est mise à jour après chaque itération basée sur la condition initiale de l'interface. L'interaction entre les SWCNT et la matrice de copolymère P (VDFTrFE) est déterminée par les propriétés dès l'élément de contacts / élément cible paires.

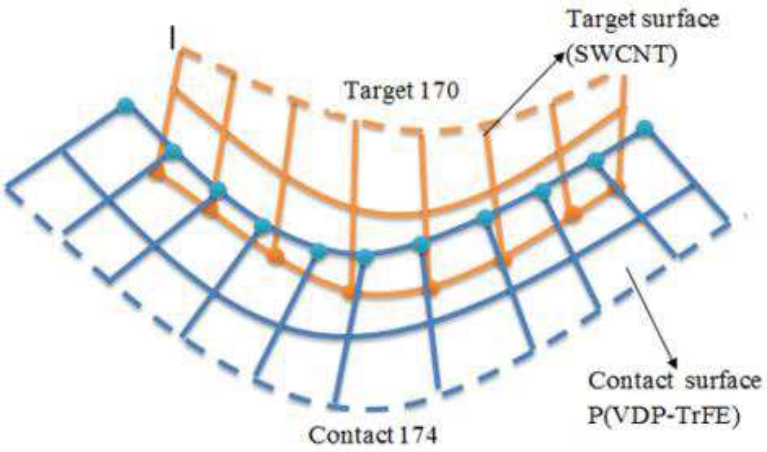

(a)

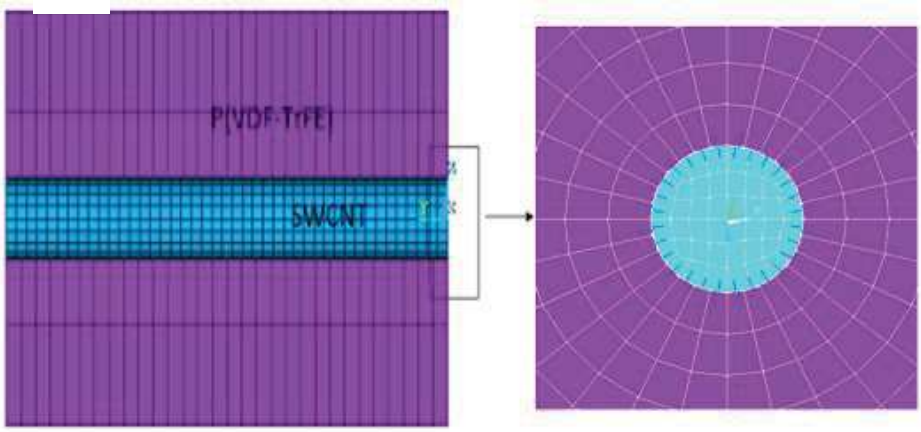

(b)

Fig. 6.14 (a) La configuration de la SWCNT / P (VDP-TrFE) Interface (b) Le modèle éléments finis de SWCNT / P (VDP-TrFE) interface.

6.2.4.2. Numerical results and discussion

Dans ce travail, la conductivité de SWCNTs est adopté comme le carbone commerciale de 285 Scm^{-1} (Li et al. 2007). Les modules d'élasticité et les constantes diélectriques des SWCNT estimées à partir des littératures (Lu 1997), (Baowan & M. Hill 2007), (Kozinsky & Marzari 2008). Les propriétés constantes élastiques et électriques de P (VDF-TrFE) sont obtenus à partir des littératures (Rao & Li 2004) et (Lonjon et al. 2010). La capacité du Interface de P (VDF-TrFE) / SWCNT est obtenu à partir de la littérature K.J.LohetJ.Kim (Loh et al. 2008).

- **L'effet de la fraction volumique des SWCNTs**

L'effet de la fraction volumique des SWCNTs pour l'électrostriction du composite est étudiée dans un premier temps. La souche d'épaisseur S33 de composite avec la fraction volumique de SWCNT de 0.5 vol% à 10 vol% en volume sont tracées dans la Fig. 6.15. Les

résultats démontrent que les souches augmentent de façon non linéaire avec la fraction volumique de SWCNT. Ce résultat est en accord avec l'étude de Junhee Kim et Kenneth J.Loh (J. Kim et al. 2008), que les SWCNT / P (VDP-TrFE) composites démontrer des constantes diélectriques plus élevées que la ferroélectricité P (VDP-TrFE), qui est dependendent sur la fraction pondérale de CNT.

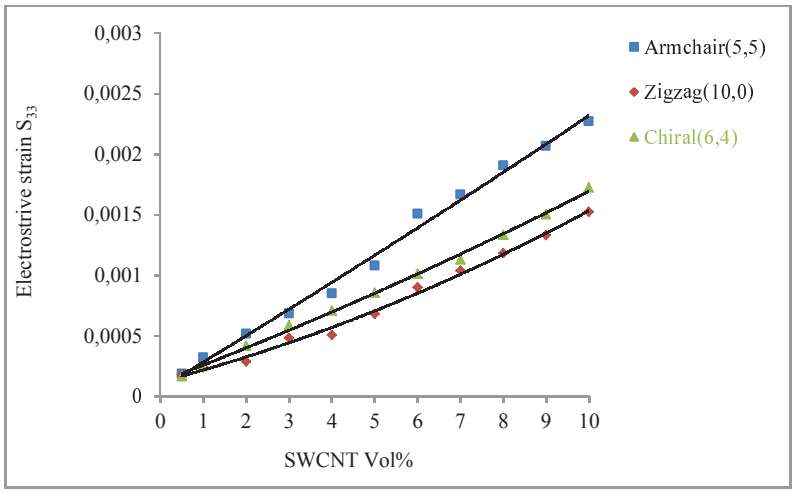

Fig. 6.15 La déformation du composite électrostrictif SWCNT / P (VDP-TrFE) avec la fraction de SWCNT. Les lignes continues sont aptes quadratique.

- **L'effet du champ électrique**

La variation de electrostrictions pour les composites à base de SWCNTs Fauteuil (5, 5), Zigzag (10, 0), et chiral (6, 4) avec le champ électrique respectés ont étudié. Car nous supposé qu'il n'y a pas décohésion entre SWCNT et P (VDP-TrFE) sous la force électrique, nous applieda série de relativement faible champ électrique au matériau composite. Fig. 6.16 représente les souches électrostrictives des composites SWCNT / P (VDF-TrFE) sous champ électrique. Il démontre que les souches augmentent linéairement avec le champ électrique.

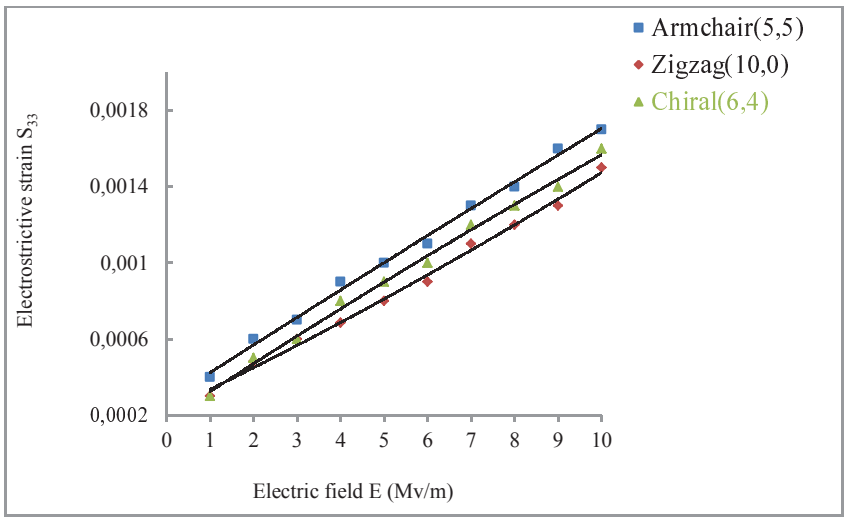

Fig. 6.16 La déformation de la électrostrictif de composite SWCNT / P (VDP-TrFE) avec le champ électrique. Les lignes continues sont ajustement linéaire.

De Fig. 6.15 et Fig. 6.16, nous trouvons que la fraction volumique des SWCNT a plus d'influence sur la électrostriction du composite SWCNT / P (VDP-TrFE) que le champ électrique. Cela pourrait se expliquer à: (a) la variation de la constante diélectrique du matériau composite causés par différentes structures de SWCNT, (b) intension de champ électrique dans le composite en raison de la seconde phase.

Fig. 6.17 illustre la répartition du champ électrique dans 0.5vol% fauteuil (5, 5) SWNT / P (VDF-TrFE) composite. Fig.16 (a) et (b) montrent que la force des champs électriques à l'interface est supérieure à centuple le bord du composite. Cette observation peut se expliquer par le travail de Takuma et T., Kouno's (Takuma & Techaumnat 2010).

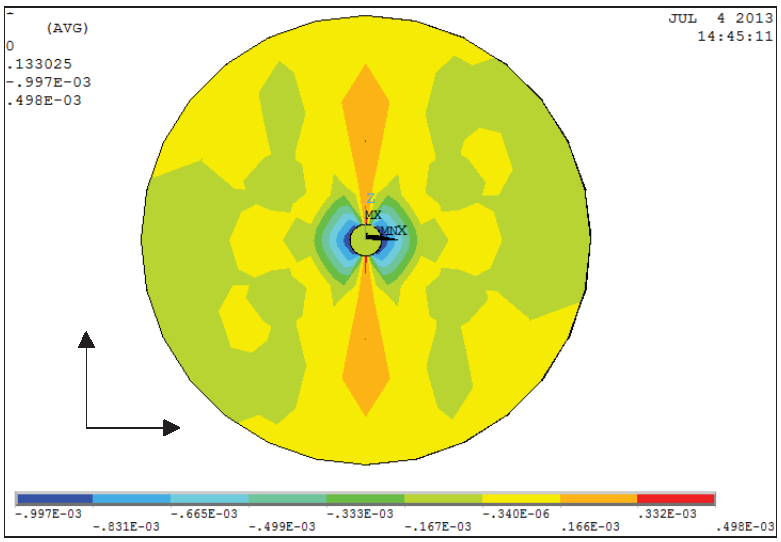

(a)

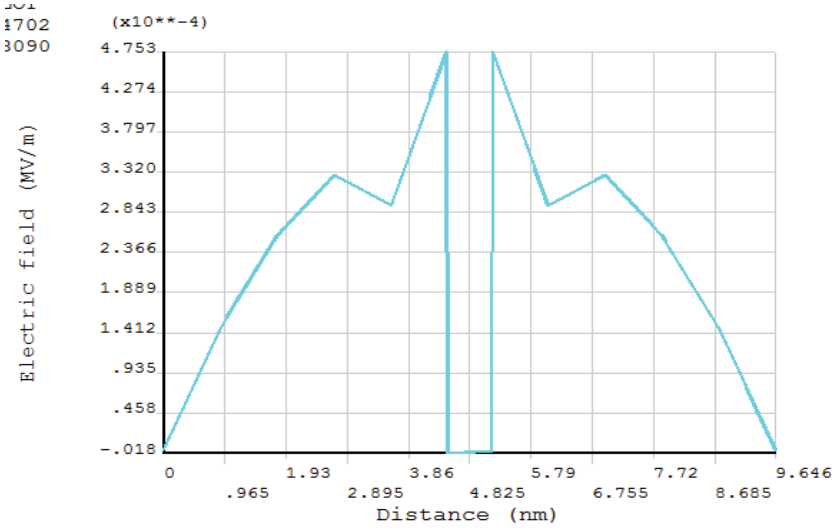

(b)

Fig. 6.17 La distribution de champ électrique dans le composite à base de 0.5vol% fauteuil (5, 5). (a) La composante z de la distribution de champ électrique, (b) la répartition de champ électrique sur l'axe de symétrie z.

- **L'effet de chiralité**

De Fig.15 et Fig.16 nous pouvons également conclure que les composites présentent des diamètres approximatifs mais de chiralité différente de SWCNT, le fauteuil (5, 5) / P (VDP-TrFE) composite possède la plus grande déformation électrostrictif, tandis que, Zigzag (10,0) / P (VDP-TrFE) composite présente la plus petite déformation électrostrictif dans le même champ électrique externe et la fraction volumique de SWCNT. Ce sont surtout en raison de la différence des constantes diélectriques entre SWCNT et P (VDF-TrFE). Les constants diélectriques statiques de SWCNT et le rapport des deux constantes diélectriques sont répertoriés dans le tableau 3. En comparant le rapport des constantes diélectriques pour SWCNT à P (VDP-TrFE), que nos résultats sont bien d'accord avec l'analyse théorique composite diélectrique dans la littérature (Takuma & Techaumnat 2010).

Table 3 le constante diélectrique statique de SWCNT de (Guo et al. 2004) et le constante diélectrique P (VDF-TrFE) de (Baowan & M. Hill 2007).

	ε_{xx} (ε_{zz})	ε_{yy}	$\varepsilon_{xxCNT}/\varepsilon_p$
Armchair (5, 5)	16	34.1	16/11
Zigzag (10, 0)	8.2	26.8	8.2/11
Chiral (6, 4).	7.3	22.1	7.3/11
P(VDP-TrFE)	11	11	

- **Conclusions**

Les résultats numériques indiquent que l'électrostriction de SWCNT / P (VDP-TrFE) composite est fortement dépendante de la fraction volumique de SWCNT et les différences de constante diélectrique entre les SWCNT et P (VDP-TrFE). Alors que, la constante diélectrique du SWCNT est dépendant de la chiralité des SWCNT, qui fournissent un guide numérique pour la conception et l'optimisation pour SWCNTs base nano-composites et autres composite électrostrictif.

6.2.5. Le cinquième chapitre: Modèle bilinéaire pour la SWCNT film

Dans le chapitre 6, les propriétés élasto-plastique de la SWCNTs mince film sous indentation ont été estimées en combinant la technique des éléments finis avec le teste de nanoindentation. RBO méthodologie est appliquée pour assurer la fiabilité de l'estimation. Dans cette étude, la distribution de la courbe charge-déplacement dans le processus de déchargement est considérée dans l'analyse de la fiabilité.

6.2.5.1. Le SWCNT thin film

Selon l'analyse des cycles complets de charge-décharge de l'indentation de film SWCNT, on approche le comportement élasto-plastique du film SWCNT par une description linéaire. Son véritable comportement contrainte-déformation est supposé suivre le modèle bilinéaire:

$$\sigma = \begin{cases} E\varepsilon, & for\ \sigma \le \sigma_Y \\ \sigma_Y + E_t(\varepsilon - \varepsilon_Y), & for\ \sigma \ge \sigma_Y \end{cases} \tag{6–7}$$

où σ_Y et ε_Y sont la limite d'élasticité et la souche respectivement, et $\varepsilon_Y = \sigma_Y/E$; E est le module d'Young, et E_t est le module tangent.

Sur la base du modèle élasto-plastique linéaire présenté et la transition de phase dépendant de la pression, le module réduit E_r en cours de déchargement est modifié (Fig. 6.18), Le module réduite de la phase 2 peut être exprimée comme analogiquement:

$$E_r^* = \frac{1}{2}\frac{\sqrt{\pi}}{\sqrt{A}}\frac{dP}{dh}|_{\text{phase2}} \tag{6–8}$$

où E_r^* est le module réduite de la phase 2, $\frac{dP}{dh}|_{\text{phase2}}$ est la pente de la dernière partie de la courbe de déchargement. D'après la mécanique du contact, le module tangent E_t peut être obtenu par :

$$\frac{1}{E_r^*} = \frac{(1-v^2)}{E_t} + \frac{(1-v_i^2)}{E_i} \tag{6–9}$$

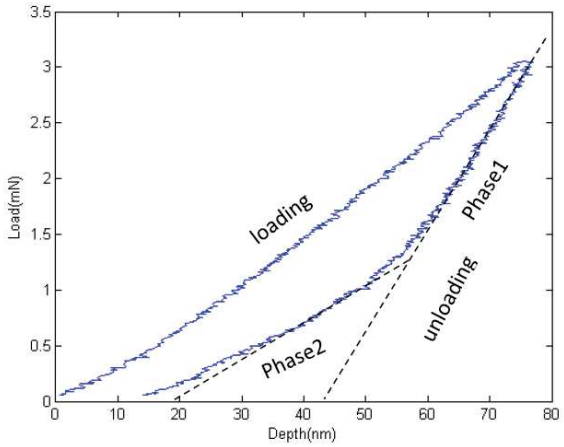

Fig. 6.18 l'illustration d'une réaction de charge - déplacement du film mince de SWCNT dans le nanoindentation

En raison de la complexité due à changement de phase dans sa morphologie, nous décrivons la relation charge-déplacement (p-h) du film de SWCNT dans indentation implicitement:

$$P = P(h, E_r, \sigma_y, E_t, \theta) \tag{6–10}$$

où θ est l'angle au sommet de l'inventeur.

Le programme pour l'évaluation des propriétés des matériaux est réalisé par la fiabilité - basée de calcul par éléments finis. La courbe de déchargement de charge - déplacement obtenu par simulation de éléments finis doivent en cohérence avec le résultat testé qui a démontré dans le chapitre 3:

$$\min: \ \left\| p^i - \overline{p}_t \right\| \tag{6–11}$$

Sous:

$$\left| \frac{\overline{h}_{max} - h^i_{max}}{\overline{h}_{max}} \right| \leq \Delta_1 \tag{6–12}$$

$$\left| \frac{\bar{s} - S^i}{\bar{S}} \right| \leq \Delta_2 \tag{6–13}$$

où p^i est le vecteur de la charge à l'itération ième, $\overline{p}_t$ est le vecteur de la charge moyenne dans indentation teste, et la répartition des p_t est démontré dans le chapitre 3. $\overline{h}_{max}$ et $\bar{s}$ ont valeur moyenne de déplacement maximal et la raideur de contact, séparément. Δ_1, Δ_2 sont la contrainte de variation de h_{max} et S, qui dépendent de la répartition de la charge - distribution de test expérimental démontré dans le chapitre 3. La procédure d'évaluation est illustrée sur la Fig. 6.19.

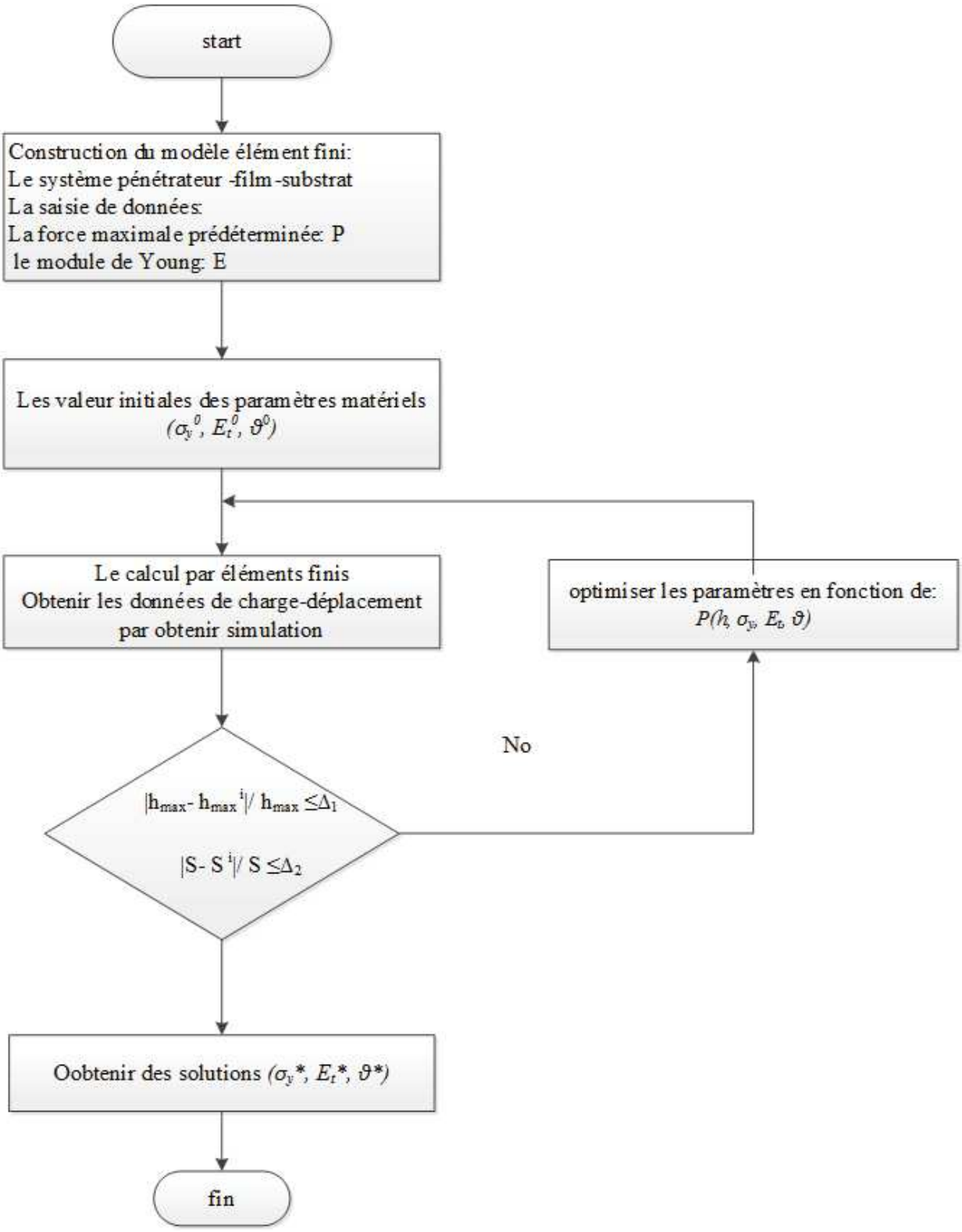

Fig. 6.19 Organigramme de la procédure d'analyse proposé de déterminer les propriétés mécaniques des SWCNT film mince par indentation et la simulation de FE

6.2.5.2. Modèle numérique des SWCNT film mince

- **les propriétés initiales des matériaux**

Le module de Yong et le coefficient de Poisson de l'indenteur et le substrat de silicium sont respectivement prises comme 1.143 GPa et 0.07 (Klein & Cardinale 1993), 180 GPa et 0.278 (Hopcroft et al. 2010). Le module de SWCNT film mince de Young est originaire de résultats de tests de nanoindentation que 192.83±13.922 GPa; la valeur initiale de la limite d'élasticité Y_0 est dérivé de l'équation empirique de la relation entre la dureté Vickers du matériau et la limite d'élasticité (Tabor 1956),(Larsson 2001), (Busby et al. 2005).

$$H_v \cong KY \tag{6–14}$$

où H_v est la dureté de la matière plastique, Y est le stress de rendement, K=1.5 ~ 3 est une constante qui dépend de la géométrie de sertissage et les propriétés des matérielles. La dureté moyenne de film SWCNT ici est 12.57719 ± 0.759 GPa selon les résultats expérimentaux. K_0=3, donc la valeur initiale de la limite d'élasticité est prise Y_0=4.2 GPa. Le module tangent E_t est initialement calculé en fonction des équations (7-3) et (3-3) de la partie inférieure de déchargement informations qui est d'environ 42 GPa. En tant la ration du poission de matériel retrait a faible incidence sur la vue d'ensemble de la courbe de charge – distribution, nous supposons que la ration du poission du film SWCNTs ne change pas au cours du processus d'indentation et de l'adopter à partir de littérature $v = 0.18$ (Hall et al. 2008).

- **FEM model construction**

Dans ce travail, les calculs ont été effectués en utilisant le paquet des éléments finis ANSYS (Canonsburg 2009). Le matériau de critère "Von Mises à écrouissage isotrope bilinéaire" est utilisé pour extraire approximativement les propriétés plastiques du film mince de SWCNT. L'indenteur, le film mince de SWCNT et le substrat sont maillés par un 20 node 3-D élément solide. L'interaction de l'indenteur et le spécimen est modélisée comme un contact pair surface-surface sans friction. L'interface entre le film et le substrat a été supposé être perfectionné collé. Les mailles proches de l'indenteur ont été affinées pour décrire la déformation et le stress gradient avec précision, comme représenté sur la Fig. 6.20. Une force moyenne est appliquée en continu sur la surface supérieure de l'indenteur dans la direction z, tous les degrés de liberté pour les nœuds inférieurs de substrat sont fixés. La valeur maximale prédéterminée de la force est définie en tant 3mN selon l'expérience. La grande déformation de calculs FEM a été réalisée sous le processus de chargement et de déchargement en continu.

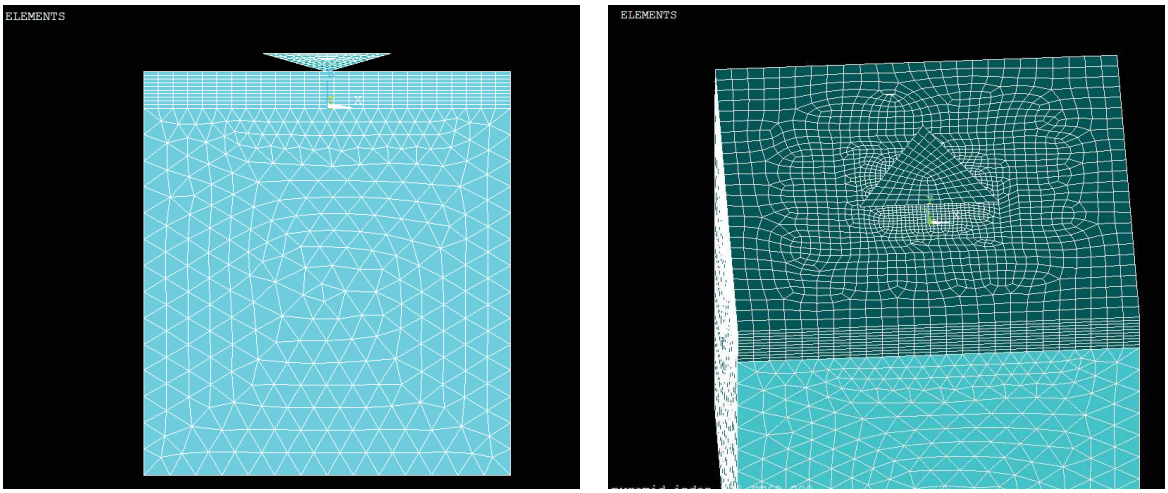

(a) (b)

Fig. 6.20 FE-modèle du système pénétrateur-film-substrat

6.2.5.3. Résultats numériques

Fig. 6.21 est la comparaison des résultats typiques d'essai avec des résultats de simulation. La comparaison démontre que, avec la même force maximale prédéterminée le résultat de la simulation présente une beaucoup plus grande déformation (environ 40% plus grande).

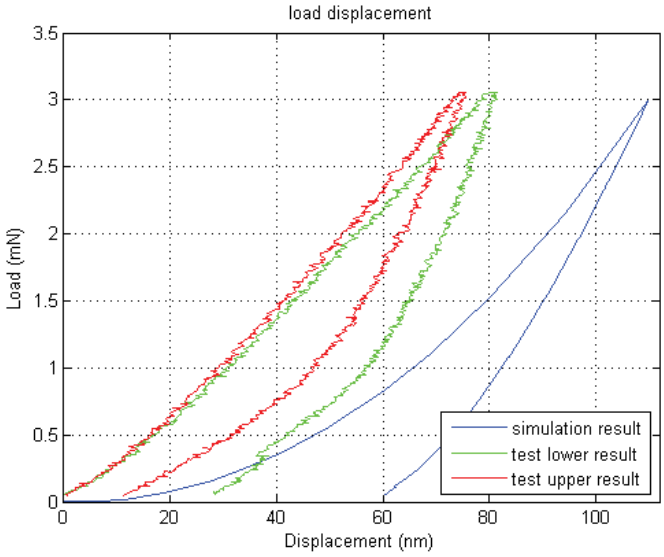

Fig. 6.21 Comparaison des résultats des tests avec des résultats de simulation

Comme présenté dans le chapitre 3, les erreurs et les incertitudes de nanoindentation peuvent être causées par les propriétés du matériau testé et l'indenteur. Un des facteurs importants est la forme de l'indenteur. La forme d'un indenteur véritable ne pourra jamais être idéale pointu, mais émoussé dans une certaine mesure. Cette déviation est importante, surtout pour les très petites profondeurs de pénétration (Chen & Chang 2007). Ce qui est plus l'angle réel peut différer légèrement de la valeur nominale, et même varier avec la profondeur

(Menčík 2012). Par conséquent, une calibration de la zone doit être faite pour estimer la zone de contact projetée en fonction de la profondeur de contact A=A(h_c). Un autre facteur important est l'effet de substrat, ce qui peut entraîner des problèmes qu'on appelle pile-up ou subsidence (Saha & Nix 2002). Fig. 6.22 ~ Fig. 6.24 sont les distributions des déformations et le stress pour le système SWCNT film – substrate. Fig. 23 ~ Fig. 24 indiquent que le déplacement du indenteur est les déformations combinatoires de SWCNT film et le substrat de silicium.

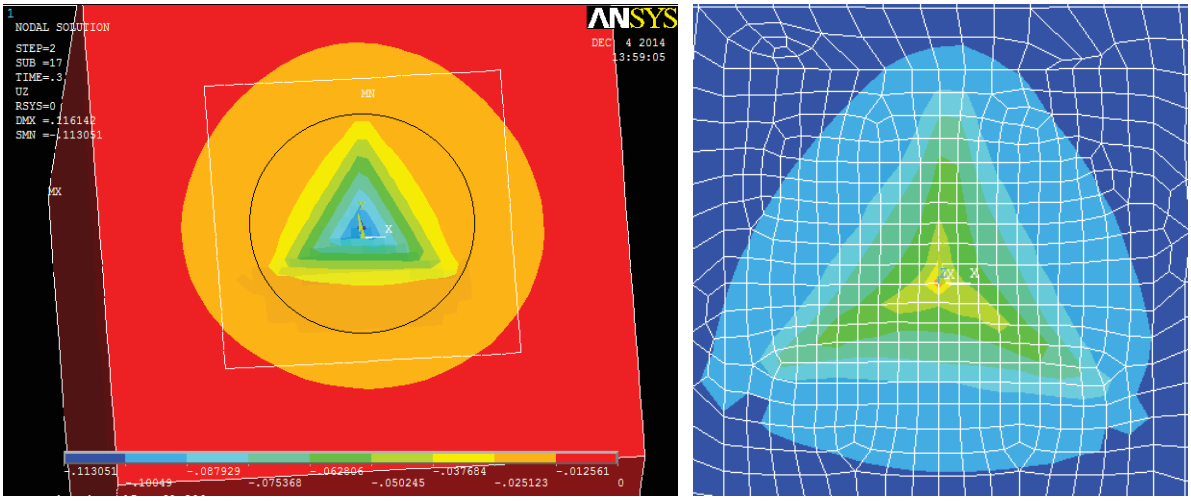

Fig. 6.22 Deformation of the SWCNT film-substrate system

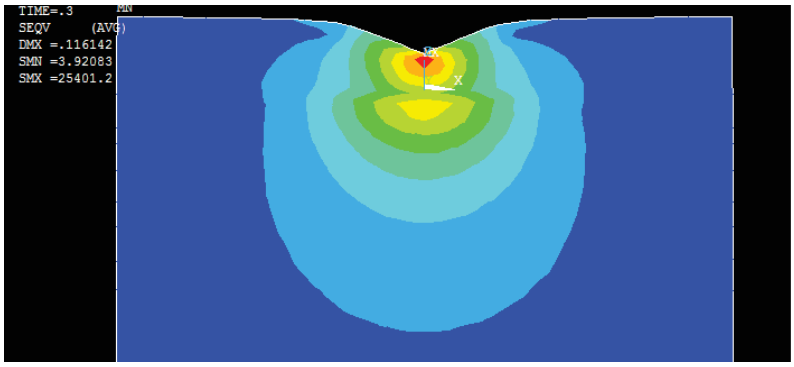

Fig. 6.23 Stress distribution of the SWCNT film-substrate system

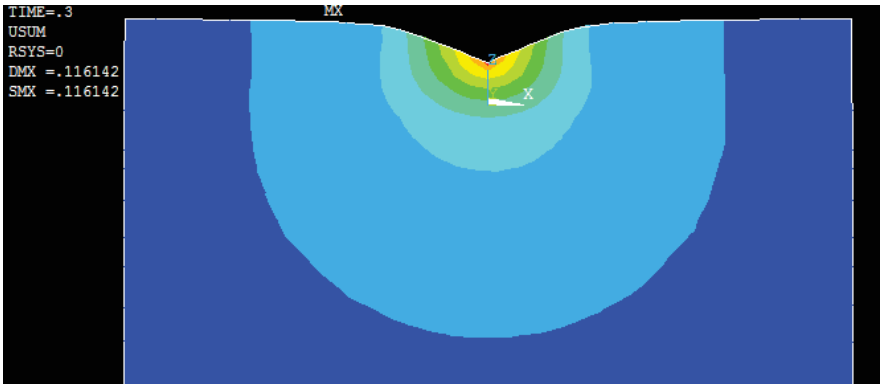

Fig. 6.24 Strain distribution of the SWCNT film-substrate system

Les effets de forme de l'indenteur, l'épaisseur du film mince, et le module d'Young de substrat de silicium sont analysés. Figue. 26 représente les comparaisons de la performance de SWCNT film mince sous différents paramètres de réglage avec la même charge maximale. La comparaison de la Fig. 6.25 indique que la forme de l'indenteur dispose beaucoup plus grand effet sur les performances de charge déplacement de matière (environ 21,3%) que l'effet de l'épaisseur du film et les variations de module d'Young de substrat, qui sont environ 4,7% et 7%.

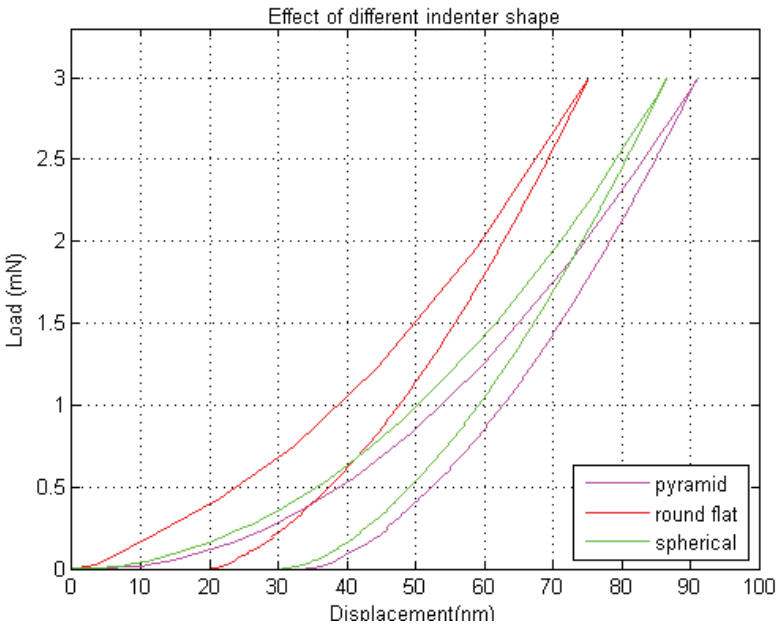

(a)

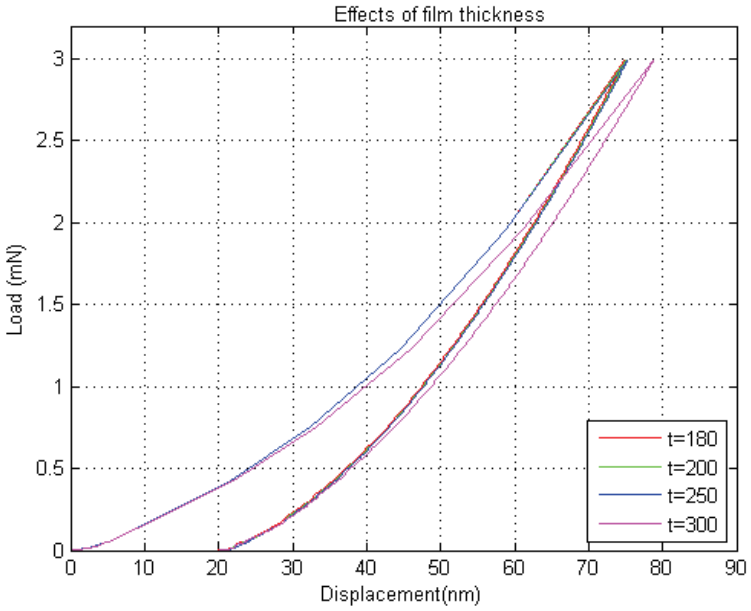

(b)

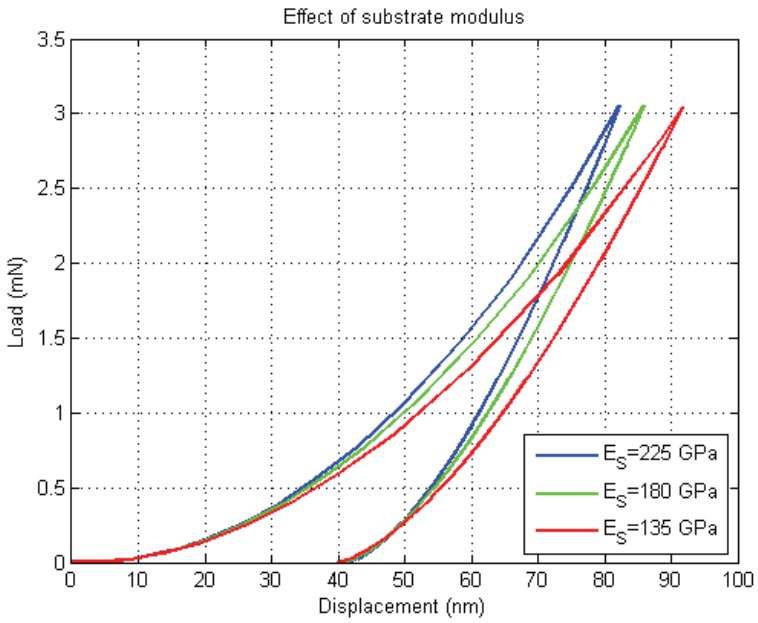

(c)

Fig. 6.25 Les comparaisons des performances du SWCNT film mince sous différents paramètre : (a) Les effets de indenteur forme différente; (b) Les effets de l'épaisseur de SWCNT film; (c) Les effets du module d'Young de substrat en silicium.

Le défaut de l'indenteur affecte directement la zone de contact prévu dans indentation, nous compensons les erreurs de l'indenteur en simulation FE par la mise à jour de l'angle du sommet de l'indenteur par des approximations de (3–17) et (5–53):

$$A_{proj} = c_2 {h_c}^2 + c_1 h_c + c_0 = 3\sqrt{3} {h_c}^2 tan^2\theta \qquad (6\text{–}15)$$

D'après l'estimation projetée des contacts (zone A) dans le chapitre 3 et le chapitre 5, θ est d'environ 70 ° C. Tableau 4 présente le résultat d'itération de simulations FE. Il démontre qu'après cinq itérations les données de simulation bien en adéquation avec les résultats expérimentaux (Fig. 6.26).

Table 4 Les résultats d'itération de simulations FE

Parameters / Items		θ °C	σ_y (Gpa)	E_t (Gpa)	h_{max}		$\frac{dp}{dh}$	
					h_{max} nm	Δ_1	$\frac{dp}{dh}$ mN/nm	Δ_2
Mean value of experiment test		–	–	–	77.68	–	0.0963	–
FE simulation	Iteration 1	65.3	4.2	42	108.881	40.17%	0.0867	9.97%
	Iteration 2	70	4.2	42	87.59	12.76%	0.10845	12.62%
	Iteration 3	70	2.1	42	90.4407	16.43%	0.114	18.38%
	Iteration 4	70	8.385	21	85.903	10.6%	0.10256	6.5%
	Iteration 5	70	8.385	31.5	84.6446	8.97%	0.10098	4.86%
	Iteration 6	70	8.385	42	82.8116	6.61%	0.09858	2.37%

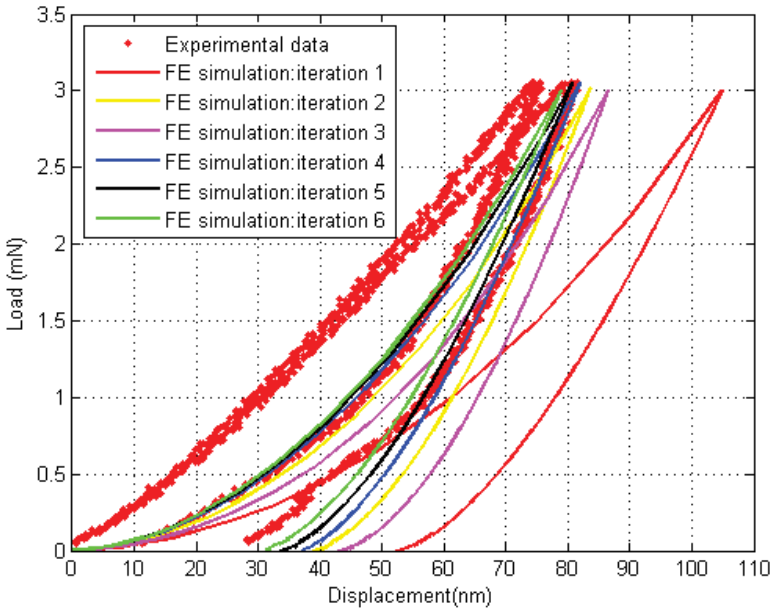

Fig. 6.26 Les comparaisons des courbes de charge-déplacement pour l'expérience et les simulations FE

Fig. 6.27 illustre la distribution des données de déchargement pour l'expérience, simulation de Monte Carlo et des simulations FE. Fig. 6.27 démontre que les résultats numériques se intègre bien les résultats d'indentation.

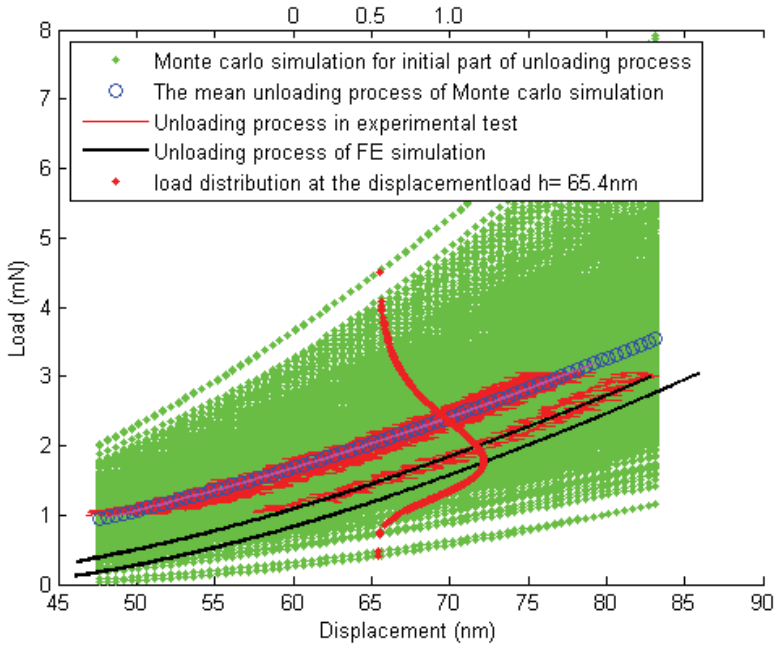

Fig. 6.27 Déchargement courbes distribution pour expérimentation, simulation de Monte Carlo et des simulations FE

6.3. Conclusion et perspectives

Les propriétés mécaniques et électromécaniques de SWCNTs sont deux des questions les plus importantes dans les applications d'ingénierie (capteur, les puces électroniques, réacteur, etc.). La contribution de ce travail est de fournir aux lecteurs les informations sur les propriétés mécaniques et électromécaniques des matériaux de SWCNT avec différentes morphologie.

Nous proposons quelques perspectives :

1. Les différentes propriétés d'un CNT individuel sont en interaction. Par exemple, la déformation mécanique de NTC peut provoquer des changements considérables dans ses propriétés électroniques, optiques, magnétiques et chimiques (Shima 2011). Ils présentent un couplage entre les propriétés électriques et les déformations mécaniques (Tombler et al. 2000). Pour plusieurs applications concrètes et pour certaines demandes de haute précision, ces propriétés sont instables et doivent être bien étudiés.

2. Les CNT en composite ne sont pas généralement parfaitement alignées dans la matrice de copolymère. Ils peuvent être orienté ou dispersé dans la matrice sous forme de faisceaux ou de façon aléatoire. La dispersion des CNT dans la matrice pourrait être un problème critique dans les applications pratiques. Par ailleurs, La distribution de champ électrique dans le composite SWCNT/P (VDF-TrFE) est fortement dépendante des conditions de contact qui doit être bien évalué en fonction de la tension appliquée.
3. Comme on l'a démontré dans le chapitre 5, le film mince SWCNT présente un comportement de transformation de phase dans le processus de nanoindentation. Cela signifie que les microstructures de SWCNT film mince peuvent avoir un changement significatif sous la pression hydrostatique. Le critère de la contrainte hydrostatique pourrait être essentiel dans des applications pratiques.

Ces problèmes mentionnés ci-dessus existent généralement pour des applications de CNT. En raison de la diversité et de la variabilité des propriétés des matériaux, un bon contrôle de la performance des matériaux est difficile. La méthode RBO que nous avons présenté intègre les incertitudes sur les paramètres du modèle présenté.

Reference

A. E. Giannakopoulos and S. Suresh, 1999. Determination of elastoplastic properties by instrumented sharp indentation. *Scripta Materialia*, 40(10), pp.1191–1198.

Affe B, Cook Jr W, J.H., 1971. *Piezo electric ceramics*, New York: Academic Press.

Aghaei, A. & Dayal, K., 2012. Tension and twist of chiral nanotubes: torsional buckling, mechanical response and indicators of failure. *Modelling and Simulation in Materials Science and Engineering*, 20(8), p.085001.

Aliev, A.E. et al., 2010. Thermal conductivity of multi-walled carbon nanotube sheets: radiation losses and quenching of phonon modes. *Nanotechnology*, 21(3), p.035709.

American Elements, 2014. Properties, Applications, Research, and Safety Guidelines for Nanotechnology Materials. *the materials science company*.

Anon, 2002. *Biomedical Applications of Nanotechnology*.

Anon, 2013a. Category :Nanomaterials. Available at: http://en.wikipedia.org/wiki/Category: Nanomaterials.

Anon, 2014. Nonparametric skew. Available at: http://en.wikipedia.org/wiki/Nonparametric_ skew.

Anon, 2013b. Spin coating theory. , (October).

ANSYS, 2005. *Coupled Field Analysis Guide, ANSYS Release 10.0*, Canonsburg (PA).

Arora, J.S. ed., 2007. *Optimization of Structural and Mechanical Systems*, World Scientific.

Ayatollahi, M.R. et al., 2011. Effect of multi-walled carbon nanotube aspect ratio on mechanical and electrical properties of epoxy-based nanocomposites. *Polymer Testing*, 30(5), pp.548–556.

Bachtold, A. et al., 1999. letters to nature Aharonov ± Bohm oscillations in carbon nanotubes. , pp.673–675.

Bai, Y. et al., 2000. High-dielectric-constant ceramic-powder polymer composites. *Applied Physics Letters*, 76(25), pp.3804–3806.

Baker, R.T.K. et al., 1972. Nucleation and Growth of Carbon Deposits from the Nickel Catalyzed Decomposition of Acetylene. *Journal of Catalysis*, 62, pp.51–62.

Banerjee, S., Hemraj-Benny, T. & Wong, S.S., 2005. Covalent Surface Chemistry of Single-Walled Carbon Nanotubes. *Advanced Materials*, 17(1), pp.17–29.

Baowan, D. & M. Hill, J., 2007. Wave-like deformations for oscillating carbon nanotubes. *International Journal of Solids and Structures*, 44(25-26), pp.8297–8312.

Beake,] Ben et al., 2002. *Micro Materials NanoTest User Manual*,

Beek, W.J.E., Wienk, M.M. & Janssen, R. a. J., 2004. Efficient Hybrid Solar Cells from Zinc Oxide Nanoparticles and a Conjugated Polymer. *Advanced Materials*, 16(12), pp.1009–1013.

Bell, G., Robust Test Designs for Dynamic Marketing, Retail, and Advertising Programs. *Citeseer*, pp.1–8.

Belytschko, T. et al., 2002. Atomistic simulations of nanotube fracture. *Physical Review B*, 65(23), p.235430.

Ben-Tal, A. & Nemirovski, A., 2000. Robust solutions of Linear Programming problems contaminated with uncertain data. *Mathematical Programming*, 88(3), pp.411–424.

Berber, S., Kwon, Y.-K. & Tománek, D., 2000. Unusually High Thermal Conductivity of Carbon Nanotubes. *Physical Review Letters*, 84(20), pp.4613–4616.

Bertsimas, D., Brown, D. & Caramanis, C., 2011. Theory and applications of robust optimization. *SIAM review*, 53(3), pp.464–501.

Birge, J. & Louveaux, F., 2011. *Introduction to stochastic programming* Second. J. R. Birge & F. Louveaux, eds., Springer New York.

Bolotin, K.I. et al., 2004. Metal-nanoparticle single-electron transistors fabricated using electromigration. *Applied Physics Letters*, 84(16), p.3154.

Bonaccorso, F. et al., 2007. Pulsed laser deposition of multiwalled carbon nanotubes thin films. *Applied Surface Science*, 254(4), pp.1260–1263.

Boyd, S. & Vandenberghe, L., 2009. *Convex Optimization*, Cambridge: Cambridge University Press.

Bozovic, D. et al., 2001. Electronic properties of mechanically induced kinks in single-walled carbon nanotubes. *Applied Physics Letters*, 78(23), p.3693.

Brenner, D.W. et al., 2002. A second-generation reactive empirical bond order (REBO) potential energy expression for hydrocarbons. *Journal of Physics: Condensed Matter*, 14(4), pp.783–802.

Brockwell, A.E., 2007. Universal Residuals : A Multivariate Transformation ∗. *Statistics & probability letters*, 77, pp.1473–1478.

Busby, J.T., Hash, M.C. & Was, G.S., 2005. The relationship between hardness and yield stress in irradiated austenitic and ferritic steels. *Journal of Nuclear Materials*, 336(2-3), pp.267–278.

Cai, L. et al., 2013. Super-stretchable, transparent carbon nanotube-based capacitive strain sensors for human motion detection. *Scientific reports*, 3, p.3048.

Canonsburg, T.D., 2009. ANSYS Parametric Design Language Guide. , 15317(April), pp.724–746.

Cao, Q. et al., 2008. Medium-scale carbon nanotube thin-film integrated circuits on flexible plastic substrates. *Nature*, 454(7203), pp.495–500.

Cao, Q. & Rogers, J. a., 2009. Ultrathin Films of Single-Walled Carbon Nanotubes for Electronics and Sensors: A Review of Fundamental and Applied Aspects. *Advanced Materials*, 21(1), pp.29–53.

Castrup, H., 2000. Estimating category b degrees of freedom. In *In : Proc. Measurement Science Conference*.

Chan, S.-P. et al., 2003. Carbon nanotube bundles under high pressure: Transformation to low-symmetry structures. *Physical Review B*, 68(7), p.075404.

Chang, T., 2010. A molecular based anisotropic shell model for single-walled carbon nanotubes. *Journal of the Mechanics and Physics of Solids*, 58(9), pp.1422–1433.

Chang, T., 2007. Torsional behavior of chiral single-walled carbon nanotubes is loading direction dependent. *Applied Physics Letters*, 90(20), p.201910.

Chen, F. & Chang, R., 2007. Study of the effect of imperfect tips on nanoindentation by FEM. *Journal of mechanical science and technology*, 21, pp.1471–1476.

CHEN, X., HASSELMAN, T.K. & NEILL, D.J., 1997. Reliability based structural design optimization for practical applications. *Proceedings of the 38th AIAA/ASME/ ...*, (1).

Cheng, G., Xu, L. & Jiang, L., 2006. A sequential approximate programming strategy for reliability-based structural optimization. *Computers & Structures*, 84(21), pp.1353–1367.

Cheng, Y. & Cheng, C., 1998. Relationships between hardness, elastic modulus, and the work of indentation. *Applied physics letters*, 73(5), pp.614–616.

Cheng, Y., Cheng, C. & Introduction, I., 1998. Scaling approach to conical indentation in elastic-plastic solids with work hardening. , 84(3), pp.1284–1291.

Cheng, Z.-Y. et al., 2001. Electrostrictive poly (vinylidene fluoride-trifluoroethylene) copolymers. *Sensors and Actuators A: Physical*, 90(1), pp.138–147.

Choi et al., 2007. *Reliability-based Structural Design*, London: Springe.

Chollacoop, N., Dao, M. & Suresh, S., 2003. Depth-sensing instrumented indentation with dual sharp indenters. *Acta Materialia*, 51(13), pp.3713–3729.

Crippa, M. et al., 2013. High dielectric constant rutile--polystyrene composite with enhanced percolative threshold. *Journal of Materials Chemistry C*, 1(3), pp.484–492.

D.H.Robertson, D.W.Brenner & J.W.Mintmire, 1992. Energetic of nanoscale graphic tubules.pdf. *Physical Review B*, 45, p.21.

Daniel, S. et al., 1999. Ab-initio structural, elastic, and vibrational properties of carbon nanotubes. *Physical Review B*, 59, p.12678.

Dao, M. et al., 2001. Computational modeling of the forward and reverse problems in instrumented sharp indentation. *Acta Materialia*, 49(19), pp.3899–3918.

Deshmukh, S. & Ounaies, Z., 2009. Single walled carbon nanotube (SWNT)–polyimide nanocomposites as electrostrictive materials. *Sensors and Actuators A: Physical*, 155(2), pp.246–252.

Despres, J.F., Daguerre, E. & Lafdi, K., 1996. Flexibility of graphene layers in carbon nanotubes. *Carbon Nanotubes*, 149, pp.1–2.

Dinulović, M. & Rašuo, B., 2009. Dielectric properties modeling of composite materials. *FME Transactions*, 37(3), pp.117–122.

Doerner, M. & Nix, W., 1986. A method for interpreting the data from depth-sensing indentation instruments. *Journal of Materials Research*, 1, pp.601–609.

Doria, G. et al., 2012. Noble metal nanoparticles for biosensing applications. *Sensors (Basel, Switzerland)*, 12(2), pp.1657–87.

Dubnikova, I. et al., 2010. The Effect of Multiwalled Carbon Nanotube Dimensions on the Morphology , Mechanical , and Electrical Properties of Melt Mixed Polypropylene-Based Composites. *Journal of Applied Polymer Science,*, 117, pp.59–272.

Duyne, R.P. Van, Haes, A.J. & Mcfarland, A.D., 2003. Nanoparticle optics : sensing with nanoparticle arrays and single nanoparticles. *Proceedings of SPIE*, 5223, pp.197–207.

El-Hami, K. & Matsushige, K., 2003. Covering single walled carbon nanotubes by the poly (VDF--co--TrFE) copolymer. *Chemical physics letters*, 368(1), pp.168–171.

El-Hami, K. & Matsushige, K., 2005. Electrostriction in single-walled carbon nanotubes. *Ultramicroscopy*, 105(1-4), pp.143–147.

Fábián, C. & Szőke, Z., 2007. Solving two-stage stochastic programming problems with level decomposition. *Computational Management Science*, 4(4), pp.313–353.

Falvo, M.R. et al., 1997. Bending and buckling of carbon nanotubes under large strain. *Nature*, 389(October 1997), pp.21–23.

Ghaderi, S.H. & Hajiesmaili, E., 2012. Molecular structural mechanics applied to coiled carbon nanotubes. *Computational Materials Science*, 55, pp.344–349.

Giannakopoulos, A.E. Larsson, P.-L., 1997. Analysis of pyramid indentation of pressure-sensitive hard metals and ceramics. *Mechanics of Materials*, 25(1), pp.1–35.

Giannakopoulost, A.E. & Vestergaard, R., 1994. ANALYSIS OF VICKERS INDENTATION. , 31(19), pp.2679–2708.

Giannopoulos, G.I., Kakavas, P. a. & Anifantis, N.K., 2008. Evaluation of the effective mechanical properties of single walled carbon nanotubes using a spring based finite element approach. *Computational Materials Science*, 41(4), pp.561–569.

Ginga, N.J. & Sitaraman, S.K., 2011. New Method to Measure Tensile Strength of Low Modulus Thin Films. *International Journal of Fracture*, 170(2), pp.199–206.

Gogotsi, Y., Libera, J. a. & Yoshimura, M., 2000. Hydrothermal synthesis of multiwall carbon nanotubes. *Journal of Materials Research*, 15(12), pp.2591–2594.

Golnabi, H., 2012. Carbon nanotube research developments in terms of published papers and patents, synthesis and production. *Scientia Iranica*, 19(6), pp.2012–2022.

Guo, G.Y. et al., 2004. Linear and nonlinear optical properties of carbon nanotubes from first-principles calculations. *Physical Review B*, 69(20), p.205416.

Guo, T. et al., 1995. Self-Assembly of Tubular Fullerenes. *J. Phys. Chem*, 99, pp.10694–10697.

Guo, W. & Guo, Y., 2003. Giant axial electrostrictive deformation in carbon nanotubes. *Physical review letters*, 91(11), p.115501.

Gupta, S., Dharamvir, K. & Jindal, V., 2005. Elastic moduli of single-walled carbon nanotubes and their ropes. *Physical Review B*, 72(16), p.165428.

Hafner, J.H. et al., 1998. Catalytic growth of single-wall carbon nanotubes from metal particles. *Chemical Physics Letters*, 296(October), pp.195–202.

Hall, D.B., Underhill, P. & Torkelson, J.M., 1998. Spin Coating of Thin and Ultrathin Polymer Films. *Polymer Engineering & Science*, 38(12), pp.2039–2045.

Hall, L.J. et al., 2008. Sign Change of Poisson's Ratio for Carbon Nanotube Sheets. *Science (New York, N.Y.)*, 320(5875), pp.504–7.

EL HAMI, A. & BOUCHAIB, R., 2013. *Uncertainty and Optimization in Structural Mechanics*, John Wiley & Sons.

HANDBOOK, N., 2010. *Measurement Uncertainty Analysis Principles and Methods NASA Measurement Quality Assurance Handbook – ANNEX 3*, Washington DC.

Harper, T., 2011. GLOBAL FUNDING OF NANOTECHNOLOGIES & ITS IMPACT JULY 2011 e Global Funding Of Nanotechnologies & Its Impact. , (July).

HARRIS, P.J. & HARRIS, P.J.F., 2009. *Carbon Nanotube Science: synthesis, properties and Applications*, Cambridge University Press.

Harris, P.J.F. & Harris, P.J.P.J.F., 2009. *Carbon nanotube science: synthesis, properties and applications*, Cambridge University Press.

Hasegawa, M. & Nishidate, K., 2006. Radial deformation and stability of single-wall carbon nanotubes under hydrostatic pressure. *Physical Review B*, 74(11), p.115401.

Hecht, S. & Fre, J.M.J., 2001. Dendritic Encapsulation of Function : Applying Nature s Site Isolation Principle from Biomimetics to Materials Science. *Angew. Chem. Int. Ed*, 40, pp.74–91.

Hernández, E. et al., 1998. Elastic Properties of C and BxCyNz Composite Nanotubes. *Physical Review Letters*, 80(20), pp.4502–4505.

Hill, R. et al., 1989. A theoretical study of the Brinell hardness test. *Proceedings of the Royal Society of London. A. Mathematical and Physical Sciences*, 423, pp.301–330.

Hone, J. et al., 2000. Electrical and thermal transport properties of magnetically aligned single wall carbon nanotube films. *Applied Physics Letters*, 77(5), p.666.

Hone, J., 2001. Phonons and Thermal Properties of Carbon Nanotubes. , 286, pp.273–286.

Hone, J. et al., 1999. Thermal conductivity of single-walled carbon nanotubes. *Physical Review B*, 59(4), pp.R2514–R2516.

Hopcroft, M. a., Nix, W.D. & Kenny, T.W., 2010. What is the Young's Modulus of Silicon? *Journal of Microelectromechanical Systems*, 19(2), pp.229–238.

Huh, Y.-H. et al., 2009. Measurement of Mechanical Properties of Thin Film by Membrane Deflection Test. *Experimental Mechanics*, 50(4), pp.429–435.

Hutter, E. & Maysinger, D., 2011. Gold nanoparticles and quantum dots for bioimaging. *Microscopy research and technique*, 74(7), pp.592–604.

Iijima, S., 1991. Helical microtubules of graphitic carbon. *Nature*, 354(56–58).

Iijima, S. et al., 1996. Structural flexibility of carbon nanotubes. *The Journal of Chemical Physics*, 104(5), p.2089.

Jennett, N. & Meneve, J., 1998. Depth sensing indentation of thin hard films: a study of modulus measurement sensitivity to indentation parameters. *MRS Proceedings*, 522, pp.239–244.

Jensen, K. et al., 2007. Buckling and kinking force measurements on individual multiwalled carbon nanotubes. *Physical Review B*, 76, p.195436.

Jeon, S. et al., 2006. Fabricating three dimensional nanostructures using two photon lithography in a single exposure step. , 14(6), pp.1369–1373.

Jiang, M.-J. et al., 2007. Effect of aspect ratio of multiwall carbon nanotubes on resistance-pressure sensitivity of rubber nanocomposites. *Applied Physics Letters*, 91(7), p.072907.

Kalamkarov, a. L. et al., 2006. Analytical and numerical techniques to predict carbon nanotubes properties. *International Journal of Solids and Structures*, 43(22-23), pp.6832–6854.

Kam, K. et al., 2013. Graphene nanofilm as pressure and force sensor: A mechanical analysis. , 2089(10), pp.2085–2089.

Kamarudin, S.K., Achmad, F. & Daud, W.R.W., 2009. Overview on the application of direct methanol fuel cell (DMFC) for portable electronic devices. *International Journal of Hydrogen Energy*, 34(16), pp.6902–6916.

Khan, M.K. et al., 2010. A combined experimental and finite element approach for determining mechanical properties of aluminium alloys by nanoindentation. *Computational Materials Science*, 49(4), pp.751–760.

Kim, J., Loh, K.J. & Lynch, J.P., 2008. Piezoelectric polymeric thin films tuned by carbon nanotube fillers. In *The 15th International Symposium on: Smart Structures and Materials & Nondestructive Evaluation and Health Monitoring*. p. 693232.

Kim, K. et al., 2008. Determination of Elastic modulus of thin materials by Speckle Interferometry 2 . Time Average ESPI. , pp.25–28.

Kim, K.T. et al., 2010. Smart nanocontainers and nanoreactors. *Nanoscale*, 2(6), pp.844–58.

Klein, C. a. & Cardinale, G.F., 1993. Young's modulus and Poisson's ratio of CVD diamond. *Diamond and Related Materials*, 2(5-7), pp.918–923.

Kohnke, P., 2001. *ANSYS, Inc. theory*, Canonsburg (PA): SAS IP Press.

Kozinsky, B. & Marzari, N., 2008. Static dielectric properties of carbon nanotubes from first principles. , 24, pp.1–5.

Krishnan, A., Dujardin, E., Ebbesen, T., et al., 1998. Young's modulus of single-walled nanotubes. *Physical Review B*, 58(20), pp.14013–14019.

Krishnan, A., Dujardin, E., Ebbesen, T.W., et al., 1998. Young'smodulus of single-walled nanotubes. *Phys.Rev. B*, 58, pp.14013–14019.

Kucharski, S. & Mróz, Z., 2007. Identification of yield stress and plastic hardening parameters from a spherical indentation test. *International Journal of Mechanical Sciences*, 49(11), pp.1238–1250.

Kudin, K., Scuseria, G. & Yakobson, B., 2001. C2F, BN, and C nanoshell elasticity from ab initio computations. *Physical Review B*, 64(23), p.235406.

Kumar, M. & Ando, Y., 2010. Chemical Vapor Deposition of Carbon Nanotubes: A Review on Growth Mechanism and Mass Production. *Journal of Nanoscience and Nanotechnology*, 10(6), pp.3739–3758.

Kwon, Y. & Toma, D., 1998. Electronic and structural properties of multiwall carbon nanotubes. , 58(24), pp.1–4.

Langer, L. et al., 1996. Quantum transport in a multiwalled carbon nanotube. *Physical review letters*, 76(3), p.479.

Laplaze, D. et al., 1998. Carbon nanotubes: The solar approach. *Carbon*, 36(5–6), pp.685–688.

Larsson, P., 2001. Investigation of sharp contact at rigid - plastic conditions. , 43(February 2000), pp.895–920.

Lau, K.K.S. et al., 2003. Superhydrophobic Carbon Nanotube Forests. *Nano Letters*, 3(12), pp.1701–1705.

Li, C. & Chou, T.-W., 2003a. A structural mechanics approach for the analysis of carbon nanotubes. *International Journal of Solids and Structures*, 40(10), pp.2487–2499.

Li, C. & Chou, T.-W., 2003b. Elastic moduli of multi-walled carbon nanotubes and the effect of van der Waals forces. *Composites Science and Technology*, 63(11), pp.1517–1524.

Li, H. & Guo, W., 2008. Transversely isotropic elastic properties of single-walled carbon nanotubes by a rectangular beam model for the C[Single Bond]C bonds. *Journal of Applied Physics*, 103(10), p.103501.

Li, J. & Rao, N., 2002. Dramatically enhanced effective electrostriction in ferroelectric polymeric composites. *Applied physics letters*, 81(10), pp.1860–1862.

Li, J. & Rao, N., 2004. Micromechanics of ferroelectric polymer-based electrostrictive composites. *Journal of the Mechanics and Physics of Solids*, 52(3), pp.591–615.

Li, Q.W. et al., 2007. Structure-Dependent Electrical Properties of Carbon Nanotube Fibers. *Advanced Materials*, 19(20), pp.3358–3363.

Li, W. & Landis, C.M., 2012. Deformation and instabilities in dielectric elastomer composites. *Smart Materials and Structures*, 21(9), p.94006.

Li, W. & Yang, L., 1994. AN EFFECTrVE OPTIMIZATION PROCEDURE ON STRUCTURAL RELIABILITY. *Computers & structures*, 52(2), pp.1061–1067.

Li, X. & Bhushan, B., 2002. A review of nanoindentation continuous stiffness measurement technique and its applications. *Materials Characterization*, 48(1), pp.11–36.

Liu, B. et al., 2005. Atomic-scale finite element method in multiscale computation with applications to carbon nanotubes. *Physical Review B*, 72(3), p.035435.

Liu, L., Cao, G. & Chen, X., 2008. Mechanisms of Nanoindentation on Multiwalled Carbon Nanotube and Nanotube Cluster. *Journal of Nanomaterials*, 2008, pp.1–12.

Loh, K.J., Kim, J. & Lynch, J.P., 2008. Self-sensing and power harvesting carbon nanotube-composites based on piezoelectric polymers. *Bridge Maintenance, Safety, Management, Health Monitoring and Informatics, IABMAS*, 8.

Lonjon, A. et al., 2010. Structural and electrical properties of gold nanowires/P (VDF-TrFE) nanocomposites. *Journal of Physics D: Applied Physics*, 43(34), p.345401.

Lourie, O., Cox, D. & Wagner, H., 1998. Buckling and Collapse of Embedded Carbon Nanotubes. *Physical Review Letters*, 81(8), pp.1638–1641.

Lourie, O., Wagner, H.D. & Introduction, I., 1998. by micro-Raman spectroscopy. *J. Mater. Res*, 13, p.9.

Lu, J., 1997. Elastic Properties of Carbon Nanotubes and Nanoropes. *Physical Review Letters*, 79(7), pp.1297–1300.

Lu, W., Chou, T.-W. & Kim, B.-S., 2011. Erratum: Radial deformation and its related energy variations of single-walled carbon nanotubes [Phys. Rev. B 83, 134113 (2011)]. *Physical Review B*, 84(5), p.059901.

Lu, X. & Hu, Z., 2012. Mechanical property evaluation of single-walled carbon nanotubes by finite element modeling. *Composites Part B: Engineering*, 43(4), pp.1902–1913.

Ma, Y.J. et al., 2010. Carbon nanotube films change Poisson's ratios from negative to positive. *Applied Physics Letters*, 97(6), p.061909.

Ma, Z. et al., 2013. Applications of gold nanorods in biomedical imaging and related fields. *Chinese Science Bulletin*, 58(21), pp.2530–2536.

Mahmoudinezhad, E. et al., 2012. An accurate spring-mass model for predicting mechanical properties of single-walled carbon nanotubes. *Computational Materials Science*, 62, pp.6–11.

Maier, P. et al., 2002. Application of nanoindentation technique for structural characterisation of weld materials. *Materials Characterization*, 48(4), pp.329–339.

Manbachi, A. & Cobbold, R.S.C., 2011. Development and application of piezoelectric materials for ultrasound generation and detection. *Ultrasound*, 19(4), pp.187–196.

Mansoori, G. Ali, T. Rohani Bastami, A.A., 2008. ENVIRONMENTAL APPLICATION OF NANOTECHNOLOGY. In *Annual Review of Nano Research*. World Scientific, pp. 1–73.

McEuen, P.L., Fuhrer, M.S. & Park, H., 2002. Single-walled carbon nanotube electronics. *Nanotechnology, IEEE Transactions on*, 1(1), pp.78–85.

Menčík, J., 2012. *Nanoindentation in Materials Science* J. Nemecek, ed., InTech, Chapters published.

Miller, R.E. & Tadmor, E.B., 2009. A unified framework and performance benchmark of fourteen multiscale atomistic/continuum coupling methods. *Modelling and Simulation in Materials Science and Engineering*, 17(5), p.053001.

Mittal, V. ed., 2010. *Polymer Nanotube Nanocomposites: Synthesis, Properties, and Applications*, scrivener publishing LLC.

Moriyama, Q.W. and H., 2011. *Carbon Nanotube-Based Thin Films: Synthesis and Properties* Dr. Siva Yellampalli (Ed.), ed., InTech Published.

Mulvey, J., Vanderbei, R. & Zenios, S., 1995. Robust optimization of large-scale systems. *Operations research*, 43(2), pp.264–281.

Nanomat Inc, 2013. Nanomaterials and Their Applications.

Nasdala, L. & Ernst, G., 2005. Development of a 4-node finite element for the computation of nano-structured materials. *Computational Materials Science*, 33(4), pp.443–458.

National Geographic, 2014. nanotechnology. , pp.1–12.

Nazir, S. et al., 2014. Nanomaterials in combating cancer: therapeutic applications and developments. *Nanomedicine : nanotechnology, biology, and medicine*, 10(1), pp.19–34.

Nishidate, K. & Hasegawa, M., 2010. Deformation and transfer doping of a single-walled carbon nanotube adsorbed on metallic substrates. *Physical Review B*, 81(12), p.125414.

Nocedal, J., Wright, S.J. & Robinson, S.M., 1999. *Numerical Optimization* P. Glynn & S. M. Robinson, eds., Springer.

Novoselova, I. a. et al., 2008. Electrolytic synthesis of carbon nanotubes from carbon dioxide in molten salts and their characterization. *Physica E: Low-dimensional Systems and Nanostructures*, 40(7), pp.2231–2237.

Oliver, Warren Carl, and G.M.P., 1992. An Improved Technique for Determining Hardness and Elastic Modulus Using Load and Displacement Sensing Indentation Experiments.pdf. , pp.1564–1583.

Paul, A. & Klimeck, G., 2011. Strain effects on the phonon thermal properties of ultra-scaled Si nanowires. *Applied Physics Letters*, 99(8), p.083115.

Phadke, M.S., 1995. *Quality Engineering Using Robust Design.pdf*, Prentice Hall PTR.

Pissuwan, D., Valenzuela, S.M. & Cortie, M.B., 2008. Prospects for Gold Nanorod Particles in Diagnostic and Therapeutic Applications. *Biotechnology and Genetic Engineering Reviews*, 25(1), pp.93–112.

Pokropivny, V., Hussainova, I. & Vlassov, S., 2007. Introduction to nanomaterials and nanotechnology.

Poncharal, P. et al., 1999. Electrostatic Deflections and Electromechanical Resonances of Carbon Nanotubes. *Science*, 283(5407), pp.1513–1516.

Popov, V.N., Van Doren, V.E. & Balkanski, M., 2000. Elastic properties of crystals of single-walled carbon nanotubes. *Solid State Communications*, 114(7), pp.395–399.

Prasek, J. et al., 2011. Methods for carbon nanotubes synthesis—review. *Journal of Materials Chemistry*, 21(40), p.15872.

Qi, H.J. et al., 2003. Determination of mechanical properties of carbon nanotubes and vertically aligned carbon nanotube forests using nanoindentation. *Journal of the Mechanics and Physics of Solids*, 51(11-12), pp.2213–2237.

Rajasekaran, S. & Chitra, P., 2009. Structural mechanics approach for Carbon Nanotubes. *KSCE Journal of Civil Engineering*, 13(5), pp.347–358.

Rao, N. & Li, J.Y., 2004. The electrostriction of P (VDF-TrFE) copolymers embedded with textured dielectric particles. *International journal of solids and structures*, 41(11), pp.2995–3011.

Rao, R., Bradby, J. & Williams, J., 2007. NANOINDENTATION-INDUCED PHASE TRANSFORMATION IN SILICON To cite this version : *arXiv preprint arXiv*, pp.46–49.

Rao, R.S. et al., 2008. The Taguchi methodology as a statistical tool for biotechnological applications: a critical appraisal. *Biotechnology journal*, 3(4), pp.510–23.

Ray, M.C. & Batra, R.C., 2009. Effective Properties of Carbon Nanotube and Piezoelectric Fiber Reinforced Hybrid Smart Composites. *Journal of Applied Mechanics*, 76(3), p.034503.

Ren, Z. et al., 2013. Hierarchically nanostructured materials for sustainable environmental applications. *Frontiers in chemistry*, 1(November), p.18.

Romano-rodr, A., Morante, J.R. & Esteve, J., 1999. Test microstructures for measurement of SiC thin film mechanical properties. *J. Micromech. Microeng*, 190(9), pp.190–193.

Rosenblatt, M., 1952. Remarks on a multivariate transformation. *The annals of mathematical statistics*, pp.470–472.

Ruoff, R.S., Qian, D. & Liu, W.K., 2003. Mechanical properties of carbon nanotubes: theoretical predictions and experimental measurements. *Comptes Rendus Physique*, 4(9), pp.993–1008.

Russ, M. et al., 2013. Length-dependent electrical and thermal properties of carbon nanotube-loaded epoxy nanocomposites. *Composites Science and Technology*, 81, pp.42–47.

Saha, R. & Nix, W.D., 2002. Effects of the substrate on the determination of thin film mechanical properties by nanoindentation. *Acta Materialia*, 50(1), pp.23–38.

Salvendy, G., 2001. *Handbook of industrial engineering: technology and operations management* Third., ohn Wiley & Sons.

Salvetat, J.-P. et al., 1999. Elastic and Shear Moduli of Single-Walled Carbon Nanotube Ropes. *Physical Review Letters*, 82(5), pp.944–947.

Salvetat, J.-P. et al., 1999. Mechanical properties of carbon nanotubes. *Applied Physics A: Materials Science & Processing*, 69(3), pp.255–260.

Schuh, C.A., 2006. Nanoindentation opportunities for futures scientific inquiry, 9(5), pp.32–40.

Shi1, Y. et al., 2012. 1D magnetite nanostructures obtained without templates for energy applications. *Nanotechnology*, 23, p.395601.

Shima, H., 2011. Buckling of Carbon Nanotubes: A State of the Art Review. *arXiv preprint arXiv*, 1112, p.38.

Sri D. Suneel, S., Role of Bottom-up and Top-Down approaches in Nano technology.

Stouwdam, J.W. & Janssen, R. a. J., 2008. Red, green, and blue quantum dot LEDs with solution processable ZnO nanocrystal electron injection layers. *Journal of Materials Chemistry*, 18(16), p.1889.

Stramel, a. a. et al., 2010. Pulsed laser deposition of carbon nanotube and polystyrene–carbon nanotube composite thin films. *Optics and Lasers in Engineering*, 48(12), pp.1291–1295.

Sun, D. et al., 2004. Pressure-induced hard-to-soft transition of a single carbon nanotube. *Physical Review B*, 70(16), p.165417.

Szabó, A. et al., 2010. Synthesis Methods of Carbon Nanotubes and Related Materials. *Materials*, 3(5), pp.3092–3140.

Tabor, D., 1956. The physical meaning of indentation and scratch hardness. *British Journal of Applied Physics*, 159.

Takesue, I. et al., 2006. Superconductivity in Entirely End-Bonded Multiwalled Carbon Nanotubes. *Physical Review Letters*, 96(5), p.057001.

Takuma, T. & Techaumnat, B., 2010. Electric Fields in Composite Dielectrics and their Applications. , pp.15–30.

Tang, C., Guo, W. & Guo, Y., 2006. Electrostrictive effect on electronic structures of carbon nanotubes. *Applied Physics Letters*, 88(24), p.243112.

Tans, S.J., Verschueren, A.R.M. & Dekker, C., 1998. Room-temperature transistor based on a single carbon nanotube. , 672(1989), pp.669–672.

Teo, K.B.K. et al., 2001. Uniform patterned growth of carbon nanotubes without surface carbon. *Applied Physics Letters*, 79(10), p.1534.

Thostenson, E., Li, C. & Chou, T., 2005. Nanocomposites in context. *Composites Science and Technology*, 65(3-4), pp.491–516.

Timmermans, M.Y. et al., 2012. Effect of carbon nanotube network morphology on thin film transistor performance. *Nano Research*, 5(5), pp.307–319.

Tombler, T. et al., 2000. Reversible electromechanical characteristics of carbon nanotubes under local-probe manipulation. *Nature*, 405(6788), pp.769–72.

Treacy, M., Ebbesen, T. & Gibson, J., 1996. Exceptionally high Young's modulus observed for individual carbon nanotubes.pdf. *nature*, 381, pp.678 – 680.

Tsang, S.C., Oliveira, P. De & Davis, J.J., 1996. The structure of the carbon nanotube and its surface topography probed by transmission electron microscopy and atomic force microscopy. , 4(February).

Tserpes, K.I. & Papanikos, P., 2005. Finite element modeling of single-walled carbon nanotubes. *Composites Part B: Engineering*, 36(5), pp.468–477.

Tunvisut, K. et al., 2002. Determination of the mechanical properties of metallic thin films and substrates from indentation tests. *Philosophical Magazine A*, 82(10), pp.2013–2029.

Vajtai, R., 2013. *Springer Handbook of Nanomaterials*, Springer.

Valdebenito, M. a. & Schuëller, G.I., 2010. A survey on approaches for reliability-based optimization. *Structural and Multidisciplinary Optimization*, 42(5), pp.645–663.

Wainwright, M.J. & Jordan, M.I., 2008. Graphical Models, Exponential Families, and Variational Inference. *Foundations and Trends® in Machine Learning*, 1(1–2), pp.1–305.

Wan, H. & Delale, F., 2009. A structural mechanics approach for predicting the mechanical properties of carbon nanotubes. *Meccanica*, 45(1), pp.43–51.

Wang, S. et al., 2007. Controlled nanostructure and high loading of single-walled carbon nanotubes reinforced polycarbonate composite. *Nanotechnology*, 18(9), p.095708. Wikipedia, 2014. Nanomaterials. Available at: http://en.wikipedia.org/wiki/ Nanomaterials.

Wilder, J.W.G. et al., 1998. Electronic structure of atomically resolved carbon nanotubes. *Nature*, 391(6662), pp.59–62.

Wong, E.W., 1997. Nanobeam Mechanics: Elasticity, Strength, and Toughness of Nanorods and Nanotubes. *Science*, 277(5334), pp.1971–1975.

Woods, A.P. and L.M., 2008. simple model of van der waals interaction between two radially deformed single-walled carbon nanotubes.pdf. , p.115443.

Wu, D. et al., 2010. Relations between the aspect ratio of carbon nanotubes and the formation of percolation networks in biodegradable polylactide/carbon nanotube composites. *Journal of Polymer Science Part B: Polymer Physics*, 48(4), pp.479–489.

Wu, J., Hwang, K. & Huang, Y., 2008. An atomistic-based finite-deformation shell theory for single-wall carbon nanotubes. *Journal of the Mechanics and Physics of Solids*, 56(1), pp.279–292.

Wu, Z. et al., 2004. Transparent, conductive carbon nanotube films. *Science (New York, N.Y.)*, 305(5688), pp.1273–6.

Xiao, J.R., Gama, B. a. & Gillespie, J.W., 2005. An analytical molecular structural mechanics model for the mechanical properties of carbon nanotubes. *International Journal of Solids and Structures*, 42(11-12), pp.3075–3092.

Xie, X., Mai, Y. & Zhou, X., 2005. Dispersion and alignment of carbon nanotubes in polymer matrix: A review. *Materials Science and Engineering: R: Reports*, 49(4), pp.89–112.

Xin, Z. et al., 2000. Strain energy and Young's modulus of single-wall carbon nanotubes calculated from electronic energy-band theory. *Physical Review B*, 62(20), pp.13692–13696.

Yakobson, B., Brabec, C. & Bernholc, J., 1996. Nanomechanics of Carbon Tubes: Instabilities beyond Linear Response. *Physical Review Letters*, 76(14), pp.2511–2514.

Yang, D. et al., 2002. Thermal conductivity of multiwalled carbon nanotubes. *Physical Review B*, 66(16), p.165440.

Yao, Z., Kane, C.L. & Dekker, C., 1999. High-Field Electrical Transport in Single-Wall Carbon Nanotubes. , pp.2–5.

Yi, W. et al., 1999. Linear specific heat of carbon nanotubes. *Physical Review B*, 59(14), pp.R9015–R9018. Available at: http://link.aps.org/doi/10.1103/PhysRevB.59.R9015.

Yu, M., Lourie, O., et al., 2000. Strength and breaking mechanism of multiwalled carbon nanotubes under tensile load. *Science (New York, N.Y.)*, 287(5453), pp.637–40.

Yu, M., Files, B., et al., 2000. Tensile loading of ropes of single wall carbon nanotubes and their mechanical properties. *Physical review letters*, 84(24), pp.5552–5.

Yu, M.-F., 2004. Fundamental Mechanical Properties of Carbon Nanotubes: Current Understanding and the Related Experimental Studies. *Journal of Engineering Materials and Technology*, 126(3), p.271.

Zen, N. et al., 2014. Engineering thermal conductance using a two-dimensional phononic crystal. *Nature communications*, 5, p.3435.

Zhang, D. et al., 2006. Transparent, conductive, and flexible carbon nanotube films and their application in organic light-emitting diodes. *Nano letters*, 6(9), pp.1880–6.

Zhang, T. et al., 2011. Numerical verification for instrumented spherical indentation techniques in determining the plastic properties of materials. *Journal of Materials Research*, 24(12), pp.3653–3663.

Zhang, W., Picu, R.C. & Koratkar, N., 2008. The effect of carbon nanotube dimensions and dispersion on the fatigue behavior of epoxy nanocomposites. *Nanotechnology*, 19(28), p.285709.

Zhao, Z.S. et al., 2013. High-pressure behaviors of carbon nanotubes. *Journal of Superhard Materials*, 34(6), pp.371–385.

Zhi-Qiang Feng, Qi-Chang He, Q.Z. & Joli, P., 2010. Theory of Nanoindentation. , pp.1–15.

Zhou, X. et al., 2005. Band Structure, Phonon Scattering, and the Performance Limit of Single-Walled Carbon Nanotube Transistors. *Physical Review Letters*, 95(14), p.146805.

Appendix

Appendix A

Uncertainty quantification methodologies

Lots of research work has been conducted to solve the uncertainty quantification problems**.** These problems can be divided into two major types: forward uncertainty propagation problem and inverse uncertainty propagation problem. The former is to assess the effect of variability and lack of knowledge on the output of a computational model. While, the latter problem is to use observations/experiments to infers the input quantities.

Forward propagation of uncertainty

For forward uncertainty propagation problem, a number of probabilistic and non-probabilistic approaches have been developed. This section provides a briefly summary of these methods.

Analytical methods

The mean-value first-order second-moment (MFOSM) is the most common analytical uncertainty analysis method. This method is a technique for finding approximations to the moments of functions of random variables when these moments cannot be directly evaluated. The MFOSM method works by the Taylor series expansion of the model output function *h* around the mean values of the n random variables X.

$$h(X) = h(\bar{X}) + \sum_{i=1}^{n} (x_i - \bar{x}_i) \left[\frac{\partial h}{\partial x_i}\right]_{x=\bar{x}} + \sum_{i=1}^{n}\sum_{j=1}^{n} (x_i - \bar{x}_i)\,(x_j - \bar{x}_j) \left[\frac{\partial^2 h}{\partial x_i \partial x_j}\right]_{x=\bar{x}} + O \tag{A–1}$$

where $\bar{X} = (\bar{x}_1, \bar{x}_2, \ldots \bar{x}_n)$ are the mean values of the random variables x_i, and O is the higher order terms in the Taylor series expansion. In practical applications, the higher order terms and cross product terms in (A–1) are usually ignored, which leaves the first order approximation of the function *h(x)*:

$$h(X) \approx h(\bar{X}) + \sum_{i=1}^{n} (x_i - \bar{x}_i) \left[\frac{\partial h}{\partial x_i}\right]_{x=\bar{x}} \quad \text{(A–2)}$$

So, the first-order approximation for the mean and variance are

$$E[h(X)] \approx h(\bar{X}) \quad \text{(A–3)}$$

$$var[h(X)] \approx \sum_{i=1}^{n} var(x_i) \left[\frac{\partial h}{\partial x_i}\right]^2_{x=\bar{x}} + 2 \sum_{i=1}^{n} \sum_{j=1}^{n} cov(x_i, x_j) \left[\frac{\partial h}{\partial x_i}\right]^2_{x=\bar{x}} \left[\frac{\partial h}{\partial x_j}\right]^2_{x=\bar{x}} \quad \text{(A–4)}$$

This method in dealing with relatively small input variables and outputs that don't express high nonlinearity is simple. It only requires the estimation of first-order derivatives of the model output function at the mean values. However, if the cross-product terms or any of the higher order terms in (A–1) are retained, the complexity of the algebra increases rapidly. Besides, in many cases the propagation of uncertainty is restricted to the parameters of the distribution and the method is not accurate if the output function is not smooth or if important covariance terms are omitted.

Beside MFOSM uncertainty method, there are other analytical uncertainty methods applied in some specific situations. For example, to overcome some defects of the MFOSM method, MASKEY et al. (Maskey & Guinot, 2003) proposed an improved FOSM method. Kuo et al. (KUO, YEN, HSU, & Lin, 2007) estimate the overtopping risk of Feitsui Dam by five uncertainty analysis methods, and they indicate that some analytical methods (MFOSM, Rosenblueth's point estimation method (RPEM) and Harr's point estimation method (RPEM)) can avoid the computational burden by applying sampling methods. While, Yu et al. (S. Bell, 2001) suggest that when using RPEM and HPEM methods, the produced parameter sets should be carefully checked for their plausibility.

Probabilistic methods

Uncertainty quantification has been traditionally performed by probabilistic methods. In this approach, every input parameter is treated as a random variable defined on a certain interval by its probability distribution. The probability of any event is defined on the sample space as the sum of probabilities assigned to the outcomes of the event. The uncertainties are characterized by probabilities associated with the events (Dutt & Kurian, 2013). Many probabilistic approaches already exist for uncertainties quantification, such as Monte Carlo simulation method, probability boxes and probability bounds analysis method.

Probabilistic graphical model method

Probabilistic graphical models use a graph-based representation as the basis for compactly encoding a complex distribution over a high-dimensional space (Koller & Friedman, 2009). The graph model in fact is a data structure consisting of a set of nodes and a set of edges, in which each node represents a random variable or a group of random variables and the edge represents the conditional relationship between variables. The graphical models allow us to abstract out the conditional independence relationships between the variables from the details of their parametric forms. Commonly used graphical models are directed graphical models (or Bayesian networks) and undirected graphical models (or Markov random field). Assume that a set of nodes $\mathbf{X}=\{X_1,...,X_n\}$, we named one pair of nodes X_i, X_j connected by a directed edge $X_i \rightarrow X_j$ as directed graphs and an undirected edge $X_i — X_j$ as undirected graphs. As shown in Fig. A.1 (a) is a simple directed graphical model with five variables, the joint probability distribution of the five variables is:

$$P(X_1, \dots, X_5) = P(X_5|X_3, X_4)P(X_4|X_3)P(X_3|X_1, X_2)P(X_2)P(X_1) \quad \text{(A–5)}$$

Generally, any joint distribution $P(X_1,...,X_n)$ of 'dependency-graph' represented by directed graphical model can be represent as the following notation, where $P_{pa(i)}$ is the set of parents of node i.

$$P(X_1, \dots, X_n) = \prod_{i=1}^{n} P(X_i|P_{pa(i)}) \quad \text{(A–6)}$$

Fig. A.1 (b) is a simple undirected graphical model; here the interactions between the variables do not have a specific direction. In this case, the joint probability according to functions defined on the cliques of the graph (Wainwright & Jordan, 2008).

$$P(X_1, \dots, X_n) = \frac{1}{Z}\prod_{C \epsilon c} \psi_C(x_C) \quad \text{(A–7)}$$

where Z is the normalisation constant, ψ_C is the compatibility function defined only for elements x_C within the clique C, the set C is often taken to be the set of all maximal cliques of the graph.

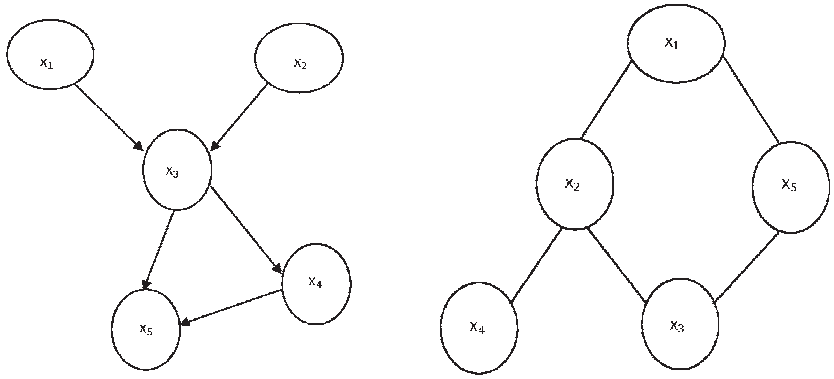

(a) (b)

Fig. A.1 Diffrtent perspectives on probabilistic graphical models: (a) A simple directed graphical model with five variables. (b) A simple undirected graphical model.

Graphical models combine graph theory and probability theory together has become a focus of research in many statistical, computational and mathematical fields.

Non-probabilistic methods

Non-probabilistic methods were developed in solving optimization problems where the probability distribution of uncertainty variables is unknown (EL HAMI & BOUCHAIB, 2013). Usually, physical and geometrical uncertainties in designing are modelled by probabilistic methods, which treat the uncertain parameters as random variables or random processes. However, the applicability of these methods require large amount of information to determine the probability distribution of the uncertain parameters. In practical engineering, sufficient data are sometimes unavailable to construct the probabilistic model. In this cases that not much data are available, the non-probabilistic approaches such as interval analysis methods, fuzzy set theory, and info-gap theory are useful.

Interval analysis is one of the simplest ways to propagate all forms of variability and epistemic uncertainty through a response function (Hayes, 2011). The principal objective of interval analysis is to estimate the upper or lower bounds of an uncertainty quantity by some indicated confidence that the true value lies within it. Mathematically, the interval of an uncertainty quantity X can be expressed as (Moens & Vandepitte, 2005)

$$X = [\underline{x}, \overline{x}] = \{X \in R | \underline{x} \leq x \leq \overline{x}\} \quad \text{(A–8)}$$

where $\underline{x}$ and $\overline{x}$ are the lower and upper bound of X, R is the set of complicated region of X.

Fuzzy sets were introduced by Zadeh in 1965 as a class of objects with a continuum of grades of membership (Zadeh, 1965). It was specifically designed to mathematically represent uncertainty and vagueness and to provide formalized tools for dealing with the imprecision

intrinsic to many problems. Fuzzy set theory permits the gradual assessment of the membership of elements x in a set A, described with the aid of a membership function μ_A valued in the real unit interval [0, 1].

$$A = \{x, \mu_A(x) | x \epsilon X\} \tag{A–9}$$

A relationship between fuzzy sets and imprecise probabilities occurs via the notion of the α-cut of a fuzzy set. The α-cut of a fuzzy set A is defined as the crisp set A_α that contain all the elements of the universal set X that have a membership function greater than or equal to α:

$$A_\alpha = \{x \epsilon X | \mu_A(x) \geq \alpha\} \tag{A–10}$$

Since α lies on the range [0, 1] the upper and lower distribution functions associated with a fuzzy set A are defined by the (crisp) minimum and maximum values of the α-cut of A.

Info-gap theory is a non-probabilistic methodology for supporting decisions-making under severe uncertainty. Info-gap models concentrate on the disparity between what is known and what could be known in order to make a comprehensive and reliable decision (Ben-Haim, 2006). The Info-gap decision theory is based on three elements:

- **Model of uncertainty:** An info-gap model is a non-probabilistic quantification of uncertainty. It is an unbounded family of nested sets of possible realizations which includes a number of alternative decisions, actions or choices available to a decision maker.
- **Model of the system**: The system model expresses our knowledge about the system, and may depend on uncertain elements whose uncertainty is represented by an info-gap model of uncertainty. The system model may also depends on the decisions to be made, and quantifies the outcomes of those decisions given specific realizations of the uncertainties.
- **Performance requirements**: The required performances that the decision maker requires or aspires to achieve, which may constitute success of the decision, or at least minimally acceptable values. Performance requirements can embody the concept of satisficing: doing well enough or meeting critical requirements. Alternatively, the performance requirements can express windfall aspirations for better-than-anticipated outcomes. Both satisficing and wind falling requirements arise in practice.

Info-Gap's most important property is its definition of the best decision as that which is most immune to the uncertainty in the decision maker's model of the world, represented by the reward function. This method is ideally suited to the situation wherein the analyst is

comfortable specifying one or more models for the problem at hand (the reward function), and an initial estimate for its uncertain parameters, but is uncomfortable or unwilling to specify a probabilistic model (Hayes, 2011).

Inverse uncertainty quantification

Inverse uncertainty propagation problem has drawing increasing attention in the engineering design systems. For example, in trying to predict the behavior of a physical system, we often confront the problem that we have an empirical mathematical model of the system while, some quantities that characterize the system may be incompletely known or our numerical results of the mathematical model are inconsistent with the experimental measurements. In these cases, we need to identify these parameters or bias through observations or measurement of the response of the system. These inverse identification problems are generally encountered in scenarios such as bias correction quantifies the model inadequacy, parameter calibration estimates the values of unknown parameters in a mathematical model, or problems combines the two together. Inverse uncertainty propagation problem can be generally formulated as:

$$x = f^{-1}(y) \tag{A–11}$$

where, y is the measured or observed data, x is the unknown parameters or state which we are interested, f describes the relationship between the measurements and the unknown parameters. In solving this kind of framework, Bayesian formulation is broadly recommended (Litvinenko & Matthies, 2013), (Biegle et al., 2011). Bayesian formula for an inverse problem is :

$$p(x|y) = \frac{p_{lh}(y|x)p_{pr}(x)}{p(y)} \tag{A–12}$$

where $p(x|y)$ is the pdf of a posteriori distribution, $p_{pr}(x)$ is the pdf of a priori distribution, $p_{lh}(y|x)$ is the pdf of the likelihood distribution, $p(y)$ is a scaling factor which is obtained by integrating over the state space.

Appendix B

Uncertainty assessment in measurement

Based on the method of evaluation, uncertainty in measurement can be grouped into two categories as “Type A” and “Type B” respectively. Type A evaluation of uncertainty is defined as a statistical calculation from a sample of data. Type B uncertainty covers uncertainties other than that included in Type A. For example, measurement process about the sources of uncertainty may come from data in calibration certificates, from experience with the behavior of the instruments, from computation and environmental factors and from all other relevant information. All identified standard uncertainty components, whether evaluated by Type A and Type B methods, are combined to produce an overall value of uncertainty to be associated with the result of the measurement that is called the combined standard uncertainty. In measurement process, there are many factors that may undermine the test results, the mainly sources of uncertainty in measurement are summarized in (Wainwright & Jordan 2008).

Table1 Sources of uncertainty in measurement

Sources of uncertainty	Explanation
The measuring instrument	Instruments bias errors, equipment aging and wear, or other kinds of drift, poor readability, noise, etc.
The item being measured	The item being measured may not be stable during measurement process.
The measurement process	The measurement process itself may be difficult to operate.
‘Imported’ uncertainties	Calibration of the instrument, maintenance checks, etc. caused uncertainty.
Operator skill	Different operators may have different skills and judgments. Like setting up a measurement, reading the measured value, etc.
Sampling issues	The prepared sample must be properly representative.
The environment	Temperature, air pressure, humidity and other conditions may affect the measuring instrument or the item being measured.

Uncertainty analysis procedure

Uncertainty analysis is a process of confirming the validity of the measurement result. Therefore, uncertainty analysis procedure should be truly reflects the measurement process. Generally, the uncertainty analysis procedure consists of the following steps:

- Define the Measurement Process
- Develop the Error Model
- Identify the Error Sources and Distributions
- Estimate Uncertainties
- Combine Uncertainties
- Report the Analysis Results

Define the Measurement Process

The first step in an uncertainty analysis is to identify the physical quantity that is measured, namely 'measurand'. The measurand could be a directly measured value or an interest quantity that derived from the measurement of other quantities. For the latter, a mathematical model should be developed to define the relationship between the derived quantity of interest and the directly measured quantity.

Besides, it is necessary to describe the test setup, the measured components, the technique used in the measurement, the environmental condition, the test procedure, and other information need to represent in the measure process.

The overall value of uncertainty in a measurement will be identified according to the definition of measurement Process.

Develop the Error Model

The error model is an algebraic expression of the total error that associated with all the relevant measurement process or component errors. For example, if we are measuring a quantity of interest Q, and Q is a derived value of the directly measured value X, X=(x_1, x_2... x_i, *i is the number of direct measurand*). Then Q can express as:

$$Q_j = \mathrm{f}(X_j) + \varepsilon_j \qquad \text{(B–13)}$$

where Q_j is the true value of the quantity of interest in *jth* measurement, f is the mathematical equation that define the relationship between Q and X, and ε_j is the total error of Q_j. The error model for the quantity Q can be expressed as (EL HAMI & BOUCHAIB 2013):

$$\varepsilon = \sum_{i=1}^{n} \frac{\partial Q}{\partial x_i} \varepsilon_i \qquad \text{(B–14)}$$

where $\frac{\partial Q}{\partial x_i}$ is the sensitive coefficient which represents the relative contribution of the errors ε_i to the total error ε.

Identify the Error Sources and Distributions

Measurement errors are the basic elements of uncertainty. Once the error sources have been identified, the measurement uncertainty caused by errors can be defined. The mainly encountered sources of error in measurement are summarized in Table 0.1.

Table 0.1 Sources of error in measurement

Sources of error	Explanation
Measurement Bias	The bias in the measuring device and/or the quantity being measured.
Random or Repeatability error	The error caused by the differences in measured value from measurement to measurement during a repeat measurement.
Resolution error	The error caused by the smallest discernible value of the measuring device and/or the quantity being measured.
Digital Sampling error	The error introduced by digitizing an analog signal.
Computation error	The error due to round-off or computer truncation, numerical interpolation, empirically determined equations, the use of curve fit equations, etc.
Operator Bias	The error introduced by operator who is making the measurement.
Environmental Factors error	The error results from variations in environmental conditions.
Response error	Additional error resulting from the measured value incurred during shipping and handling to the end-user after calibration.

Beside the identification of errors source, an accurate characterization of the errors distribution is also important in uncertainty analysis. In general, three error distributions that have been found to be relevant to most real world measurement applications, they are the normal, lognormal and student's t distributions.

Estimate Uncertainties

Our lack of knowledge about the sign and magnitude of measurement error is called measurement uncertainty. As previously discussed, the error distribution provides a mathematical description of how likely we are to measure certain values. To better understand the relationship between measurement error and measurement uncertainty, it is necessary to discuss three important axioms that form the basis upon which uncertainties can be estimated (HANDBOOK 2010).

- Axiom 1 - The uncertainty in a measurement quantity is equivalent to the standard deviation of the error distribution.

For example, if a quantity x is a random variable representing a population of measurements, and then the variance in x is just the variance in the error in x, which is expressed by the symbol ε

$$var(x) = var(x_{true} + \varepsilon_x) = var(\varepsilon_x) \tag{B–15}$$

This statement indicates that with a basic understanding of error distributions and their statistics, we can estimate uncertainties.

- Axiom 2 - The uncertainty in a measurement is the square root of the variance in the measurement error.

Axiom 2 provides the link between measurement error and measurement uncertainty. If x is a measured value, then we can write

$$\mu_x = \sqrt{var(x)} = \sqrt{var(\varepsilon_x)} \tag{B–16}$$

- Axiom 3 - The uncertainty in a measured value is equal to the uncertainty in the measurement error.

The truth of axiom 3 is because:

1. By definition, measurement error is the difference between the measured value and the true value. Conversely, the measured value is equal to the true value plus the measurement error.

Measured Value = True Value + Measurement Error

2. We define the function for uncertainty in the value x as

Uncertainty (x) = Uncertainty in x

3. The uncertainty in the measured value can then be expressed as

Uncertainty (Measured Value) = Uncertainty (True Value) + Uncertainty (Measurement Error)

As the uncertainty in the true value is zero,

Uncertainty (Measured Value) = Uncertainty (Measurement Error)

According to these three important axioms, the computation and combination of measurement uncertainty can be carried out.

Combine Uncertainties

Individual standard uncertainties calculated by Type A or Type B evaluations then can be combined validly by 'summation in quadrature' according to the above-mentioned axioms.

Report the Analysis Results

Reporting the results of an uncertainty analysis is an important aspect of quality assessment of measurements. The analysis results must be readily understood and interpreted by others. When reporting the uncertainty in a measured value, it is often desirable to include confidence limits or expanded uncertainty.

Calculation of measurement uncertainty

As aforementioned, there are two approaches to estimating variance and uncertainty. Type A uncertainty estimates involve data sampling and analysis. Type B uncertainty estimates use engineering knowledge or recollected experience of measurement processes.

Type A Estimates

Data sampling involves making repeat measurements of the quantity of interest. It is important that each repeated measurement is independent, representative and randomly taken. Type A estimates usually apply to the uncertainty due to repeatability or random error. When a set of several repeated readings has been taken, the uncertainty qualification is dependent on the samples. Statistical information of the interested quantities can be obtained by analysis of the sample distribution.

Type B Estimates

Contract to Type A estimate, Type B estimate cannot recourse to the sample data. Dr. Howard Castrup (Castrup 2000) proposed a rigorous approach for estimating both Type B

uncertainty and the estimated degrees of freedom. The formalism of Type B uncertainty estimation is:

$$u_B = \frac{L}{\Phi^{-1}[(1+p)/2]} \tag{B–17}$$

where L is the containment limits, p is the probability that the variable lies within limits ± L or namely containment probability, and $\Phi^{-1}(\cdot)$ is the inverse normal distribution function.

The degree of freedom for Type B estimated variables proposed as:

$$V \cong \frac{1}{2}\frac{u_B^2}{\sigma^2(u_B)} \tag{B–18}$$

where $\sigma^2(u_B)$ is the variance of u_B. Setting $\varphi(p) = \Phi^{-1}[(1+p)/2]$, the error in u_B due to errors in L and p obtained from (B–17) is:

$$\begin{aligned} \varepsilon(u_B) &= \frac{\partial u_B}{\partial L}\varepsilon(L) + \frac{\partial u_B}{\partial p}\varepsilon(p) \\ &= \frac{\varepsilon(L)}{\varphi} + \frac{L}{\varphi^2}\frac{d\varphi}{dp}\varepsilon(p) \end{aligned} \tag{B–19}$$

$\varepsilon(L)$ and $\varepsilon(p)$ are separately the errors in L and p. Suppose $\varepsilon(L)$ and $\varepsilon(p)$ statistically independent, the variance of u_B follows:

$$\begin{aligned} \sigma^2(u_B) &= var[\varepsilon(u_B)] \\ &= \frac{u_L^2}{\varphi^2} + \frac{L^2}{\varphi^4}(\frac{d\varphi}{dp})^2 u_p^2 \end{aligned} \tag{B–20}$$

Then we get

$$\frac{\sigma^2(u_B)}{u_B^2} = \frac{u_L^2}{L^2} + \frac{1}{\varphi^2}(\frac{d\varphi}{dp})^2 u_p^2 \tag{B–21}$$

So, in practical when we obtain u_L and u_p, the uncertainties of Type B can be estimated by applying Eqns. (B–17) ~ (B–21).

Appendix C

Lognormal distribution table

A lognormal-distributed variable x with mean μ_x and standard deviation σ_x, denoted $LN(\mu_x, \sigma_x^2)$, the variable y, where

$$y = lnx \tag{C-1}$$

Is normally distributed with mean μ_y and standard deviation σ_y, denoted $N(\mu_y, \sigma_y^2)$. The probability density function f(x) of the lognormal distribution is given by

$$f(x) = \frac{1}{x\sigma_y\sqrt{2\pi}} e^{-\frac{1}{2}[\frac{lnx-\mu_y}{\sigma_y}]^2} \tag{C-2}$$

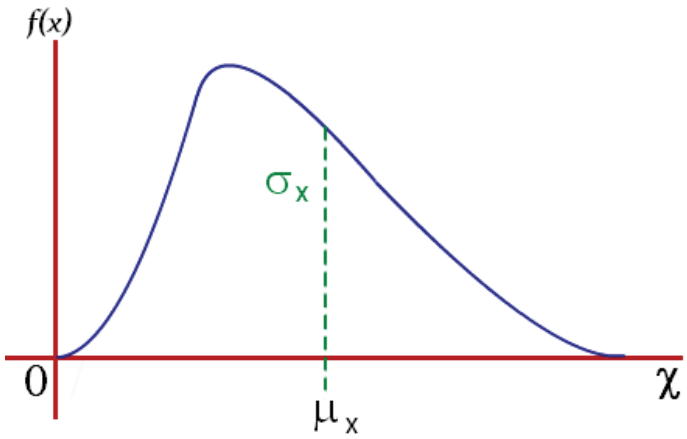

Fig. B-1 –probability density function of the lognormal distribution

The "critical value" associated with α^{th} percentile point of the standardized lognormal distribution at x_α and corresponds to the lognormal-distributed random variable x at which the cumulative distribution function $F(x)$ is equal to α

$$F(x_\alpha) = \mathrm{P}(\mathrm{x} \leq x_\alpha) = \alpha \tag{C-3}$$

Let Z_α denote the standardized normal variate associated with the α^{th} percentile of that distribution. Then, x_α can be calculated as

$$x_\alpha = e^{\mu_y + Z_\alpha \sigma_y} \tag{C-4}$$

Tables of critical values of the lognormal variable x can be generated for general use.

Table Critical values of x_α for σ_y from 0.1 to 1.0 ($\mu_y = 0$)

$y{:}N(\mu_y,\ \sigma_y^2)$										
	μ_y	0	0	0	0	0	0	0	0	0	0
	σ_y	0.10	0.20	0.30	0.40	0.50	0.60	0.70	0.80	0.90	1.00
	μ_x	1.0005	1.020	1.046	1.083	1.133	1.019	1.278	1.377	1.499	1.649
$x{:}LN(\mu_x, \sigma_x^2)$	σ_x	0.101	0.206	0.321	0.451	0.604	0.788	1.016	1.304	1.675	2.161
	c_x	0.100	0.202	0.307	0.417	0.533	0.658	0.795	0.947	1.117	1.311
	F(x)	Values of x_α for $F(x_\alpha) = \alpha$									
	0.01	0.792	0.628	0.498	0.394	0.312	0.248	0.196	0.156	0.123	0.098
	0.02	0.814	0.663	0.540	0.440	0.358	0.292	0.237	0.193	0.157	0.128
	0.03	0.829	0.686	0.569	0.471	0.390	0.324	0.268	0.222	0.184	0.152
	0.04	0.839	0.705	0.591	0.496	0.417	0.350	0.294	0.246	0.207	0.174
	0.05	0.848	0.720	0.611	0.518	0.439	0.373	0.316	0.268	0.228	0.193
	0.10	0.880	0.774	0.681	0.599	0.527	0.464	0.408	0.359	0.316	0.278
	0.15	0.902	0.813	0.733	0.661	0.596	0.537	0.484	0.436	0.393	0.355
	0.20	0.919	0.845	0.777	0.714	0.657	0.604	0.555	0.510	0.469	0.431
	0.25	0.935	0.874	0.817	0.764	0.714	0.667	0.624	0.583	0.545	0.509
	0.30	0.949	0.900	0.854	0.811	0.769	0.730	0.693	0.657	0.624	0.592
	0.35	0.962	0.926	0.891	0.857	0.825	0.794	0.764	0.735	0.707	0.680
	0.40	0.975	0.951	0.927	0.904	0.881	0.859	0.837	0.817	0.796	0.776
	0.45	0.988	0.975	0.963	0.951	0.939	0.927	0.916	0.904	0.893	0.882

0.50	1.000	1.000	1.000	1.000	1.000	1.000	1.000	1.000	1.000	1.000
0.55	1.013	1.025	1.038	1.052	1.065	1.078	1.092	1.106	1.120	1.134
0.60	1.026	1.052	1.079	1.107	1.135	1.164	1.194	1.225	1.256	1.288
0.65	1.039	1.080	1.123	1.167	1.212	1.260	1.310	1.361	1.415	1.470
0.70	1.054	1.111	1.170	1.233	1.300	1.370	1.444	1.521	1.603	1.689
0.75	1.070	1.144	1.224	1.310	1.401	1.499	1.603	1.715	1.835	1.963
0.80	1.088	1.183	1.287	1.400	1.523	1.657	1.802	1.961	2.133	2.320
0.85	1.109	1.230	1.365	1.514	1.679	1.862	2.066	2.291	2.542	2.819
0.90	1.137	1.292	1.469	1.670	1.898	2.157	2.452	2.788	3.169	3.602
0.95	1.179	1.390	1.638	1.931	2.276	2.683	3.163	3.728	4.395	5.180
0.96	1.191	1.419	1.691	2.014	2.400	2.859	3.406	4.057	4.834	5.759
0.97	1.207	1.457	1.758	2.122	2.561	3.091	3.731	4.502	5.434	6.559
0.98	1.228	1.508	1.852	2.274	2.792	3.429	4.221	5.171	6.349	7.797
0.99	1.262	1.592	2.010	2.536	3.200	4.038	5.096	6.431	8.115	10.24